Research Topics

Electromicrobiology – from electrons to ecosystems, volume II

Edited by
Nils Risgaard-Petersen and Amelia-Elena Rotaru

Published in
Frontiers in Microbiology

ISSN 1664-8714
ISBN 978-2-8325-3177-8
DOI 10.3389/978-2-8325-3177-8

About Frontiers

Frontiers is more than just an open access publisher of scholarly articles: it is a pioneering approach to the world of academia, radically improving the way scholarly research is managed. The grand vision of Frontiers is a world where all people have an equal opportunity to seek, share and generate knowledge. Frontiers provides immediate and permanent online open access to all its publications, but this alone is not enough to realize our grand goals.

Frontiers journal series

The Frontiers journal series is a multi-tier and interdisciplinary set of open-access, online journals, promising a paradigm shift from the current review, selection and dissemination processes in academic publishing. All Frontiers journals are driven by researchers for researchers; therefore, they constitute a service to the scholarly community. At the same time, the *Frontiers journal series* operates on a revolutionary invention, the tiered publishing system, initially addressing specific communities of scholars, and gradually climbing up to broader public understanding, thus serving the interests of the lay society, too.

Dedication to quality

Each Frontiers article is a landmark of the highest quality, thanks to genuinely collaborative interactions between authors and review editors, who include some of the world's best academicians. Research must be certified by peers before entering a stream of knowledge that may eventually reach the public - and shape society; therefore, Frontiers only applies the most rigorous and unbiased reviews. Frontiers revolutionizes research publishing by freely delivering the most outstanding research, evaluated with no bias from both the academic and social point of view. By applying the most advanced information technologies, Frontiers is catapulting scholarly publishing into a new generation.

What are Frontiers Research Topics?

Frontiers Research Topics are very popular trademarks of the *Frontiers journals series*: they are collections of at least ten articles, all centered on a particular subject. With their unique mix of varied contributions from Original Research to Review Articles, Frontiers Research Topics unify the most influential researchers, the latest key findings and historical advances in a hot research area.

Find out more on how to host your own Frontiers Research Topic or contribute to one as an author by contacting the Frontiers editorial office: frontiersin.org/about/contact

Electromicrobiology – from electrons to ecosystems, volume II

Topic editors
Nils Risgaard-Petersen — Aarhus University, Denmark
Amelia-Elena Rotaru — University of Southern Denmark, Denmark

Citation
Risgaard-Petersen, N., Rotaru, A.-E., eds. (2023). *Electromicrobiology – from electrons to ecosystems, volume II*. Lausanne: Frontiers Media SA.
doi: 10.3389/978-2-8325-3177-8

Table of contents

frontiers | Frontiers in Microbiology

TYPE Editorial
PUBLISHED 24 July 2023
DOI 10.3389/fmicb.2023.1253550

Editorial: Electromicrobiology—from electrons to ecosystems, volume II

Nils Risgaard-Petersen[1] and Amelia-Elena Rotaru[2]*

[1]Department of Bioscience, University of Aarhus, Aarhus, Denmark, [2]Department of Biology, University of Southern Denmark, Odense, Denmark

KEYWORDS

electromicrobiology, cable bacteria, extracellular electron transfer, bioelectrochemical technologies, *Geobacter*

OPEN ACCESS

EDITED AND REVIEWED BY
Bradley M. Tebo,
Oregon Health and Science University,
United States

*CORRESPONDENCE
Amelia-Elena Rotaru
✉ arotaru@biology.sdu.dk

RECEIVED 05 July 2023
ACCEPTED 11 July 2023
PUBLISHED 24 July 2023

CITATION
Risgaard-Petersen N and Rotaru A-E (2023) Editorial: Electromicrobiology—from electrons to ecosystems, volume II.
Front. Microbiol. 14:1253550.
doi: 10.3389/fmicb.2023.1253550

Editorial on the Research Topic
Electromicrobiology—from electrons to ecosystems, volume II

Introduction

Electromicrobiology is the study of microorganisms that have evolved the ability to exchange electrons with the extracellular environment via Extracellular Electron Transfer or EET. This ability allows them to exchange electrons with one another and to exploit electron acceptors and donors that are distantly located or cannot pass the cell envelope. As a research field, electromicrobiology is young and multidisciplinary, with many questions to address, including the diversity of EET mechanisms, cellular structures involved in EET, and the role of EET microorganisms in ecosystem functioning and future biotechnologies.

In this Research Topic "*Electromicrobiology—From Electrons to Ecosystems*"—*Volume II*, we collect recent advancements regarding the ecology, physiology, and applications of microorganisms capable of extracellular electron transfer. Some of the articles in this collection deal with cable bacteria, their interactions with their environment or other microorganisms, and their potential as bioremediation agents. Others deal with mechanistic aspects of extracellular electron transfer in both model and non-model organisms and biotechnologies relying on such properties.

Diversity of EET mechanisms

To harness the metabolic potential of electroactive microorganisms, it is crucial to understand how cells exchange electrons with the extracellular environment. Until now, extracellular electron transfer (EET) has been studied primarily on model microorganisms like *Geobacter sulfurreducens* and *Shewanella oneidensis*. In *S. oneidensis*, EET has been unequivocally pinned on a porin-multiheme c-type cytochrome complex (Clarke, 2022). On the other hand, in *G. sulfurreducens*, the electron transfer mechanism is assumed to either use a network of conductive molecules (type IV pili and multiheme cytochromes/MHCs) or solely multiheme cytochromes (Clarke, 2022). Recently, Gu et al. (2021) disputed the involvement of pili in EET. Instead, the authors suggest that pili play a secretory role, helping translocate multiheme cytochromes. In this volume, Lovley presents his counterarguments pointing at the role of pili in EET. It was particularly compelling that genetic manipulations modifying the aromatic amino acid content of pili resulted in variable conductivities that correlated to variable growth performances when performing EET. For example, lessening the aromatic amino acid content leads to a 1,000-fold less conductive structure, which is ineffective for EET. On the other hand, increasing the aromatic amino acid content, leads to a 5,000-fold more conductive structure that is more effective for EET.

It remains unclear why *Geobacter* employs type IV pili alongside MHCs. They may do so to ensure access to electron acceptors that are spatially far away from the cell surface.

Geobacter uses different sets of multiheme c-type cytochromes (MHCs) to access electron acceptors with dissimilar reductive potentials (Clarke, 2022). To accesses electron acceptors with redox potentials below −100 mV, *Geobacter* requires CbcL on the inner membrane and OmcZ on the outer membrane. In this volume, Antunes et al. studied in detail the structure of CbcL and how it injects electrons from the inner membrane into the periplasm of the cell. CbcL formed a redox complex with a periplasmic MHC—PpcA through which electrons get injected from the inner membrane into the periplasm, from one MHC to another.

Geobacter can also use its MHCs to reduce toxic metal salts like Co^{3+}, V^{5+}, or Cr^{6+}. In the present volume, Karamash et al. link the reduction of toxic metal salts like Co^{3+}, V^{5+}, or Cr^{6+} to Fe^{2+}/heme concentrations. They observed that a mutant strain, lacking four multiheme cytochromes Δ*omcBSTE* (lacking genes for OmcB, OmcS, OmcT, OmcE), could still reduce toxic metal ions. It is likely that other extracellular multiheme cytochromes, like OmcZ, are used to reduce toxic metal ions as they were for reducing the toxic radionuclide U^{6+} (Orellana et al., 2013).

In non-model organisms, extracellular electron transfer (EET) mechanisms remain obscure. To identify essential components for EET in non-model organisms Sackett et al., used genome-wide transposon mutagenesis and high-throughput sequencing (Tn-Seq) to probe the genetic underpinnings for oxidative EET by *Thioclava electrotropha*. Only 14 genes were identified as membrane-bound and essential for oxidative EET. None of the encoded proteins contain typical redox-active centers, so how precisely *T. electrotropha* does EET remains to be uncovered.

Cable bacteria

Cable bacteria are electrically conducting filamentous bacteria of the Desulfubulbaceae family that have been discovered 10 years ago (Pfeffer et al., 2012). Cable bacteria have been found in various environments, including marine and freshwater sediments.

One of the essential functions of cable bacteria in the environment is their role in cycling nutrients and metals (Risgaard-Petersen et al., 2012). It has been suggested that cable bacteria have a role in bioremediation (Marzocchi et al., 2020). Conflicting reports indicate that they can either have a detrimental or a beneficial effect on the environment. Detrimental effects include disturbances of nitrogen (Kessler et al., 2019; Marzocchi et al., 2022) and phosphorus cycles (Sulu-Gambari et al., 2016). Beneficial effects includes reducing methane fluxes (Scholz et al., 2020), protecting against euxinia (Seitaj et al., 2015), and against the release of contaminants (van de Velde et al., 2017). In this volume, van de Velde et al. show that cable bacteria have a seasonal impact on the flux of arsenic from uncontaminated sediments to the water column. Cable bacteria act as a barrier in spring, building an iron oxide layer that sequesters arsenic. On the other hand, during the summer, this barrier disperses when anoxia is established, and arsenic fluxes become comparable to those measured in contaminated marine sediments. Additionally, Vasquez-Cardenas et al. investigate the detoxifying role of cable bacteria on Icelandic coastal sediments exposed to fish farming where substantial sedimentation of organic-rich particle leads to euxinic conditions. Cable bacteria and other sulfur oxidizers were anticipated to act as ecosystem engineers and detoxify sulfide. However, the authors did not detect significant cable bacteria activity in these sediments. It could be because sulfide accumulated above the highest limit reported for cable bacteria activity or because it is challenging to detect the cables' electroactive signals in these fish farm sediments constantly perturbed by particle input and bioturbation. Lab tests indicate that removal of the particle input increases cable bacteria activity and that of associated microorganisms, detoxifying sulfide effectively. The authors advise removing top sediment below fish farms during the fallow periods to ensure the buildup of the cable bacteria iron curtain fighting sulfide emissions and euxinia.

The activity of cable bacteria changes the sediment geochemistry influencing the surrounding microbial communities. Cable bacteria are surrounded by a veil of microorganisms that swim around them (Thorup et al., 2021). These veil microorganisms dispersed once the cable bacterium was physically cut (Bjerg et al., 2023). In this volume, Lustermans et al. investigate whether the presence of the microbial veil is connected to a cable bacteria progression and senescence in its environment and the subsequent geochemical changes. The authors follow the progression of a *Ca.* Electronema aureum from a single cable bacterium to a cable bacteria community, the activity of its veil microbiome and local geochemical changes. They observed a veil of swarming cells surrounding living and motile cable bacteria. In contrast, dead and non-motile cable bacteria were not surrounded by their associated microbial veil. Surprisingly, geochemical parameters did not appear to impact the veil activity.

Digging deeper into the physiology of cable bacteria, Geerlings et al. investigate the dynamics of polyphosphates in cable bacteria. Polyphosphates are one of the most widely distributed biopolymers and have been observed in both Archaea and Bacteria, where they have been associated with functions like regulation of gene expression and enzyme activity, response to oxidative stress, signaling, and cation sequestration (Rao et al., 2009). For cable bacteria, polyphosphates have been observed in both marine and freshwater strains (Sulu-Gambari et al., 2016; Geerlings et al.). It has been hypothesized that these phosphates act as a substitute for ATP or protect cable bacteria against oxidative stress (Kjeldsen et al., 2019; Geerlings et al., 2020). Here, Geerlings et al. dismiss that polyphosphates are used for ATP synthesis in cable bacteria by looking at the spatial-temporal dynamics of polyphosphate using labeling experiments and state-of-the-art chemical imaging.

The authors now anticipate that cable bacteria use polyphosphates to protect against oxidative stress, and perhaps for motility and gene regulation.

Applications

Electrons are transported across the cell wall via biological polymers like pili or MHCs. These biopolymers spatially separate oxidative metabolic reactions from the reduction of the terminal electron acceptor, with the first happening inside the cell and the second outside. The properties of these biopolymers, electrical conduction, ability to self-assemble and self-repair make them attractive in fabricating sustainable and biodegradable nano-electronic devices. On the other hand, the possibility to drive spatially distant redox reactions gives rise to macroscale applications like electrochemically assisted wetland treatment.

In this volume, Bonné et al. present an insightful review regarding emerging applications for conductive biological polymers like pilins (stacked peptides rich in aromatic aminoacids), multiheme cytochromes (stacked proteins with Fe-centers) and the conductive fibers extending along cable bacteria filaments. The first, pilins, have been applied in building nanowire sensors (Smith et al., 2020). The latter, cable bacteria fibers, are centimeter–long, with conductivities above any other biological nanowires and therefore promising for biodegradable electronics (Bonné et al.).

Bioelectrochemical technologies employ electroactive microorganisms as biocatalysts. A few of the applications relying on EET-metabolisms are: promoting the degradation of organics in wastewater (Yadav et al., 2023), facilitating the bioremediation of toxic pollutants (Wang et al., 2020), sensing the presence of pollutants in the environment (Smith et al., 2020), enabling methane, or other chemical syntheses (Roy et al., 2022).

Since certain bioelectrochemical technologies are intended to bioremediate environmental pollutants from sediments, it is imperative to understand how bioelectrochemical technologies impact macrofauna in sediments. Shono et al. looked at the impact of voltage exposure on an oligochaete, *Thalassodrilides* cf. *briani,* which is often found in polluted environments and is effective at cleaning up organic pollutants (Ito et al., 2016). The oligochete responded with reversible changes in movements and metabolism in response to increased organic load and dynamic fluctuations in sediment redox potential. After heavy organic input, the sediments and the macrofauna exhibited rapid recovery. However, a too-high organic input below fish-farming rafts may be fatal to the oligochete population; therefore, monitoring the redox-potential changes could be promising for informing when fishery farms could reinitiate farming after fallow periods.

Last but not least, Peñacoba-Antona et al. present how treatment of wasteland could be bioelectrochemicaly assisted at full scale. The technology is known as METland and is expected to be an effective solution to treating wastewaters in decentralized locations. The authors monitor the bioelectrochemical behavior of two full scale METlands, one in Spain and one in Denmark. They reveal that electron current density could be used as an indicator for effective removal of organic matter.

In this volume, authors unveiled new properties of electroactive microorganisms, new physiology, and new roles in ecosystem functioning. At the nanoscale, authors showed we could develop applications for electron-conducting biopolymers. At the macroscale, the metabolic responses of electroactive microorganisms could be used to sense pollutants or applied at full scale in pollutant removal technologies like METland. Harnessing the metabolic potential of electroactive microorganisms is seen as a commodity for future sustainable technologies. Therefore, a better understanding of microorganisms capable of EET is fundamental to future developments.

Author contributions

All authors listed have made a substantial, direct, and intellectual contribution to the work and approved it for publication.

Funding

A-ER was supported by the Novo Nordisk Foundation grant NNF21OC0067353, the Danish Research Council grant DFF 1026-00159, and the European Research Council ERC-CoG grant 101045149.

Conflict of interest

The authors declare that the research was conducted in the absence of any commercial or financial relationships that could be construed as a potential conflict of interest.

Publisher's note

References

Bjerg, J. J., Lustermans, J. J. M., Marshall, I. P. G., Mueller, A. J., Brokjær, S., Thorup, C. A., et al. (2023). Cable bacteria with electric connection to oxygen attract flocks of diverse bacteria. *Nat. Commun.* 14:1614. doi: 10.1038/s41467-023-37272-8

Clarke, T. A. (2022). Plugging into bacterial nanowires: a comparison of model electrogenic organisms. *Curr. Opin. Microbiol.* 66, 56–62. doi: 10.1016/j.mib.2021.12.003

Geerlings, N. M. J., Karman, C., Trashin, S., As, K. S., Kienhuis, M. V. M., Hidalgo-Martinez, S., et al. (2020). Division of labor and growth during electrical cooperation in multicellular cable bacteria. *Proc. Natl. Acad. Sci. U.S.A.* 117, 5478–5485. doi: 10.1073/pnas.1916244117

Gu, Y., Srikanth, V., Salazar-Morales, A. I., Jain, R., O'Brien, J. P., Yi, S. M., et al. (2021). Structure of Geobacter pili reveals secretory rather than nanowire behaviour. *Nature* 597, 430–434. doi: 10.1038/s41586-021-03857-w

Ito, M., Ito, K., Ohta, K., Hano, T., Onduka, T., Mochida, K., et al. (2016). Evaluation of bioremediation potential of three benthic annelids in organically polluted marine sediment. *Chemosphere* 163, 392–399. doi: 10.1016/j.chemosphere.2016.08.046

Kessler, A. J., Wawryk, M., Marzocchi, U., Roberts, K. L., Wong, W. W., Risgaard-Petersen, N., et al. (2019). Cable bacteria promote DNRA through iron sulfide dissolution. *Limnol. Oceanogr.* 64, 1228–1238. doi: 10.1002/lno.11110

Kjeldsen, K. U., Schreiber, L., Thorup, C. A., Boesen, T., Bjerg, J. T., Yang, T., et al. (2019). On the evolution and physiology of cable bacteria. *Proc. Natl. Acad. Sci. U.S.A.* 116, 19116–19125. doi: 10.1073/pnas.1903514116

Marzocchi, U., Palma, E., Rossetti, S., Aulenta, F., and Scoma, A. (2020). Parallel artificial and biological electric circuits power petroleum decontamination: the case of snorkel and cable bacteria. *Water Res.* 173:115520. doi: 10.1016/j.watres.2020.115520

Marzocchi, U., Thorup, C., Dam, A.-S., Schramm, A., and Risgaard-Petersen, N. (2022). Dissimilatory nitrate reduction by a freshwater cable bacterium. *ISME J.* 16, 50–57. doi: 10.1038/s41396-021-01048-z

Orellana, R., Leavitt, J. J., Comolli, L. R., Csencsits, R., Janot, N., Flanagan, K. A., et al. (2013). U(VI) reduction by diverse outer surface *c* -type cytochromes of *Geobacter sulfurreducens. Appl. Environ. Microbiol.* 79, 6369–6374. doi: 10.1128/AEM.02551-13

Pfeffer, C., Larsen, S., Song, J., Dong, M., Besenbacher, F., Meyer, R. L., et al. (2012). Filamentous bacteria transport electrons over centimetre distances. *Nature* 491, 218–221. doi: 10.1038/nature11586

Rao, N. N., Gómez-García, M. R., and Kornberg, A. (2009). Inorganic polyphosphate: essential for growth and survival. *Annu. Rev. Biochem.* 78, 605–647. doi: 10.1146/annurev.biochem.77.083007.093039

Risgaard-Petersen, N., Revil, A., Meister, P., and Nielsen, L. P. (2012). Sulfur, iron-, and calcium cycling associated with natural electric currents running through marine sediment. *Geochim. Cosmochim. Acta* 92, 1–13. doi: 10.1016/j.gca.2012.05.036

Roy, M., Aryal, N., Zhang, Y., Patil, S. A., and Pant, D. (2022). Technological progress and readiness level of microbial electrosynthesis and electrofermentation for carbon dioxide and organic wastes valorization. *Curr. Opin. Green Sustain. Chem.* 35:100605. doi: 10.1016/j.cogsc.2022.100605

Scholz, V. V., Meckenstock, R. U., Nielsen, L. P., and Risgaard-Petersen, N. (2020). Cable bacteria reduce methane emissions from rice-vegetated soils. *Nat. Commun.* 11:1878. doi: 10.1038/s41467-020-15812-w

Seitaj, D., Schauer, R., Sulu-Gambari, F., Hidalgo-Martinez, S., Malkin, S. Y., Burdorf, L. D. W., et al. (2015). Cable bacteria generate a firewall against euxinia in seasonally hypoxic basins. *Proc. Natl. Acad. Sci. U.S.A.* 112, 13278–13283. doi: 10.1073/pnas.1510152112

Smith, A. F., Liu, X., Woodard, T. L., Fu, T., Emrick, T., Jiménez, J. M., et al. (2020). Bioelectronic protein nanowire sensors for ammonia detection. *Nano Res.* 13, 1479–1484. doi: 10.1007/s12274-020-2825-6

Sulu-Gambari, F., Seitaj, D., Meysman, F. J. R., Schauer, R., Polerecky, L., and Slomp, C. P. (2016). Cable bacteria control iron–phosphorus dynamics in sediments of a coastal hypoxic basin. *Environ. Sci. Technol.* 50, 1227–1233. doi: 10.1021/acs.est.5b04369

Thorup, C., Petro, C., Bøggild, A., Ebsen, T. S., Brokjær, S., Nielsen, L. P., et al. (2021). How to grow your cable bacteria: establishment of a stable single-strain culture in sediment and proposal of Candidatus Electronema aureum GS. *Syst. Appl. Microbiol.* 44:26236. doi: 10.1016/j.syapm.2021.126236

van de Velde, S., Callebaut, I., Gao, Y., and Meysman, F. J. R. (2017). Impact of electrogenic sulfur oxidation on trace metal cycling in a coastal sediment. *Chem. Geol.* 452, 9–23. doi: 10.1016/j.chemgeo.2017.01.028

Wang, X., Aulenta, F., Puig, S., Esteve-Núñez, A., He, Y., Mu, Y., et al. (2020). Microbial electrochemistry for bioremediation. *Environ. Sci. Ecotechnol.* 1:100013. doi: 10.1016/j.ese.2020.100013

Yadav, R. K., Das, S., and Patil, S. A. (2023). Are integrated bioelectrochemical technologies feasible for wastewater management? *Trends Biotechnol.* 41, 484–496. doi: 10.1016/j.tibtech.2022.09.001

frontiers | Frontiers in Microbiology

ORIGINAL RESEARCH
published: 05 April 2022
doi: 10.3389/fmicb.2022.843135

Microbial Electrochemically Assisted Treatment Wetlands: Current Flow Density as a Performance Indicator in Real-Scale Systems in Mediterranean and Northern European Locations

*Lorena Peñacoba-Antona[1,2,3]†, Carlos Andres Ramirez-Vargas[4,5]†, Colin Wardman[1,3], Alessandro A. Carmona-Martinez[1], Abraham Esteve-Núñez[3], Diego Paredes[6], Hans Brix[4,5] and Carlos Alberto Arias[4,5]**

[1] IMDEA Water, Parque Científico Tecnológico, Universidad de Alcalá, Madrid, Spain, [2] METfilter S.L., Seville, Spain, [3] Department of Analytical Chemistry, Physical Chemistry and Chemical Engineering, University of Alcalá, Madrid, Spain, [4] WATEC, Aarhus University, Aarhus, Denmark, [5] Department of Biology—Aquatic Biology, Aarhus University, Aarhus, Denmark, [6] Water and Sanitation Research Group (GIAS), Universidad Tecnológica de Pereira, Pereira, Colombia

OPEN ACCESS

Edited by:
Amelia-Elena Rotaru,
University of Southern Denmark, Denmark

Reviewed by:
Tian Li,
Nankai University, China
Nannan Zhao,
Zhejiang Gongshang University, China

***Correspondence:**
Carlos Alberto Arias
carlos.arias@bio.au.dk

† These authors have contributed equally to this work and share first authorship

Specialty section:
This article was submitted to Microbiological Chemistry and Geomicrobiology, a section of the journal Frontiers in Microbiology

Received: *24 December 2021*
Accepted: *14 February 2022*
Published: *05 April 2022*

Citation:
Peñacoba-Antona L, Ramirez-Vargas CA, Wardman C, Carmona-Martinez AA, Esteve-Núñez A, Paredes D, Brix H and Arias CA (2022) Microbial Electrochemically Assisted Treatment Wetlands: Current Flow Density as a Performance Indicator in Real-Scale Systems in Mediterranean and Northern European Locations. Front. Microbiol. 13:843135. doi: 10.3389/fmicb.2022.843135

A METland is an innovative treatment wetland (TW) that relies on the stimulation of electroactive bacteria (EAB) to enhance the degradation of pollutants. The METland is designed in a short-circuit mode (in the absence of an external circuit) using an electroconductive bed capable of accepting electrons from the microbial metabolism of pollutants. Although METlands are proven to be highly efficient in removing organic pollutants, the study of *in situ* EAB activity in full-scale systems is a challenge due to the absence of a two-electrode configuration. For the first time, four independent full-scale METland systems were tested for the removal of organic pollutants and nutrients, establishing a correlation with the electroactive response generated by the presence of EAB. The removal efficiency of the systems was enhanced by plants and mixed oxic–anoxic conditions, with an average removal of 56 g of chemical oxygen demand (COD) $m_{\text{bed material}}{}^{-3}$ day^{-1} and 2 g of total nitrogen (TN) $m_{\text{bed material}}{}^{-3}$ day^{-1} for Ørby 2 (partially saturated system). The estimated electron current density (*J*) provides evidence of the presence of EAB and its relationship with the removal of organic matter. The tested METland systems reached the max. values of 188.14 mA m^{-2} (planted system; IMDEA 1), 223.84 mA m^{-2} (non-planted system; IMDEA 2), 125.96 mA m^{-2} (full saturated system; Ørby 1), and 123.01 mA m^{-2} (partially saturated system; Ørby 2). These electron flow values were remarkable for systems that were not designed for energy harvesting and unequivocally show how electrons circulate even in the absence of a two-electrode system. The relation between organic load rate (OLR) at the inlet and coulombic efficiency (CE; %) showed a decreasing trend, with values ranging from 8.8 to 53% (OLR from 2.0 to 16.4 g COD m^{-2} day^{-1}) for IMDEA systems and from 0.8 to 2.5%

(OLR from 41.9 to 45.6 g COD m^{-2} day^{-1}) for Ørby systems. This pattern denotes that the treatment of complex mixtures such as real wastewater with high and variable OLR should not necessarily result in high CE values. METland technology was validated as an innovative and efficient solution for treating wastewater for decentralized locations.

Keywords: constructed wetlands (CWs), electric potential sensor, electroactive bacteria (EAB), microbial electrochemical snorkel, METland, real-scale

INTRODUCTION

The treatment wetland (TW; a.k.a. as constructed wetlands—CW) is an engineered and sustainable nature-based system for the treatment and pretreatment of wastewaters of different origins (Langergraber et al., 2019). These systems mimic and optimize the physical, chemical, and biological processes occurring in natural wetlands (Dotro et al., 2017). These interactions lead to the occurrence of different mechanisms for pollutant removal, such as precipitation, sedimentation, filtration, volatilization, adsorption, plant uptake, and microbial-driven degradation (Kadlec and Wallace, 2008). The removal efficiency of TWs is determined by their design, operative settings (loading rate, loading pattern, etc.), and environmental conditions inside the wetland bed (e.g., substrate type, pH, temperature, dissolved oxygen, and redox conditions) (Wu et al., 2015). The TW is considered a robust and cost-effective technology that offers low-effort operation and maintenance, hence, is being extensively used worldwide as a developed decentralized wastewater treatment solution (Brix et al., 2007; Vymazal, 2009; Langergraber and Masi, 2018). However, one of the limiting factors of TW implementation is the footprint required to reach the desired treatment targets, which is much larger when compared with other conventional wastewater treatment technologies (Dotro et al., 2017). Therefore, to minimize surface area requirements, the use of more conventional treatment solutions or intensified wetland-based systems must be considered (Langergraber et al., 2019).

In the last decade, a combination of TWs with electrobioremediation strategies has been developed aiming at the intensification of TWs (Wang et al., 2020). Electrobioremediation relies on the metabolic activity of electroactive bacteria (EAB) capable of exchanging electrons from metabolism with electroconductive materials (Aguirre-Sierra et al., 2016; Ramírez-Vargas et al., 2018). EAB have been identified in different environments including natural aquatic sediments, aerobic/anaerobic sludge from wastewater treatment facilities, and also in wastewater (Aguirre-Sierra et al., 2016; Ramírez-Vargas et al., 2020). In microbial electrochemically assisted TW systems, several EAB strains have been identified as able to grow as electroactive biofilms. These biofilms are composed mainly, but not exclusively, of microorganisms from *Desulfuromonas*, *Pseudomonas*, *Shewanella*, and *Geobacter* genera (Aguirre-Sierra et al., 2016; Ramírez-Vargas et al., 2019; Saba et al., 2019; Rotaru et al., 2021). TWs operating under water-saturated conditions are anaerobic along almost their entire depth profile with anoxic/aerobic conditions only occurring in the uppermost section of the system at the water–air interface (Aguirre et al., 2005). These conditions generate a natural redox profile that matches the gradient of ions and electrons reported in other microbial electrochemical technologies (MET) such as microbial fuel cells (MFC) and combined TW–MFC systems (Yadav et al., 2012; Doherty et al., 2015a; Ramírez-Vargas et al., 2018; Kabutey et al., 2019; Srivastava et al., 2020). Applications of TW–MFCs at laboratory scale have expanded from treating conventional pollutants (Oon et al., 2016) and nutrients (Wang et al., 2016), to more persistent compounds such as oil (Yang et al., 2016), pharmaceuticals, or heavy metals (Nitisoravut and Regmi, 2017). Such studies show satisfactory removal rates and energy yields at a laboratory scale, but there are technical challenges to scale up these technologies and reach energy harvesting comparable with other sustainable sources.

In contrast with TW–MFCs, a different design has been developed in the past years by using an electroconductive bed under short circuit (snorkel configuration). Such system's only aim is to optimize wastewater treatment and is known as microbial electrochemically assisted TW, or the METland®. In METlands, EAB growth is stimulated by transferring electrons to an electroconductive material that acts as an unlimited acceptor, therefore maximizing organic pollutant oxidation (Esteve-Núñez, 2015). The METland operates as a microbial electrochemical snorkel (Erable et al., 2011) using a conductive material to connect anoxic (anode) and oxic zones (cathode). Aguirre-Sierra et al. (2016) tested the first laboratory-scale METland for the removal of organic pollutants and nitrogen from real urban wastewater. The flooded configuration showed removal rates of 91% for chemical oxygen demand (COD) and 96% for biochemical oxygen demand (BOD_5) (HRT = 0.5 day), 97% for NH_4–N, and 69% for total nitrogen (TN) (HRT = 3.5 days). Similar results were shown by Ramírez-Vargas et al. (2019), in terms of organic removal rates using mesocosm set-ups treating real wastewater at loading rates of approximately 60 g m^{-2} day^{-1} and reached removal efficiencies of 90% for COD, 88% for BOD, 46% for NH_4–N, and 86% for PO_4–P. Interestingly, METlands can also be operated under non-flooded downflow conditions. Unexpectedly, EAB like *Geobacter* were found to coexist with nitrifying microorganisms, a system under oxic conditions (Aguirre-Sierra et al., 2020). Most recently, Prado et al. (2020) reported removals of up to 95% for COD and 71% for TN with the integration of an artificial device, the e-sink, for consuming electrons. These results suggest that the METland system can enhance biodegradation rates, reducing the footprint of classical TWs by 10-fold (Peñacoba-Antona et al., 2021b).

Moreover, direct and accurate measurements of the bioelectrochemical reactions in a METland system have been a challenge. The lack of electrodes and external circuits did not allow for the monitoring of electrical current flowing between an anode and a cathode. However, the charge imbalance due to the activity of electroactive biofilms inside a METland system is similar to the electrochemical potential differences between anodic and cathodic regions that exist in certain environments, as in the biogeobattery model (Ptushenko, 2020). Such charge differences create electric potentials (EPs) that trigger ionic/electron fluxes that can be detected in electrolyte conductors (Nielsen and Risgaard-Petersen, 2015). To detect those fluxes, tailor-made EP sensors could be used (Damgaard et al., 2014). These devices can collect low current signals in highly conductive matrixes and are insensitive to redox-active compounds that can affect EP readings. The measurement of EPs in METlands has been previously reported at the mesocosm scale (Ramírez-Vargas et al., 2019; Prado et al., 2020).

Based on the hypothesis that high electron currents in an electroactive system are correlated with high removal rates of pollutants, the study aimed to test the removal of organic matter in real-scale METland systems (treating wastewaters of different natures and at different geographical locations) and the correlation with the presence of EAB through the recording of electron current density in the water column. The measure of EP and current density profiles will establish different vertical profile zones in the METland bed regarding their bioelectrochemical activity and, consequently, their electrobioremediation performance. Indeed, the tested electrochemical strategy constitutes a tool for *in situ* monitoring of the performance of this new type of TW.

MATERIALS AND METHODS

Design and Construction of METland Systems

The study was carried out in four full-scale METland systems constructed in two different latitudes: Mediterranean (Spain) and Northern Europe (Denmark) (**Figure 1**). Each location presented climatic and demographic conditions that allowed the testing of the technology under different environmental conditions. For instance, the climate in Southern Denmark is humid, with abundant and frequent precipitation throughout the year and cold winters. On the contrary, summers in the center of Spain are dry with scarce precipitation. Regarding the demographic distribution, decentralized households and small villages characterize southern Denmark. In each location, two METland beds were constructed to treat the local wastewater generated. Each METland system presents different configurations with plants adapted to the local climate. Regarding the wastewater flow, the systems were fed downflow and operated under saturated conditions. The material used as a substrate is an electroconductive coke (ec-coke) with the following characteristics: porosity 48% ± 1%, specific weight 0.8 ± 0.5 g ml^{-1}, granulometry 0.3–1.0 ± 1.0 cm, and resistance 1.5 ± 0.5 Ω.

METland Unit at IMDEA Water (Spain)

The first treatment system was in the facilities of IMDEA Water (Alcalá de Henares, Spain). The system was built in January 2017 and has 5.5-m length, 2-m width, and 1.25-m depth (11 m^2). The TW is divided into two separated chambers (5.5 m^2 each), isolated with high-density polyethylene (HDPE) to avoid water fluxes to and from the beds (**Figure 2**). Each bed was filled with 0.6-m-deep electroconductive material and 0.05 m of gravel at the bottom, engulfing the drainage system built from Ø75 mm PVC perforated pipes. The two beds operated in parallel with a total effective surface area of 11 m^2. The system operated as a vertical subsurface flow TW. The wastewater was distributed over the surface by Ø32-mm pressurized perforated pipes and flowed down through the filtering media. Treated water flowed to a chamber where the water level was controlled by a vertical pipe. The sampling points were in the middle of each bed (A1 and A2).

- IMDEA 1: with an effective surface area of 5.5 m^2 and was planted with three different species, divided into three sections, from the influent to the effluent direction, *Bambusa bambos*, *Typha angustifolia*, and *Iris germanica.*
- IMDEA 2: with an effective surface area of 5.5 m^2 without plants.

During the first year of operation, the system was fed with real urban wastewater generated at the research center in an intermittent flow regime varying from 0.5 to 2.0 m^3 day^{-1}. Solids from raw wastewater were removed by an Imhoff tank as a primary treatment. The influent water shows a low concentration of organic matter, as is expected from wastewater produced by an office building. The COD concentration was in a range of 50–130 mg l^{-1} and TN between 40 and 70 mg l^{-1} mainly in a reduced state (ammonium).

METland Unit at Ørby (Denmark)

A METland unit was built in the municipality of Ørby (Haderslev, Denmark) to treat domestic wastewater produced by a population equivalent (p.e.) of 200, with an effective surface area of 80 m^2 in two beds each of 40 m^2 (10 m × 4 m × 1 m deep). The beds were filled with 0.8-m ec-coke supplied by METfilter (Spain) (**Figure 3**). The wastewater was evenly distributed on the top of the beds. The perforated distribution pipes (PE Ø50 mm) were embedded in gravel to guarantee a homogeneous dispersal of the wastewater on the surface. Once wastewater was distributed on the surface, it flowed vertically down through the bed. Then, it was collected at the bottom by a Ø110-mm pipe manifold to evacuate it from the system to a chamber where the water level was regulated using swirling pipes.

- Ørby 1: a saturated bed with a surface area of 40 m^2.
- Ørby 2: partially saturated bed (water level abated at 20 cm) with a surface area of 40 m^2.

The urban community had a separate sewer system where no runoff was collected. Each of the ca. 40 houses was fitted with a septic tank as primary treatment, so pre-settled wastewater was transported to the treatment units by gravity. Water was collected in a pumping well that works as a homogenization tank before pulse feeding the METlands using a level-controlled pump. Each pulse delivered around 600 l that were evenly discharged on the surface of the beds at a rate of 300 l/pulse to each bed. The

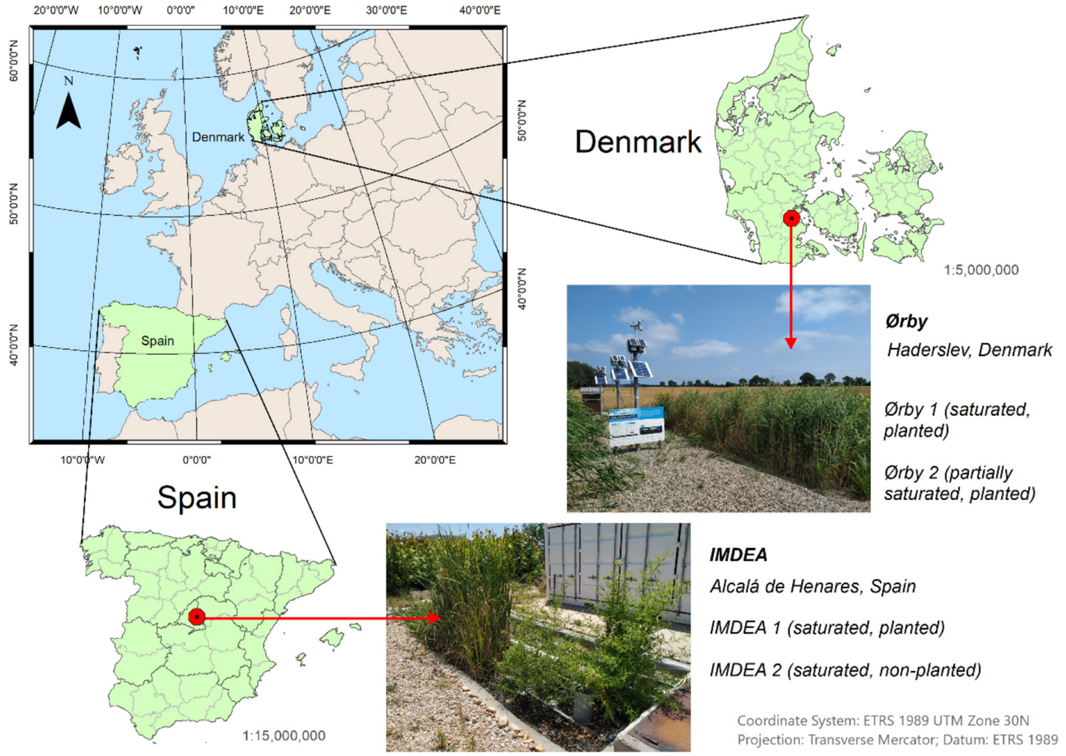

FIGURE 1 | Location map of the METlands analyzed in the study.

frequency of the pulses varied according to the water produced by the urban community, which varied by the day as well as throughout the year. The average wastewater characteristics were as follows: conductivity 1,600 µS cm^{-1}, pH of 7.11, BOD_5 260–510 mg l^{-1}, COD within the range of 540–910 mg l^{-1}, total suspended solids (TSS) up to 100 mg l^{-1}, and TN 60–110 mg l^{-1} mainly corresponding to ammonium. According to the data, the influent wastewater corresponds to an urban-type characterized by high COD and ammonium concentration (Metcalf and Eddy Inc, 2004).

Sampling and Analysis of Pollutants (Physicochemical and Statistical)

Both systems were monitored for a period of 6 weeks, once a week, taking samples of the influent and the effluent for analyzing both organic matter (COD) and nutrients (PO4–P, TN, NH_4–N, and NO_3–N) to determine the removal performance of the systems. *In situ* measurements using calibrated electrodes and meters included pH (Hach PHC101), electrical conductivity (Hach sensION + 5060), temperature, dissolved oxygen (Hach LDO101), and redox potential (Hach MTC101) in the Ørby system. COD analysis was done by photometric evaluation (Hach LCI 400 cuvette test + DR 3900 spectrophotometer); TN was analyzed by combustion catalytic oxidation/NDRI method (Shimadzu TOC-VCPH); whereas orthophosphate (PO_4–P), ammonia (NH_4–N), and nitrate (NO_3–N) were determined by ion chromatography (Lachat QuickChem® 8000). All samples were analyzed following standard methods (APHA, 2012).

The removal efficiency (E) of the systems was evaluated with water measurements and mass balances at inlets and outlets according to Equation 1 (without considering the impact of evapotranspiration, where V_{in} and V_{out} correspond to the water inlet and outlet volume, respectively, and C_{in} and C_{out} correspond to the inlet and outlet concentrations of the monitored pollutants, respectively). Statistical analysis was conducted using the OriginPro 2019 statistical software. Thus, a one-way analysis of variance (ANOVA) was conducted to test the data's statistical significance. The comparison among means was tested with Tukey's test with a significance level of $p < 0.05$ (95% confidence).

$$E = \frac{C_{\text{in}} - C_{\text{out}}}{C_{\text{in}} \times V_{\text{in}}} \times 100\% \tag{1}$$

Microbial Electrochemical Activity

The evaluation of the microbial electrochemical activity of the full-scale METland systems was carried out based on the measurements of the EPs, estimation of ionic current densities (J), coulombic efficiencies (CE), and electron transfer rates. To measure the EP (mV), custom-made sensors, based on the design proposed by Damgaard et al. (2014), were used (h: 60 cm; Ø: 0.12 cm). The sensors were inserted in two different measuring ports in each METland. EP was measured at 1-cm intervals along the depth of the bed, with a resolution of ± 45 s, as previously reported (Ramírez-Vargas et al., 2019; Prado et al., 2020). To

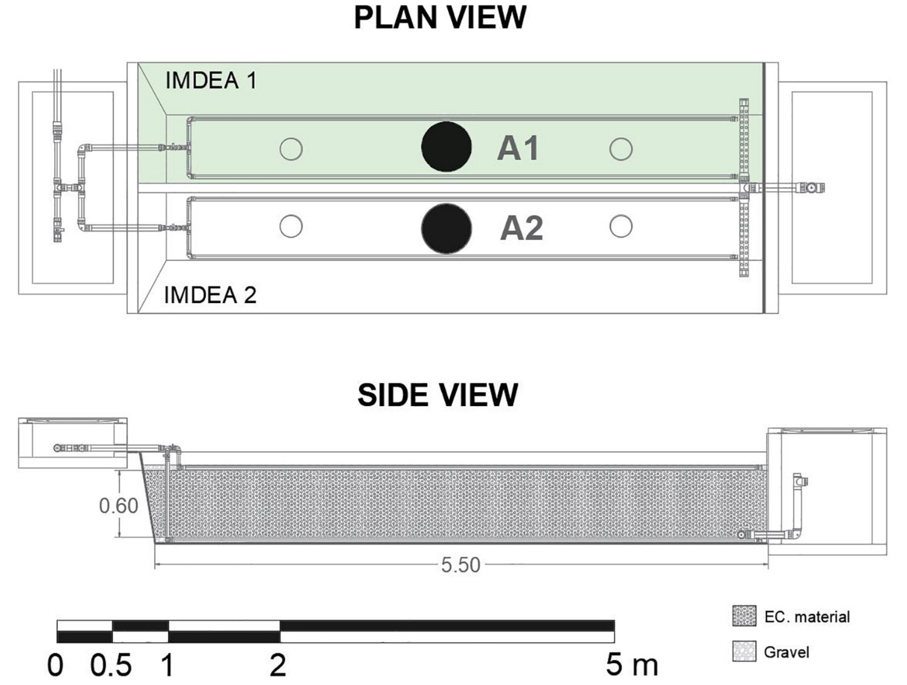

FIGURE 2 | Plan view and profile of the METland system at IMDEA water (Alcalá de Henares). Sample points: A1 = planted with *Bambusa bambos*, *Typha angustifolia*, and *Iris germanica*; A2 = not planted.

ease the graphical representation, the EP values (mV) were normalized using, as reference electrode, the water/atmosphere interface (0 mV at 0-cm depth). The ionic current density was calculated with an adapted version of Ohm's Law (Equation 2) (Nielsen and Risgaard-Petersen, 2015), where J is the ionic current density (A m^{-2}), σ is the electrical conductivity of water in the ports (S m^{-1}), and $d\Psi/dz$ is the EP gradient (V m^{-1}),

$$J = -\sigma \times d\psi/dz \times 1/F \tag{2}$$

The CE, defined as the fraction of electrons recovered as current with regard to the maximum possible recovery from a substrate, was calculated based on Equation 3 (Logan et al., 2006). On Equation 3, M is the molecular weight of oxygen (32 g mol^{-1} O_2), I is the current density (A m^{-2}), F is the Faraday's constant (96,485 C mol^{-1}), b is the number of electrons exchanged per mole of oxygen (4 mol mol^{-1} O_2), q is the hydraulic load rate (l m^{-2} s^{-1}), and ΔCOD is the difference between influent and effluent concentrations of the substrate (g COD l^{-1}),

$$CE\,(\%) = \frac{MI}{Fbq\triangle COD} \times 100 \tag{3}$$

The electron transfer was estimated with an adapted version of the model presented by Risgaard-Petersen et al. (2014) (Equation 4), where R_{agg} is the aggregated electron transfer (μmol l^{-1} day^{-1}) from anodic/cathodic reactions, dJ/dz is the gradient of current density between different levels inside the system (A m^{-3}), and F is the Faraday's constant (96,485 C mol^{-1}),

$$R_{agg} = -dJ/dz \times 1/F \tag{4}$$

RESULTS AND DISCUSSION

Full-scale METlands implemented at Mediterranean and Northern European locations using identical electroconductive material were tested and validated regarding (i) bioremediation performance and (ii) microbial electrochemical behavior. The following results revealed that such a variety of TWs is a promising configuration for treating urban wastewater of different natures.

Treatment Performance

The METlands constructed at Mediterranean (IMDEA) and Northern European (Ørby) locations were operated with real urban wastewater after primary treatment. In the case of IMDEA, the organic load of wastewater from an office building was lower than typical urban wastewater. In the case of Ørby, the organic load from urban wastewater was higher than at IMDEA, but due to seasonal variation, the flow rate was limited to 2 m^3/day. Both situations revealed organic removal rates lower than other METland studies reported in the literature (Aguirre-Sierra et al., 2016; Prado et al., 2019; Ramírez-Vargas et al., 2019; Peñacoba-Antona et al., 2021b). Each system was analyzed independently considering the removal efficiencies based on inlet/outlet concentrations (**Figure 4**).

Case Study for Treating Wastewater From an Office Building (IMDEA Water) at a Mediterranean Location

At IMDEA, the systems reached average removal rates above 10.0 g of COD $m_{\text{bed material}}^{-3}$ day^{-1} (80%), 3.0 g

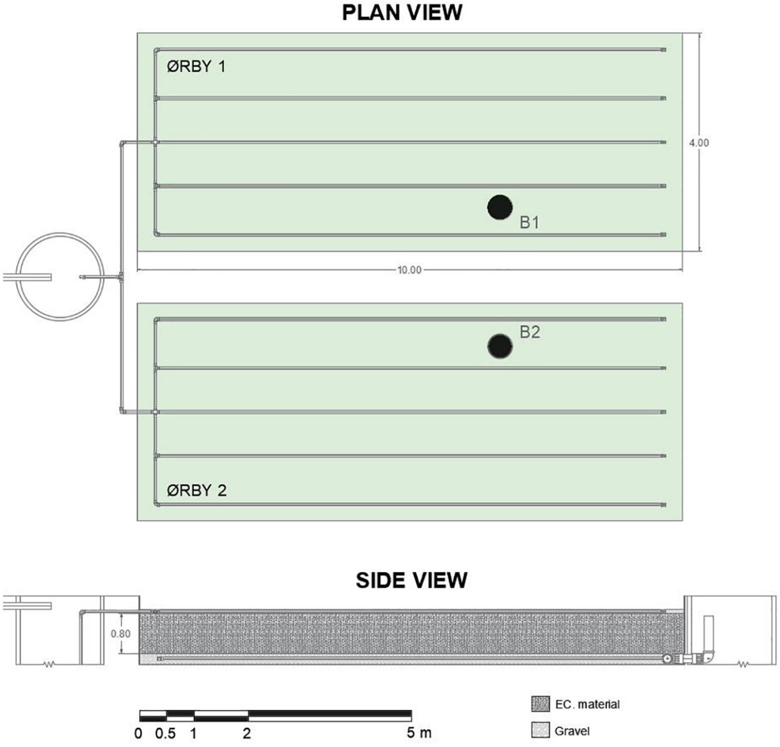

FIGURE 3 | Plan view and profile of the METland system at Ørby. Both parallel systems were planted with *Phragmites australis*. Sample points B1 and B2 were located in the bed at the position marked in the figure.

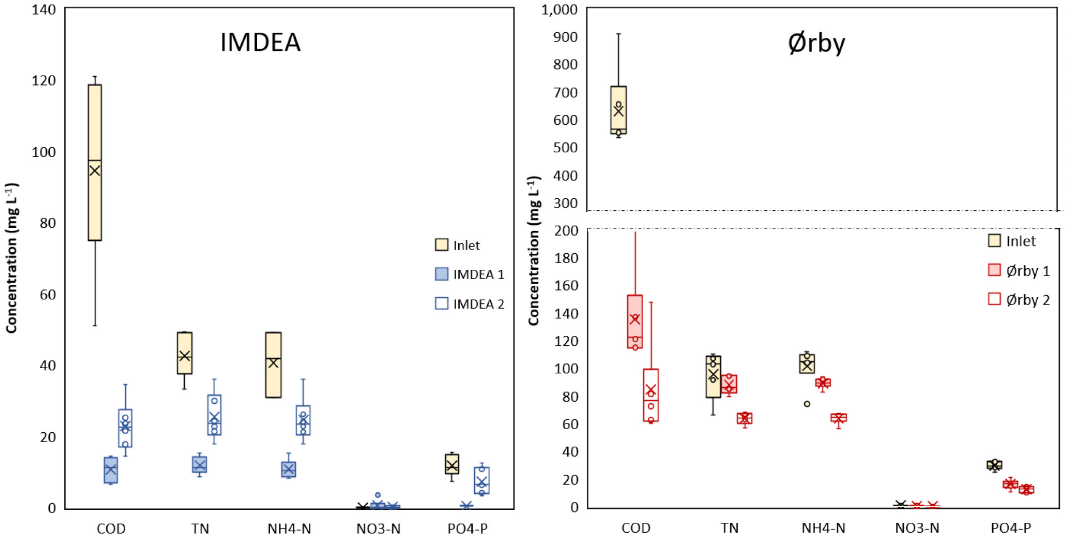

FIGURE 4 | Concentrations of COD and nutrients from both inlet and outlet for METland units operating at IMDEA (Spain) and Ørby (Denmark). Within each box, a horizontal central line denotes median values; boxes extend from the 25th to the 75th percentile of each dataset; vertical lines denote adjacent values, the minimum and the maximum; and outliers are shown as circles.

of TN $m_{\text{bed material}}^{-3}$ day^{-1} (50%), 2.9 g of NH_4—N $m_{\text{bed material}}^{-3}$ day^{-1} (47%), and 1.0 g of PO_4–P $m_{\text{bed material}}^{-3}$ day^{-1} (61%) (**Figure 4**). COD removal efficiencies had slightly higher values in the planted section (IMDEA 1) compared to the non-planted section (IMDEA 2), with significant differences between planted and non-planted systems in terms of nitrogen removal. For the IMDEA units, the average COD removal was 10% higher in the planted system (IMDEA 1) in comparison to the non-planted (IMDEA 2), with significant differences between both parallel beds ($p < 0.05$). The differences might be related to the higher oxygen transfer through plant roots as previously reported in standard TWs (Brix, 1997; Saz et al., 2018). The results suggest a similar performance of the METlands regardless of the different water levels (see **Supplementary Figure 1**) or influent concentrations, due to the adaptability of the microbial community to different oxygen availabilities without impact on the efficiency for removing organic pollutants. COD removal efficiency was similar to the ones previously reported using METlands at the mesocosm scale (Aguirre-Sierra et al., 2016; Ramírez-Vargas et al., 2018).

The removal of nitrogen is performed in two stages: the first, nitrification, is typically promoted by aerobic conditions, and the second, denitrification, under anoxic conditions. Therefore, the combination of both conditions in the same system may increase the removal of TN (Cabred et al., 2019). TN removal from both IMDEA configurations showed significant statistical differences ($p < 0.05$). At IMDEA 1, plants enhanced the degradation of nutrients, reaching an average removal of 4.1 g of TN $m_{\text{bed material}}{}^{-3}$ day^{-1} (69%) in an anoxic system, compared to the removal of 2.0 g of TN $m_{\text{bed material}}{}^{-3}$ day^{-1} (35%) in the non-planted system (IMDEA 2). This improvement suggests the positive impact of vegetation in terms of ammonia removal, as previously reported in conventional TWs (Brix, 1997; Vymazal, 2010). Additionally, the oxygen supplied by the roots promotes aerobic conditions in the upper part of the system, enhancing the nitrification processes (oxidation of ammonia to nitrate), transforming 72% of NH_4–N to nitrate (Aguirre et al., 2005). In addition, the anaerobic conditions under the water level promoted denitrification, achieving concentrations below the detection limit of nitrate in the effluent. In contrast, IMDEA 2 showed just a removal of 2.0 g of TN $m_{\text{bedmaterial}}{}^{-3}$ day^{-1} (35%), suggesting a lower oxygen availability to transform ammonia into nitrate. These results were consistent with the 37% TN removal reported in a down-flow non-planted mesocosm METland (Aguirre-Sierra et al., 2016).

In terms of phosphorous removal, the IMDEA 1 system (planted bed) showed a maximum removal of 3.9 g of PO_4–P $m_{\text{bed material}}{}^{-3}$ day^{-1} during the initial plant growth, surpassing the removal rates of the other METland systems analyzed and the rates reported in the literature about TWs (Kadlec and Wallace, 2008). After this initial period, the phosphorus removal stabilized at lower rates. Usually, the removal of phosphorus involves physical processes like precipitation or sorption, and in electroconductive materials, the PO_4–P removal could be related to surface chemistry. Indeed, the chemistry of the electroconductive material is more complex than that of gravel and may have some metal content that favors the P adsorption (Prado et al., 2019). Additionally, these results suggest that the plants could enhance the phosphorus removal through uptake mechanisms as has been reported in TWs (Vymazal and Kröpfelová, 2008). On the other hand, IMDEA 2 accounts for an average removal of 40% of PO_4–P (0.5 g PO_4–P $m_{\text{bed material}}{}^{-3}$ day^{-1}), presenting significant differences between planted and non-planted beds ($p < 0.05$).

Case Study for Treating Wastewater From an Urban Community (Ørby) at a North European Location

At the location in Denmark, the METland systems reached average removal rates above 51.3 g of COD $m_{\text{bed material}}{}^{-3}$ day^{-1} (80%), 2.1 g of TN $m_{\text{bed material}}{}^{-3}$ day^{-1} (20%), 2.6 g of NH_4–N $m_{\text{bed material}}{}^{-3}$ day^{-1} (22%), and 1.6 g of PO_4–P $m_{\text{bed material}}{}^{-3}$ day^{-1} (50%) (**Figure 4**). COD removal efficiencies had slightly higher values in the saturated section (Ørby 1) in comparison with the partially saturated section (Ørby 2). Thus, no significant differences were found between the two beds, with an average removal of 46.4 g of COD $m_{\text{bed material}}{}^{-3}$ day^{-1} (74%) in the saturated bed while 56.3 g of COD $m_{\text{bed material}}{}^{-3}$ day^{-1} (86%) in the partially saturated (Ørby 2), even though influent concentration was as high as 900 mg COD l^{-1}, with an average organic load rate (OLR) of 52.0 g m^{-2} day^{-1}. There were significant differences in TN removal, which was explained by the fact that the water level in one of the beds (Ørby 2) was abated at 0.20 m, favoring higher nitrification, and consequently, doubling the TN removal when compared to the saturated bed. The Ørby system had between 30 and 70% of PO_4–P removal (0.8–2.4 g of PO_4—P $m_{\text{bed material}}{}^{-3}$ day^{-1}), without significant statistical difference regarding the water level between beds. These results suggest similar P removal rates to the ones achieved in METlands at mesocosm scale, that fluctuate between 40 and 76% of removal (Aguirre-Sierra et al., 2016; Ramírez-Vargas et al., 2019).

This study of full-scale METland systems corroborates the results obtained in the laboratory experiments (Aguirre-Sierra et al., 2016; Prado et al., 2019; Ramírez-Vargas et al., 2019). The results from the four different systems, together with the data from previous laboratory and mesocosms could set the bases for determining design parameters. Furthermore, it has demonstrated the viability of the technology, treating waters under different climatic conditions, water characteristics, and geographical locations (Peñacoba-Antona et al., 2021a).

Bioelectrochemical Behavior of Full-Scale METlands

The high efficiency of the METland for removing organic pollutants has been correlated with the metabolism of EAB through measuring the EP profiles at mesocosm scale (Ramírez-Vargas et al., 2019; Prado et al., 2020). These studies have revealed that EPs measured at different water depths typically shift if electron flow is taking place along the electroconductive bed. This variable was null in conventional TWs made of an inert material like gravel as reported elsewhere. The present study reports for the first time the EP profiles monitored at METland units operating at full scale under real conditions (**Figure 5A**). All METlands operated in the current study were made of identical electroconductive material, so, differences in the EP profile were due to the metabolic activity subjected to the different chemical compositions of the water and the operation of the system.

Electrochemical Behavior for Treating Urban Wastewater

At IMDEA 1 (planted), the electric field extended to a depth of ca. 19 cm with an electric potential of 278.93 mV, and in

IMDEA 2 (non-planted) the electric field developed down to 20 cm with an electric potential of 239.90 mV. Likewise, for Ørby systems, the extension of electric fields along the water column was detected. For Ørby 1 (saturated), the electric field developed was 30 cm below the water level (the lowest level measured with the EP sensor) with an EP of 102.94 mV. Furthermore, in Ørby 2 (partially saturated), the electric field was developed to 27 cm below water level with an EP of 60.90 mV. These EP profiles were similar to those reported for METland-based mesocosm systems (Ramírez-Vargas et al., 2019; Prado et al., 2020), whose profiles showed the development of microbial electrical activity using different electroconductive materials (e.g. electroconductive coke and electroconductive biochar) as substrate media.

Besides the development of electric fields along the water depth in the systems, it was possible to identify differences in the maximal EP reached by each system. In the case of IMDEA systems, the highest EP was reached by the planted system (IMDEA 2); in the case of Ørby, the highest EP was reached by the system operating under partial saturation (Ørby 2). The highest potentials measured in the systems can be associated to the highest availability of O_2 as the final electron acceptor. In the case of IMDEA 2 system, this could be associated with the oxygen released from the plants' rhizomes together with diffusion from the atmosphere. In a conventional TW, the O_2 availability due to the presence of roots promotes a gradient of oxidation-reduction potential between the upper and lower sections of the system (Aguirre et al., 2005); such oxygen presence enhances electron flows in METlands, and eventually, also removal rates (Prado et al., 2020). In the Ørby 2 system, a high oxygen availability can be generated by the oxygen availability inside the METland bed when it is fed intermittently, as has been reported in tidal flow TWs (Saeed et al., 2020) and mesoscale TW–MFC systems (Han et al., 2019).

Derived from the EP measured in the field, it was possible to estimate the electron current density (*J*) in the METland system, which provide evidence of the presence of EAB and its relationship with the removal of organic matter (**Figure 5B**). For IMDEA systems, the *J* values for the planted system (IMDEA 1) vary in the range of 100.58 to 188.14 mA m^{-2} and from 45.09 to 223.84 mA m^{-2} for the non-planted system (IMDEA 2). The difference between the planted and non-planted systems suggests a possible impact of plants on the microbial communities inside the METland system, facilitating the EAB metabolism, therefore boasting the removal of pollutants (Prado et al., 2022). Indeed, the oxygen exchange between the atmosphere and the plant root's oxygen release increases the oxygen concentration in TWs (Brix, 1997), promoting higher oxidation-reduction potentials in the upper sections of the systems in contrast with the lower ones, therefore providing a redox gradient necessary for MET-based systems (Shen et al., 2018). In the case of the Ørby systems, the *J* values varied from 36.96 to 125.96 mA m^{-2} for the fully saturated system (Ørby 1) and between 45.84 and 123.01 mA m^{-2} for the partially saturated system (Ørby 2). Even though the system was not designed to harvest energy, the registered *J* values were comparable and even surpassed the current densities reported for TW–MET-based systems designed for simultaneous wastewater treatment and energy harvesting (Corbella et al., 2017; Ramírez-Vargas et al., 2018).

When assessing the association between electron current density (*J*) and the ORR, a positive relation between *J* and ORR was established (**Figure 5B**). However, despite the similarities in terms of bioelectrical response (expressed as *J*) between the systems, there were differences in terms of ORR, with higher values for Ørby systems in comparison to IMDEA ones. Such difference was probably due to the nature of the wastewater treated by every system (**Figure 4**), as well as differences in terms of OLR, with higher values for the Ørby systems in comparison to IMDEA systems. Low COD content (ca. 100 mg l^{-1}) present in wastewater from office buildings may host a higher oxygen content capable of stimulating electron flow and eventually consuming the electrons generated by microbial oxidation. So, it is possible to use bioelectrical parameters such as electron current density (*J*) as an indicator of the removal of organic matter for METland systems. However, this kind of analysis should also consider other parameters like oxygen level or the presence of alternative oxidizing chemicals (e.g., nitrate).

Even though Ørby systems received a higher OLR in comparison to the IMDEA systems, the EPs showed an opposite pattern, with lower values in the Ørby systems and higher in IMDEA systems (**Figure 5A**). The result showed an impact on the bioelectrochemical productivity of the systems expressed in terms of CE. The relation between OLR and the CE of the systems showed a decreasing pattern (**Figure 5C**). In the case of systems at IMDEA, CE was between 8.8 and 53% (with OLR between 2.0 and 16.4 g of COD m^{-2} day^{-1}), whereas in the Ørby systems, the CE values ranged from 0.8 to 2.5% (with OLR between 41.9 and 45.6 g of COD m^{-2} day^{-1}). The CE values are within the reported ranges of the merging of TWs and other MET-based systems (Doherty et al., 2015a; Ramírez-Vargas et al., 2018).

The treatment of complex mixtures, such as real wastewater, with high and variable OLR should not necessarily result in high CE values. Indeed, the decrease of CE in MET-based systems as the OLR at influent increases has been previously reported (Ghangrekar and Shinde, 2008; Guadarrama-Pérez et al., 2019; Srivastava et al., 2020). The decrease can be attributed to different factors that may hinder the metabolic activity of electroactive microbial communities such as (i) the complexity of organic substrates in wastewater, (ii) the competition with abundant and varied microbial communities, (iii) the presence of anaerobic or methanogenic bacteria, (iv) the change of the internal electric resistance of conductive materials due to heterotrophic biofilm growth, (v) the physical removal of organic matter, and (vi) the increase in acidity affecting the growth of EAB and proton diffusion (Capodaglio et al., 2015; Doherty et al., 2015b; Corbella and Puigagut, 2018; Ramírez-Vargas et al., 2018; Hartl et al., 2019). Despite this decrease, the removal efficiencies from the METland systems were remarkable when operating under high OLR, and were a result of the interaction of different microorganism assemblages (Aguirre-Sierra et al., 2016; Ramírez-Vargas et al., 2020).

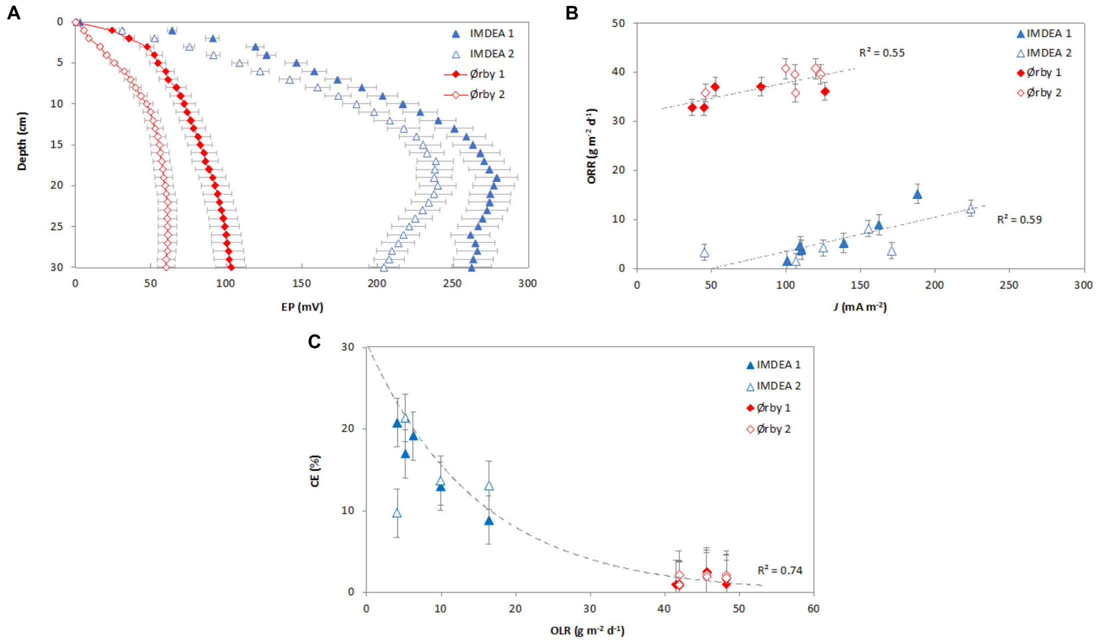

FIGURE 5 | Bioelectrical response of tested METland systems. **(A)** Electric potential (EP) profiles along water depth; **(B)** the relation between electron flow density (*J*) and removed organic load rate (ORR) in terms of COD (%); **(C)** the relation between OLR at the inlet in terms of COD and coulombic efficiency—CE (%). In panel **(A)**, the EP profiles represent the average of different sampling values (for IMDEA systems: *n* = 18; for Ørby systems: *n* = 6). In panels **(B,C)**, each marker represents average values (for IMDEA systems: *n* = 3; for Ørby systems: *n* = 2). In all figures, error bars indicate the standard error of the mean.

Impact on the Distribution of Anodic and Cathodic Zones

Based on the local differences in electron fluxes, the electron transfer rates can be estimated (R_{agg}) along the bed depth (**Figure 6** and **Supplementary Figure 2**). Furthermore, such transfer rates allow for distinguishing anodic and cathodic zones, which match with the displacement of electric fields within the tested systems (**Figure 5A**). Thus, positive R_{agg} values represent the existence of an anodic zone, where the electrons are transferred from a donor (i.e., oxidation of organic pollutants) to an extracellular electron acceptor (electroconductive bed), and negative R_{agg} values represent a cathodic zone, where the electron transfer from the bed to bacteria is capable of reducing oxygen or nitrate (Prado et al., 2020).

In the case of the Ørby systems, operative conditions had an impact on the location and extension of both anodic and cathodic zones. In Ørby 1, there was a predominance of cathodic conditions that extended to 30 cm below the water level (R_{agg} of -5.85 µmol l^{-1} day^{-1}), including a remarkable transfer rate reaching up to -136.27 µmol l^{-1} day^{-1} on the uppermost area of the system (**Figure 6**). This could be attributed to the saturated conditions, which limited the availability of terminal electron acceptors like O_2 to the interphase in the uppermost zones, where exchange with the atmosphere or diffusion through the plant roots is possible. Additionally, NO_3 can also play a role as an electron acceptor for denitrifying microorganisms. The lack of detectable NO_3 in the effluent but the presence of ammonia in the influent shows strong evidence for nitrification (**Figure 4**). In Ørby 2, the cathodic zone reached 21 cm below the water level (R_{agg} of -11.89 µmol l^{-1} day^{-1}), including a high cathodic activity present in the uppermost 10 cm (with R_{agg} between -95.43 and -42.83 µmol l^{-1} day^{-1}). This distribution of the R_{agg} profile was mainly an effect of the partially saturated condition, where diffusion and mobilization of O_2 from the atmosphere were promoted after feeding by a pulse; likewise, in Ørby 1, nitrate was not detected in the effluent.

Regarding IMDEA, the systems showed similarities between them in terms of the location of the cathodic and anodic zones, ca. 20 cm below the water surface (**Figure 6**). The main difference between them was the potential impact of the presence of plants in the IMDEA 1 system, which should contribute to higher O_2 availability in the uppermost part of the bed. Likewise, in the Ørby systems, the presence of O_2 and NO_3 as a terminal electron acceptor contributes to the establishment of the cathodic and anodic zones, therefore allowing higher electron transfer values in the IMDEA 1 system (max. R_{agg} of -292.50 µmol l^{-1} day^{-1}) than in the IMDEA 2 (max. R_{agg} of -168.70 µmol l^{-1} day^{-1}). The cathodic and anodic zones detected in the systems seemed to be developed, not only by the type of configuration or operative conditions of the systems but also by the composition of the wastewater. The cathodic zones in the Ørby systems were deeper in comparison to the IMDEA systems, which could be associated with the highest OLR, whereas in the IMDEA systems, the electron transfer was higher than in the Ørby systems, a fact that could be derived from the relatively higher bioelectrochemical efficiency of the IMDEA systems that received a lower OLR. Likewise, in natural environments such as marine sediments or artificial

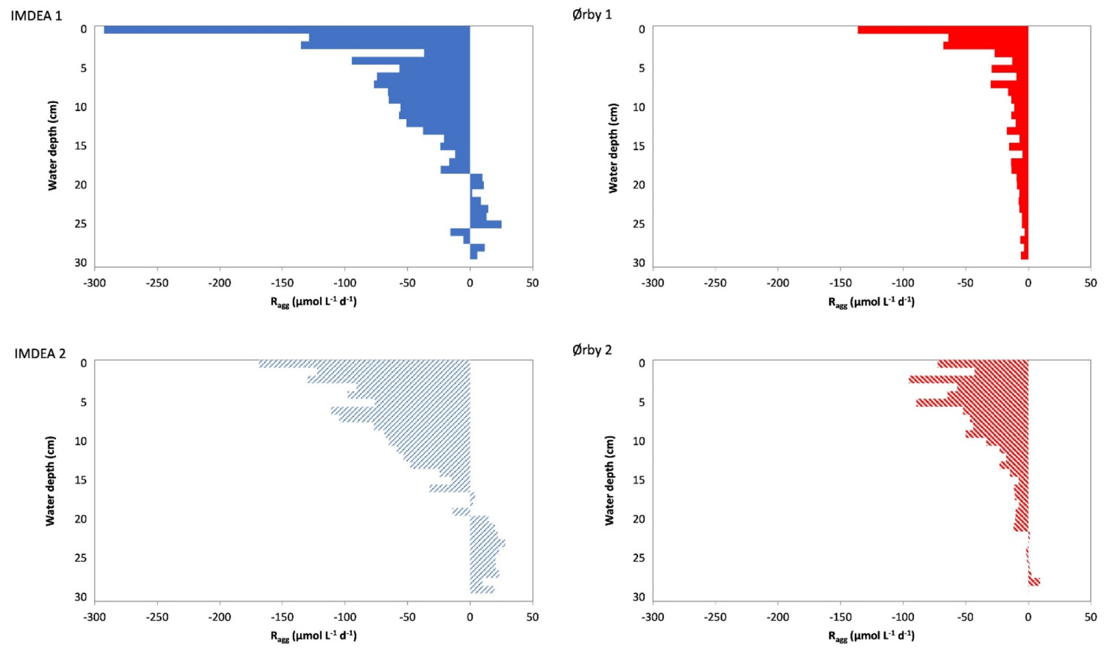

FIGURE 6 | Aggregated electron transfer rate (R_{agg}) for METland units treating wastewater (i) from an office building (planted IMDEA 1 and non-planted IMDEA 2) and (ii) from an urban community (fully saturated Ørby 1 and partially saturated Ørby 2). Positive values indicate zones where the bed is accepting electrons from an electron donor (anodic reaction), and negative values indicate zones where the bed is donating electrons (cathodic reactions).

electroactive biofilters like METlands, the assessment of electron fluxes is evident in the spatial mobilization of electrons from donors to acceptors that are physically in different environments (Prado et al., 2020). There are still open research questions and opportunities to study, in-depth, those dynamics of electron transfers that ultimately trigger an optimal performance of (EAB) in electrobioremediation systems.

CONCLUSION

METlands operated at full scale are an innovative and effective solution for wastewater treatment, capable of reaching removal efficiencies of 90% COD (87 g of COD $m_{\text{bed material}}{}^{-3}$ day^{-1}) and 70% TN (10.6 g of TN $m_{\text{bed material}}{}^{-3}$ day^{-1}). This was clearly shown in these two case studies operating at different geographical locations with different wastewater compositions.

The study suggests the possibility of using bioelectrochemical parameters such as electron fluxes (J) to monitor the performance of a METland system in terms of organic matter removal. Keeping in mind that the correlation between electron fluxes and organic matter removal is site-specific, as a future perspective, these results open the possibility for using the current densities to monitor the performance remotely. In addition, the EP monitoring, the estimation of electron fluxes (J), and the electron transfer rate (R_{agg}) calculations would allow for the detection of the most active zones inside the systems.

In summary, the bioelectrochemical behavior of full-scale electrobioremediation systems is not only a consequence of its operational conditions or configuration but is also affected by the type and composition of the influent wastewater. Lastly, METland technology was validated as an innovative and efficient solution for treating wastewater in decentralized locations.

DATA AVAILABILITY STATEMENT

The raw data supporting the conclusions of this article will be made available by the authors, without undue reservation.

AUTHOR CONTRIBUTIONS

CR-V, LP-A, CW, AC-M, DP, and CA: conceptualization. CR-V and LP-A: data curation, formal analysis, methodology, investigation, software, and visualization. AE-N, CA, and HB: funding acquisition and supervision. CR-V, LP-A, AE-N, and CA: writing—original draft. All authors contributed to the article and approved the submitted version.

FUNDING

This research was supported by the project “iMETland: A new generation of Microbial Electrochemical Wetland for effective decentralized wastewater treatment systems,” funded by the European Union’s Horizon 2020 Research and Innovation

Program (No. 642190). LP-A kindly acknowledges the Regional Government of Madrid for granting her Industrial Ph.D. fellowship program (IND2017/AMB-7648). CR-V was funded by a grant from the Independent Research Fund Denmark, project 8022-00076B.

SUPPLEMENTARY MATERIAL

The Supplementary Material for this article can be found online at: https://www.frontiersin.org/articles/10.3389/fmicb.2022.843135/full#supplementary-material

REFERENCES

Aguirre, P., Ojeda, E., García, J., Barragán, J., and Mujeriego, R. (2005). Effect of water depth on the removal of organic matter in horizontal subsurface flow constructed wetlands. *J. Environ. Sci. Heal. A Tox. Hazard. Subst. Environ. Eng.* 40, 1457–1466. doi: 10.1081/ESE-200055886

Aguirre-Sierra, A., Bacchetti-De Gregoris, T., Berná, A., Salas, J. J., Aragón, C., and Esteve-Núñez, A. (2016). Microbial electrochemical systems outperform fixed-bed biofilters in cleaning up urban wastewater. *Environ. Sci. Water Res. Technol.* 2, 984–993. doi: 10.1039/C6EW00172F

Aguirre-Sierra, A., Bacchetti-De Gregoris, T., Salas, J. J., De Deus, A., and Esteve-Núñez, A. (2020). A new concept in constructed wetlands: assessment of aerobic electroconductive biofilters. *Environ. Sci. Water Res. Technol.* 6, 1312–1323. doi: 10.1039/c9ew00696f

APHA (2012). *Water Environment Federation (2012) Standard methods for the examination of water and wastewater*. (Washington, D.C: American Public Health Association)

Brix, H. (1997). Do macrophytes play a role in constructed treatment wetlands? *Water Sci. Technol.* 35, 11–17. doi: 10.1016/S0273-1223(97)00047-4

Brix, H., Koottatep, T., and Laugesen, C. H. (2007). Wastewater treatment in tsunami affected areas of Thailand by constructed wetlands. *Water Sci. Technol.* 56, 69–74. doi: 10.2166/wst.2007.528

Cabred, S., Giunta Ramos, V., Busalmen, J. E., Busalmen, J. P., and Bonanni, S. (2019). Reduced depth stacked constructed wetlands for enhanced urban wastewater treatment. *Chem. Eng. J.* 372, 708–714. doi: 10.1016/J.CEJ.2019.04.180

Capodaglio, A. G., Molognoni, D., Puig, S., Balaguer, M. D., and Colprim, J. (2015). Role of Operating Conditions on Energetic Pathways in a Microbial Fuel Cell. *Energy Procedia* 74, 728–735. doi: 10.1016/j.egypro.2015.07.808

Corbella, C., and Puigagut, J. (2018). Improving domestic wastewater treatment efficiency with constructed wetland microbial fuel cells: Influence of anode material and external resistance. *Sci. Total Environ.* 631–632, 1406–1414. doi: 10.1016/J.SCITOTENV.2018.03.084

Corbella, C., Puigagut, J., and Garfí, M. (2017). Life cycle assessment of constructed wetland systems for wastewater treatment coupled with microbial fuel cells. *Sci. Total Environ.* 584–585, 355–362. doi: 10.1016/J.SCITOTENV.2016.12.186

Damgaard, L. R., Risgaard-Petersen, N., and Nielsen, L. P. (2014). Electric potential microelectrode for studies of electrobiogeophysics. *J. Geophys. Res. G Biogeosci.* 119, 1906–1917. doi: 10.1002/2014JG002665

Doherty, L., Zhao, Y., Zhao, X., Hu, Y., Hao, X., Xu, L., et al. (2015a). A review of a recently emerged technology: Constructed wetland - Microbial fuel cells. *Water Res.* 85, 38–45. doi: 10.1016/j.watres.2015.08.016

Doherty, L., Zhao, Y., Zhao, X., and Wang, W. (2015b). Nutrient and organics removal from swine slurry with simultaneous electricity generation in an alum sludge-based constructed wetland incorporating microbial fuel cell technology. *Chem. Eng. J.* 266, 74–81. doi: 10.1016/j.cej.2014.12.063

Dotro, G., Langergraber, G., Molle, P., Nivala, J., Puigagut, J., Stein, O., et al. (2017). "Treatment Wetlands," in *Biological Wastewater Treatment Series*, eds G. Dotro, G. Langergraber, P. Molle, J. Nivala, J. Puigagut, O. Stein, et al. (London: IWA Publishing), doi: 10.2166/9781789062526

Erable, B., Etcheverry, L., and Bergel, A. (2011). From microbial fuel cell (MFC) to microbial electrochemical snorkel (MES): maximizing chemical oxygen demand (COD) removal from wastewater. *Biofouling* 27, 319–326. doi: 10.1080/08927014.2011.564615

Esteve-Núñez, A. (2015). Electricity-generating bacteria Bioelectrogenesis: sustainable biotechnology. *Int. Innov.* 181, 109–111.

Ghangrekar, M. M., and Shinde, V. B. (2008). Simultaneous sewage treatment and electricity generation in membrane-less microbial fuel cell. *Water Sci. Technol.* 58, 37–43. doi: 10.2166/wst.2008.339

Guadarrama-Pérez, O., Gutiérrez-Macías, T., García-Sánchez, L., Guadarrama-Pérez, V. H., and Estrada-Arriaga, E. B. (2019). Recent advances in constructed wetland-microbial fuel cells for simultaneous bioelectricity production and wastewater treatment: A review. *Int. J. Energy Res.* 43, 5106–5127. doi: 10.1002/er.4496

Han, Z., Dong, J., Shen, Z., Mou, R., Zhou, Y., Chen, X., et al. (2019). Nitrogen removal of anaerobically digested swine wastewater by pilot-scale tidal flow constructed wetland based on *in-situ* biological regeneration of zeolite. *Chemosphere* 217, 364–373. doi: 10.1016/J.CHEMOSPHERE.2018.11.036

Hartl, M., Bedoya-Ríos, D. F., Fernández-Gatell, M., Rousseau, D. P. L., Du Laing, G., Garfí, M., et al. (2019). Contaminants removal and bacterial activity enhancement along the flow path of constructed wetland microbial fuel cells. *Sci. Total Environ.* 652, 1195–1208. doi: 10.1016/J.SCITOTENV.2018.10.234

Kabutey, F. T., Zhao, Q., Wei, L., Ding, J., Antwi, P., Quashie, F. K., et al. (2019). An overview of plant microbial fuel cells (PMFCs): Configurations and applications. *Renew. Sustain. Energy Rev.* 110, 402–414. doi: 10.1016/J.RSER.2019.05.016

Kadlec, R., and Wallace, S. (2008). *Treatment Wetlands*, 2nd Edn, (Florida: CRC Press)

Langergraber, G., Dotro, G., Nivala, J., Rizzo, A., and Stein, O. R. (2019). *Wetland Technology. Practical Information on the Design and Application of Treatment Wetlands.* (London: IWA Publishing)

Langergraber, G., and Masi, F. (2018). Treatment wetlands in decentralised approaches for linking sanitation to energy and food security. *Water Sci. Technol.* 77, 859–860. doi: 10.2166/wst.2017.599

Logan, B. E., Hamelers, B., Rozendal, R., Schröder, U., Keller, J., Freguia, S., et al. (2006). Microbial fuel cells: Methodology and technology. *Environ. Sci. Technol.* 40, 5181–5192. doi: 10.1021/es0605016

Metcalf and Eddy Inc (2004). *Wastewater Engineering: Treatment and Reuse*, (New York, NY: McGraw-Hill).

Nielsen, L. P., and Risgaard-Petersen, N. (2015). Rethinking Sediment Biogeochemistry After the Discovery of Electric Currents. *Ann. Rev. Mar. Sci.* 7, 425–442. doi: 10.1146/annurev-marine-010814-015708

Nitisoravut, R., and Regmi, R. (2017). Plant microbial fuel cells: A promising biosystems engineering. *Renew. Sustain. Energy Rev.* 76, 81–89. doi: 10.1016/j.rser.2017.03.064

Oon, Y.-L., Ong, S.-A., Ho, L.-N., Wong, Y.-S., Dahalan, F. A., Oon, Y.-S., et al. (2016). Synergistic effect of up-flow constructed wetland and microbial fuel cell for simultaneous wastewater treatment and energy recovery. *Bioresour. Technol.* 203, 190–197. doi: 10.1016/j.biortech.2015.12.011

Peñacoba-Antona, L., Gómez-Delgado, M., and Esteve-Núñez, A. (2021a). Multi-criteria evaluation and sensitivity analysis for the optimal location of constructed wetlands (METland) at oceanic and Mediterranean locations. *Int. J. Environ. Res. Public Health* 18:5415. doi: 10.3390/ijerph18105415

Peñacoba-Antona, L., Senán-Salinas, J., Aguirre-Sierra, A., Letón, P., Salas, J. J., García-Calvo, E., et al. (2021b). Assessing METland®design and performance through LCA: technoenvironmental study with multifunctional unit perspective. *Front. Microbiol.* 12:652173. doi: 10.3389/fmicb.2021.652173

Prado, A., Berenguer, R., and Esteve-Núñez, A. (2019). Electroactive biochar outperforms highly conductive carbon materials for biodegrading pollutants by enhancing microbial extracellular electron transfer. *Carbon N. Y.* 146, 597–609. doi: 10.1016/J.CARBON.2019.02.038

Prado, A., Berenguer, R., and Esteve-Núñez, A (2022). Evaluating bioelectrochemically-assisted constructed wetland (METland®) for treating wastewater: analysis of materials, perfomance and electroactive communities. *Chem. Eng. J.* (Accepted).

Prado, A., Ramírez-Vargas, C. A., Arias, C. A., and Esteve-Núñez, A. (2020). Novel bioelectrochemical strategies for domesticating the electron flow in constructed wetlands. *Sci. Total Environ.* 735:139522. doi: 10.1016/j.scitotenv.2020.139522

Ptushenko, V. V. (2020). Electric Cables of Living Cells. II. Bacterial Electron Conductors. *Biochem. Moscow* 85, 955–965. doi: 10.1134/S0006297920080118

Ramírez-Vargas, C. A., Arias, C. A., Carvalho, P., Zhang, L., Esteve-Núñez, A., and Brix, H. (2019). Electroactive biofilm-based constructed wetland (EABB-CW): A mesocosm-scale test of an innovative setup for wastewater treatment. *Sci. Total Environ.* 659, 796–806. doi: 10.1016/J.SCITOTENV.2018.12.432

Ramírez-Vargas, C. A., Arias, C. A., Zhang, L., Paredes, D., and Brix, H. (2020). Community level physiological profiling of microbial electrochemical-based constructed wetlands. *Sci. Total Environ.* 721:137761. doi: 10.1016/j.scitotenv.2020.137761

Ramírez-Vargas, C. A., Prado, A., Arias, C. A., Carvalho, P. N., Esteve-Núñez, A., and Brix, H. (2018). Microbial electrochemical technologies for wastewater treatment : principles and evolution from microbial fuel cells to bioelectrochemical-based constructed wetlands. *Water* 10:1128. doi: 10.20944/preprints201807.0369.v1

Risgaard-Petersen, N., Damgaard, L. R., Revil, A., and Nielsen, L. P. (2014). Mapping electron sources and sinks in a marine biogeobattery. *J. Geophys. Res. G Biogeosci.* 119, 1475–1486. doi: 10.1002/2014JG002673

Rotaru, A. E., Yee, M. O., and Musat, F. (2021). Microbes trading electricity in consortia of environmental and biotechnological significance. *Curr. Opin. Biotechnol.* 67, 119–129. doi: 10.1016/j.copbio.2021.01.014

Saba, B., Khan, M., Christy, A. D., and Kjellerup, B. V. (2019). Microbial phyto-power systems – A sustainable integration of phytoremediation and microbial fuel cells. *Bioelectrochemistry* 127, 1–11. doi: 10.1016/j.bioelechem.2018.12.005

Saeed, T., Miah, M. J., Khan, T., and Ove, A. (2020). Pollutant removal employing tidal flow constructed wetlands: Media and feeding strategies. *Chem. Eng. J.* 382:122874. doi: 10.1016/j.cej.2019.122874

Saz, Ç, Türe, C., Türker, O. C., and Yakar, A. (2018). Effect of vegetation type on treatment performance and bioelectric production of constructed wetland modules combined with microbial fuel cell (CW-MFC) treating synthetic wastewater. *Environ. Sci. Pollut. Res.* 25, 8777–8792. doi: 10.1007/s11356-018-1208-y

Shen, X., Zhang, J., Liu, D., Hu, Z., and Liu, H. (2018). Enhance performance of microbial fuel cell coupled surface flow constructed wetland by using submerged plants and enclosed anodes. *Chem. Eng. J.* 351, 312–318. doi: 10.1016/J.CEJ.2018.06.117

Srivastava, P., Abbassi, R., Garaniya, V., Lewis, T., and Yadav, A. K. (2020). Performance of pilot-scale horizontal subsurface flow constructed wetland coupled with a microbial fuel cell for treating wastewater. *J. Water Process Eng.* 33:100994. doi: 10.1016/J.JWPE.2019.100994

Vymazal, J. (2009). The use constructed wetlands with horizontal sub-surface flow for various types of wastewater. *Ecol. Eng.* 35, 1–17. doi: 10.1016/j.ecoleng.2008.08.016

Vymazal, J. (2010). Constructed Wetlands for Wastewater Treatment. *Water* 2, 530–549. doi: 10.3390/w2030530

Vymazal, J., and Kröpfelová, L. (2008). *Wastewater Treatment in Constructed Wetlands with Horizontal Sub-Surface Flow. Environmental Pollution*, (Dordrecht: Springer), 14

Wang, J., Song, X., Wang, Y., Abayneh, B., Li, Y., Yan, D., et al. (2016). Nitrate removal and bioenergy production in constructed wetland coupled with microbial fuel cell: Establishment of electrochemically active bacteria community on anode. *Bioresour. Technol.* 221, 358–365. doi: 10.1016/j.biortech.2016.09.054

Wang, X., Aulenta, F., Puig, S., Esteve-Núñez, A., He, Y., Mu, Y., et al. (2020). Microbial electrochemistry for bioremediation. *Environ. Sci. Ecotechnol.* 1:100013. doi: 10.1016/j.ese.2020.100013

Wu, H., Zhang, J., Ngo, H. H., Guo, W., Hu, Z., Liang, S., et al. (2015). A review on the sustainability of constructed wetlands for wastewater treatment: Design and operation. *Bioresour. Technol.* 175, 594–601. doi: 10.1016/j.biortech.2014.10.068

Yadav, A. K., Dash, P., Mohanty, A., Abbassi, R., and Mishra, B. K. (2012). Performance assessment of innovative constructed wetland-microbial fuel cell for electricity production and dye removal. *Ecol. Eng.* 47, 126–131. doi: 10.1016/j.ecoleng.2012.06.029

Yang, Q., Wu, Z., Liu, L., Zhang, F., and Liang, S. (2016). Treatment of oil wastewater and electricity generation by integrating constructed wetland with microbial fuel cell. *Materials* 9:885. doi: 10.3390/ma9110885

Conflict of Interest: The authors declare that the research was conducted in the absence of any commercial or financial relationships that could be construed as a potential conflict of interest.

frontiers | Frontiers in Microbiology

ORIGINAL RESEARCH
published: 10 May 2022
doi: 10.3389/fmicb.2022.898015

Electron Flow From the Inner Membrane Towards the Cell Exterior in *Geobacter sulfurreducens*: Biochemical Characterization of Cytochrome CbcL

Jorge M. A. Antunes*[1,2], *Marta A. Silva*[1,2], *Carlos A. Salgueiro*[1,2]* *and Leonor Morgado*[1,2]

[1] Associate Laboratory i4HB – Institute for Health and Bioeconomy, NOVA School of Science and Technology, NOVA University Lisbon, Caparica, Portugal, [2] UCIBIO – Applied Molecular Biosciences Unit, Chemistry Department, NOVA School of Science and Technology, NOVA University Lisbon, Caparica, Portugal

Exoelectrogenic microorganisms are in the spotlight due to their unique respiratory mechanisms and potential applications in distinct biotechnological fields, including bioremediation, bioenergy production and microbial electrosynthesis. These applications rely on the capability of these microorganisms to perform extracellular electron transfer, a mechanism that allows the bacteria to transfer electrons to the cell's exterior by establishing functional interfaces between different multiheme cytochromes at the inner membrane, periplasmic space, and outer membrane. The multiheme cytochrome CbcL from *Geobacter sulfurreducens* is associated to the inner membrane and plays an essential role in the transfer of electrons to final electron acceptors with a low redox potential, as Fe(III) oxides and electrodes poised at −100 mV. CbcL has a transmembranar di-heme *b*-type cytochrome domain with six helices, linked to a periplasmic cytochrome domain with nine *c*-type heme groups. The complementary usage of ultraviolet-visible, circular dichroism and nuclear magnetic resonance permitted the structural and functional characterization of CbcL's periplasmic domain. The protein was found to have a high percentage of disordered regions and its nine hemes are low-spin and all coordinated by two histidine residues. The apparent midpoint reduction potential of the CbcL periplasmic domain was determined, suggesting a thermodynamically favorable transfer of electrons to the putative redox partner in the periplasm – the triheme cytochrome PpcA. The establishment of a redox complex between the two proteins was confirmed by probing the electron transfer reaction and the molecular interactions between CbcL and PpcA. The results obtained show for the first time how electrons are injected into the periplasm of *Geobacter sulfurreducens* for subsequent transfer to the cell's exterior.

Keywords: *Geobacter*, extracellular electron transfer, inner membrane associated cytochrome, protein-protein interactions, NMR

Edited by:
Amelia-Elena Rotaru,
University of Southern Denmark,
Denmark

Reviewed by:
Pia Ädelroth,
Stockholm University, Sweden
Okamoto Akihiro,
National Institute for Materials
Science, Japan

****Correspondence:***
Carlos A. Salgueiro
csalgueiro@fct.unl.pt
Leonor Morgado
mlmorgado@fct.unl.pt

Specialty section:
This article was submitted to
Microbiological Chemistry
and Geomicrobiology,
a section of the journal
Frontiers in Microbiology

Received: *16 March 2022*
Accepted: *04 April 2022*
Published: *10 May 2022*

Citation:
Antunes JMA, Silva MA,
Salgueiro CA and Morgado L (2022)
Electron Flow From the Inner
Membrane Towards the Cell Exterior
in Geobacter sulfurreducens:
Biochemical Characterization
of Cytochrome CbcL.
Front. Microbiol. 13:898015.
doi: 10.3389/fmicb.2022.898015

INTRODUCTION

Microorganisms are the most important biogeochemical agents affecting the chemistry, distribution, and the bioavailability of almost all elements (Popescu et al., 2002). A wide group called dissimilatory metal reducing bacteria (DMRB) plays an important role, namely in the biogeochemical cycles of transition metals as chromium, iron, uranium and manganese (Cavalier-Smith et al., 2006). DMRB can couple their oxidative metabolism to the reduction of extracellular metals like Fe(III), U(VI) or Mn(IV) oxides, as well as electrode surfaces. Unlike the most common respiratory pathways, in which a soluble terminal electron acceptor is reduced inside the cell, DMRB developed an electron transport chain capable of transfering the electrons from inside the cell to the exterior (Nealson and Saffarini, 1994). The best characterized DMRB belong to the *Geobacteraceae* and *Shewanellaceae* families, particularly the bacterium *Geobacter sulfurreducens* that produces the highest power densities of all known exoelectrogenic microorganisms (Vasyliv et al., 2013; Logan et al., 2019). The abundance of *c*-type cytochromes encoded in *G. sulfurreducens* genome provides a unique respiratory flexibility (Lovley et al., 2011; Speers and Reguera, 2012). This flexibility can be explored for different applications including the reduction of soluble metals (e.g., Cr(VI), U(VI)) to insoluble precipitates (Cr(III) and U(IV)) in contaminated waters, or the decomposition of hydrocarbon contaminants in soils, which simplifies the bioremediation process of these pollutants (Lovley et al., 2004, 2011). The transport of electrons to the cells' exterior, a mechanism called extracellular electron transfer (EET), led to the development of different biotechnological applications using bioelectrochemical systems (BES) (Kumar et al., 2015). Microbial fuel cells (MFC), which can couple the oxidation of organic compounds to the production of electric current are the best known BESs, establishing a promising synergy between green energy production and wastewater treatment (Koffi and Okabe, 2020). However, BESs are not limited to MFCs. Microbial electrolysis cells that produce biohydrogen, or microbial desalination cells that desalinate sea water, are also blooming (Al-Amshawee et al., 2020). This wide range of applications makes important to understand the functional mechanism of EET. Studies based on gene-knockout and proteomic analysis in different growth conditions constantly provide new findings that bring more insights on the proteins involved in the EET pathways (Levar et al., 2014; Zacharoff et al., 2016). To date it is well known that these respiratory pathways in *G. sulfurreducens* encompass different multiheme cytochromes along the inner membrane, periplasmic space, and outer membrane (Ueki, 2021). One remarkable finding was that EET in *G. sulfurreducens* could only be described when the contribution of multiple governing redox processes was considered (Marsili et al., 2010; Yoho et al., 2014; Rimboud et al., 2015). In 2014, Levar and co-workers showed that a strain without the gene that encodes for the inner membrane cytochrome ImcH (Δ*imcH*) lost the ability to reduce the electron acceptors Fe(III)-EDTA, Fe(III) citrate, and insoluble Mn(IV) oxides – all with reduction potentials above −100 mV (Levar et al., 2014). However, the Δ*imcH* mutant was still able to reduce Fe(III) oxides with reduction potentials below −100 mV. These results, in agreement with the hypothesis that distinct routes are necessary to describe EET, suggested that at least one alternative quinone oxidoreductase should be active to permit the growth of the mutated *G. sulfurreducens* strain in the presence of electron acceptors with low redox potentials. This was further confirmed by Zacharoff and co-workers by the deletion of a gene coding for another inner membrane cytochrome [*c*- and *b*-type cytochrome for low potential (CbcL)] and the concomitant inability of the mutated strain to reduce low potential electron acceptors, such as Fe(III) oxides and electrodes poised at −100 mV (Zacharoff et al., 2016). Finally, and more recently, Joshi and co-workers described a third inner membrane cytochrome, designated CbcBA, that was shown to be necessary in the final stages of Fe(III) reduction (Joshi et al., 2021). A *G. sulfurreducens* strain lacking this multiheme cytochrome ceased Fe(III) reduction at −210 mV and couldn't perform electron transfer to electrodes between −210 and −280 mV.

The present work focuses on the cytochrome CbcL which is constituted by two domains: a membrane domain with six transmembrane helices and two *b*-type heme groups, and a periplasmic domain containing nine *c*-type heme groups. The periplasmic domain of cytochrome CbcL was successfully produced and its characterization was obtained by the complementary usage of different spectroscopic techniques, including UV-visible, circular dichroism (CD) and nuclear magnetic resonance (NMR). Interaction studies between cytochrome CbcL and the triheme cytochrome PpcA, one of its putative redox partners in the periplasm, were also monitored by NMR.

MATERIALS AND METHODS

Cloning

DNA sequence of the gene *cbcL* (GSU0274, GenBank accession number AAR33608.1) was obtained from *G. sulfurreducens* PCA genome database from Kyoto Encyclopedia of Genes and Genomes database (Kanehisa et al., 2016). Residues 30-279 (CbcL periplasmic domain) were amplified from genomic DNA using Phusion DNA polymerase (Thermo Scientific) together with primers with restriction sites for NotI and HindIII enzymes. The resulting DNA fragment and vector pVA203 (Londer et al., 2002; Pokkuluri et al., 2004a) were digested, the E-gel® electrophoresis system (Invitrogen) was used to purify them, and T4 DNA ligase (Thermo Scientific) was used to ligate the DNA fragment to the vector. The plasmid was further modified by the addition of a C-terminal Strep-tag®. Plasmids were propagated in *Escherichia coli* DH5α cells and colony screenings performed by PCR using Taq DNA polymerase (VWR). Positive clones were cultured in liquid medium. The plasmids were then purified using the NZYMiniprep kit (NZYTech) and sequenced by STABVida (Caparica, Portugal). The resulting plasmid pVA203-CbcL-St codes for the signal peptide of the protein OmpA from *E. coli* followed by the periplasmic domain of CbcL and a C-terminal Strep-tag®.

Protein Expression and Purification

Isolated colonies of *E. coli* Tuner (DE3)/pEC86+pVA203-CbcL-St were selected and inoculated in liquid 2xYT medium supplemented with 100 $\mu g \cdot mL^{-1}$ of ampicillin and 34 $\mu g \cdot mL^{-1}$ of chloramphenicol, and incubated overnight at 30°C and 200 rpm. On the following day, 15 mL of this culture were transferred to 2 L conical flasks, each containing 1 L of liquid 2xYT medium with antibiotics in the same concentration. The cultures were incubated at 30°C and 180 rpm for approximately 8 h until an OD_{600} ∼1.7 was reached. Cells were collected by centrifugation at 5,500 ×*g* for 15 min at 4°C. The pellets were then resuspended in buffer W (100 mM Tris-HCl pH 8, 150 mM NaCl, 1mM EDTA), in a ratio of 1 mL of buffer per gram of cells and frozen at −20°C. Cell lysis was performed by a combined method of three freeze/thaw cycles followed by 18 cycles of ultrasonication (3 min on plus 1 min off) with an Ultrasonic homogenizer (Branson) regulated for 65% of amplitude and in the presence of DNase I, 2 mM benzamidine and 1 mM phenylmethanesulfonylfluoride. Cell debris were removed by centrifugation at 48,000 ×*g* for 1 h at 6°C. The supernatant containing the soluble extract was loaded directly onto a 5 mL Strep-Tactin® XT 4Flow (IBA Lifesciences) column, previously equilibrated with buffer W. The flowthrough was collected and the unbound proteins washed by passing 25 mL of buffer W. The protein was eluted with buffer BXT (buffer W with 50 mM biotin). The eluted sample was dialyzed against 10 mM Tris-HCl pH 8, using a dialysis membrane with a molecular weight cut off (MWCO) 12–14 kDa (Spectrum). After the dialysis step, the sample was loaded onto a 5 mL anion exchange UNOsphere™ Q (Bio-Rad) column, equilibrated with the same dialysis buffer. The protein was eluted with a 75 mL gradient of 0–300 mM NaCl. The fractions were analyzed by SDS-PAGE (12.5%) and stained with BlueSafe (NZYTech). Fractions containing CbcL (unless stated otherwise CbcL's periplasmatic domain will be referred as CbcL) were concentrated and the buffer exchanged using an Amicon Ultra-4 centrifugal filter unit with a MWCO 10 kDa (Merck-Millipore). After, the samples were loaded onto a Superdex™ 75 Increase 10/300 GL (GE Healthcare) equilibrated with 100 mM sodium phosphate buffer pH 8. Chromatographic steps were performed with an ÄKTA Pure or with an ÄKTA Prime Plus. Final protein purity was evaluated by SDS-PAGE. The molecular weight of CbcL was confirmed by matrix assisted laser desorption ionization coupled to time-of-flight mass spectrometry (MALDI-TOF/TOF MS) performed by the Mass Spectrometry Unit (UniMS), ITQB/iBET, Oeiras, Portugal. For interaction studies with CbcL, PpcA was expressed and purified as previously described (Londer et al., 2002).

UV-Visible Spectroscopy, Protein Quantification, Heme Content and Molar Extinction Coefficient Determination

UV-visible spectra were acquired on a Thermo Scientific Evolution 201 spectrophotometer at room temperature in the reduced and oxidized states. A freshly prepared solution of sodium dithionite was added to the sample to reduce the protein. Protein concentration was measured with the Pierce™ Modified Lowry Protein Assay Kit (Thermo Scientific Pierce; Ohnishi and Barr, 1978), using horse heart cytochrome *c* as protein standard, and used to determine molar extinction coefficients. Subsequent protein concentrations were calculated using the determined molar extinction coefficients. The protein heme content was determined by the pyridine hemochromogen assay, by measuring the absorbance at 550 nm (for *c*-type hemes ϵ_{550nm} = 30.27 $mM^{-1} \cdot cm^{-1}$) of a 1.2 μM CbcL solution prepared in 50 mM of NaOH/20% pyridine and reduced by the addition of a freshly prepared sodium dithionite solution (Berry and Trumpower, 1987).

Circular Dichroism Spectroscopy

CD characterization in the Far-UV was performed with a CbcL sample at 10 μM prepared in 10 mM sodium phosphate buffer pH 8. Measurements were performed in an Applied Photophysics Chirascan™ qCD spectropolarimeter using a 300 μL quartz cuvette with 1 mm of path length. The CD spectra at 25°C are an average of three spectral acquisitions with a step-size of 1 nm. A temperature ramp was measured in the range of 10–94°C, with a temperature increment of 2°C for each measurement with 1 min period for stabilization in each temperature. A two-state transition model from folded to unfolded was used to determine the melting temperature and the enthalpy of unfolding (ΔH) (Greenfield, 2007b). The analysis of the CD spectra, including the determination of the composition of the secondary structure elements, was carried out using the online program DichroWeb with the CDSSTR algorithm and SPM180 as a reference dataset (Whitmore and Wallace, 2004).

Nuclear Magnetic Resonance Spectroscopy

NMR experiments were performed either on a Bruker Avance Neo 500 MHz spectrometer or on a Bruker Avance III 600 MHz spectrometer at 25°C. The water signal was used as internal reference for the calibration of the ^1H chemical shifts to sodium trimethylsilylpropanesulfonate (Pierattelli et al., 1996). All 1D ^1H NMR spectra were acquired with 1024 increments, a sweep width of 70 kHz and processed using TOPSPIN 4.1.1™ (Bruker).

Electron Transfer Experiments

To monitor the electron transfer reaction between CbcL and PpcA, a sample of 100 μM (160 μL) of CbcL prepared in 10 mM sodium phosphate buffer pH 8 was lyophilized (NMR spectra were acquired before and after lyophilization − in the reduced and oxidized states − to confirm that the protein integrity and their redox behavior was not affected) and resuspended in ^2H_2O inside an anaerobic glovebox (LABstar, MBraun) to avoid the presence of oxygen. The NMR tube was sealed with a gas-tight serum cap and flushed with gaseous hydrogen for reduction in the presence of a catalytic amount of hydrogenase from *Desulfovibrio vulgaris*. After reduction, argon was used to remove all the hydrogen from the sample. Similarly, a sample of PpcA was lyophilized and resuspended in 20 μL of ^2H_2O inside the glovebox, resulting in a 3.2 mM sample. The electron transfer reaction between reduced CbcL and oxidized PpcA was followed by a series of 1D ^1H NMR spectra each acquired after the addition of increasing equivalents of PpcA to the reduced CbcL sample, inside the anaerobic glovebox.

Protein-Protein Interaction Studies in the Oxidized Form

The molecular interactions between CbcL and PpcA were followed by NMR chemical shift perturbation experiments. For the monitorization of perturbations on PpcA's NMR signals, a sample of 50 μM PpcA (160 μL) and a sample of CbcL at 800 μM (30 μL) both in 10 mM sodium phosphate buffer pH 8 were prepared by lyophilization and resuspended in ^2H_2O. A series of 1D ^1H NMR spectra were obtained after the addition of increasing amounts of CbcL to PpcA. For the monitorization of perturbations on CbcL's NMR signals, a sample of 100 μM CbcL (160 μL) and a sample of PpcA at 3.2 mM (50 μL) both in 10 mM sodium phosphate buffer pH 8 were lyophilized and resuspended in ^2H_2O. A series of 1D ^1H NMR spectra were obtained after the addition of increasing amounts of PpcA to CbcL. The pH was monitored to confirm that it was maintained throughout the experiments.

The chemical shift variations of the heme methyl signals of PpcA were used to determine the dissociation constant (K_d). The K_d was determined by a two-parameter non-linear least-square fitting estimated under fast exchange conditions for a one binding site model corrected for the dilution effect, using OriginPro 8.5. The value was determined by the following equation, as described by Kannt et al. (1996).

$$\Delta\delta_{\text{bind}} = 0.5\Delta\delta_{\max}(\text{A} - \sqrt{\text{A}^2 - 4\text{R}}),$$

$$\text{with A} = 1 + \text{R} + \text{K}_d \frac{[\text{CbcL}]_0 + \text{R}[\text{PpcA}]_0}{[\text{CbcL}]_0[\text{PpcA}]_0}$$

In the equation, $\Delta\delta_{\text{bind}}$ is the chemical shift change at a determined protein ratio, $\Delta\delta_{\max}$ is the maximum chemical shift difference between the free and complex form of PpcA, R is the [CbcL]/[PpcA] ratio at each point. $[\text{PpcA}]_0$ and $[\text{CbcL}]_0$ correspond to the stock concentrations of each protein.

Redox Titrations Monitored by UV-Visible Spectroscopy

Redox titrations were performed in anaerobic conditions with ~3 μM of CbcL in 80 mM sodium phosphate buffer with NaCl (250 mM final ionic strength) pH 8. The UV-visible spectrophotometer (Thermo Scientific Evolution 300) was coupled to a circulating bath to keep the sample at 15°C. The solution potential was measured by a platinum pin electrode associated with an AgCl/Ag reference (Crison) and corrected for the Standard Hydrogen Electrode (SHE). The electrode was calibrated at the start and at the end of each titration with freshly prepared saturated quinhydrone solutions at pH 7 and pH 4. The following mixture of redox mediators, each at 1 μM final concentration, was added to the protein solution to promote a fast exchange between the redox centers of the protein and the electrode: 1,2-naphtoquinone-4-sulphonic acid ($E^{0'} = +215$ mV), 1,2-napthoquinone ($E^{0'} = +143$ mV), trimethylhydroquinone ($E^{0'} = +115$ mV), phenazine methosulfate ($E^{0'} = +80$ mV), phenazine ethosulfate ($E^{0'} = +55$ mV), gallocyanine ($E^{0'} = +21$ mV), methylene blue ($E^{0'} = +11$ mV), indigo tetrasulfonate ($E^{0'} = -30$ mV), indigo trisulfonate ($E^{0'} = -70$ mV), indigo disulfonate ($E^{0'} = -120$ mV), 2-hidroxy-1,4-naphthoquinone ($E^{0'} = -145$ mV), anthraquinone-2,6-disulfonate ($E^{0'} = -185$ mV), anthraquinone-2-sulfonate ($E^{0'} = -225$ mV), safranine O ($E^{0'} = -280$ mV), neutral red ($E^{0'} = -325$ mV), benzyl viologen ($E^{0'} = -345$ mV), diquat ($E^{0'} = -350$ mV) and methyl viologen ($E^{0'} = -440$ mV) (Dutton, 1978). Potassium ferricyanide and sodium dithionite were used as oxidizing and reducing agents, respectively. The experiment was performed two times, and the reduction potentials were found to be reproducible within ± 2 mV.

The reduced fraction of CbcL was calculated by integrating the area of the α band above the isosbestic points (541 and 559 nm), as previously described (Paquete et al., 2007). The macroscopic apparent midpoint reduction potential (E_{app}) value was determined after a nonlinear fit of the experimental data to a model with nine sequential one electron Nernst equations using OriginPro 8.5.

RESULTS AND DISCUSSION

Production of CbcL

The purification of CbcL involved three consecutive chromatographic steps: an affinity step followed by an anion exchange and a size exclusion step (**Figure 1A**). The purity of CbcL was evaluated by SDS-PAGE (**Figure 1A** inset) and confirmed by MALDI-TOF/TOF-MS. The peak for pure CbcL in the mass spectra at 34.5 kDa is in agreement with the expected molecular mass of 28.9 kDa of the apo-protein plus 5.6 kDa for the nine heme groups. The presence of the nine heme groups was further confirmed by the pyridine hemochrome assay. The molar extinction coefficients for CbcL were determined by the Lowry colorimetric assay at 408 nm in the oxidized form ($\varepsilon_{408\text{nm}} = 923\ \text{mM}^{-1}\cdot\text{cm}^{-1}$) and at 552 nm in the reduced form ($\varepsilon_{552\text{nm}} = 230\ \text{mM}^{-1}\cdot\text{cm}^{-1}$) and were used to calculate the purification yield of CbcL per liter of culture (0.3 mg).

Analysis of CbcL Amino Acid Sequence and Structure Prediction

The local alignment search tool (BLAST) was used to search for similar amino acid sequences to full-length CbcL in the database from NCBI (Altschul et al., 1997). The alignment of the sequences with more than 65% pairwise identity was performed with Clustal Omega (**Supplementary Figure 1**) (Sievers and Higgins, 2018). The sequences correspond to proteins from the Desulfuromonadales order belonging to Deltaproteobacteria in which the nine binding motifs (CXXCH) characteristic of *c*-type hemes are conserved. The alignment between CbcL and homologous sequences shows ten conserved histidine residues in the periplasmic domain, in addition to those of the binding motifs, and no conserved methionine residues, suggesting that all the hemes are bis-histidine coordinated. This was further confirmed by the AlphaFold protein structure prediction method

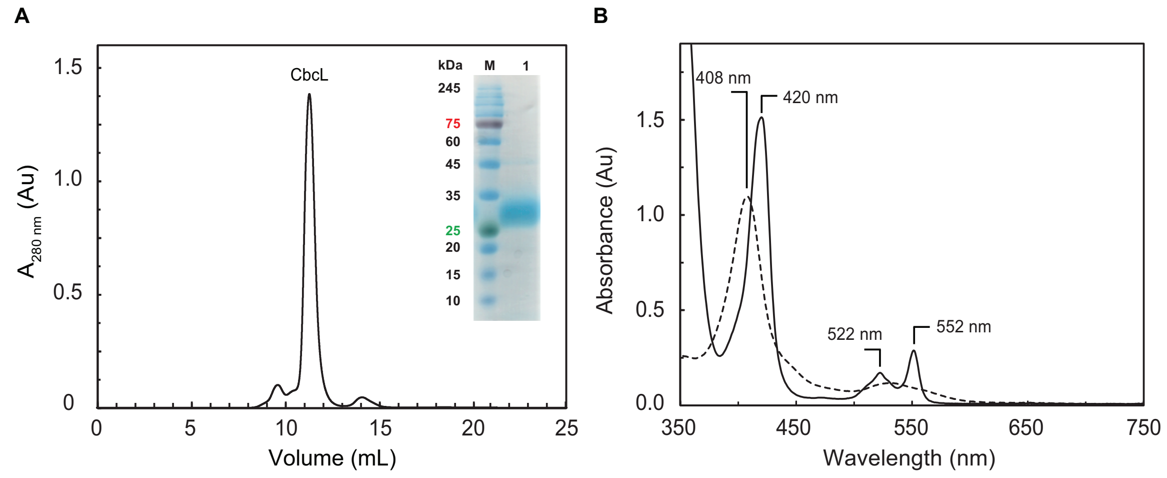

FIGURE 1 | Purification of cytochrome CbcL and its UV-visible spectral features. **(A)** Size exclusion chromatography elution profile for the last step of CbcL purification. The inset shows an SDS-PAGE gel for purified CbcL (lane 1) and molecular weight marker (lane M). **(B)** UV-visible spectra of CbcL (1 μM in 10 mM phosphate buffer pH 8) at room temperature. The solid and dashed lines correspond to the reduced and oxidized state (as purified), respectively.

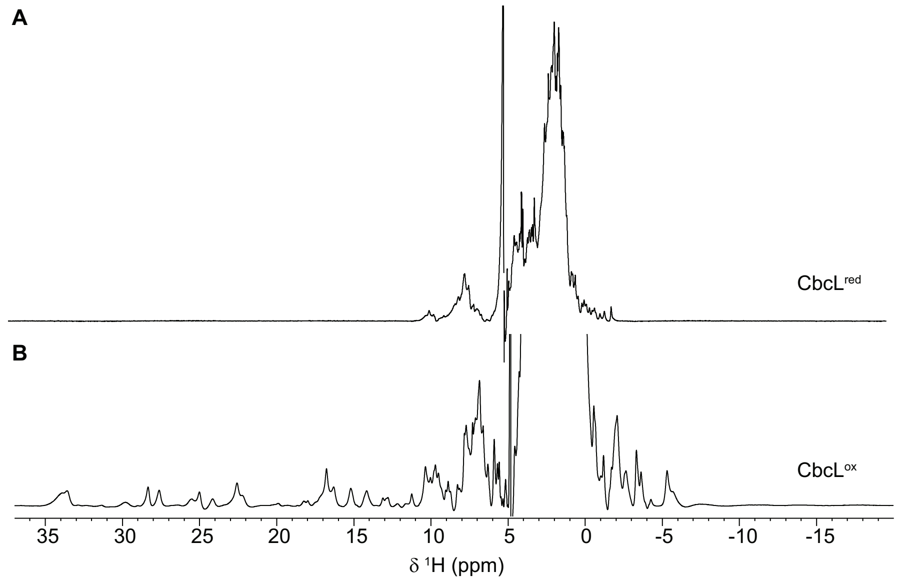

FIGURE 2 | 1D ^{1}H NMR spectra of cytochrome CbcL in the reduced **(A)** and oxidized **(B)** forms. The spectra were acquired at 25°C with 100 μM of CbcL in 10 mM sodium phosphate pH 8.

(Jumper et al., 2021) using the ChimeraX software tool (Pettersen et al., 2021) (**Supplementary Figure 2**).

Spectroscopic Characterization of CbcL

Complementary spectroscopic techniques were used for the structural and functional characterization of CbcL. The UV-visible spectra of the oxidized and reduced states (**Figure 1B**) showed features characteristic of low-spin hexacoordinated *c*-type hemes: the Soret band (at 408 and 420 nm in the oxidized and reduced states, respectively), and the typical β and α bands at 522 and 552 nm in the reduced state. The spin state of the heme groups was further confirmed by NMR. The 1D ^{1}H NMR spectra of cytochromes provide important information regarding the spin-state of the heme groups and their axial ligands. In fact, the signals for high- or low-spin hemes appear in very distinct spectral regions for each redox state. Cytochromes containing high-spin hemes typically show broad heme methyl signals above 40 ppm (Moore and Pettigrew, 1990). On the other hand, for low-spin hemes these resonances are mainly found up to 35 ppm. For the reduced form, the spectra are also distinct. Cytochromes containing high-spin hemes show larger spectral regions, typically from 30 to −15 ppm, compared to those with low-spin hemes (from 10 to −5 ppm). In the case of CbcL, the 1D ^{1}H NMR spectra in the oxidized and reduced

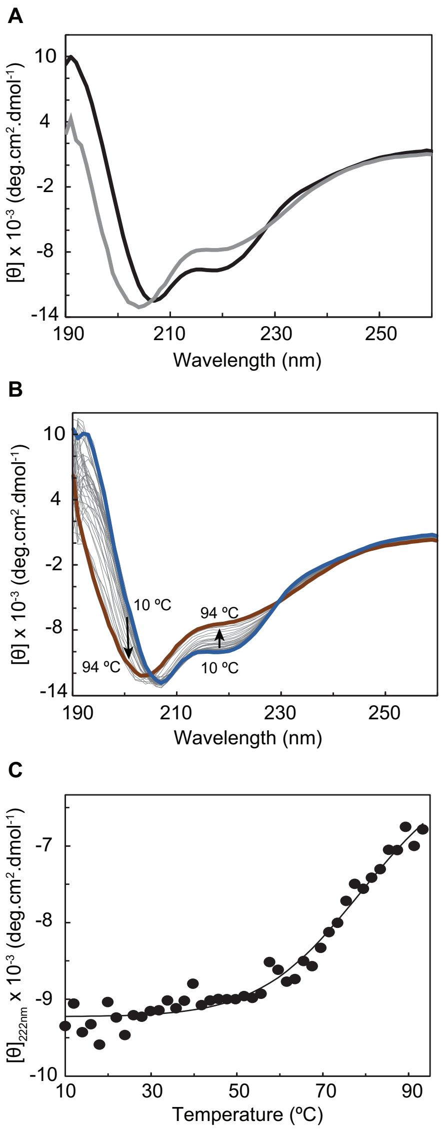

FIGURE 3 | Circular dichroism studies of cytochrome CbcL. **(A)** Far-UV CD spectra of CbcL (10 μM in 10 mM sodium phosphate pH 8) as purified (black) and after the temperature ramp (gray) at 25°C. **(B)** Far-UV CD spectra of CbcL at different temperatures (10–94°C). **(C)** Thermal unfolding of CbcL. Mean residue ellipticity [θ] variation at 222 nm as a function of temperature. The solid line represents the fitting of the experimental data to a two-state transition, resulting in a melting temperature of 81 ± 5°C.

states are considerably different (**Figure 2**). In the reduced state (**Figure 2A**), the signals cover the spectral width between 10 and −5 ppm, which is characteristic of a low spin cytochrome (Fe(II), $S = 0$). In the oxidized state, the signals are broader and cover a larger spectral region from 35 to −7 ppm, as expected from the paramagnetic effect caused by the unpaired electron of each heme (**Figure 2B**). The shape and the spectral region covered by the signals in the oxidized state also confirms that the heme groups are low-spin (Fe(III), $S = 1/2$).

Circular dichroism (CD) spectroscopy in the far-UV region (190–260 nm) was then used to probe the secondary structural elements and the thermal stability of CbcL. The CD spectrum of CbcL (**Figure 3A**, black line) has a positive maximum at 191 nm and two minima at 207 nm and 218. The signal at 207 is characteristic of α-helical structures whereas that at 218 nm represents a mixture of α-helix and β-sheet structure (Wei et al., 2014). The percentages of secondary structural elements of CbcL were calculated by the program DichroWeb (Whitmore and Wallace, 2004) and are listed in **Table 1**. The results obtained show that the secondary structure of CbcL is mostly disordered (37%) followed by 29, 18, and 15% of α-helix, β-sheet and turns, respectively. As observed for other multiheme cytochromes, CbcL also has a low ratio of amino acids per heme (28 residues), which restrains the amount of ordered secondary structure as observed for example for the triheme cytochrome PpcA (Pokkuluri et al., 2011) and the dodecaheme cytochrome GSU1996 (Pokkuluri et al., 2010), which have 24 and 26 residues per heme, respectively (**Table 1**). This is also in agreement with the structural model predicted by AlphaFold that mostly shows disordered and helical elements (**Supplementary Figure 2**).

The conformational stability of CbcL was assessed by performing temperature-induced denaturation (from 10 to 94°C), monitored by far-UV CD at 222 nm, which reports on the stability of the α-helical secondary structural elements. The data show that the protein unfolding results in the loss of secondary structure, evidenced by the decrease in the ellipticity of the 222 nm signal, particularly above 50°C (**Figures 3B,C**). An unfolding enthalpy of 82.0 ± 13.2 kJ·mol^{-1} (19.6 ± 3.1 kcal·mol^{-1}) was also determined. This value is in line with enthalpy values of unfolding for model monomer proteins (17.7 and 21.5 kcal·mol^{-1}) (Greenfield, 2007a). Analyzing the spectra before and after the temperature ramp, it can also be observed that the thermal unfolding is not fully reversible, as the far-UV CD absorption fingerprints are not fully restored. In fact, after the temperature ramp, the spectrum obtained at 25°C (**Figure 3A**, gray line) shows a shift of the negative band maximum from 207 to 204 nm, as well as a considerable change in ellipticity at 191 nm, when compared with the spectrum obtained before the temperature ramp.

Functional Characterization of CbcL

The next step on the characterization of CbcL was the determination of its reduction potential and redox working functional range. The distinct spectral UV-visible spectroscopic features of CbcL in the oxidized and reduced forms (**Figure 1B**) were explored to monitor the variation of its reduced fraction with the solution redox potential. Thus, redox titrations followed by UV-visible spectroscopy were performed for CbcL at pH 8 by monitoring the variation of the α-band (552 nm) with the solution redox potential (**Figure 4A**). The apparent reduction potential (E_{app}) of −194 ± 2 mV was determined for CbcL. Given the cellular localization of CbcL at the inner membrane, it is most likely that the electrons are transferred from CbcL to periplasmic proteins also involved in the same extracellular electron transfer pathway. The triheme cytochrome PpcA is

TABLE 1 | Structural features of cytochromes CbcL, PpcA and GSU1996 from *G. sulfurreducens*.

Cytochromes	Secondary structure elements (%)				Number of residues	Number of heme groups
	α-Helix	β-Sheet	Turn	Disordered		
CbcL (25°C)[1]	29	18	15	37	250	9
PpcA[2]	28	15	41	17	71	3
GSU1996[2]	19	12	52	18	318	12

The percentage of secondary structure elements of CbcL was determined by CD spectroscopy in the far-UV region. Data for PpcA and GSU1996 is also presented for comparison.

[1] *According to the results obtained from the DichroWeb online platform.*

[2] *According to the results obtained from the online platform STRIDE (Frishman and Argos, 1995) using the PDB files: 2MZ9 (Pokkuluri et al., 2004b) and 3OV0 (Pokkuluri et al., 2011) for PpcA and GSU1996, respectively.*

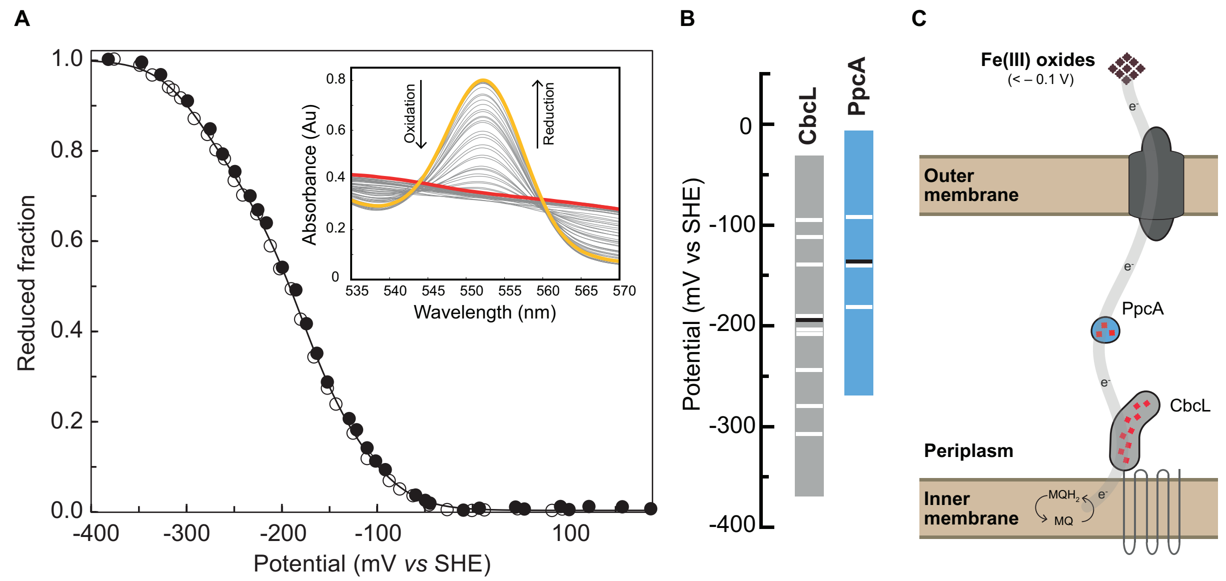

FIGURE 4 | Redox characterization of cytochrome CbcL. **(A)** Redox titrations at pH 8 monitored by UV-visible spectroscopy. The experimental data are represented by closed (reductive direction) and open (oxidative direction) circles. The solid line represents the fitted curve. The inset shows the α-band region monitored throughout the redox titration. Fully reduced and fully oxidized spectra are represented in yellow and red, respectively. **(B)** Redox-active windows (1–99% range for protein reduction/oxidation) of CbcL (this work) and PpcA (Morgado et al., 2008) at pH 8. Horizontal black lines correspond to the E_{app} of each cytochrome, and horizontal white lines correspond to the fitted sequential macroscopic reduction potential values. **(C)** Proposed model for extracellular electron transfer to Fe(III) oxides and electrodes poised at -100 mV in *G. sulfurreducens*.

the most abundant periplasmic cytochrome and is a putative redox partner of CbcL. The E_{app} value of PpcA (−138mV (Morgado et al., 2008)) is less negative then the one obtained for CbcL, suggesting a thermodynamically favorable electron transfer from CbcL to PpcA.

Monitorization of the Electron Transfer Reaction Between CbcL and PpcA by NMR

The redox properties of CbcL and PpcA, as well as their cellular localization, strongly suggest that CbcL is most likely able to transfer electrons to PpcA. To verify this hypothesis, the electron transfer reaction between CbcL and PpcA was probed by NMR. The spectral features of the 1D ^{1}H NMR spectra of CbcL and PpcA in the reduced and oxidized states were used to assess the electron transfer reaction between the two proteins, following a newly developed strategy to monitor electron transfer between cytochromes (Morgado and Salgueiro, 2022). Thus, a reduced sample of CbcL (CbcL^{red}) was prepared and then titrated with increasing equimolar amounts of oxidized PpcA (PpcA^{ox}). After the first addition of PpcA^{ox} (**Figure 5**, 1:1 NMR spectrum) the signals characteristic of reduced PpcA (PpcA^{red}; **Supplementary Figure 3**) are visible in the region between 5 and 11 ppm (yellow rectangle in **Figure 5**) and no typical fingerprint of PpcA^{ox} is observed (resonances between 11 and 22 ppm), confirming that electrons were transferred from CbcL to PpcA.

Following the subsequent additions of PpcA^{ox} the NMR signals of CbcL in the low field region of the spectra above 22 ppm are visible. Since the reduction potential of CbcL is more negative and it has three times more hemes than

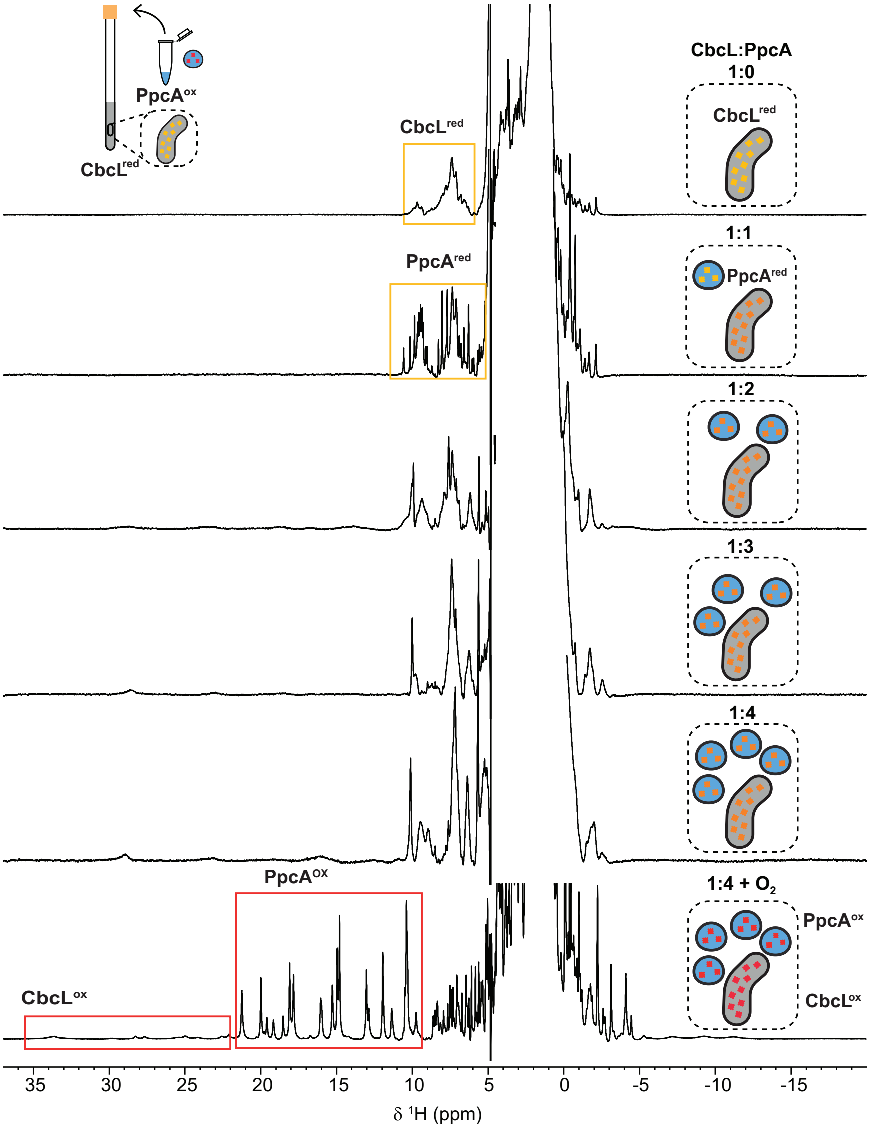

FIGURE 5 | Monitorization of the electron transfer reaction between cytochromes CbcL and PpcA by NMR. 1D ^{1}H NMR spectra were acquired at 25°C with 100 μM of CbcL in 10 mM sodium phosphate pH 8 with increasing equimolar amounts of PpcA, up to 1:4 ratio. The rectangles highlight the cytochromes' fingerprints in the reduced and oxidized states. The schemes represent the addition of equimolar amounts of oxidized PpcA (blue) to the NMR tube containing initially reduced CbcL (yellow). Red represents fully oxidized states, yellow fully reduced states, and intermediate redox states are represented in orange.

PpcA, it could be expected that, after the addition of three molar equivalents of PpcA^{ox}, CbcL would be fully oxidized. However, this was not observed and, instead, CbcL and PpcA were both in intermediate oxidation states since broad signals are observed between 11 and 30 ppm (1:3 NMR spectrum in **Figure 5**). Even after the addition of four molar equivalents of PpcA^{ox}, an intermediate oxidation state remained for both cytochromes (1:4 NMR spectrum in **Figure 5**). To confirm that the two cytochromes were in an intermediate oxidation state, the NMR tube was unsealed. The contact with atmospheric O_2 led to the fully oxidation of both cytochromes, as confirmed by the typical signals of CbcL^{ox} and PpcA^{ox} (1:4 + O_2 NMR spectrum in **Figure 5**). This experimental setup allowed to observe the partial reduction of PpcA with electrons provided by CbcL, indicating that this redox pair is indeed able to transfer electrons with the directionality expected from their reduction potential values. The results also indicate that the physiological state of the cytochromes is neither fully reduced nor oxidized. Indeed, the difference of 56 mV in their apparent midpoint reduction potential values assures an overlap of their redox windows (**Figure 4B**). This overlap explains why electrons are not fully transferred from CbcL to PpcA. Instead, they remain in equilibrium acting as a reservoir of electrons to permit a constant flow whenever CbcL is loaded with electrons by the quinone pool, and PpcA oxidized by its redox partner (**Figure 4C**).

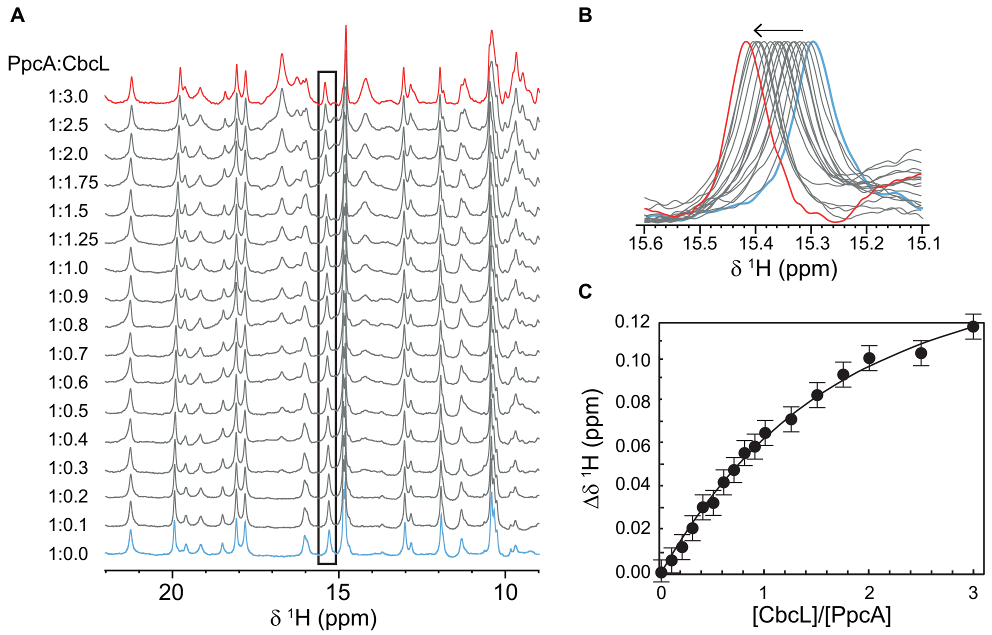

FIGURE 6 | Binding studies between cytochromes PpcA and CbcL followed by NMR chemical shift perturbation experiments. **(A)** 1D ^{1}H NMR spectra of PpcA acquired with increasing amounts of CbcL (ratio PpcA:CbcL indicated on the left side of each spectrum). Spectra were acquired at 25°C with 50 μM of PpcA in 10 mM sodium phosphate pH 8. **(B)** Expansion of the region containing the most affected heme methyl signal $18^1CH_3{}^I$. **(C)** Binding curve for CbcL and PpcA monitored by the chemical shift changes of heme methyl $18^1CH_3{}^I$. The error bars represent estimated experimental errors. The solid line represents the fitting for a K_d of 57 ± 9 μM.

Interaction Studies Between CbcL and the Periplasmic Cytochrome PpcA

Having shown that CbcL and PpcA can exchange electrons, the distinct NMR spectral features of the two cytochromes were then explored to determine the affinity constant of the redox complex. NMR chemical shift perturbation experiments have been used to probe interacting regions between redox proteins, particularly in the oxidized state for which the signal dispersion is considerably larger compared to the reduced form (Bashir et al., 2011; Fonseca et al., 2013; Dantas et al., 2017; Fernandes et al., 2017). This is case of cytochromes CbcL and PpcA whose spectra in the oxidized state are considerably different (**Figure 2**). In the case of redox complexes between multiheme *c*-type cytochromes, it is expected that at least one heme from each protein would be in close contact. Thus, if interacting, the chemical environment in the vicinity of these groups would be altered and the chemical shift (or broadening) of the heme methyl(s) signal(s) would be affected. Therefore, in the present work, NMR chemical shift perturbation experiments were carried out for the two cytochromes in the oxidized state by adding successive amounts of one cytochrome to the other. **Supplementary Figure 4** depicts the 1D ^{1}H NMR spectra of CbcL in the low-field region titrated with increasing amounts of PpcA. The heme methyl signals of CbcL that are detected between 22 and 35 ppm are not affected upon addiction of PpcA. However, this does not completely exclude the interaction, since the binding region could be in the vicinity of the heme groups whose resonances are not detected in that region of the spectra. Consequently, the chemical shifts perturbations were also probed for PpcA heme methyl signals (**Figure 6A**). The higher perturbation was observed for the heme methyl $18^1CH_3{}^I$ and the variation of its chemical shift was used to determine the dissociation constant (K_d) of the complex (**Figures 6B,C**). The value obtained in the micromolar range (57 ± 9 μM) suggests the formation of a low affinity complex characteristic of redox partners and is in line with values previously reported for redox proteins (Bashir et al., 2011; Meschi et al., 2011; Fonseca et al., 2013).

CONCLUSION

Multiheme cytochromes have a crucial role in extracellular electron transfer mechanisms in exoelectrogenic microorganisms, acting as electron capacitors and carriers. Cytochrome CbcL is one of the inner membrane quinone oxidoreductases identified in *G. sulfurreducens* and was shown to be essential for the reduction of extracellular electron acceptors with reduction potentials lower than −100 mV. CbcL is composed by a transmembrane domain and a soluble periplasmic domain, and the latter is a *c*-type cytochrome with nine heme groups and was biochemically characterized in this work. The spectroscopic characterization revealed that the hemes are low spin and coordinated by two histidine residues and that the polypeptide chain has a low content of secondary structural elements, features that are typically observed for multiheme cytochromes. Compared to the one of the periplasmic cytochrome PpcA (−138 mV), the reduction potential value of CbcL (−194 mV) is more negative. This suggests a thermodynamically favorable electron transfer from CbcL to PpcA and a putative formation of a redox complex. Using NMR it was possible to unequivocally confirm the formation of this complex. In fact, direct electron transfer from reduced CbcL to oxidized PpcA was observed in 1D ^{1}H NMR titrations. Additionally, NMR chemical shift perturbation experiments also showed the formation of a low affinity complex between the two cytochromes.

The unequivocal demonstration of the formation of a complex between CbcL and PpcA, as well as the superimposition of their redox active windows assures the continuous flow of electrons from the inner membrane towards the periplasm and ultimately to the extracellular electron acceptors.

DATA AVAILABILITY STATEMENT

The original contributions presented in the study are included in the article/**Supplementary Material**, further inquiries can be directed to the corresponding authors.

AUTHOR CONTRIBUTIONS

LM and CS designed and supervised the project. JA, MS, and LM performed the experiments and data analysis. JA, CS, and LM wrote the manuscript. All authors contributed to the article and approved the submitted version.

FUNDING

This work was supported by Fundação para a Ciência e Tecnologia (Portugal) through the grants SFRH/BPD/114848/2016 (LM), PTDC/BIA-BQM/31981/2017 (CAS) and PTDC/BIA-BQM/4967/2020 (CAS). This work was also supported by national funds from FCT in the scope of the project UIDP/04378/2020 and UIDB/04378/2020 (UCIBIO) and project LA/P/0140/2020 (i4HB). The NMR spectrometers are part of the National NMR Network (PTNMR) and are supported by FCT-MCTES (ROTEIRO/0031/2013 – PINFRA/22161/2016) co-funded by FEDER through COMPETE 2020, POCI, and PORL and FCT through PIDDAC.

ACKNOWLEDGMENTS

Elisabete Ferreira (BioLab, UCIBIO, NOVA School of Science and Technology) for the technical assistance with the CD experiments.

SUPPLEMENTARY MATERIAL

The Supplementary Material for this article can be found online at: https://www.frontiersin.org/articles/10.3389/fmicb.2022.898015/full#supplementary-material

REFERENCES

Al-Amshawee, S., Yunus, M. Y. B. M., Azoddein, A. A. M., Hassell, D. G., Dakhil, I. H., and Hasan, H. A. (2020). Electrodialysis desalination for water and wastewater: a review. *Chem. Eng. J.* 380:122231. doi: 10.1016/j.cej.2019.122231

Altschul, S. F., Madden, T. L., Schäffer, A. A., Zhang, J., Zhang, Z., Miller, W., et al. (1997). Gapped BLAST and PSI-BLAST: a new generation of protein database search programs. *Nucleic Acids Res.* 25, 3389–3402. doi: 10.1093/nar/25.17.3389

Bashir, Q., Scanu, S., and Ubbink, M. (2011). Dynamics in electron transfer protein complexes. *FEBS J.* 278, 1391–1400. doi: 10.1111/j.1742-4658.2011.08062.x

Berry, E. A., and Trumpower, B. L. (1987). Simultaneous determination of hemes *a*, *b*, and *c* from pyridine hemochrome spectra. *Anal. Biochem.* 161, 1–15. doi: 10.1016/0003-2697(87)90643-9

Cavalier-Smith, T., Brasier, M., and Embley, T. M. (2006). Introduction: how and when did microbes change the world? *Philos. Trans. R. Soc. B Biol. Sci.* 361, 845–850. doi: 10.1098/rstb.2006.1847

Dantas, J. M., Brausemann, A., Einsle, O., and Salgueiro, C. A. (2017). NMR studies of the interaction between inner membrane-associated and periplasmic cytochromes from *Geobacter sulfurreducens*. *FEBS Lett.* 591, 1657–1666. doi: 10.1002/1873-3468.12695

Fernandes, A. P., Nunes, T. C., Paquete, C. M., and Salgueiro, C. A. (2017). Interaction studies between periplasmic cytochromes provide insights into extracellular electron transfer pathways of *Geobacter sulfurreducens*. *Biochem. J.* 474, 797–808. doi: 10.1042/BCJ20161022

Fonseca, B. M., Paquete, C. M., Neto, S. E., Pacheco, I., Soares, C. M., and Louro, R. O. (2013). Mind the gap: cytochrome interactions reveal electron pathways across the periplasm of *Shewanella oneidensis* MR-1. *Biochem. J.* 449, 101–108. doi: 10.1042/BJ20121467

Frishman, D., and Argos, P. (1995). Knowledge-based secondary structure assignment. *Proteins Struct. Funct. Genet.* 23, 566–579. doi: 10.1093/nar/gkh429

Greenfield, N. J. (2007b). Using circular dichroism spectra to estimate protein secondary structure. *Nat. Protoc.* 1, 2876–2890. doi: 10.1038/nprot.2006.202

Greenfield, N. J. (2007a). Using circular dichroism collected as a function of temperature to determine the thermodynamics of protein unfolding and binding interactions. *Nat. Protoc.* 1, 2527–2535. doi: 10.1038/nprot.2006.204

Joshi, K., Chan, C. H., and Bond, D. R. (2021). *Geobacter sulfurreducens* inner membrane cytochrome CbcBA controls electron transfer and growth yield near the energetic limit of respiration. *Mol. Microbiol.* 116, 1124–1139. doi: 10.1111/mmi.14801

Jumper, J., Evans, R., Pritzel, A., Green, T., Figurnov, M., Ronneberger, O., et al. (2021). Highly accurate protein structure prediction with AlphaFold. *Nature* 596, 583–589. doi: 10.1038/s41586-021-03819-2

Kanehisa, M., Sato, Y., Kawashima, M., Furumichi, M., and Tanabe, M. (2016). KEGG as a reference resource for gene and protein annotation. *Nucleic Acids Res.* 44, D457–D462. doi: 10.1093/nar/gkv1070

Kannt, A., Young, S., and Bendall, D. S. (1996). The role of acidic residues of plastocyanin in its interaction with cytochrome *f. Biochim. Biophys. Acta Bioenerg.* 1277, 115–126. doi: 10.1016/S0005-2728(96)00090-4

Koffi, N. J., and Okabe, S. (2020). High voltage generation from wastewater by microbial fuel cells equipped with a newly designed low voltage booster multiplier (LVBM). *Sci. Rep.* 10:18985. doi: 10.1038/S41598-020-75916-7

Kumar, R., Singh, L., Wahid, Z. A., and Din, M. F. M. (2015). Exoelectrogens in microbial fuel cells toward bioelectricity generation: a review. *Int. J. Energy Res.* 39, 1048–1067. doi: 10.1002/er.3305

Dutton, P. L. (1978). Redox potentiometry: determination of midpoint potentials of oxidation-reduction components of biological electron-transfer systems. *Methods Enzymol.* 54, 411–435. doi: 10.1016/S0076-6879(78)54026-3

Levar, C. E., Chan, C. H., Mehta-Kolte, M. G., and Bond, D. R. (2014). An inner membrane cytochrome required only for reduction of high redox potential extracellular electron acceptors. *MBio* 5:e0203414. doi: 10.1128/mBio.02034-14

Logan, B. E., Rossi, R., Ragab, A., and Saikaly, P. E. (2019). Electroactive microorganisms in bioelectrochemical systems. *Nat. Rev. Microbiol.* 17, 307–319. doi: 10.1038/s41579-019-0173-x

Londer, Y. Y., Pokkuluri, P. R., Tiede, D. M., and Schiffer, M. (2002). Production and preliminary characterization of a recombinant triheme cytochrome c_7 from *Geobacter sulfurreducens* in *Escherichia coli*. *Biochim. Biophys. Acta - Bioenerg.* 1554, 202–211. doi: 10.1016/S0005-2728(02)00244-X

Lovley, D. R., Holmes, D. E., and Nevin, K. P. (2004). Dissimilatory Fe(III) and Mn(IV) reduction. *Adv. Microb. Physiol.* 49, 219–286. doi: 10.1016/S0065-2911(04)49005-5

Lovley, D. R., Ueki, T., Zhang, T., Malvankar, N. S., Shrestha, P. M., Flanagan, K. A., et al. (2011). Geobacter. The Microbe Electric's Physiology, Ecology, and Practical Applications. *Adv Microb Physiol* 59, 1–100. doi: 10.1016/B978-0-12-387661-4.00004-5

Marsili, E., Sun, J., and Bond, D. R. (2010). Voltammetry and growth physiology of *Geobacter sulfurreducens* biofilms as a function of growth stage and imposed electrode potential. *Electroanalysis* 22, 865–874. doi: 10.1002/elan.200800007

Meschi, F., Wiertz, F., Klauss, L., Blok, A., Ludwig, B., Merli, A., et al. (2011). Efficient electron transfer in a protein network lacking specific interactions. *J. Am. Chem. Soc.* 133, 16861–16867. doi: 10.1021/ja205043f

Moore, G. W., and Pettigrew, G. R. (1990). *Cytochromes c: Evolutionary, Structural and Physicochemical Aspects*. New York: Springer Science & Business Media.

Morgado, L., Bruix, M., Orshonsky, V., Londer, Y. Y., Duke, N. E. C., Yang, X., et al. (2008). Structural insights into the modulation of the redox properties of two *Geobacter sulfurreducens* homologous triheme cytochromes. *Biochim. Biophys. Acta - Bioenerg.* 1777, 1157–1165. doi: 10.1016/j.bbabio.2008.04.043

Morgado, L., and Salgueiro, C. A. (2022). Elucidation of complex respiratory chains: a straightforward strategy to monitor electron transfer between cytochromes. *Metallomics* mfac012. [Epub online ahead of print]. doi: 10.1093/mtomcs/mfac012

Nealson, K. H., and Saffarini, D. (1994). Iron and manganese in anaerobic respiration: environmental significance, physiology, and regulation. *Annu. Rev. Microbiol.* 48, 311–343. doi: 10.1146/annurev.mi.48.100194.001523

Ohnishi, S. T., and Barr, J. K. (1978). A simplified method of quantitating protein using the biuret and phenol reagents. *Anal. Biochem.* 86, 193–200. doi: 10.1016/0003-2697(78)90334-2

Paquete, C. M., Turner, D. L., Louro, R. O., Xavier, A. V., and Catarino, T. (2007). Thermodynamic and kinetic characterisation of individual haems in multicentre cytochromes c_3. *Biochim. Biophys. Acta - Bioenerg.* 1767, 1169–1179. doi: 10.1016/j.bbabio.2007.06.005

Pettersen, E. F., Goddard, T. D., Huang, C. C., Meng, E. C., Couch, G. S., Croll, T. I., et al. (2021). UCSF ChimeraX: Structure visualization for researchers, educators, and developers. *Protein Sci.* 30, 70–82. doi: 10.1002/pro.3943

Pierattelli, R., Banci, L., and Turner, D. L. (1996). Indirect determination of magnetic susceptibility tensors in peroxidases: a novel approach to structure elucidation by NMR. *J. Biol. Inorg. Chem.* 1, 320–329. doi: 10.1007/s007750050060

Pokkuluri, P. R., Londer, Y. Y., Duke, N. E. C., Erickson, J., Pessanha, M., Salgueiro, C. A., et al. (2004a). Structure of a novel c_7 -type three-heme cytochrome domain from a multidomain cytochrome *c* polymer. *Protein Sci.* 13, 1684–1692. doi: 10.1110/ps.04626204

Pokkuluri, P. R., Londer, Y. Y., Duke, N. E. C., Long, W. C., and Schiffer, M. (2004b). Family of Cytochrome c_7-Type Proteins from *Geobacter sulfurreducens*: structure of One Cytochrome c_7 at 1.45 Å Resolution. *Biochemistry* 43, 849–859. doi: 10.1021/bi0301439

Pokkuluri, P. R., Londer, Y. Y., Duke, N. E. C., Pessanha, M., Yang, X., Orshonsky, V., et al. (2011). Structure of a novel dodecaheme cytochrome *c* from *Geobacter sulfurreducens* reveals an extended 12nm protein with interacting hemes. *J. Struct. Biol.* 174, 223–233. doi: 10.1016/j.jsb.2010.11.022

Pokkuluri, P. R., Londer, Y. Y., Yang, X., Duke, N. E. C., Erickson, J., Orshonsky, V., et al. (2010). Structural characterization of a family of cytochromes c_7 involved in Fe(III) respiration by *Geobacter sulfurreducens*. *Biochim. Biophys. Acta Bioenerg.* 1797, 222–232. doi: 10.1016/j.bbabio.2009.10.007

Popescu, D.-M., Newman, D. K., and Banfiel, J. F. (2002). Geomicrobiology: how Molecular-Scale Interactions. *Science* 296, 1071–1077. doi: 10.1126/science.1010716

Rimboud, M., Desmond-Le Quemener, E., Erable, B., Bouchez, T., and Bergel, A. (2015). Multi-system Nernst-Michaelis-Menten model applied to bioanodes formed from sewage sludge. *Bioresour. Technol.* 195, 162–169. doi: 10.1016/j.biortech.2015.05.069

Sievers, F., and Higgins, D. G. (2018). Clustal Omega for making accurate alignments of many protein sequences. *Protein Sci.* 27, 135–145. doi: 10.1002/pro.3290

Speers, A. M., and Reguera, G. (2012). Electron donors supporting growth and electroactivity of *Geobacter sulfurreducens* anode biofilms. *Appl. Environ. Microbiol.* 78, 437–444. doi: 10.1128/AEM.06782-11

Ueki, T. (2021). Cytochromes in Extracellular Electron Transfer in *Geobacter*. *Appl. Environ. Microbiol.* 87, 1–16. doi: 10.1128/AEM.03109-20

Vasyliv, O. M., Bilyy, O. I., Ferensovych, Y. P., and Hnatush, S. O. (2013). "Application of acetate, lactate, and fumarate as electron donors in microbial fuel cell," in *Reliab. Photovolt. Cells, Modul. Components, Syst. VI* 8825, 88250Q, Proc. SPIE 8825. doi: 10.1117/12.2021381

Wei, Y., Thyparambil, A. A., and Latour, R. A. (2014). Protein helical structure determination using CD spectroscopy for solutions with strong background absorbance from 190 to 230 nm. *Biochim. Biophys. Acta Proteins Proteomics* 1844, 2331–2337. doi: 10.1016/j.bbapap.2014.10.001

Whitmore, L., and Wallace, B. (2004). A. DICHROWEB, an online server for protein secondary structure analyses from circular dichroism spectroscopic data. *Nucleic Acids Res.* 32, W668–W673. doi: 10.1093/nar/gkh371

Yoho, R. A., Popat, S. C., and Torres, C. I. (2014). Dynamic potential-dependent electron transport pathway shifts in anode biofilms of *Geobacter sulfurreducens*. *Chem. Sus. Chem.* 7, 3413–3419. doi: 10.1002/cssc.201402589

Zacharoff, L., Chan, C. H., and Bond, D. R. (2016). Reduction of low potential electron acceptors requires the CbcL inner membrane cytochrome of *Geobacter sulfurreducens*. *Bioelectrochemistry* 107, 7–13. doi: 10.1016/j.bioelechem.2015.08.003

Conflict of Interest: The authors declare that the research was conducted in the absence of any commercial or financial relationships that could be construed as a potential conflict of interest.

Frontiers in Microbiology

ORIGINAL RESEARCH
published: 19 May 2022
doi: 10.3389/fmicb.2022.883807

Polyphosphate Dynamics in Cable Bacteria

Nicole M. J. Geerlings[1]*, Michiel V. M. Kienhuis[1], Silvia Hidalgo-Martinez[2,3], Renee Hageman[1], Diana Vasquez-Cardenas[2], Jack J. Middelburg[1], Filip J. R. Meysman[2,3] and Lubos Polerecky[1]*

[1] Department of Earth Sciences, Utrecht University, Utrecht, Netherlands, [2] Excellence centre for Microbial Systems Technology, University of Antwerp, Wilrijk, Belgium, [3] Department of Biotechnology, Delft University of Technology, Delft, Netherlands

Cable bacteria are multicellular sulfide oxidizing bacteria that display a unique metabolism based on long-distance electron transport. Cells in deeper sediment layers perform the sulfide oxidizing half-reaction whereas cells in the surface layers of the sediment perform the oxygen-reducing half-reaction. These half-reactions are coupled *via* electron transport through a conductive fiber network that runs along the shared cell envelope. Remarkably, only the sulfide oxidizing half-reaction is coupled to biosynthesis and growth whereas the oxygen reducing half-reaction serves to rapidly remove electrons from the conductive fiber network and is not coupled to energy generation and growth. Cells residing in the oxic zone are believed to (temporarily) rely on storage compounds of which polyphosphate (poly-P) is prominently present in cable bacteria. Here we investigate the role of poly-P in the metabolism of cable bacteria within the different redox environments. To this end, we combined nanoscale secondary ion mass spectrometry with dual-stable isotope probing (^{13}C-DIC and ^{18}O-H_2O) to visualize the relationship between growth in the cytoplasm (^{13}C-enrichment) and poly-P activity (^{18}O-enrichment). We found that poly-P was synthesized in almost all cells, as indicated by ^{18}O enrichment of poly-P granules. Hence, poly-P must have an important function in the metabolism of cable bacteria. Within the oxic zone of the sediment, where little growth is observed, ^{18}O enrichment in poly-P granules was significantly lower than in the suboxic zone. Thus, both growth and poly-P metabolism appear to be correlated to the redox environment. However, the poly-P metabolism is not coupled to growth in cable bacteria, as many filaments from the suboxic zone showed poly-P activity but did not grow. We hypothesize that within the oxic zone, poly-P is used to protect the cells against oxidative stress and/or as a resource to support motility, while within the suboxic zone, poly-P is involved in the metabolic regulation before cells enter a non-growing stage.

Keywords: cable bacteria, polyphosphate, nanoSIMS, stable isotope probing, cell cycle

Edited by:
Amelia-Elena Rotaru,
University of Southern Denmark, Denmark

Reviewed by:
Nils Risgaard-Petersen,
Aarhus University, Denmark
Ke-Qing Xiao,
University of Leeds, United Kingdom

***Correspondence:**
Nicole M. J. Geerlings
N.M.J.Geerlings@uu.nl
Lubos Polerecky
L.Polerecky@uu.nl

Specialty section:
This article was submitted to Microbiological Chemistry and Geomicrobiology, a section of the journal Frontiers in Microbiology

Received: 25 February 2022
Accepted: 18 April 2022
Published: 19 May 2022

Citation:
Geerlings NMJ, Kienhuis MVM, Hidalgo-Martinez S, Hageman R, Vasquez-Cardenas D, Middelburg JJ, Meysman FJR and Polerecky L (2022) Polyphosphate Dynamics in Cable Bacteria. Front. Microbiol. 13:883807. doi: 10.3389/fmicb.2022.883807

INTRODUCTION

Cable bacteria are long, unbranched filamentous microorganisms consisting of thousands of cells that metabolically cooperate through electrical currents (Pfeffer et al., 2012). A given filament spatially couples sulfide oxidation ($H_2S + 4\ H_2O \rightarrow SO_4^{2-} + 10\ H^+ + 8\ e^-$) in deeper sediment layers to oxygen reduction ($O_2 + 4\ H^+ + 4\ e^- \rightarrow 4\ H_2O$) at the sediment-water interface via a process termed long-distance electron transport (Nielsen et al., 2010; Pfeffer et al., 2012). These two redox half-reactions are thus occurring in different cells of the same filament, with the necessary electrical coupling ensured by the transport of electrons over centimeter-scale distances through a conductive fiber network that runs internally (i.e., within the shared periplasmic space) along the entire filament (Meysman et al., 2019; Thiruvallur Eachambadi et al., 2020). This spatial separation of redox half-reactions gives cable bacteria a competitive advantage over other sulfide-oxidizing bacteria, because it allows them to harvest energy from aerobic sulfide oxidation even though free sulfide is spatially separated from molecular oxygen by centimeter-scale distances (Pfeffer et al., 2012; Risgaard-Petersen et al., 2012; Meysman, 2018).

Cable bacteria are facultative autotrophs that mainly assimilate inorganic CO_2 via the Wood-Ljungdahl pathway, but can also assimilate propionate (Vasquez-Cardenas et al., 2015; Kjeldsen et al., 2019; Geerlings et al., 2020). They are found in a wide range of aquatic sediment environments including marine (Malkin et al., 2014; Burdorf et al., 2017), freshwater (Risgaard-Petersen et al., 2015), and aquifer (Müller et al., 2016) sediments. They have also been found in association with oxygenated zones around plant roots (Scholz et al., 2019) and worm tubes in marine sediments (Aller et al., 2019), or attached to the anode of a benthic microbial fuel cell placed in anaerobic conditions (Reimers et al., 2017).

A conspicuous aspect of the metabolism of cable bacteria is that the metabolic energy harvested through long-distance electron transport is not made equally available to all cells within a filament (Geerlings et al., 2020). Specifically, cable bacteria filaments display a remarkable division of "energy rewards," in which only the sulfide oxidizing cells gain enough energy for biosynthesis and growth, whereas the oxygen reducing cells dispense electrons as quickly as possible without biosynthesis and growth (Kjeldsen et al., 2019; Geerlings et al., 2020). Therefore, the oxygen reducing cells appear to provide a kind of "community service" to the filament by ensuring that the electrical current can flow, but only facilitates the growth of the sulfide oxidizing cells (Geerlings et al., 2020).

To maintain their function, oxygen reducing cells have been hypothesized to temporarily rely on storage compounds, of which polyphosphate (poly-P) is the most ubiquitous within cable bacteria (Kjeldsen et al., 2019; Geerlings et al., 2019). For example, poly-P granules have been observed in both marine (Sulu-Gambari et al., 2016; Geerlings et al., 2019) and freshwater (Kjeldsen et al., 2019) cable bacteria. The size and density of the granules widely vary among filaments from the same redox environment and to a lesser extent also within individual filaments (Geerlings et al., 2019).

Poly-P is a ubiquitous inorganic biopolymer consisting of tens to hundreds of phosphate residues linearly linked together by the same high-energy phosphoanhydride bond that is also found in ATP (Rao et al., 2009). Poly-P granules are found in cells across all three domains of life (Rao et al., 2009) and were actually one of the first subcellular structures described in bacteria (Meyer, 1904). The enzymes involved in poly-P metabolism are highly conserved (Rao et al., 2009), and it is believed that poly-P has played a key role in the origin of life (Brown and Kornberg, 2004; Achbergerová and Nahálka, 2011). In microbial cells, poly-P appears to have distinctive biological functions depending on the abundance, chain length, biological source, and subcellular location of the granules. It is thought to act as an ATP substitute and energy storage molecule, although the metabolic turnover of ATP is considerably faster than that of poly-P (Kornberg, 1995; Ault-Riché et al., 1998). Poly-P granules can also serve as reservoir for orthophosphate (P_i). Due to their anionic nature, poly-P molecules typically form complexes with cations, so they can also function as a chelator of metal ions and a buffer against alkali ions (Kornberg, 1995; Seufferheld et al., 2008; Rao et al., 2009). Finally, poly-P has been claimed to aid the channeling of DNA from the environment into the cell and appears to regulate the responses to stresses and adjustments for survival, especially in the stationary phase of culture growth and development (Kornberg, 1995; Rao and Kornberg, 1996; Ault-Riché et al., 1998; Rao et al., 1998). Recent research has demonstrated that poly-P chains can also function as a protein chaperone during stress conditions, where a poly-P chain counteracts irreversible protein aggregation by stabilizing proteins and maintaining them in a refolding-competent formation (Gray et al., 2014).

In cable bacteria, it was hypothesized that poly-P acts as a "survival energy package" for cells that glide into the oxic zone when performing "community service", thus functioning as a substitute for ATP or as a protection against oxidative stress (Kjeldsen et al., 2019; Geerlings et al., 2020). Indeed, differences in the relative phosphorus content (i.e., cellular P/C) between cells residing in the suboxic and oxic zone have been observed and attributed to a build-up of poly-P in the suboxic zone and a breakdown of poly-P in the oxic zone (Geerlings et al., 2020). However, this hypothesis needs further testing, as other roles for poly-P are possible. For example, it has been argued that poly-P can be involved in Ca^{2+}/H^{+} homeostasis to maintain optimum intracellular pH levels in the alkaline oxic zone (Geerlings et al., 2019), or act as an internal energy storage that drives the motility of cable bacteria (Bjerg et al., 2016). In this research we aim to assess the dynamics of poly-P in individual cells of cable bacteria and explore how this data can help us further elucidate the possible role(s) of poly-P in cable bacteria, both in the oxic and suboxic zone of the sediment.

Assessment of poly-P dynamics in cable bacteria is hampered by methodological challenges. Stable isotopes exist for elements such as carbon and nitrogen, which allows tracing of metabolic pathways involving these elements on a single-cell level using stable isotope probing (SIP) combined with nanoscale secondary ion mass spectrometry (nanoSIMS) (Musat et al., 2016). However, P can only be traced through radiolabelling that involves the addition of the short-lived ^{33}P isotope and a subsequent quantification of the enrichment in the daughter isotope ^{33}S (Schoffelen et al., 2018), since it only has one stable isotope.

Recently, an indirect method was applied to study poly-P metabolism in bacteria, which utilizes SIP with ^{18}O-labeled water ($H_2{}^{18}O$) in combination with nanoSIMS (Langer et al., 2018). This method exploits the relatively rapid exchange of O-atoms between phosphate and water molecules catalyzed by enzymes. Still, labeled O-atoms from water molecules can also be incorporated into proteins and other molecules. Thus, the ^{18}O-enrichment of biomass resulting from an incubation with $H_2{}^{18}O$ provides an indicator of a *general* metabolic activity of a cell (Ye et al., 2009) and cannot be assigned to a specific metabolic pathway such as poly-P synthesis. However, when SIP with $H_2{}^{18}O$ is combined with nanoSIMS, the general and poly-P-specific activity can be assessed separately through separate and spatially resolved measurement on poly-P granules and other cell material offered by nanoSIMS (Langer et al., 2018).

In this study, we combine dual-label SIP (^{13}C and ^{18}O) and nanoSIMS to investigate the poly-P metabolism in cable bacteria, including the spatial-temporal dynamics of poly-P synthesis and its connection to carbon metabolism. To this end, we amended sediment cores containing an active cable bacteria population with ^{18}O-labeled water (targeting both poly-P synthesis and general metabolism) and ^{13}C-labeled bicarbonate (targeting inorganic carbon assimilation and thus biomass growth). After 6 and 24 h of incubation, we retrieved individual cable bacterium filaments from three zones in the sediment (oxic, transition, and suboxic) and measured their ^{18}O and ^{13}C isotope labeling and relative phosphorus content with nanoSIMS.

MATERIALS AND METHODS

Cable Bacteria Culturing

Enrichment cultures with cable bacteria were prepared from natural sediment collected on 27-09-2019 within a creek bed from the Rattekaai Salt Marsh (Netherlands; 51.4391°N, 4.1697°E). At this site, earlier studies have documented the presence of cable bacteria *in situ* (Malkin et al., 2014). After collection in the field, the sediment was brought to the laboratory at Utrecht University, where it was sieved (500 μm mesh size) to remove fauna and large debris, homogenized, and subsequently re-packed into polycarbonate cores (height: 12 cm, inner diameter: 5.2 cm). The sediment cores were submerged in artificial seawater (ASW; salinity of 32, the *in situ* value) and incubated in the dark for several weeks until an active cable bacteria population developed. The overlying seawater was continuously bubbled with air to maintain 100% air saturation, and the temperature (20°C) and salinity were kept constant throughout the incubation. A total of 19 cores were incubated, all prepared from the same batch of sediment.

Microsensor Depth Profiling

Cable bacteria activity was monitored within the incubated cores using microsensor depth profiling (O_2, H_2S, and pH). This so-called geochemical fingerprint provides information about the developmental state and metabolic activity of the cable bacteria population (Nielsen et al., 2010; Risgaard-Petersen et al., 2012; Malkin et al., 2014). The microsensor depth profiles were also used to delineate the oxic, transition, and suboxic zones in the sediment at the time of core sectioning (see Section "Filament Retrieval from the Sediment").

Microsensors (tip diameters; O_2: 50 μm, H_2S: 100 μm, pH: 200 μm) were purchased from Unisense A/S (Denmark), connected to a four-channel Microsensor Multimeter (Unisense), and mounted in a two-dimensional micro-profiling system that enabled stepwise movement of sensors. The SensorTrace PRO software (Unisense) was used to control the vertical movement of the microsensors and record sensor signals. A general-purpose reference electrode (REF201 Red Rod electrode; Radiometer Analytical, Denmark) was used during pH measurements. Calibration of the microsensors was performed as previously described (Malkin et al., 2014).

Cable bacteria population developed in all but one of the incubated sediment cores. Five cores with the largest ΔpH were selected for the SIP experiment. The quantity ΔpH, defined as the difference between the maximum and minimum pH in the oxic and suboxic zone, respectively, provides a good proxy for comparing cable bacteria activity among different populations (Burdorf et al., 2018).

Stable Isotope Probing

For the SIP experiment, 10 mL of stock solution was prepared by mixing 2 mL of $H_2{}^{18}O$ (Sigma-Aldrich; ^{18}O atom fraction of 0.99) and 8 mL of artificial seawater (ASW) with a natural abundance of ^{18}O (^{18}O atom fraction of 0.002). Hence, the ^{18}O atom fraction of water in the stock solution was 0.2. The ASW contained no Mg^{2+} and Ca^{2+} ions (to avoid precipitation of $Mg^{13}CO_3$ and $Ca^{13}CO_3$) and no bicarbonate ions (to avoid ^{13}C label dilution). The stock solution was additionally labeled in ^{13}C by adding ^{13}C-bicarbonate ($NaH^{13}CO_3$, Sigma-Aldrich; ^{13}C atom fraction of 0.99) to a final concentration of 62 mM. This concentration and labeling were chosen because they were successfully applied in previous SIP experiments (Vasquez-Cardenas et al., 2015; Geerlings et al., 2020, 2021).

Dual labeling ($H_2{}^{18}O$ and $H^{13}CO_3{}^{-}$) of the sediment cores was done by first inserting a sub-core (inner diameter 1.2 cm, length 5 cm) into each culturing core without disturbing the sediment, and then injecting 500 μL of the labeled stock solution into the sub-core in ten separate and parallel 50 μL injections. To ensure homogeneous spread of the label throughout the sediment, the syringe needle was first inserted to a depth of 5 cm, and then the 50 μL dose of liquid was released while slowly retracting the needle upward. The use of the sub-core ensured that the label was spread within a well-constrained volume. Subsequently, the cores were incubated for 6 h (two replicate cores) and 24 h (two replicate cores), with one additional core chosen as an unlabeled control. Temperature was kept constant at 20°C during all incubations. At the end of the SIP incubation period, the sub-core was carefully pulled out of the sediment core and sectioned based on the redox zonation (see next section). Cable bacteria were retrieved from each sediment section and imaged by scanning electron microscopy (SEM) and NanoSIMS.

During the SIP incubation, each sub-core was overlain with a thin layer of water (~2 mm) with the same ^{18}O and ^{13}C labeling as the porewater. Additionally, the cores were placed in a sealed container filled with air and the bottom covered with a thin layer of ASW with the natural abundance of ^{18}O and a similar ^{13}C labeling as that of the porewater. This setup ensured similar ^{13}C labeling of the porewater and the CO_2 pool in the surrounding atmosphere inside the sealed contained and thus negligible ^{13}C label loss from the porewater due to air-water gas exchange. Because the system was stagnant, the loss of ^{18}O label from the porewater due exchange with the thin layer of ASW at the bottom of the sealed container was also negligible.

Based on the volume of the sub-core (5.65 mL) and the porosity of sediments from the Rattekaai salt marsh (0.75; L. Burdorf, 2017 thesis, p. 141), the porewater volume in the sub-core was estimated at 4.24 mL. Since 500 μL of the porewater was replaced by the stock solution, the estimated final ^{18}O atom fraction of the porewater was 0.025. This is about two-fold greater than the ^{18}O-labeling of water used in the SIP experiment by Langer et al. (2018) (S. Langer, personal communication). We assumed that all sub-cores in the replicate cores had the same ^{18}O-labeling, as the sub-core dimensions and the volume of the injected stock solution were identical.

Filament Retrieval From the Sediment

Cable bacterium filaments were retrieved from the sediment matrix under a stereo microscope using fine glass hooks custom-made from Pasteur pipettes. Filaments were retrieved separately from the oxic zone (0-2 mm depth), middle of the suboxic zone (5-10 mm depth), and the oxic-suboxic transition zone, the latter defined here as the zone up to 1 mm below the oxic zone (**Supplementary Figure 1**). The depth range of these zones were derived from microsensor measurements conducted just before core sectioning. Previous studies showed that in the transition zone, the density (Seitaj et al., 2015) and motility (Bjerg et al., 2016) of cable bacteria are highest. Retrieved filaments were washed several times (> 3) in Milli-Q water (Millipore, Netherlands) to eliminate precipitation of salts, transferred onto polycarbonate filters (pore size 0.2 μm; Isopore, Millipore, Netherlands) that were pre-coated with a 5-10 nm thin gold layer, and air-dried in a desiccator for about 24 h.

Scanning Electron Microscopy

Filaments on the polycarbonate filters were imaged with a scanning electron microscope (JEOL Neoscope II JCM-6000, Japan) to identify filament segments suitable for NanoSIMS analysis. Imaging was done under a 0.1-0.3 mbar vacuum and a high accelerating voltage (15 kV) using a backscatter electron detector.

NanoSIMS Analysis

NanoSIMS analysis was performed with the nanoSIMS 50L instrument (Cameca, France) operated at Utrecht University. Fields of view (FOV) selected through SEM imaging were pre-sputtered with Cs^{+} ions until secondary ion yields stabilized. Subsequently, the primary Cs^{+} ion beam (current: 0.5-10 pA, energy: 16 keV, beam size: 130 nm, dwell time: 1-2 ms per pixel) was scanned over the FOV (areas between 10 × 10 μm and 20 × 20 μm in size) while detecting secondary ions $^{12}C^{14}N^{-}$, $^{13}C^{14}N^{-}$, $^{31}P^{-}$, $^{16}O^{-}$, $^{18}O^{-}$, and $^{32}S^{-}$.

Initial measurements employed a relatively short pre-sputtering interval (10 min) and a low primary ion current (0.5-2 pA), which resulted in relatively low $^{18}O^{-}$ and $^{31}P^{-}$ ion yields during the subsequent analysis conducted with the same current. Thus, during the analysis, the primary ion current was increased to 10 pA to enable quantification of ^{18}O labeling in poly-P granules with a desirable precision and within a reasonable time interval (few hours). This increase in the primary ion current resulted, however, in excessive count rates on the electron multiplier used for the detection of $^{12}C^{14}N^{-}$ (> 10^5 cps). To prevent detector aging due to such high count rates, $^{12}C^{14}N^{-}$ ions were therefore not detected during these measurements. As a downside, ^{13}C labeling could not be determined for these initial measurements.

Later in the analysis, we noted that the $^{18}O^{-}$ and $^{31}P^{-}$ secondary ion yields were low during the initial measurements because the probed volume was too close to the cell surface, whereas the poly-P granules were present deeper within the cell biovolume. Therefore, we changed the measurement protocol by including much longer pre-sputtering intervals (20-30 min), which allowed us to probe the more inner parts of the cells during the subsequent analysis using low primary ion currents (0.5-2 pA). Specifically, it allowed us to detect all target secondary ions and thus simultaneously determine both ^{13}C and ^{18}O labeling of the biomass of cable bacteria, including poly-P granules.

NanoSIMS analysis of most samples focused on the variation of the mean isotopic and elemental composition among cells within filaments. In these analyses, the same FOV was imaged multiple times (100-300 frames) and the resulting ion count images were aligned and accumulated. For selected samples, we aimed to obtain additional insight into the 3D distribution of the isotopic and elemental composition within cells. These measurements were therefore conducted with a substantially larger number of frames (up to 7,000) until the sample material was completely sputtered by the primary ion beam.

NanoSIMS data were processed using the Matlab-based software Look@NanoSIMS (Polerecky et al., 2012). After alignment and accumulation of the measured planes, regions of interest (ROIs) corresponding to the poly-P granules were drawn manually using the combined $^{12}C^{14}N^{-}$ (or $^{13}C^{14}N^{-}$), $^{18}O^{-}$ and $^{31}P^{-}$ ion count images. ROIs were not drawn for cells that appeared damaged. For each ROI, the ROI-specific ^{18}O atom fraction was calculated as $x(^{18}O) = {}^{18}O^{-}/({}^{16}O^{-} + {}^{18}O^{-})$ using the total counts of $^{18}O^{-}$ and $^{16}O^{-}$ accumulated over the ROI pixels. Similarly, the ROI-specific ^{13}C atom fraction was calculated as $x(^{13}C) = {}^{13}C^{14}N^{-}/({}^{12}C^{14}N^{-} + {}^{13}C^{14}N^{-})$ from the total counts of $^{12}C^{14}N^{-}$ and $^{13}C^{14}N^{-}$ (only if the $^{12}C^{14}N^{-}$ ions were detected). Note that when detecting secondary ions from a given poly-P granule, the probed volume partly also included the cytoplasm of a cell in which the poly-P granule was embedded (e.g., "above" or "below" the granule; see Results, **Figure 1**). Thus, the ^{13}C atom fraction determined in the ROI drawn around a poly-P granule represents the ^{13}C atom fraction in the surrounding cytoplasm.

To quantify ^{13}C and ^{18}O labeling, we used excess atom fractions calculated according to $x^E(^{13}C) = x(^{13}C) - x_i(^{13}C)$ and $x^E(^{18}O) = x(^{18}O) - x_i(^{18}O)$, respectively, where $x_i(^{13}C)$ and $x_i(^{18}O)$ correspond to the atom fractions determined for control cells. Based on these quantities, we classified filaments as 'inactive' when $x^E(^{13}C) < 0.0006$ and $x^E(^{18}O) < 0.00025$ (the threshold levels correspond to 3 standard deviations of the respective excess

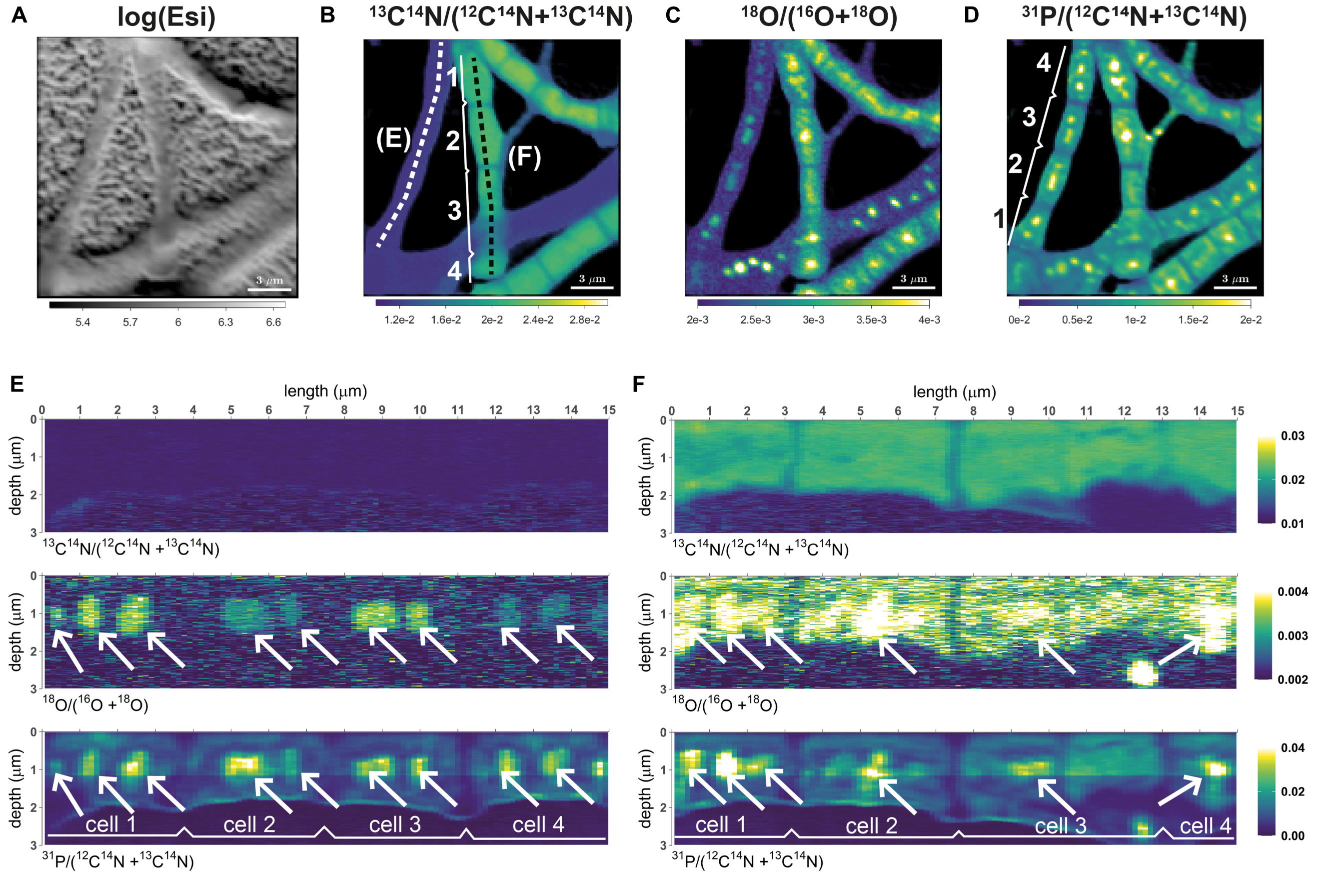

FIGURE 1 | Distributions of ^{13}C and ^{18}O labeling in cable bacteria. Shown are representative data for filament segments retrieved from the suboxic zone after 6 h of incubation. **(A)** Intensity of secondary electrons (log-transformed). **(B)** ^{13}C atom fraction, calculated as $^{13}C^{14}N/(^{12}C^{14}N + ^{13}C^{14}N)$. **(C)** ^{18}O atom fraction, calculated as $^{18}O/(^{16}O + ^{18}O)$. **(D)** Relative phosphorus content, approximated as $^{31}P/(^{12}C^{14}N + ^{13}C^{14}N)$. **(E,F)** Depth profiles of the ^{13}C atom fraction, ^{18}O atom fraction, and the relative phosphorus content along profiles spanning across four cells from two filaments. Profiles correspond to filaments that showed no (panel **E**) and some of the highest (panel **F**) carbon assimilation during the incubation. The corresponding profile locations are shown by the white and black dotted lines in panel **(B)**. White arrows point toward selected polyphosphate granules present in the cells. Color scales for panels **(E,F)** are the same. Scale bar is 3 μm.

atom fractions determined for control filaments), 'minimally active' when $x^E(^{13}C) \leq 0.001$ (reflecting the lowest 25% of measured filament fragments and 2% of the maximum measured excess ^{13}C atom fraction) and $x^E(^{18}O) \leq 0.0004$ (which reflects the lowest 10% of measured filament fragments), and 'active' when $x^E(^{13}C) > 0.001$ or $x^E(^{18}O) > 0.0004$.

To gain insight into the 3D distribution of the isotopic and elemental composition and the position of the poly-P granules within cells, Look@NanoSIMS was additionally used to visualize the depth variation in the nanoSIMS data along a lateral or transversal profile. This analysis was done as previously described (Geerlings et al., 2021).

Statistical Analysis

Overall, data was obtained for 1887 poly-P granules in 884 cells from 203 filament segments (**Table 1**). Out of these, 126 poly-P granules in 29 cells from 7 filament segments belong to the control samples. Both the ^{18}O and ^{13}C atom fractions are available for 704 cells (from 164 filament segments), while data available for the remaining 151 cells (from 32 filament segments) only includes the ^{18}O fraction.

Statistical analysis of this dataset focused on the following aspects: (i) the effect of the redox environment and labeling period on the ^{13}C labeling of the cytoplasm and the ^{18}O labeling of the poly-P granules, (ii) variation in the ^{18}O labeling of the poly-P granules within a cell, within a filament, and among filaments, and (iii) the relationship between the average ^{18}O labeling of the poly-P granules and the corresponding ^{13}C labeling of the surrounding cytoplasm within each filament fragment.

The first two aspects were assessed by fitting the data with a linear mixed model (separately for the ^{13}C and ^{18}O data), which was done in R using the package *nlme* (Pinheiro et al., 2021). The analysis considered the hierarchical structure of the data (i.e., nesting of cells within filaments for the ^{13}C data, and nesting of poly-P granules within cells, which are further nested within filaments, for the ^{18}O data) and the unbalanced experimental design (**Table 2**). The 'redox zone' (oxic, transition,

TABLE 1 | Number of poly-P granules, cells and filament fragments measured in this study.

		6h incubation						24h incubation							
		core 1			core 2			core 3			core 4				
	redox zone	oxic	transit	subox	oxic	transit	subox	oxic	transit	subox	oxic	transit	subox	control	total
^{18}O atom fraction	# poly-P	147	432	164	121	333	42	64	66	260	101	15	16	126	1887
	# cells	51	166	45	82	243	24	30	33	110	50	10	11	29	884
	# filaments	8	35	8	22	64	6	8	5	25	9	3	3	7	203
^{13}C atom fraction	# cells	32	117	45	82	243	24	-	-	101	50	10	-	-	704
	# filaments	4	25	8	22	64	6	-	-	23	9	3	-	-	164
Porewater ^{18}O atom fraction		0.0234			0.0164			0.0151			0.0160			0.002	

Numbers are shown separately for the two replicate cores, three redox zones, two incubation periods, and two isotope labels used. Note that the ^{13}C labeling data is available for a subset of filament fragments for which the ^{18}O labeling data is available.

suboxic) and the 'labeling period' (6 h, 24 h) were defined as fixed effects, whereas 'filament' (when testing the excess ^{13}C labeling of cells) and 'cell' and 'filament' (when testing the ^{18}O labeling of poly-P granules) were chosen as random effects in the model. For model selection, a step-up approach was used, which starts with a reference model that contains all fixed components and their interactions. This so-called "beyond optimal model" was then used to find the best variance structure and random structure (Zuur et al., 2009). Using the output of the linear mixed model for the poly-P-specific ^{18}O data, we calculated the percentage of variance in the data explained by differences among filaments, among cells within the same filament, and differences within the same cell. Similarly, we calculated the percentage of variance explained by differences among filaments and among cells within the same filament for the cell-specific ^{13}C data. The third aspect was assessed by calculating the Kendall rank correlation coefficient (τ), which is a robust parameter used for testing correlations in non-normally distributed data (Dalgaard, 2013). Details of the statistical analysis are provided in the **Supplementary Methods**.

RESULTS

Patterns in ^{13}C and ^{18}O Labeling of Cable Bacterium Filaments

Patterns shown by the ^{13}C data in the present study are similar to those observed previously (Geerlings et al., 2020, 2021). ^{13}C labeling was mainly restricted to filaments from the transition and suboxic zone, whereas filaments from the oxic zone displayed no, or only very low, ^{13}C labeling (SI Appendix, **Supplementary Figure 2**). Furthermore, the ^{13}C labeling was highly variable among filaments from the transition and suboxic zone, but highly similar when compared among cells within the same filament (**Figure 1** and **Supplementary Figure 2**).

In contrast to the low intra-filament variability in ^{13}C labeling, there was a clear variation in the ^{18}O labeling of poly-P granules among cells from the same filament (**Figure 1**). However, adjacent cells displayed a similar pattern when compared with respect to the size, position, and number of granules per cell, which is congruent with earlier observations on poly-P granules in cable bacteria (Geerlings et al., 2019).

Depending on the diameter of the filament and the intracellular spatial organization of the poly-P granules, two different morphotypes of cable bacteria were distinguished: (i) "thin" filaments (diameter ∼0.5-1 μm), which mostly contained two similarly-sized (diameter ∼100-300 nm) poly-P granules per cell, one at each cell pole (**Figure 2A**), and (ii) "thicker" filaments (diameter above 1 μm), which contained variable spatial organizations of the poly-P granules within cells. Some cells in the thicker filaments contained many small poly-P granules, while others contained only a few larger ones (**Figure 2B**). It is unknown whether the different morphotypes represent different species of cable bacteria or they are different manifestations of the same species in a different stage of the life cycle.

TABLE 2 | Description of the different variables used in the linear mixed models.

Name	Description	Type of variable	Levels in model 1	Levels in model 2
frac_18O	^{18}O atom fraction in the ROI defined as a poly-P granule	continuous response	1761	-
frac_13C	^{13}C atom fraction of the cell cytoplasm	continuous response	-	704
Cell	unique label for each cell	categorical random explanatory	855	
Filament	unique label for each individual filament fragment	categorical random explanatory	196	164
Core	the core from which the measurement was extracted	categorical random explanatory	4	4
Zone	redox zonation	categorical fixed explanatory	3	3
labeling period	labeling period of the polyphosphate granule	categorical fixed explanatory	2	2

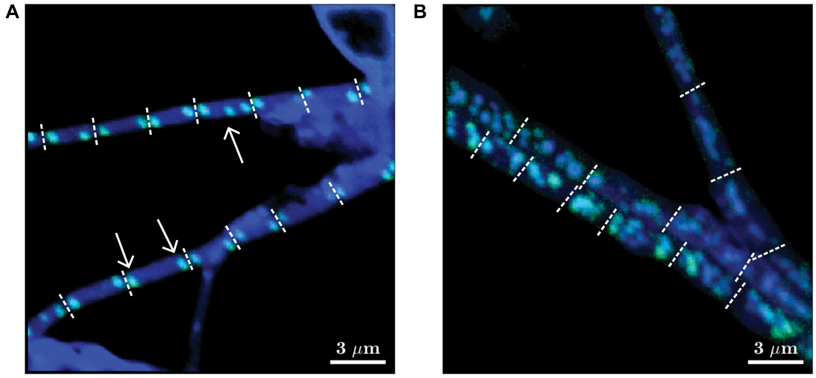

FIGURE 2 | Representative images of two morphotypes of cable bacteria observed in this study. Images are shown as overlays of the ^{18}O atom fraction (in green) and ^{31}P ion counts (in blue). **(A) "**Thin" filaments (diameter 0.5-1 μm) mostly contained two poly-P granules at the poles of each cell, but cells containing three poly-P granules were occasionally also observed (see white arrows). **(B)** "Thicker" filaments (diameter $>$ 1 μm) contained multiple poly-P granules per cell. Filaments shown in panels **(A,B)** were retrieved from the transition zone after 24 h of labeling and from the suboxic zone after 6 h of labeling, respectively. Dotted white lines depict cell junctions. Scaling for the green and blue colors was optimized independently for each image to enhance the visibility of the poly-P granules. Scale bar is 3 μm. The original images of the ^{18}O atom fraction and ^{31}P ion counts are shown in **Supplementary Figure 3**.

Both the ^{13}C labeling of the cytoplasm and the ^{18}O labeling of the poly-P granules were highly variable when compared among different filaments (**Figures 1**, **3**, **4**, **Table 3** and **Supplementary Figure 2**). Based on the combined ^{13}C and ^{18}O data, we divided the filaments into four classes (see Methods for details). Class 1 includes filaments considered as metabolically inactive or minimally active during the labeling period. This class contained 4.3% (7/164) of filaments (1 inactive and 6 minimally active), all originating from sediment cores incubated for 6 h. Note that this number does not include filaments without detectable poly-P granules at the end of the nanoSIMS analysis. Class 2 includes filaments that showed ^{13}C labeling of the cytoplasm but no, or only minimal, ^{18}O labeling of the poly-P granules. This pattern was observed in 3.7% (6/164) of filament fragments, all from the 6 h incubation. Class 3 includes filaments that showed no, or only minimal, ^{13}C labeling but contained poly-P granules with a significant ^{18}O labeling (**Figure 1E**). This pattern, observed in 23% (38/164) of filament fragments, indicates that the filaments did not grow during the SIP incubation but were still active with respect to poly-P metabolism (see Discussion). The highest proportion of filaments (113/164, i.e., 69%) was assigned to class 4, which includes filaments with high labeling in both ^{13}C and ^{18}O. For these filaments, ^{18}O labeling of the poly-P granules was significantly greater than that of the cytoplasm (**Figure 1F**). This labeling pattern indicates that these filaments were simultaneously active with respect to growth and poly-P metabolism. Overall, around 78% of filaments from the transition and suboxic zone were actively growing during the 6 h or 24 h incubation period, and around 92% of all measured filaments (from all redox zones) displayed poly-P activity (**Table 3**).

Effect of Redox Zonation and Labeling Period

^{18}O labeling of poly-P granules was observed in filaments from all redox zones and varied greatly among filaments (**Figures 3– 5**). Despite this high variability, statistical analysis revealed that the labeling values in filaments from the oxic zone were, on average, significantly lower than those from the transition and suboxic zones. In contrast, the transition and suboxic zones showed no significant differences (**Figures 4D,E** and **Supplementary Table 2**). This pattern was detected for both labeling periods (6 h and 24 h), although it was more pronounced for the longer period. Furthermore, a comparison made separately for each redox zone revealed a significantly higher ^{18}O labeling of poly-P granules in filaments incubated for 24 h compared to 6 h (**Figures 4D,E** and **Supplementary Table 1**).

Variation Within Cells, Within Filaments, and Among Filaments

Statistical analysis further revealed that most of the variability in the ^{18}O labeling of poly-P granules (about 52-88%) was explained by differences among filaments, with the percentage being highest in the oxic zone (consistent for each labeling period) and higher for the shorter labeling period compared to the longer one (consistent for each redox zone) (**Table 4**). The percentage of variance explained by differences among cells within filaments was relatively minor (about 5-8%) and similar for both labeling periods and all redox zones. Finally, a sizeable fraction of the variance (about 4-44%) was unexplained, i.e., was due to unknown differences within cells, with the percentage being lowest in the oxic zone (consistently for each labeling period) and higher for the longer labeling period compared to the shorter one (consistently for each redox zone) (**Table 4**). For the ^{13}C labeling of cell cytoplasm, most of the variability among cells (86-99%) was explained by differences among filaments and only minor differences (1-14%) were observed among cells within the same filament (**Supplementary Table 3**). Thus, similar to previously observed patterns (Geerlings et al., 2020, 2021), there was only a minimal variability in ^{13}C labeling among cells within a given filament from a given redox zone. Additionally, variability

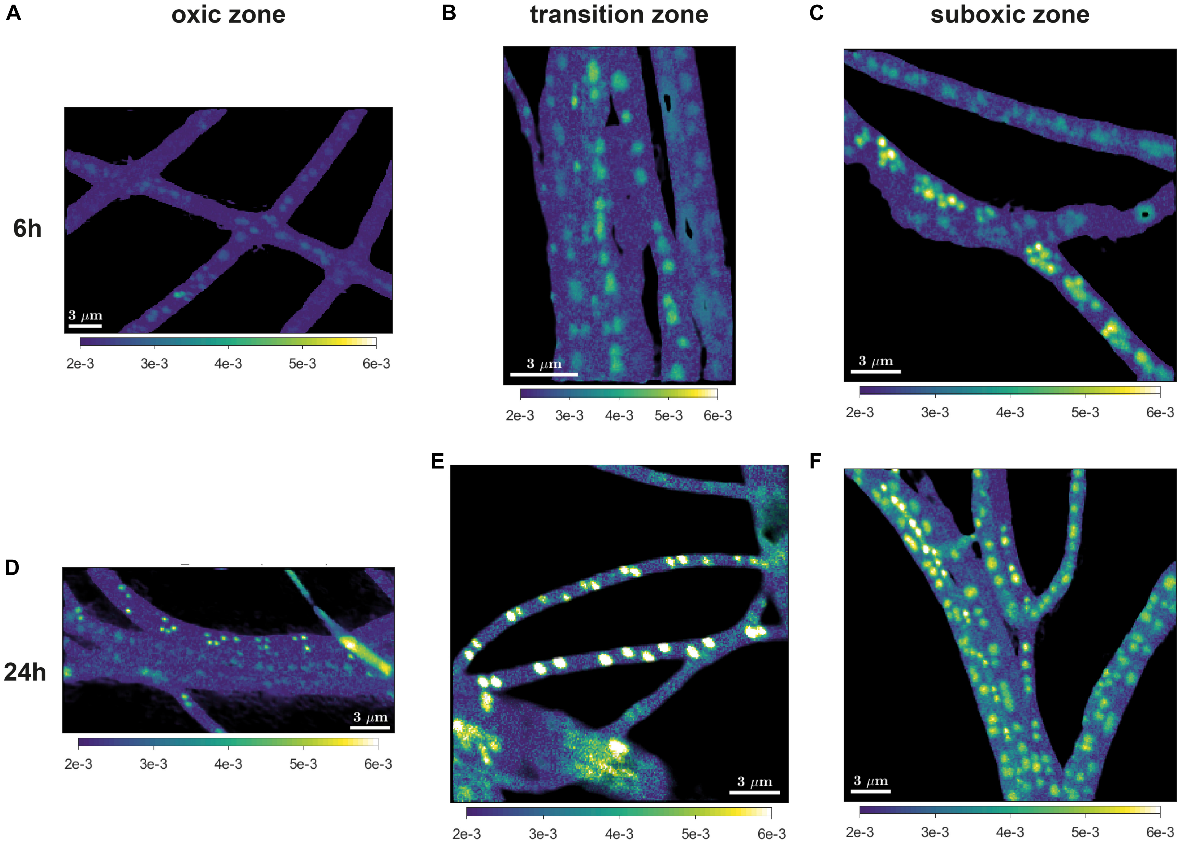

FIGURE 3 | Representative images of the ^{18}O atom fraction in cable bacteria. Filaments were retrieved after 6 h **(A–C)** and 24 h **(D–F)** of incubation and retrieved from the oxic **(A,D)**, transition **(B,E)**, and suboxic **(C,F)** zone. All scale bars are 3 μm. Color scale in all images is the same (0.002-0.006).

among cells within filaments was lower for the ^{13}C labeling of the cell cytoplasm compared to the ^{18}O labeling of poly-P granules.

Correlation Between ^{18}O and ^{13}C Labeling of Cable Bacterium Filament Fragments

The filament-averaged ^{18}O atom fractions of poly-P granules and the corresponding averaged ^{13}C atom fractions of the cytoplasm were determined for the same filament fragment for each of the labeling periods. Correlation analysis showed that these quantities were significantly correlated for each of the labeling periods ($p = 0.0005$, **Figure 5**). However, this correlation was largely a collinearity effect caused by the dependence of both variables on the redox environment. In all cases, however, the predictive power of the correlation was poor, as indicated by the low value of the Kendall rank correlation coefficient ($\tau = 0.208$ and 0.405 for the 6 h and 24 h labeling period, respectively).

DISCUSSION

Overall, detailed nanoSIMS imaging revealed that poly-P granules are a prominent feature of cable bacteria that takes up a large fraction of the cell biovolume (**Figure 1**). Poly-P granules were detected in nearly all cable bacteria filaments (**Supplementary Figure 2**), and nearly all detected poly-P granules were labeled by ^{18}O (**Figure 4** and **Table 3**). Significant label incorporation was observed after a time interval (6 h and 24 h) that is shorter or comparable to the doubling time of cable bacteria cells in laboratory conditions (~20 h; Schauer et al., 2014). Additionally, the ^{18}O labeling of poly-P granules was highly variable and significantly influenced by the duration of the labeling interval and redox environment. Based on these patterns, we discuss possible factors that control the poly-P metabolism in cable bacteria and suggest a possible role played by poly-P in their life cycle.

Investigating Polyphosphate Metabolism Using ^{18}O-Labeled Water

Before we interpret our data, we briefly review possible pathways through which ^{18}O derived from $H_2{}^{18}O$ can enter poly-P granules.

The first step involves ^{18}O exchange between water and the inorganic (ortho)phosphate (P_i) pool, which occurs when inorganic pyrophosphate (PP_i) is hydrolyzed. This process can occur both inside and outside of a cell (**Figure 6**, reactions 1 and

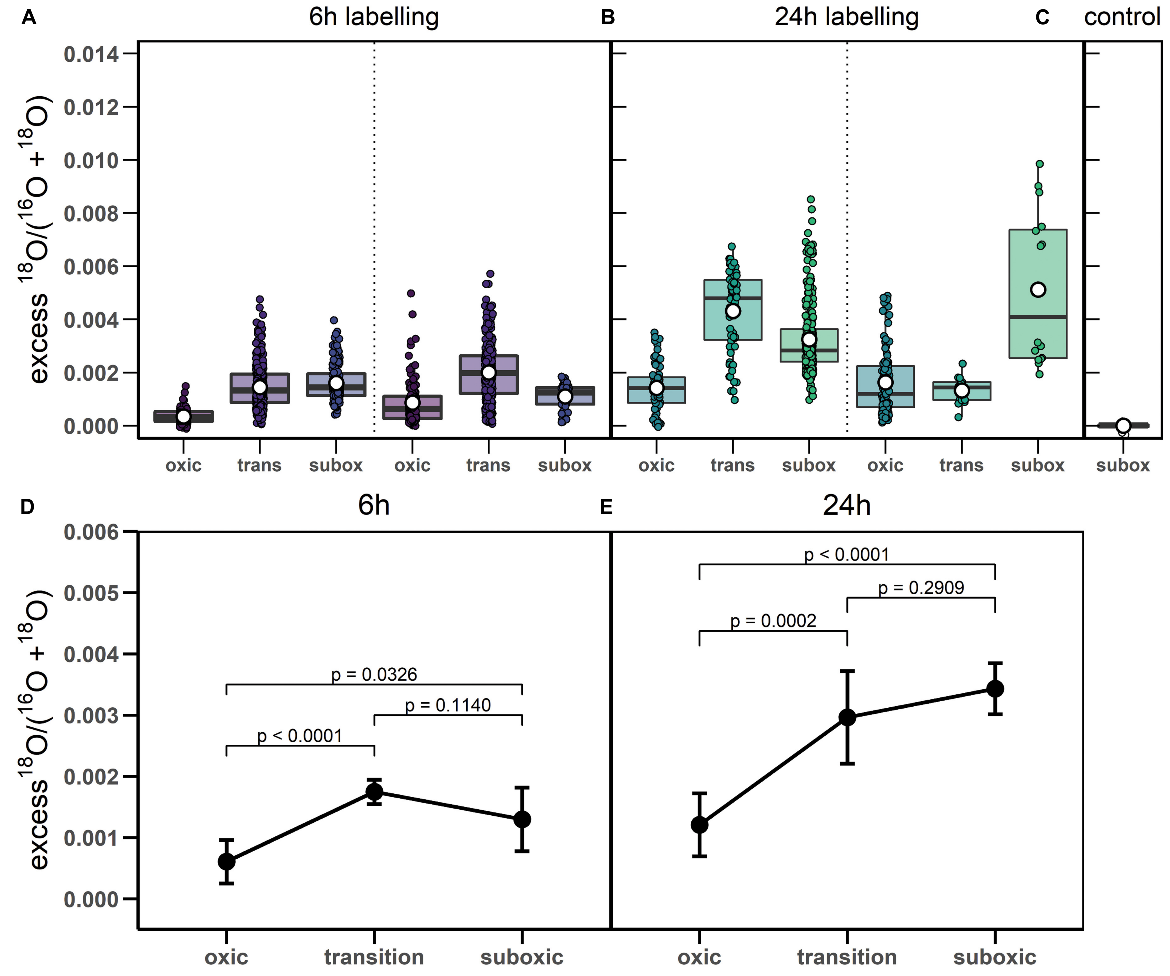

FIGURE 4 | ^{18}O labeling of polyphosphate granules in cable bacteria. **(A-C)** Boxplots show excess ^{18}O atom fractions in individual poly-P granules, separately for the 6 h and 24 h labeling periods and for the control cells. Dotted lines separate data obtained from replicate sediment cores. Shown are the corresponding mean (white open dot), median (black line) and upper and lower quantiles of the excess ^{18}O atom fraction. Note that grouping of poly-P granules within cells and within filaments is not indicated in the graphs. **(D,E)** Results of the linear mixed model used for fitting the variance in the excess ^{18}O atom fractions in poly-P granules. Results are shown separately for the 6 h and 24 h labeling period. Black circles and error-bars depict the best estimates and the lower and upper confidence limits (95%) of the mean value for each zone and labeling period (exact values provided in **Supplementary Table 1**). The p-values indicate the significance of differences between zones (summarized in **Supplementary Table 2**). Raw data is provided as **Supplementary Dataset 1**, the step-by-step build-up and outcomes of the linear mixed model are available in **Supplementary Methods**.

2). The PP_i required in this step is produced in a metabolically active cell by many different processes, such as hydrolysis of ATP into AMP or breakdown of large biomolecules. At temperatures below 80°C, abiotic phosphoryl-transfer reactions such as PP_i hydrolysis are very slow but are significantly accelerated by enzymes (Lassila et al., 2011). Therefore, in natural systems, the ^{18}O signature of the P_i pool ($\delta^{18}O_p$) is dominated by enzyme-mediated ^{18}O exchange with water (Blake et al., 2001, 2005). When this process occurs intracellularly, $H_2{}^{18}O$ first enters the cell via diffusion and the ^{18}O exchange is then catalyzed by the enzyme pyrophosphatase (PPase). In contrast, the ^{18}O exchange outside of a cell occurs, e.g., due to the activity of microorganisms that use extracellular phosphatases (e.g., phosphomonoesterases) as a strategy to acquire P_i from organic compounds (Liang and Blake, 2006; Von Sperber et al., 2014), and the ^{18}O-labeled P_i then enters the cell via diffusion. We assume that in both cases the intracellular ^{18}O isotope equilibrium between H_2O and P_i is established within a few hours (Blake et al., 2005; Chang and Blake, 2015).

Once the intracellular P_i pool is labeled with ^{18}O, the label can enter the poly-P granule via poly-P synthesis. This process is catalyzed by two families of poly-P kinases, PPK1 and PPK2 (Rao et al., 2009), and involves incorporation of P_i into a nucleoside triphosphate (NTP, such as ATP or GTP) followed by a transfer of P_i from NTP to a poly-P chain (**Figure 6**, reactions 3 and 4). As these reactions consume NTP, poly-P synthesis hence requires the investment of metabolic energy. Cable bacteria carry the

TABLE 3 | Number of cable bacterium filament fragments with a specific ^{13}C labeling of their cytoplasm and ^{18}O labeling of their poly-P granules.

	6h			24h		
	Oxic	transition	suboxic	oxic	transition	suboxic
Minimally active	5	2	0	0	0	0
Only ^{13}C labeled	4	1	1	0	0	0
Only ^{18}O labeled	8	20	6	3	0	1
Both ^{13}C & ^{18}O labeled	9	66	7	6	3	22
Total	26	89	14	9	3	23
	129			35		

Numbers are shown separately for each incubation period and redox zone. Details of the classification are explained in Methods. Images of filaments from each class are shown in ***Supplementary Figure 2****.*

genes necessary to produce enzymes from both of these families (Kjeldsen et al., 2019).

Poly-P breakdown was suggested as another mechanism how ^{18}O could enter the poly-P granule (Langer et al., 2018). Poly-P breakdown can proceed via hydrolysis, which is catalyzed by an exopolyphosphatase (PPX) and leads to the cleavage of the terminal P_i from the poly-P chain (Kornberg et al., 1999). However, evidence suggests that this pathway proceeds via a concerted mechanism with a single transition state where the nucleophilic water attacks the P-atom at the end of the poly-P chain. As a result, the O-atom from the water molecule eventually ends up in the P_i residue *leaving* the chain, and so there is no labeling of the poly-P (Lassila et al., 2011). Another possible pathway of poly-P breakdown involves phosphorylation of nucleoside monophosphates (AMP or GMP) or diphosphates (ADP and GDP) (Ishige et al., 2002; Nocek et al., 2008, 2018). This process is aided by PPK2-type enzymes, and most likely also proceeds via a concerted mechanisms with a single “loose” transition state (Nocek et al., 2018) where the O-atom from the water molecule ends up in the NDP or NTP molecule rather than in the terminal P_i group on the remaining poly-P chain. Thus, poly-P breakdown in the presence of $H_2{}^{18}O$ is unlikely to increase significantly the ^{18}O atom fraction of an unlabeled poly-P granule (a minor effect, expected to occur due to kinetic isotope fractionation, is neglected in this study).

Poly-P breakdown could, however, decrease the ^{18}O atom fraction of a previously ^{18}O-labeled poly-P granule, if the ^{18}O-labeled P_i groups added to the granule during poly-P synthesis were removed preferentially during the subsequent phase of poly-P breakdown. This could occur, for instance, if the newly synthesized poly-P was incorporated into a specific location within a granule, such as the outer surface, and the breakdown involved poly-P from the same location. Our detailed 3D nanoSIMS analysis revealed, however, that there is no significant variability in ^{18}O labeling within a poly-P granule (**Figure 1**), indicating that, on the scale of hours, the poly-P pool within a granule becomes well mixed. This mixing is likely the result of structural organization of a granule where the negatively charged poly-P chains are connected to one another via ion bridges involving divalent cations which causes the tertiary structure to be rearranged and the ^{18}O label to become well-mixed. This hypothesis is supported by the recently documented association between Ca^{2+} and Mg^{2+} ions and poly-P granules in cable bacteria (Geerlings et al., 2019) and a modeling study on the conformation and organization of poly-P molecules and Ca^{2+} ions (Müller et al., 2019). Thus, due to the well-mixed nature of the poly-P granule, poly-P breakdown has no significant effect on the ^{18}O atom fraction of an ^{18}O-labeled poly-P granule.

Based on these arguments, we conclude that in the presence of $H_2{}^{18}O$ and an ^{18}O-labeled P_i pool, the ^{18}O atom fraction of a poly-P granule can only increase (during poly-P synthesis) or stay constant (during poly-P breakdown). Thus, a significant enrichment of poly-P granules in ^{18}O indicates that poly-P synthesis occurred *at some point* during the SIP incubation with $H_2{}^{18}O$, but it may be insufficient to provide insights into the actual rate of poly-P synthesis or the cycling between poly-P synthesis and breakdown.

Polyphosphate Turnover in Cable Bacteria

Our poly-P-specific ^{18}O data indicate that on the time scale of 24 h, cable bacteria cells turn over a significant amount of poly-P. This conclusion derives from the comparison of ^{18}O data between the 6 h and 24 h labeling intervals. Specifically, if poly-P synthesis and incorporation into existing poly-P granules at a constant rate were the only processes during the incubation, the expected excess ^{18}O atom fraction of poly-P granules after 24 h of incubation would be, on average, around 5 to 7-fold greater than after 6 h of incubation (**Supplementary Model**). This estimate considers that, for the incubation temperature of 22°C, it takes about 27 h for the ^{18}O exchange between the P_i pool and $H_2{}^{18}O$ to reach an equilibrium (Blake et al., 2005). However, the excess ^{18}O atom fractions of poly-P granules only increased, on average, by a factor of 1.8-2.7 between the 6 h and 24 h incubation periods (**Figure 4** and **Supplementary Table 1**). When combined with the ^{18}O labeling asymmetry between poly-P synthesis and breakdown proposed above, this discrepancy suggests that poly-P breakdown occurred during a significant fraction of the 24 h labeling interval. Present data is, however, insufficient to constrain the rates of poly-P synthesis and breakdown or the number of turnover cycles. Research on shorter time scales (∼1 h) is required to gain more insight into the dynamics of poly-P turnover in cable bacteria. Since SIP using ^{18}O-labeled water requires an exchange between the P_i pool and $H_2{}^{18}O$ to produce ^{18}O-labeled P_i, research on shorter time scales may be hampered and it is therefore advised to directly add labeled ^{18}O-labeled phosphate. This can be prepared either using a minimal abiotic system with commercially available PPase (Blake et al., 2005) or by the hydrolysis of PCl_5 using $H_2{}^{18}O$ (Versaw and Metzenberg, 1996).

Polyphosphate Metabolism Is Governed by Redox Zonation

Poly-P metabolism in cable bacteria is governed by the redox environment, with higher levels of synthesis in the suboxic (and transition) zone and lower levels of synthesis, or higher levels of

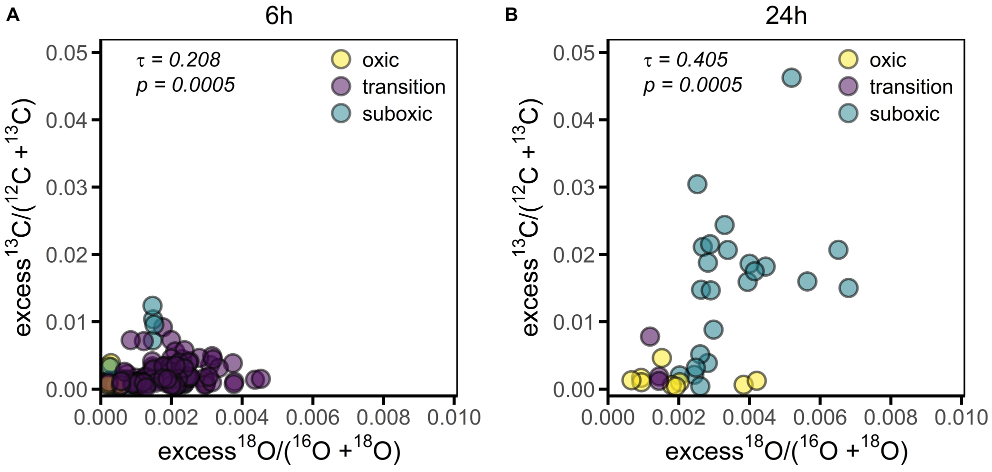

FIGURE 5 | ^{13}C labeling of the cell cytoplasm versus ^{18}O labeling of the poly-P granules in cable bacteria. Each data point represents a mean value for an individual filament segment. **(A)** Values obtained for filaments incubated for 6 h (n = 129). **(B)** Values obtained for filaments incubated for 24 h (n = 35). Colors differentiate among redox zones. Kendall's correlation coefficient (τ) and the corresponding p-value are also shown.

TABLE 4 | Structure of the variance in the ^{18}O labeling of poly-P granules and ^{13}C labeling of the cytoplasm in the measured cable bacteria.

		Excess $^{18}O/O$			**% of variance explained by differences**			**Excess $^{13}C/C$**		**% of variance explained by differences**	
Labeling period	**Redox zone**	**σ^2**	**ICC_{cell}**	**$ICC_{filament}$**	**among filaments**	**among cells within filaments**	**within cells**	**σ^2**	**$ICC_{filament}$**	**among filaments**	**among cells within filaments**
6h	oxic	0.00021	0.96	0.8836	88.4%	7.6%	4.0%	0.00018	0.992	99.2%	0.8%
	transition	0.00049	0.8133	0.7485	74.9%	6.5%	18.7%	0.00057	0.956	95.6%	4.4%
	suboxic	0.00043	0.8477	0.7802	78.0%	6.8%	15.2%	0.00065	0.965	96.5%	3.5%
24h	oxic	0.00047	0.8274	0.7615	76.2%	6.6%	17.3%	0.00039	0.96	96.0%	4.0%
	transition	0.00062	0.7248	0.6671	66.7%	5.8%	27.5%	0.00060	0.929	92.9%	7.1%
	suboxic	0.00090	0.5592	0.5146	51.5%	4.5%	44.1%	0.00069	0.864	86.4%	13.6%

The values of σ^2 and the intraclass correlation coefficient (ICC) were determined by fitting the data with linear mixed models (see ***Supplementary Methods*** *for details). The ICC values indicate that the largest portions of the variance can be explained by differences among filaments (52-88% for ^{18}O labeling and 86-99% for ^{13}C labeling) and there is little variation among cells within a filament (5-8% for ^{18}O labeling and 1-14% for ^{13}C labeling). Since for most cells the ^{18}O labeling was determined in more than one poly-P granule, there is also a variation within a cell, i.e., an unexplained variance (4-44%).*

breakdown, in the oxic zone. This conclusion is supported by the statistical analysis of the poly-P-specific ^{18}O labeling, which revealed, consistently for both labeling intervals (6 h and 24 h), a significantly lower mean value in the oxic zone compared to the transition and suboxic zones and no significant differences between the transition and suboxic zones (**Figures 4C-D** and **Supplementary Table 2**).

The dependence of poly-P metabolism on the redox environment, as observed in the present study for cable bacteria, seems to follow an opposite pattern to that observed for other poly-P accumulating microorganisms. For most of these organisms, phosphate is stored as poly-P under aerobic conditions, whereas poly-P is broken down under anaerobic conditions (He and Mcmahon, 2011; Saia et al., 2021). This pattern was observed, e.g., for the giant sulfur-oxidizing bacteria *Thiomargarita namibiensis* (Schulz and Schulz, 2005), for the large filamentous sulfide oxidizing bacteria *Beggiatoa spp*. (Brock and Schulz-Vogt, 2011), or when investigating the phosphorus cycling in wetland sediments from South Gippsland (Southern Australia) (Khoshmanesh et al., 1999, 2002).

This apparent inconsistency between cable bacteria and other poly-P accumulating organisms can be explained by considering the peculiar energy metabolism of cable bacteria facilitated by long-distance electron transport along the filament. Although poly-P appears to be synthesized predominantly by cells residing in the anoxic sediment, these cells can only gain energy if part of the filament is connected to oxygen (Geerlings et al., 2020). Thus, the energy metabolism of the poly-P synthesizing cable bacteria cells is *de facto* aerobic.

Another theoretical possibility could be anoxic poly-P synthesis. Based on genomic data, cable bacteria have a metabolic potential for sulfur disproportionation (Kjeldsen et al., 2019), which could be a mechanism for gaining energy required for poly-P synthesis when a filament is disconnected from oxygen. However, the function of cells in their native habitat often cannot

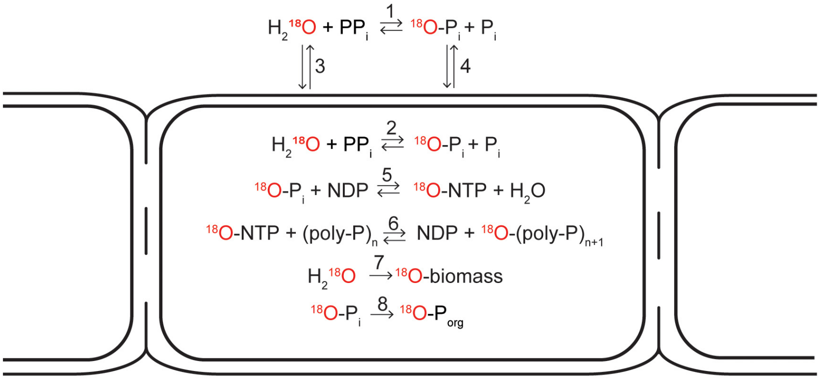

FIGURE 6 | Schematic diagram depicting possible pathways how the ^{18}O atom from an ^{18}O-labeled water molecule can end up in the cellular inorganic polyphosphate pool, cell biomass, and the organic phosphate pool. ^{18}O exchange between ^{18}O-labeled water and (ortho)phosphate (P_i) occurs when inorganic pyrophosphate (PP_i) is hydrolyzed. This process is catalyzed by enzymes and can occur both outside (1) and inside the cell (2). When occuring inside the cell, ^{18}O-labeled water is first transported into the cell via diffusion (3). When occuring outside the cell, the ^{18}O-labeled phosphate is transported inside the cell either actively (via membrane-bound transport proteins) or passively via diffusion (4). As soon as the ^{18}O-labeled phosphate is in the cytoplasm, it can be incorporated into a nucleoside triphosphate molecule (e.g., ATP) if energy is available (5), from which it can be added onto a polyphosphate chain (6). ^{18}O atoms from ^{18}O-labeled water can also be incorporated into cell biomass during cell growth (7). Additionally, ^{18}O-labeled phosphate can be incorporated into cellular organic phosphate pools such as DNA, RNA, or phospholipids (8). Modified from Blake et al. (2005).

be reliably predicted from genomic data (Hatzenpichler et al., 2020). More direct methods need to be employed to test whether poly-P synthesis in cable bacteria is coupled to anaerobic energy metabolism such as sulfur disproportionation.

Our measurements revealed significant ^{18}O labeling of poly-P granules in filaments retrieved from the oxic zone (**Figures 3**, **4**), indicating that these cells must have synthesized poly-P at some point during the SIP incubation. Because this process requires energy, preferentially in the form of ATP (Kornberg et al., 1999; Nocek et al., 2008; Rao et al., 2009; Wang et al., 2018), the cells from the oxic zone therefore must have been able to generate energy at some time during the incubation. However, these cells do not possess any known terminal oxidases (Kjeldsen et al., 2019) and thus cannot generate energy from oxygen reduction, as supported by the observation that cells in the oxic zone do not grow (Geerlings et al., 2020, 2021; this study, **Figure 5**).

A possible explanation for the observed ^{18}O labeling of poly-P in cells from the oxic zone is that these cells generated energy via endogenous catabolism. This process is a stress response often observed in microorganisms entering a non-growing stage, where energy is generated from the breakdown of large biomolecules (e.g., DNA, RNA, ribosomes, phospholipids) (Bergkessel et al., 2016). For example, in stressed *E. coli* cells, this stringent response redirects cellular phosphorus toward synthesis of poly-P, which is essential for adaptation to various stresses (including oxidative stress) and survival during periods of no growth (Rao and Kornberg, 1996; Ault-Riché et al., 1998; Rao et al., 1998). For cable bacteria, endogenous catabolism could theoretically be directed toward poly-P synthesis. The ^{18}O labeling of poly-P in the cells from the oxic zone could then be explained by assuming that the energy released by the endogenous catabolism is directed toward the synthesis of ATP, which is then used to "propagate" the ^{18}O-labeled P_i toward poly-P (**Figure 6**; reactions 5 & 6). Yet why direct energy from endogenous catabolism to poly-P rather than using the energy directly for maintenance and stress release?

An alternative, and perhaps more likely, explanation for the observed ^{18}O labeling pattern of poly-P is that the cells retrieved from the oxic zone spent part of the SIP incubation in the suboxic zone, where they synthesized poly-P and thus increased the ^{18}O labeling of the poly-P granules, and then migrated to the oxic zone before the end of the incubation. This hypothesis is consistent with the gliding motility of cable bacteria (Bjerg et al., 2016), which is most prominent at the oxic-suboxic boundary, where cells move transiently in and out of the oxic zone such that cell abundance in the oxic zone remains relatively constant (Scilipoti et al., 2021; Yin et al., 2021). It is also consistent with their ability to quickly switch between sulfide oxidation and oxygen reduction depending on the surrounding redox conditions (Geerlings et al., 2020). This hypothesis suggests that the average ^{18}O labeling of poly-P granules in cells from the oxic, transition, and suboxic zone reflects the average residence time of the cells in each zone.

Variability in ^{18}O Labeling of Polyphosphate Granules

For each combination of the labeling interval and redox zone, ^{18}O atom fractions of poly-P granules showed considerable variability among granules (**Figures 4A,B**). Most of this variability is explained by differences among filaments in combination with differences among granules within the same cell rather than by differences among cells within the same filament. Here, we discuss possible reasons for these patterns.

Variability Among Filaments

For each redox zone and labeling period, variability among filaments explained the largest part of the overall variability in the ^{18}O labeling of the poly-P granules (52-88%) and the ^{13}C labeling of the cytoplasm (86-99%) (**Table 4**). The latter result is consistent with previous research, which showed large differences in growth rates among filaments (Geerlings et al., 2020) and synchronized growth and cell division over millimeter length scales (Geerlings et al., 2021).

Variability Among Cells of the Same Filament

Consistently for each redox zone, the within-filament variability explained only a small part (5-8%) of variability in the ^{18}O labeling of poly-P granules (**Table 4**). Previously, small within-filament variability was observed for ^{13}C labeling of cable bacteria incubated with ^{13}C-CO_2. Specifically for filaments retrieved from the suboxic zone, this pattern was attributed to a synchronized growth and division of cells within a filament (Geerlings et al., 2021). Although synchronicity of poly-P synthesis within a filament is a plausible explanation for the ^{18}O labeling patterns observed in the present study, we have not followed individual filaments along stretches containing more than about 10 cells, and hence we cannot draw firm conclusions. On the one hand, we observed that if poly-P granules were ^{18}O-labeled in one cell, they were also labeled, to a similar degree, in the neighboring cells (e.g., **Figures 3**, **4** and **Supplementary Figure 2**), suggesting that poly-P synthesis is not independent among cells within a filament. On the other hand, differences among cells within a filament were greater for the ^{18}O labeling compared to the ^{13}C labeling (**Table 4**), indicating that ^{18}O labeling of poly-P granules is influenced by additional factors compared to those controlling ^{13}C labeling of cells (see next section). The small within-filament and large between-filament variability observed in the ^{18}O labeling of poly-P granules fits the "oxygen pacemaker hypothesis" that states that contact with oxygen serves as a "pacemaker" for long-distance electron transport and energy conservation (Geerlings et al., 2021). Access to oxygen thus determines when the sulfide-oxidizing cells within a filament have the capacity for both poly-P synthesis and growth. However, more research is required to assess the degree of synchronicity of poly-P metabolism among cells within a cable bacterium filament.

Variability Within Cells

A relatively large part of variability in the ^{18}O labeling of poly-P granules (4-44%) was explained by differences within cells (**Table 4**). This pattern could be due (1) to methodological artifacts, (2) to differences in the rate at which poly-P is synthesized and incorporated into individual granules, (3) to differences in the periods and timing over which poly-P is synthesized between granules (at the same rate), and (4) to differences in the initial size of poly-P granules. We now discuss each of these factors in more detail.

The analytical procedure used to quantify the granule-specific ^{18}O atom fraction could be a possible source of within-cell variability among poly-P granules. We collected ion counts for each field of view over hundreds of planes, which "dissected" the imaged cells across a depth interval that included poly-P granules as well as the cytoplasm above and/or below the granules. This approach provided quantitative information about the ^{18}O labeling of the poly-P granule and the corresponding ^{13}C labeling of the surrounding cytoplasm in one image stack. Because the ^{18}O labeling of the cytoplasm is lower compared to the poly-P granule (**Figures 1E,F**), the poly-P-specific ^{18}O atom fraction calculated from the $^{18}O^-$ and $^{16}O^-$ ion counts accumulated across all planes in the image stack is lower than it would be if the planes corresponding to the cytoplasm were excluded from the analysis. However, this effect is negligible because the $^{16}O^-$ ion counts detected from the poly-P granules were more than ∼50-fold higher than those from the cytoplasm (∼5-fold higher count rates, and > 10-fold greater number of planes).

Differences in the intrinsic rate at which poly-P is synthesized will obviously generate differences in ^{18}O labeling among granules. However, it is difficult to envision how the rate of poly-P synthesis can vary within a single cell, as one expects the concentration of both substrates (e.g., P_i) and catalysts (poly-P kinases) to be homogeneous within the cytoplasm of a single cell. Therefore, a more important factor could be the timing of poly-P synthesis and breakdown in individual poly-P granules in combination with the poly-P content of granules at the beginning of the labeling period (Polerecky et al., 2021). As discussed above, substantial poly-P turnover likely occurred during our incubations, potentially involving multiple cycles of synthesis and breakdown (**Supplementary Model**). Labeling differences among individual granules can arise if poly-P turnover cycles are not synchronized among granules. This can happen, for example, due to relative delays between cycle onsets or differences in cycle durations. These differences can be amplified by the progressive ^{18}O labeling of the P_i pool within the first hours of the incubation (poly-P granules formed early will hence show lower labeling levels).

Yet, even when the ^{18}O incorporation rate is similar and the labeling period is synchronized and identical among granules, one can expect variation, as differences in the ^{18}O labeling of poly-P granules can also arise due to a different granule size at the beginning of the labeling period. For example, if ^{18}O-labeled poly-P is incorporated into two differently sized granules and the rate of incorporation is the same for both granules, the smaller granule will have a greater ^{18}O atom fraction at the end of the incubation than the larger one (Polerecky et al., 2021). This is because the incorporated ^{18}O is mixed across the whole granule, thus providing lower labeling levels for larger granules.

Observation of the different morphotypes (**Figures 1**, **2** and **Supplementary Figure 2**) reveals less variation between the two similarly-sized poly-P granules at the cell poles of the "thin" morphotype whereas within-cell variation is greater in cells of the "thicker" morphotype with multiple poly-P granules in the cell. The observed within-cell differences are thus most likely the result of a combination of initial starting sizes of the granules and relative delays between cycle onsets or cycle durations.

Carbon and Polyphosphate Metabolisms Are Not Coupled

Although both ^{13}C labeling of the cell cytoplasm and ^{18}O labeling of poly-P granules are, on average, lower in the oxic zone compared to the transition and suboxic zones, the ^{13}C labeling does not predict ^{18}O labeling for individual cells (**Figure 5**). Thus, cell growth and poly-P synthesis are linked on the population level due to their common dependence on the redox environment. We cannot exclude that a connection between active growth and poly-P synthesis also exists on the filament and cell level (e.g., in the suboxic zone). However, we observed a sizeable fraction (27/129 or ∼21%) of filaments from the transition and suboxic zones that showed no, or very little, ^{13}C labeling of the cytoplasm but clear ^{18}O labeling of the poly-P granules (**Figure 1E**, **Table 3** and **Supplementary Figure 2**), which shows that, on the filament and cell level, growth and poly-P synthesis in cable bacteria can operate independently of each other.

A similar large heterogeneity in growth among filaments from the suboxic zone was observed previously in SIP experiments using DIC labeled with ^{13}C (Geerlings et al., 2020, 2021) or ^{14}C (Kjeldsen et al., 2019), which also found no significant growth in about 30-50% of filaments from the suboxic zone after 24 h of incubation. In previous studies, filaments displaying no significant growth were considered as inactive, and it was hypothesized that these filaments had no contact with oxygen during the incubation interval and thus could not generate ATP.

Our present results refine this interpretation, because most of the filaments that showed no activity in terms of growth were still actively synthesizing poly-P. Because poly-P synthesis requires energy, most likely in the form of ATP, these filaments must have had the capacity for energy generation, and were therefore most likely connected to oxygen, at least during part of the labeling interval. However, instead of directing this energy toward growth and reproduction, these filaments remained in a state of growth arrest and directed the energy, or at least part of it, toward poly-P synthesis (**Figure 7**). This way, cable bacteria appear to have two phases in their life cycle when connected to oxygen (explaining the two clusters in **Figure 5B**): period of growths, in which the suboxic cells divert the energy gained from sulfide oxidation toward biomass synthesis and poly-P production, and periods of growth arrest, where the suboxic cells divert the energy gained from sulfide oxidation exclusively toward poly-P production. In both cases, only the cells that perform sulfide oxidation are capable of ATP formation (**Figure 7**). The synchronized growth and division observed in previous research indicates that cells regularly lose their connection to oxygen as part of their life cycle (Geerlings et al., 2021). When disconnected from oxygen, both poly-P synthesis and growth cannot happen via long-distance electron transport. Thus, the variability in the ^{18}O labeling of the poly-P granules between filaments can be explained by access to oxygen and differences in the cell-cycle stage (growth vs. non-growth). The cells that perform oxygen reduction do not show energy conservation, and as a result show vanishing rates of biomass synthesis (^{13}C labeling) and poly -P formation (^{18}O labeling) (**Figure 7**).

Possible Roles of Polyphosphates in Cable Bacteria

For most poly-P accumulating organisms, poly-P is typically thought of as a “back-up” energy reservoir, but in many species it can also be essential for survival of the non-growing stage of the cell cycle or in response to oxidative stress (Rao and Kornberg, 1996; Ault-Riché et al., 1998; Kornberg et al., 1999; Rao et al., 2009; Gray et al., 2014; Gray and Jakob, 2015). We hypothesize that poly-P also plays these roles in cable bacteria, where the specific role depends on both the redox environment and cell cycle stage.

Cells in the oxic zone need to perform oxygen reduction to facilitate energy supply for the rest of the filament in the suboxic zone with no known method of energy conservation (Geerlings et al., 2020). Being in an oxic environment, these cells are likely in a constant state of oxidative stress, which is supported by the high concentrations of antioxidant proteins (e.g., catalases, superoxide reductase, rubrerythrin, and GroEL/ES chaperonins) detected by proteomic analysis of cable bacteria (Kjeldsen et al., 2019). Thus, a viable hypothesis is that cable bacteria cells use poly-P as a “back-up” energy reservoir and/or as a method of protection against oxidative stress when they (temporarily) reside in the oxic zone. Poly-P can prevent oxidative stress by acting as an ATP-independent primordial chaperone with minimal substrate specificity to stabilize a wide variety of proteins (Gray et al., 2014; Gray and Jakob, 2015). Thus, the use of poly-P as a chaperone would be ideal for cells in the oxic zone as they cannot build extra antioxidant proteins due to their inability to generate energy. Furthermore, no phosphate groups are removed from poly-P when it functions as a chaperone, so once the poly-P chain is separated from the accompanying protein, it can still be used as an energy reserve to support other tasks (e.g., to aid motility).

Microbial cells spend most of the time in a prolonged non-growing stage, with very little to no metabolic activity and growth occurring due to a limited availability of energy or nutrients, but are prepared to undergo rapid division cycles once these resources become available (Bergkessel et al., 2016). Conversely, depletion of a resource leads to a transition from a growing to a non-growing stage. The cell cycle is not arrested randomly during this transition, since this could halt key processes, especially DNA replication, at stages where severe and irreparable damage could occur (Kolter, 1993; Bergkessel et al., 2016). Thus, although the non-growing stage of the bacterial life cycle is poorly understood, even for model organisms, it is required and the transition between the growing and non-growing stage is regulated to ensure cell viability (Bergkessel et al., 2016). Previous research showed an involvement of poly-P during the non-growing stage of bacteria. For the model bacterium *Escherichia coli*, for example, mutants lacking *ppk* and thus the ability to synthesize poly-P failed to survive the state of growth arrest and lacked resistance to several stressors (e.g., heat, H_2O_2, or osmotic stress) (Rao and Kornberg, 1996; Shiba et al., 1997; Ault-Riché et al., 1998; Grillo-Puertas et al., 2016). For *Pseudomonas aeruginosa*, poly-P accumulation was also maximized during the non-growing stage (Kim et al., 1998).

Based on this evidence, we hypothesize that poly-P plays an important, perhaps regulatory, role during the non-growing stage of the cable bacteria cell cycle. This hypothesis is supported by the significant ^{18}O labeling of poly-P granules in filaments with no, or very little, labeling in ^{13}C, which was observed for filaments retrieved from all redox zones (**Figure 5** and **Table 4**). This observation indicates that, in the suboxic zone, poly-P synthesis is one of the metabolic activities performed by cable bacteria

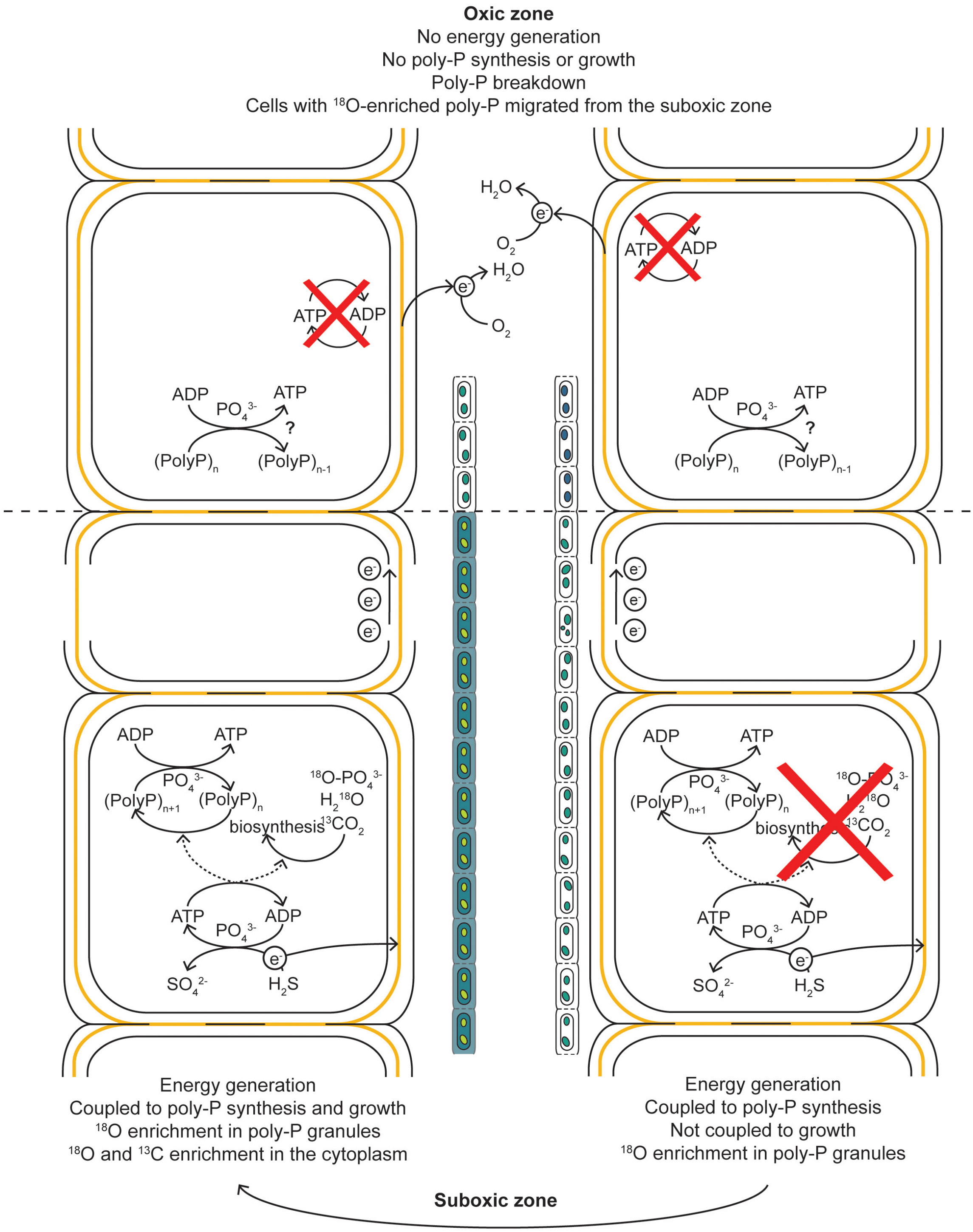

FIGURE 7 | Schematic diagram of our hypothesis explaining the observed ^{13}C and ^{18}O labeling patterns in cable bacteria. When a filament has access to O_2, the cells performing the sulfide-oxidizing half-reaction can generate energy in the form of ATP. During a period of growth arrest, this energy is not directed toward biosynthesis and growth but toward the build-up of poly-P granules, resulting in an ^{18}O enrichment of the poly-P granules but no ^{13}C and ^{18}O enrichment of the cytoplasm. During a period of growth, the energy is directed toward both growth and poly-P synthesis, resulting in a ^{13}C and ^{18}O enrichment of the cytoplasm and ^{18}O enrichment of the poly-P granules. The electrons generated via the sulfide-oxidizing half-reactions are transported toward the cells in the oxic zone via the electron-conducting fibers in the shared periplasm of a filament. Within the oxic zone, the electrons are used to reduce O_2, but this process does not lead to energy generation and thus cannot lead to an ^{18}O enrichment in the poly-P granules. That such enrichment is observed in cells from the oxic zone is explained by migration of the cells from the suboxic into the oxic zone during the incubation. Before this migration, the cells entered a non-growing stage of the cell cycle and "prepared" for a survival in the oxic zone. Part of this preparation included the build-up of poly-P granules. Within the oxic zone, the poly-P can be broken down.

during the non-growing stage of their cell cycle. For the filament fragments retrieved from the oxic zone, this observation suggests that cell growth is arrested earlier than poly-P synthesis. Recent research on *E. coli* showed that the ability of a cell to survive prolonged periods of starvation was dependent on the conditions prior to starvation where cells experiencing slower growth prior to starvation were shown to have consistently lower death rates (Biselli et al., 2020). In general, when a cell adjusts it physiology toward growth, it becomes less adapted for survival and vice versa. Synthesizing proteins that protect cells and increase their survival chances comes at the expense of synthesizing proteins needed for growth. The result is a trade-off between a fitness benefit in starvation and a fitness cost during growth (Scott et al., 2010). Thus, it appears that before cells of a filament residing in the suboxic zone enter the oxic zone and therefore a non-growing stage, they are already "prepared" to deal with oxidative stress and shortage of energy by entering into a stage of growth arrest which might enhance the chances of survival and increase the time a cell can survive in the oxic zone and thus provide energy for the cells in the suboxic zone below.

CONCLUSION AND OUTLOOK

The ubiquitous presence of ^{18}O-labeled poly-P, observed after 6 h and 24 h of incubation with ^{18}O-labeled water in almost all cable bacterium filaments collected from all sediment redox zones, highlights the importance of this inorganic molecule for the metabolism of cable bacteria. ^{18}O labeling was highly variable among poly-P granules, with most of the variability explained by differences among filaments and a lesser part by differences among granules of the same cell. Additionally, the average ^{18}O labeling of poly-P was significantly lower in filaments from the oxic zone compared to those from the transition and suboxic zones, confirming that energy conservation is principally coupled to sulfide oxidation and not oxygen reduction. The variability patterns observed in our combined ^{18}O and ^{13}C data can be explained by assuming that, within an individual cable bacterium filament, poly-P is synthesized by cells residing in the suboxic zone (using energy gained from the sulfide oxidation half-reaction) and broken down by cells in the oxic zone. These roles dynamically change as part of the filament migrates in and out of the oxic zone, and our data indicate that a significant fraction of poly-P stored by cable bacteria is turned over in this way on the timescale of 24 h. Our data also indicate that cable bacteria migrate in and out of the oxic zone in a regulated fashion where cell growth is halted before entering the oxic zone. We hypothesize that, in the oxic zone, poly-P is used as a chaperone to aid protection against oxidative stress or as an energy reserve that can be utilized for other tasks (e.g., to aid motility), while in the suboxic zone, poly-P plays an important, perhaps regulatory role, during the non-growing stage of the cable bacteria cell cycle.

Our results here provide a set of hypotheses about poly-P cycling in cable bacteria. Additional research is required to test these hypotheses and quantify the rates, regulation and environmental impact of poly-P synthesis and breakdown in cable bacteria. Ideally, such future studies will combine molecular methods (e.g., genomic and proteomic analyses) with biogeochemical analyses including chemical imaging. Our results here show that dual-label stable isotope probing using $H_2{}^{18}O$ and ^{13}C-DIC forms a viable approach to shed light on C and P metabolism in cable bacteria, but also microorganisms in general. Yet, future experiments need to be conducted on shorter time scales ($\sim$1 h) to better resolve the dynamics of poly-P synthesis and turnover within cable bacteria.

DATA AVAILABILITY STATEMENT

The original contributions presented in the study are included in the article/**Supplementary Material**, further inquiries can be directed to the corresponding author/s.

AUTHOR CONTRIBUTIONS

NG, DV-C, FM, JM, and LP conceived the study. NG, DV-C, and SH-M set up the enrichment culture and prepared all the samples for nanoSIMS analysis. MK and LP performed the nanoSIMS analysis. NG, MK, RH, and LP analyzed the nanoSIMS data. NG wrote the manuscript with contributions from all co-authors. All authors contributed to the article and approved the submitted version.

FUNDING

NG is the recipient of a Ph.D. scholarship for teachers from Netherlands Organization for Scientific Research (NWO) in Netherlands (grant 023.005.049). RH received financial support from the Olaf Schuiling fund. JM was supported by Netherlands Earth System Science Center. DV-C was supported by Research Foundation Flanders via FWO grant 1275822N. FM and SH-M were financially supported by the Research Foundation Flanders via FWO Grant No. G038819N, and Netherlands Organization for Scientific Research (VICI grant 016.VICI.170.072). The NanoSIMS facility was partly supported by an NWO large infrastructure subsidy to JM (175.010.2009.011) and through a large infrastructure funding by the Utrecht University Board awarded to LP.

ACKNOWLEDGMENTS

We also thank Martin Marzloff (IFREMER, France) for advice on statistical analysis.

SUPPLEMENTARY MATERIAL

The Supplementary Material for this article can be found online at: https://www.frontiersin.org/articles/10.3389/fmicb.2022.883807/full#supplementary-material

REFERENCES

Achbergerová, L., and Nahálka, J. (2011). Polyphosphate - an ancient energy source and active metabolic regulator. *Microb. Cell Fact.* 10:63. doi: 10.1186/1475-2859-10-63

Aller, R. C., Aller, J. Y., Zhu, Q., Heilbrun, C., Klingensmith, I., and Kaushik, A. (2019). Worm tubes as conduits for the electrogenic microbial grid in marine sediments. *Sci. Adv.* 5:eaaw3651. doi: 10.1126/sciadv.aaw3651

Ault-Riché, D., Fraley, C. D., Tzeng, C. M., and Kornberg, A. (1998). Novel assay reveals multiple pathways regulating stress-induced accumulations of inorganic polyphosphate in *Escherichia coli*. *J. Bacteriol.* 180, 1841–1847. doi: 10.1128/jb.180.7.1841-1847.1998

Bergkessel, M., Basta, D. W., and Newman, D. K. (2016). The physiology of growth arrest: uniting molecular and environmental microbiology. *Nat. Rev. Microbiol.* 14, 549–562. doi: 10.1038/nrmicro.2016.107

Biselli, E., Schink, S. J., and Gerland, U. (2020). Slower growth of *Escherichia coli* leads to longer survival in carbon starvation due to a decrease in the maintenance rate. *Mol. Syst. Biol.* 16:e9478. doi: 10.15252/msb.20209478

Bjerg, J. T., Damgaard, L. R., Holm, S. A., Schramm, A., and Nielsen, L. P. (2016). Motility of Electric Cable Bacteria. *Appl. Environ. Microbiol.* 82, 3816–3821. doi: 10.1128/AEM.01038-16

Blake, R. E., Alt, J. C., and Martini, A. M. (2001). Oxygen isotope ratios of PO4: An inorganic indicator of enzymatic activity and P metabolism and a new biomarker in the search for life. *Proc. Natl. Acad. Sci.* 98, 2148–2153. doi: 10.1073/pnas.051515898

Blake, R. E., O'Neil, J. R., and Surkov, A. V. (2005). Biogeochemical cycling of phosphorus: insights from oxygen isotope effects of phosphoenzymes. *Am. J. Sci.* 305, 596–620. doi: 10.2475/ajs.305.6-8.596

Brock, J., and Schulz-Vogt, H. N. (2011). Sulfide induces phosphate release from polyphosphate in cultures of a marine *Beggiatoa* strain. *Int. Soc. Microb. Ecol. J.* 5, 497–506. doi: 10.1038/ismej.2010.135

Brown, M. R. W., and Kornberg, A. (2004). Inorganic polyphosphate in the origin and survival of species. *Proc. Natl. Acad. Sci.* 101, 16085–16087. doi: 10.1073/pnas.0406909101

Burdorf, L. D. W., Malkin, S. Y., Bjerg, J. T., Van Rijswijk, P., Criens, F., Tramper, A., et al. (2018). The effect of oxygen availability on long-distance electron transport in marine sediments. *Limnol. Oceanogr.* 63, 1799–1816. doi: 10.1002/lno.10809

Burdorf, L. D. W. (2017). *Long Distance Electron Transport by Cable Bacteria: Global Distribution and Environmental Impact*. Ph.D. dissertation. Brussel: Vrije Universiteit Brussel.

Burdorf, L. D. W., Tramper, A., Seitaj, D., Meire, L., Hidalgo-Martinez, S., Zetsche, E. M., et al. (2017). Long-distance electron transport occurs globally in marine sediments. *Biogeosciences* 14, 683–701. doi: 10.5194/bg-14-683-2017.

Chang, S. J., and Blake, R. E. (2015). Precise calibration of equilibrium oxygen isotope fractionations between dissolved phosphate and water from 3 to 37°C. *Geochim. Cosmochim. Acta* 150, 314–329. doi: 10.1016/j.gca.2014.10.030

Dalgaard, P. (2013). "Summary for policymakers," in *Climate Change 2013 - The Physical Science Basis*, eds T. Stocker, D. Qin, and G. K. Plattner (Cambridge, CA: Intergovernmental Panel on Climate Change), 1–30. doi: 10.1017/CBO9781107415324.004

Geerlings, N. M. J., Geelhoed, J. S., Vasquez-Cardenas, D., Kienhuis, M. V. M., Hidalgo-Martinez, S., Boschker, H. T. S., et al. (2021). Cell cycle, filament growth and synchronized cell division in multicellular cable bacteria. *Front. Microbiol.* 12:620807. doi: 10.3389/fmicb.2021.620807

Geerlings, N. M. J., Karman, C., Trashin, S., As, K. S., Kienhuis, M. V. M., Hidalgo-Martinez, S., et al. (2020). Division of labor and growth during electrical cooperation in multicellular cable bacteria. *Proc. Natl. Acad. Sci. U.S.A.* 117, 5478–5485. doi: 10.1073/pnas.1916244117

Geerlings, N. M. J., Zetsche, E. M., Hidalgo-Martinez, S., Middelburg, J. J., and Meysman, F. J. R. (2019). Mineral formation induced by cable bacteria performing long-distance electron transport in marine sediments. *Biogeosciences* 16, 811–829. doi: 10.5194/bg-16-811-2019

Gray, M. J., and Jakob, U. (2015). Oxidative stress protection by polyphosphate-new roles for an old player. *Curr. Opin. Microbiol.* 24, 1–6. doi: 10.1016/j.mib.2014.12.004

Gray, M. J., Wholey, W. Y., Wagner, N. O., Cremers, C. M., Mueller-Schickert, A., Hock, N. T., et al. (2014). Polyphosphate is a primordial chaperone. *Mol. Cell* 53, 689–699. doi: 10.1016/j.molcel.2014.01.012

Grillo-Puertas, M., Rintoul, M. R., and Rapisarda, V. A. (2016). PhoB activation in non-limiting phosphate condition by the maintenance of high polyphosphate levels in the stationary phase inhibits biofilm formation in *Escherichia coli*. *Microbiol. (United Kingdom).* 162, 1000–1008. doi: 10.1099/mic.0.000281

Hatzenpichler, R., Krukenberg, V., Spietz, R. L., and Jay, Z. J. (2020). Next-generation physiology approaches to study microbiome function at single cell level. *Nat. Rev. Microbiol.* 18, 241–256. doi: 10.1038/s41579-020-0323-1

He, S., and Mcmahon, K. D. (2011). Microbiology of "*Candidatus Accumulibacter*" in activated sludge. *Microb. Biotechnol.* 4, 603–619. doi: 10.1111/j.1751-7915.2011.00248.x

Ishige, K., Zhang, H., and Kornberg, A. (2002). Polyphosphate kinase (PPK2), a potent, polyphosphate-driven generator of GTP. *Proc. Natl. Acad. Sci. U. S. A.* 99, 16684–16688. doi: 10.1073/pnas.262655299

Khoshmanesh, A., Hart, B. T., Duncan, A., and Beckett, R. (1999). Biotic uptake and release of phosphorus by a wetland sediment. *Environ. Technol. (United Kingdom).* 20, 85–91. doi: 10.1080/09593332008616796

Khoshmanesh, A., Hart, B. T., Duncan, A., and Beckett, R. (2002). Luxury uptake of phosphorus by sediment bacteria. *Water Res.* 36, 774–778. doi: 10.1016/S0043-1354(01)00272-X

Kim, H. Y., Schlictman, D., Shankar, S., Xie, Z., Chakrabarty, A. M., and Kornberg, A. (1998). Alginate, inorganic polyphosphate, GTP and ppGpp synthesis co-regulated in *Pseudomonas aeruginosa*: implications for stationary phase survival and synthesis of RNA/DNA precursors. *Mol. Microbiol.* 27, 717–725. doi: 10.1046/j.1365-2958.1998.00702.x

Kjeldsen, K. U., Schreiber, L., Thorup, C. A., Boesen, T., Bjerg, J. T., Yang, T., et al. (2019). On the evolution and physiology of cable bacteria. *Proc. Natl. Acad. Sci.* 116, 19116–19125. doi: 10.1073/pnas.1903514116

Kolter, R. (1993). The stationary phase of the bacterial life cycle. *Annu. Rev. Microbiol.* 47, 855–874. doi: 10.1146/annurev.micro.47.1.855

Kornberg, A. (1995). Inorganic polyphosphate - toward making a forgotten polymer unforgettable. *J. Bacteriol.* 177, 491–496. doi: 10.1128/jb.177.3.491-496.1995

Kornberg, A., Rao, N. N., and Ault-riché, D. (1999). Inorganic polyphosphate: a molecule of many functions. *Annu. Rev. Biochem.* 68, 89–125. doi: 10.1146/annurev.biochem.68.1.89

Langer, S., Vogts, A., and Schulz-Vogt, H. N. (2018). Simultaneous visualization of enzymatic activity in the cytoplasm and at polyphosphate inclusions in *Beggiatoa* sp. Strain 35Flor Incubated with 18 O-Labeled Water. *mSphere* 3:e00489-18. doi: 10.1128/mSphere.00489-18

Lassila, J. K., Zalatan, J. G., and Herschlag, D. (2011). Biological phosphoryl-transfer reactions: understanding mechanism and catalysis. *Annu. Rev. Biochem.* 80, 669–702. doi: 10.1146/annurev-biochem-060409-092741

Liang, Y., and Blake, R. E. (2006). Oxygen isotope signature of Pi regeneration from organic compounds by phosphomonoesterases and photooxidation. *Geochim. Cosmochim. Acta* 70, 3957–3969. doi: 10.1016/j.gca.2006.04.036

Malkin, S. Y., Rao, A. M. F., Seitaj, D., Vasquez-Cardenas, D., Zetsche, E. M., Hidalgo-Martinez, S., et al. (2014). Natural occurrence of microbial sulphur oxidation by long-range electron transport in the seafloor. *ISME J.* 8, 1843–1854. doi: 10.1038/ismej.2014.41

Meyer, A. (1904). Orientierende untersuchungen uber verbreitung, morphologie und chemie des volutins. *Bot. Zeitung* 62, 113–152.

Meysman, F. J. R. (2018). Cable bacteria take a new breath using long-distance electricity. *Trends Microbiol.* 26, 411–422. doi: 10.1016/j.tim.2017.10.011

Meysman, F. J. R., Cornelissen, R., Trashin, S., Bonné, R., Martinez, S. H., van der Veen, J., et al. (2019). A highly conductive fibre network enables centimetre-scale electron transport in multicellular cable bacteria. *Nat. Commun.* 10, 1–8. doi: 10.1038/s41467-019-12115-7

Müller, H., Bosch, J., Griebler, C., Damgaard, L. R., Nielsen, L. P., Lueders, T., et al. (2016). Long-distance electron transfer by cable bacteria in aquifer sediments. *ISME J.* 10, 2010–2019. doi: 10.1038/ismej.2015.250

Müller, W. E. G., Schröder, H. C., and Wang, X. (2019). Inorganic polyphosphates as storage for and generator of metabolic energy in the extracellular matrix. *Chem. Rev.* 119, 12337–12374. doi: 10.1021/acs.chemrev.9b00460

Musat, N., Musat, F., Weber, P. K., and Pett-Ridge, J. (2016). Tracking microbial interactions with NanoSIMS. *Curr. Opin. Biotechnol.* 41, 114–121. doi: 10.1016/j.copbio.2016.06.007

Nielsen, L. P., Risgaard-Petersen, N., Fossing, H., Christensen, P. B., and Sayama, M. (2010). Electric currents couple spatially separated biogeochemical processes in marine sediment. *Nature* 463, 1071–1074. doi: 10.1038/nature08790

Nocek, B., Kochinyan, S., Proudfoot, M., Brown, G., Evdokimova, E., Osipiuk, J., et al. (2008). Polyphosphate-dependent synthesis of ATP and ADP by the family-2 polyphosphate kinases in bacteria. *Proc. Natl. Acad. Sci. U. S. A.* 105, 17730–17735. doi: 10.1073/pnas.0807563105

Nocek, B. P., Khusnutdinova, A. N., Ruszkowski, M., Flick, R., Burda, M., Batyrova, K., et al. (2018). Structural insights into substrate selectivity and activity of bacterial polyphosphate kinases. *ACS Catal.* 8, 10746–10760. doi: 10.1021/acscatal.8b03151

Pfeffer, C., Larsen, S., Song, J., Dong, M., Besenbacher, F., Meyer, R. L., et al. (2012). Filamentous bacteria transport electrons over centimetre distances. *Nature* 491, 218–221. doi: 10.1038/nature11586

Pinheiro, J., Bates, D., and R-core. (2021). *Nlme: Linear and Nonlinear Mixed Effects Models*. Available online at: https://svn.r-project.org/R-packages/trunk/nlme/. (accessed March 1, 2021).

Polerecky, L., Adam, B., Milucka, J., Musat, N., Vagner, T., and Kuypers, M. M. M. (2012). Look@NanoSIMS - a tool for the analysis of nanoSIMS data in environmental microbiology. *Environ. Microbiol.* 14, 1009–1023. doi: 10.1111/j.1462-2920.2011.02681.x

Polerecky, L., Eichner, M., Masuda, T., Zavøel, T., Rabouille, S., Campbell, D. A., et al. (2021). Calculation and interpretation of substrate assimilation rates in microbial cells based on isotopic composition data obtained by nanoSIMS. *Front. Microbiol.* 12:621634. doi: 10.3389/fmicb.2021.621634

Rao, N., and Kornberg, A. (1996). Inorganic polyphosphate supports resistance and survival of stationary- phase *Escherichia coli*. *J. Bacteriol* 178, 1394–1400. doi: 10.1128/jb.178.5.1394-1400.1996

Rao, N. N., Gómez-García, M. R., and Kornberg, A. (2009). Inorganic polyphosphate: essential for growth and survival. *Annu. Rev. Biochem.* 78, 605–647. doi: 10.1146/annurev.biochem.77.083007.093039

Rao, N. N., Liu, S., and Kornberg, A. (1998). Inorganic polyphosphate in *Escherichia coli*: the phosphate regulon and the stringent response. *J. Bacteriol.* 180, 2186–2193. doi: 10.1128/jb.180.8.2186-2193.1998

Reimers, C. E., Li, C., Graw, M. F., Schrader, P. S., and Wolf, M. (2017). The identification of cable bacteria attached to the anode of a benthic microbial fuel cell: evidence of long distance extracellular electron transport to electrodes. *Front. Microbiol.* 8:2055. doi: 10.3389/fmicb.2017.02055

Risgaard-Petersen, N., Kristiansen, M., Frederiksen, R. B., Dittmer, A. L., Bjerg, J. T., Trojan, D., et al. (2015). Cable bacteria in freshwater sediments. *Appl. Environ. Microbiol.* 81, 6003–6011. doi: 10.1128/AEM.01064-15

Risgaard-Petersen, N., Revil, A., Meister, P., and Nielsen, L. P. (2012). Sulfur, iron-, and calcium cycling associated with natural electric currents running through marine sediment. *Geochim. Cosmochim. Acta* 92, 1–13. doi: 10.1016/j.gca.2012.05.036

Saia, S. M., Carrick, H. J., Buda, A. R., Regan, J. M., and Walter, M. T. (2021). Critical review of polyphosphate and polyphosphate accumulating organisms for agricultural water quality management. *Environ. Sci. Technol.* 55, 2722–2742. doi: 10.1021/acs.est.0c03566

Schauer, R., Risgaard-Petersen, N., Kjeldsen, K. U., Tataru Bjerg, J. J., Jørgensen, B. B., Schramm, A., et al. (2014). Succession of cable bacteria and electric currents in marine sediment. *ISME J.* 8, 1314–1322. doi: 10.1038/ismej.2013.239

Schoffelen, N. J., Mohr, W., Ferdelman, T. G., Littmann, S., Duerschlag, J., Zubkov, M. V., et al. (2018). Single-cell imaging of phosphorus uptake shows that key harmful algae rely on different phosphorus sources for growth. *Sci. Rep.* 8:17182. doi: 10.1038/s41598-018-35310-w

Scholz, V. V., Müller, H., Koren, K., Nielsen, L. P., and Meckenstock, R. U. (2019). The rhizosphere of aquatic plants is a habitat for cable bacteria. *FEMS Microbiol. Ecol.* 95, 1–9. doi: 10.1093/femsec/fiz062

Schulz, H. N., and Schulz, H. D. (2005). Large sulfur bacteria and the formation of phosphorite. *Science* 307, 416–418. doi: 10.1126/science.1103096

Scilipoti, S., Koren, K., Risgaard-petersen, N., Schramm, A., and Nielsen, L. P. (2021). Oxygen consumption of individual cable bacteria. *Sci. Adv.* 7:eabe1870. doi: 10.1126/sciadv.abe1870

Scott, M., Gunderson, C. W., Mateescu, E. M., Zhang, Z., and Hwa, T. (2010). Interdependence of cell growth and gene expression: Origins and consequences. *Science* 330, 1099–1102. doi: 10.1126/science.1192588

Seitaj, D., Schauer, R., Sulu-Gambari, F., Hidalgo-Martinez, S., Malkin, S. Y., Burdorf, L. D. W., et al. (2015). Cable bacteria generate a firewall against euxinia in seasonally hypoxic basins. *Proc. Natl. Acad. Sci. U. S. A.* 112, 13278–13283. doi: 10.1073/pnas.1510152112

Seufferheld, M. J., Alvarez, H. M., and Farias, M. E. (2008). Role of polyphosphates in microbial adaptation to extreme environments. *Appl. Environ. Microbiol.* 74, 5867–5874. doi: 10.1128/AEM.00501-08

Shiba, T., Tsutsumi, K., Yano, H., Ihara, Y., Kameda, A., Tanaka, K., et al. (1997). Inorganic polyphosphate and the induction of rpoS expression. *Proc. Natl. Acad. Sci. U. S. A.* 94, 11210–11215. doi: 10.1073/pnas.94.21.11210

Sulu-Gambari, F., Seitaj, D., Meysman, F. J. R., Schauer, R., Polerecky, L., and Slomp, C. P. (2016). Cable bacteria control iron-phosphorus dynamics in sediments of a coastal hypoxic basin - supplementary information. *Environ. Sci. Technol.* 50, 1227–1233. doi: 10.1021/acs.est.5b04369

Thiruvallur Eachambadi, R., Bonné, R., Cornelissen, R., Hidalgo-Martinez, S., Vangronsveld, J., Meysman, F. J. R., et al. (2020). An ordered and fail-safe electrical network in cable bacteria. *Adv. Biosyst.* 7:e2000006. doi: 10.1002/adbi.202000006

Vasquez-Cardenas, D., van de Vossenberg, J., Polerecky, L., Malkin, S. Y., Schauer, R., Hidalgo-Martinez, S., et al. (2015). Microbial carbon metabolism associated with electrogenic sulphur oxidation in coastal sediments. *ISME J.* 9, 1966–1978. doi: 10.1038/ismej.2015.10

Versaw, W. K., and Metzenberg, R. L. (1996). Intracellular phosphate-water oxygen exchange measured by mass spectrometry. *Anal. Biochem.* 241, 14–17. doi: 10.1006/abio.1996.0370

Von Sperber, C., Kries, H., Tamburini, F., Bernasconi, S. M., and Frossard, E. (2014). The effect of phosphomonoesterases on the oxygen isotope composition of phosphate. *Geochim. Cosmochim. Acta* 125, 519–527. doi: 10.1016/j.gca.2013.10.010

Wang, L., Yan, J., Wise, M. J., Liu, Q., Asenso, J., Huang, Y., et al. (2018). Distribution patterns of polyphosphate metabolism pathway and its relationships with bacterial durability and virulence. *Front. Microbiol.* 9:782. doi: 10.3389/fmicb.2018.00782

Ye, X., Luke, B., Andresson, T., and Blonder, J. (2009). 18O stable isotope labeling in MS-based proteomics. *Briefings Funct. Genomics Proteomic.* 8, 136–144. doi: 10.1093/bfgp/eln055

Yin, H., Aller, R. C., Zhu, Q., and Aller, J. Y. (2021). The dynamics of cable bacteria colonization in surface sediments: a 2D view. *Sci. Rep.* 11:7167. doi: 10.1038/s41598-021-86365-1

Zuur, A. F., Ieno, E. N., Walker, N., Saveliev, A. A., and Smith, G. M. (2009). *Mixed Effects Models and Extensions in Ecology with R*. New York, NY: Springer, doi: 10.1007/978-0-387-87458-6

Conflict of Interest: The authors declare that the research was conducted in the absence of any commercial or financial relationships that could be construed as a potential conflict of interest.

frontiers | Frontiers in Microbiology

OPINION
published: 06 June 2022
doi: 10.3389/fmicb.2022.872610

On the Existence of Pilin-Based Microbial Nanowires

Derek R. Lovley*

Department of Microbiology and Institute for Applied Life Sciences, University of Massachusetts, Amherst, MA, United States

Keywords: *Geobacter*, e-pili, extracellular electron transfer, electromicrobiology, protein, protein nanowires

Edited by:
Nils Risgaard-Petersen,
Aarhus University, Denmark

Reviewed by:
Tom Clarke,
University of East Anglia,
United Kingdom
Li Zhuang,
Jinan University, China

***Correspondence:**
Derek R. Lovley
dlovley@umass.edu

Specialty section:
This article was submitted to
Microbiological Chemistry and
Geomicrobiology,
a section of the journal
Frontiers in Microbiology

Received: *09 February 2022*
Accepted: *17 May 2022*
Published: *06 June 2022*

Citation:
Lovley DR (2022) On the Existence of
Pilin-Based Microbial Nanowires.
Front. Microbiol. 13:872610.
doi: 10.3389/fmicb.2022.872610

INTRODUCTION

There is a debate whether *Geobacter sulfurreducens* produces electrically conductive pili (e-pili) from its pilin monomer, PilA, a protein encoded by gene GSU 1496. *G. sulfurreducens* assembly of the PilA into e-pili was proposed over a decade ago (Reguera et al., 2005). As detailed below, many subsequent studies have provided additional data consistent with this concept (**Figure 1**). However, Gu et al. have recently concluded that *G. sulfurreducens* does not express e-pili from PilA (Gu et al., 2021).

This is not a controversy over small details of the physiology of one microbe. *Geobacter* species play an important role in natural environments and biotechnologies. For example, *Geobacter* species are typically abundant in soils and sediments in which Fe(III) oxide reduction has a significant impact on the biogeochemical cycling of carbon, nutrients, and trace metals as well as in bioremediation (Lovley et al., 2011; Reguera and Kashefi, 2019; Lovley and Holmes, 2022). *Geobacter* species are also often abundant in soils and anaerobic digesters in which direct interspecies electron transfer (DIET) appears to be an important mechanism for methane production (Zhao et al., 2020; Lovley and Holmes, 2022). *Geobacter* and closely related species are often enriched on the anodes of electrodes harvesting electricity from organic matter and *G. sulfurreducens* generates the highest current densities of all known electroactive isolates (Lovley et al., 2011; Logan et al., 2019). Although other microbes, most notably *Shewanella* species, have been helpful for developing an understanding of key extracellular electron transfer mechanisms (Shi et al., 2016; Lovley and Holmes, 2022), there are no pure cultures that are as effective in Fe(III) oxide reduction, DIET, and current production as *G. sulfurreducens* and its close relative *G. metallireducens*.

Furthermore, if it were true that PilA cannot be assembled into conductive filaments, this would mean that attempts to develop new protein-based electronic materials based on concepts for electron transport along e-pili (Creasey et al., 2018; Dorval Courchesne et al., 2018; Gutermann and Gazit, 2018; Cosert et al., 2019; Roy et al., 2020) may be misguided. The reported heterologous expression of e-pili from PilA in *Pseudomonas aeruginosa* (Liu et al., 2019) or *Escherichia coli* (Ueki et al., 2020) for mass production of e-pili for the fabrication of electronics would require new, non-obvious explanations to describe how introducing *G. sulfurreducens* PilA confers the capacity for conductive filament expression. Other apparent accomplishments for electronics applications, also achieved simply by modifying the structure of PilA, such as tuning of the conductivity of *G. sulfurreducens* filaments or the introduction of novel binding sites on filaments to enhance sensor selectivity (Lovley and Yao, 2021), would also need reevaluation. The function of electronic devices for electricity generation (Liu et al., 2020b), sensing (Liu et al., 2020a; Smith et al., 2020), and neuromorphic memory (Fu et al., 2020, 2021) would need to be reconsidered.

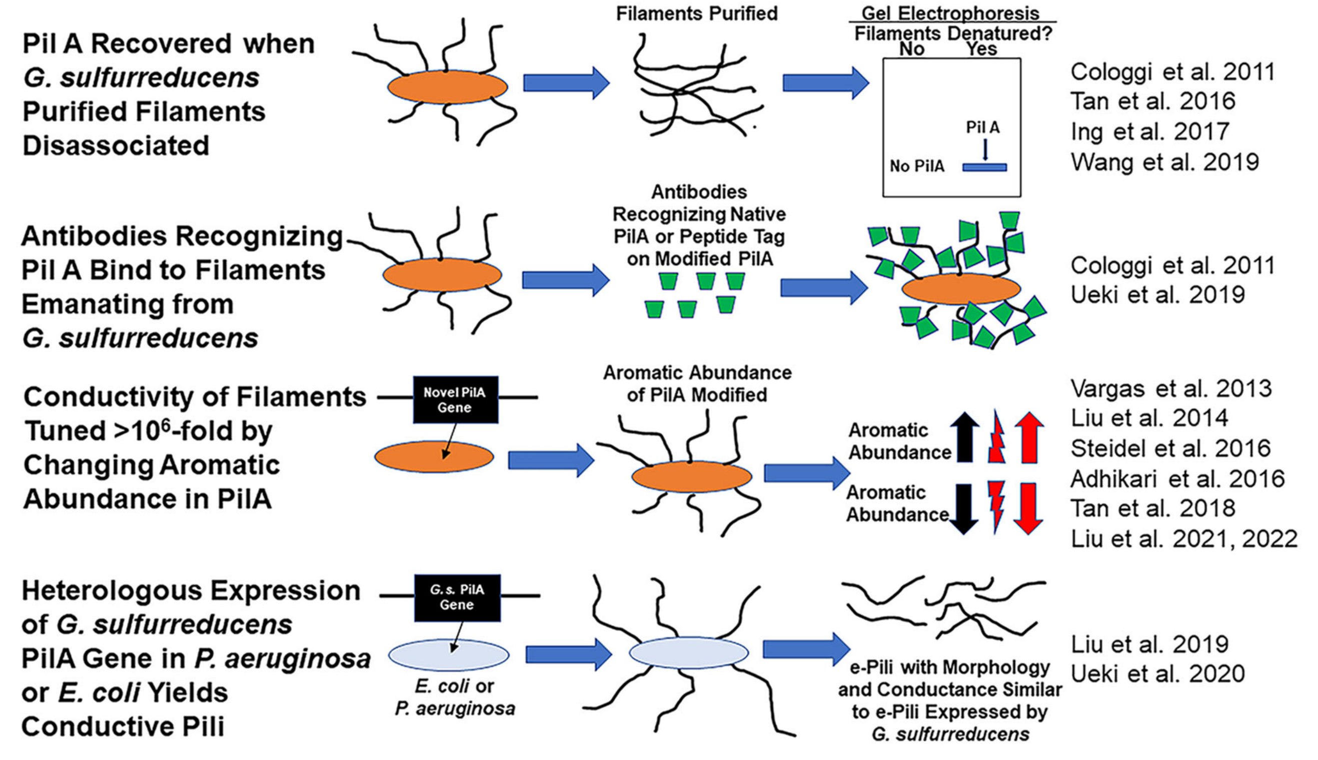

FIGURE 1 | Evidence consistent with the hypothesis that *Geobacter sulfurreducens* expresses e-pili comprised of the pilin monomer, PilA and that PilA can be assembled into conductive filaments.

THE CLAIM THAT WILD-TYPE *G. sulfurreducens* DOES NOT EXPRESS FILAMENTS COMPRISED OF PilA

Gu et al. (2021) conclude that *G. sulfurreducens* does not assemble PilA into pili because "Purified filament preparations from wild-type cells grown under these nanowire-producing conditions did not show either PilA-N or PilA-C using immunoblotting" (in Gu et al. the term PilA-N refers to the PilA protein encoded by gene GSU 1496). Yet just 2 years earlier the same lab reported that "we confirmed the presence of both PilA and OmcS with expected molecular weights of ~6.5 kDa and ~45 kDa, respectively, in our filament preparations using poly-acrylamide gel electrophoresis (SDS-PAGE), peptide mass spectrometry, and western immunoblotting" (Wang et al., 2019). Furthermore, the senior author of Gu et al. had also reported the recovery of PilA and OmcS from *G. sulfurreducens* filament preparations in another publication (Tan et al., 2016). It is important to recognize that these prior findings from some of the same investigators directly refute the Gu et al. hypothesis that wild-type *G. sulfurreducens* does not express filaments comprised of PilA. As detailed in the next section, there is also additional abundant evidence that wild-type *G. sulfurreducens* displays conductive filaments comprised of PilA.

Gu et al. did recover PilA-containing filaments from a mutant strain in which the gene for the outer-surface cytochrome OmcS was deleted (Gu et al., 2021). However, these filaments also contained another protein, and the filaments were poorly conductive. Gu et al. acknowledged that these hybrid filaments, which had a diameter of 6.5. nm, were an artifact produced only in the mutant strain; they were not expressed in wild-type *G. sulfurreducens*. As detailed below, no other study of *G. sulfurreducens* has observed 6.5 nm filaments emanating from *G. sulfurreducens* or in purified filament preparations. Such filaments were not even observed in other *omcS*-deletion mutants of *G. sulfurreducens* (Leang et al., 2010; Liu et al., 2022). Thus, the 6.5 nm PilA-containing filaments that Gu et al. report are an artifact, not replicated in other studies, and clearly have no relevance to the filament expression of wild-type *G. sulfurreducens*.

THE EVIDENCE FOR E-PILI COMPRISED OF PilA

Many studies have provided substantial evidence that wild-type *G. sulfurreducens* expresses filaments comprised of PilA (**Figure 1**). For example, the Reguera lab eloquently demonstrated that: (1) the PilA pilin monomer was the only protein recovered from purified *G. sulfurreducens* filaments sheared from cells and (2) that intact filaments harvested from the cells reacted with a PilA-specific antibody (Cologgi et al., 2011). Several other laboratories subsequently demonstrated that PilA was a major protein in filaments recovered from *G. sulfurreducens* (Tan et al., 2016; Ing et al., 2017).

G. sulfurreducens PilA is assembled into conductive filaments, not only in *G. sulfurreducens*, but also in other microbes. Expression of the *G. sulfurreducens* PilA pilin monomer gene in *P. aeruginosa* (Liu et al., 2019) or *E. coli* (Ueki et al., 2020) yielded filaments with the same morphology and conductance as *G. sulfurreducens* e-pili.

Another observation that only seems explicable if e-pili are comprised of PilA is the dynamic tuning of pili conductivity by more than one million-fold that is possible simply by modifying the abundance of aromatic amino acids in the pilin monomer protein. For example, replacing the *G. sulfurreducens* PilA gene with the *G. metallireducens* PilA gene yielded filaments with the same 3 nm diameter of the wild-type *G. sulfurreducens* pili, but with a conductivity that was 5,000-fold higher than wild-type (Tan et al., 2017). The higher conductivity was attributed to a higher abundance of aromatic amino acids in the *G. metallireducens* pilin. Conversely decreasing the abundance of aromatic amino acids in the pilin, still yielded 3 nm diameter filaments, but with a conductivity 1,000-fold lower than wild-type (Adhikari et al., 2016).

Not only is there substantial evidence that *G. sulfurreducens* expresses conductive filaments comprised of the PilA pilin monomer, but also direct examination of filaments emanating from cells revealed that e-pili are the primary filaments that *G. sulfurreducens* produces. In one approach, synthetic pilin monomer genes that yield pilin monomers with peptide tags were expressed in *G. sulfurreducens* (Ueki et al., 2019). All the pili that these strains of *G. sulfurreducens* displayed reacted with antibodies that specifically bind to the peptide tags that were incorporated in PilA. The stoichiometry of antibody binding to pili could be tuned by controlling the relative quantity of synthetic pilin with tags vs. wild-type pilin expressed in strains containing genes for both pilin types (Ueki et al., 2019).

In an alternative approach, atomic force microscopy revealed that 90% of the filaments that *G. sulfurreducens* displayed had the same 3 nm diameter, morphology, and conductance as the conductive filaments produced when *E. coli* heterologously expressed *G. sulfurreducens* PilA (Liu et al., 2021). The other 10% of the filaments had a morphology and diameter consistent with filaments comprised of the *c*-type cytochrome OmcS. Replacing the PilA gene in *G. sulfurreducens* with a gene for a pilin monomer with reduced aromatic amino acid content yielded a strain in which over 90 % of the filaments emanating from the cells were 3 nm diameter pili, morphologically similar to the pili of the strain expressing PilA, but with 1,000-fold less conductance. The abundance and conductance of the filaments comprised of OmcS was unchanged. A similar predominance of 3 nm diameter conductive pili and then decreased pili conductance when PilA was replaced with a gene for an aromatic-poor pilin was observed in studies conducted in a strain of *G. sulfurreducens* in which the gene for OmcS was deleted (Liu et al., 2022). The finding that changing the aromatic abundance of the pilin protein specifically and dramatically changed the conductance of the 3 nm diameter filaments indicated that these filaments were comprised of pilin (Liu et al., 2021, 2022). Thus, multiple lines of evidence suggest that *G. sulfurreducens* displays conductive pili comprised of PilA and that these are the most abundant filaments emanating from cells.

IMPORTANCE OF E-PILI IN EXTRACELLULAR ELECTRON TRANSFER

G. sulfurreducens requires its abundant e-pili for effective long-range extracellular electron transfer. The phenotypes of *Geobacter* strains that express poorly conductive pili provide the most direct evidence. Simply deleting the gene for PilA to prevent e-pili expression is not an appropriate approach because outer-surface *c*-type cytochromes that are also important for extracellular electron transfer are not properly localized to the outer surface in *pilA*-deletion mutants (Izallalen et al., 2008; Steidl et al., 2016; Liu et al., 2018). However, as noted above, *G. sulfurreducens* strains that express poorly conductive pili can be constructed by replacing the PilA gene with genes for pilins with a lower abundance of aromatic amino acids. These strains, which include *G. sulfurreducens* strains Aro-5, *G. sulfurreducens* strain Tyr3, *G. sulfurreducens* strain PA, and *G. metallireducens* strain Aro-5 express poorly conductive pili, while properly positioning outer-surface cytochromes on the outer cell surface (Vargas et al., 2013; Liu et al., 2014, 2021; Adhikari et al., 2016; Steidl et al., 2016; Ueki et al., 2018). None of these strains effectively reduce Fe(III) oxides or produce high current densities. *G. metallireducens* strain Aro-5 is an ineffective electron-donating partner for DIET (Ueki et al., 2018; Holmes et al., 2021).

The simplest explanation for these results is that the intrinsic conductivity of the wild-type e-pili is essential for effective extracellular electron transfer to Fe(III) oxides, other microbes, and through thick current-producing biofilms. *G. sulfurreducens* extracellular electron exchange is likely to rely on complex interactions between a suite of outer-surface *c*-type cytochromes, e-pili, and possibly other components (Lovley and Holmes, 2022). The phenotypes of strains expressing poorly conductive pili and cytochrome-deficient mutant strain phenotypes, as well as observations of cytochrome localization, demonstrate that cytochrome-based filaments alone cannot be the primary route for *G. sulfurreducens* long-range electron transfer (Lovley and Holmes, 2020, 2022).

CONCLUSIONS

In conclusion, many studies have provided evidence that *G. sulfurreducens* expresses e-pili comprised of the pilin monomer PilA. It remains a mystery as to why Gu et al. (2021) did not recover filaments comprised of PilA from their strain of 'wild-type' *G. sulfurreducens* when so many other studies, including several by the senior author of Gu et al., had previously found PilA in filament preparations. Furthermore, e-pili comprised of PilA can clearly be seen emanating from cells of *G. sulfurreducens*. Other microbes can heterologously express the *G. sulfurreducens* PilA and assemble it into the same type of e-pili found in *G. sulfurreducens*. Consistent with these observations, *G. sulfurreducens* nanowire conductivity is readily tuned simply by changing the abundance of aromatic amino acids in the pilin expressed. Expression of poorly conductive pili has demonstrated the importance of e-pili in Fe(III) oxide reduction, electron transfer to other microbial species, and for generating high current densities in bioelectrochemical systems. Therefore, at present the preponderance of evidence is that e-pili, comprised of PilA, not only exist, but are an important feature in *Geobacter* extracellular electron exchange. The pilins and archaellins of phylogenetically distinct bacteria and archaea are assembled into conductive filaments and it seems likely that e-pili and e-archaella are spread throughout the microbial world (Walker et al., 2018, 2019, 2020; Bray et al., 2020; Lovley and Holmes, 2020).

AUTHOR CONTRIBUTIONS

The author confirms being the sole contributor of this work and has approved it for publication.

REFERENCES

Adhikari, R. Y., Malvankar, N. S., Tuominen, M. T., and Lovley, D. R. (2016). Conductivity of individual Geobacter pili. *RSC Advances.* 6, 8354–8357. doi: 10.1039/C5RA28092C

Bray, M. S., Wu, J., Padilla, C. C., Stewart, F. J., Fowle, D. A., Henny, C., et al. (2020). Phylogenetic and structural diversity of aromatically dense pili from environmental metagenomes. *Environ. Microbiol. Rep.* 12, 49–57. doi: 10.1111/1758-2229.12809

Cologgi, D. L., Lampa-Pastirk, S., Speers, A. M., Kelly, S. D., and Reguera, G. (2011). Extracellular reduction of uranium via Geobacter conductive pili as a protective cellular mechanism. *Proc. Natl. Acad. Sci. U S A.* 108, 15248–15252. doi: 10.1073/pnas.1108616108

Cosert, K. M., Castro-Forero, A., Steidl, R. J., Worden, R. M., and Reguera, G. (2019). Bottom-up fabrication of protein nanowires via controlled self-assembly of recombinant Geobacter pilins. *mBio.* 10, e02721–19. doi: 10.1128/mBio.02721-19

Creasey, R. C. G., Mostert, A. B., Nguyen, T. A. H., Virdis, B., Freguia, S., et al. (2018). Microbial nanowires–electron transport and the role of synthetic analogues. *Acta Biomater.* 69, 1–30. doi: 10.1016/j.actbio.2018.01.007

Dorval Courchesne, N.-M., Debenedictis, E. P., Tresback, J., Kim, J. J., Duraj-Thatte, A., Zanuy, D., et al. (2018). Biomimetic engineering of conductive curli protein films. *Nanotechnology.* 29, 454002. doi: 10.1088/1361-6528/aadd3a

Fu, T., Liu, X., Fu, S., Woodard, T. L., Gao, H., Lovley, D. R., et al. (2021). Self-sustained green neuromorphic interfaces. *Nat. Commun.* 12, 3351. doi: 10.1038/s41467-021-23744-2

Fu, T., Liu, X., Gao, H., Ward, J. E., Liu, X., Yin, B., et al. (2020). Bioinspired bio-voltage memristors. *Nat. Commun.* 11, 1861. doi: 10.1038/s41467-020-15759-y

Gu, Y., Srikanth, V., Salazar-Morales, A. I., Jain, R., O'brien, J. P., Yi, S. M., et al. (2021). Structure of Geobacter pili reveals secretory rather than nanowire behaviour. *Nature.* 597, 430–434. doi: 10.1038/s41586-021-03857-w

Gutermann, T., and Gazit, E. (2018). Toward peptide-based bioelectronics: reductionist design of conductive pili mimetics. *Bioelectron. Med.* 1, 131–137. doi: 10.2217/bem-2018-0003

Holmes, D. E., Zhou, J., Ueki, T., Woodard, T. L., and Lovley, D. R. (2021). Mechanisms for electron uptake by Methanosarcina acetivorans during direct interspecies electron transfer. *mBio.* 12, e02344–21. doi: 10.1128/mBio.02344-21

Ing, N. L., Nusca, T. D., and Hochbaum, A. I. (2017). Geobacter sulfurreducens pili support ohmic electronic conduction in aqueous solution. *PCCP.* 19, 21791–21799. doi: 10.1039/C7CP03651E

Izallalen, M., Glaven, R. H., Mester, T., Nevin, K. P., Franks, A. E., and Lovley, D. R. (2008). Going wireless? Additional phenotypes of a pilin-deficient mutant weaken the genetic evidence for the role of microbial nanowires in extracellular electron transfer. In: *Abstracts of the 108th Annual Meeting of the American Society for Microbiology* (Boston, MA).

Leang, C., Qian, X., Mester, T., and Lovley, D. R. (2010). Alignment of the *c*-type cytochrome OmcS along pili of *Geobacter sulfurreducens*. *Appl. Environ. Microbiol.* 76, 4080–4084. doi: 10.1128/AEM.00023-10

Liu, X., Fu, T., Ward, J., Gao, H., Yin, B., Woodard, T. L., et al. (2020a). Multifunctional protein nanowire humidity sensors for green wearable electronics. *Advanced Electronic Materials.* 6, 2000721. doi: 10.1002/aelm.202000721

Liu, X., Gao, H., Ward, J., Liu, X., Yin, B., Fu, T., et al. (2020b). Power generation from ambient humidity using protein nanowires. *Nature.* 578, 550–554. doi: 10.1038/s41586-020-2010-9

Liu, X., Tremblay, P.-L., Malvankar, N. S., Nevin, K. P., Lovley, D. R., and Vargas, M. (2014). A Geobacter sulfurreducens strain expressing Pseudomonas aeruginosa type IV pili localizes OmcS on pili but Is deficient in Fe(III) oxide reduction and current production. *Appl. Environ. Microbiol.* 80, 1219–1224. doi: 10.1128/AEM.02938-13

Liu, X., Walker, D. J. F., Li, Y., Meier, D., Pinches, S., Holmes, D. E., et al. (2022). Cytochrome OmcS is not essential for extracellular electron transport via conductive pili in Geobacter sulfurreducens strain KN400. *Appl. Environ. Microbiol.* 88, e01622–21. doi: 10.1128/AEM.01622-21

Liu, X., Walker, D. J. F., Nonnenmann, S., Sun, D., and Lovley, D. R. (2021). Direct observation of electrically conductive pili emanating from Geobacter sulfurreducens. *mBio.* 12, e02209–21. doi: 10.1128/mBio.02209-21

Liu, X., Wang, S., Xu, A., Zhang, L., Liu, H., and Ma, L. Z. (2019). Biological synthesis of high-conductive pili in aerobic bacterium Pseudomonas aeruginosa. *Appl. Microbiol. Biotechnol.* 103, 1535–1544. doi: 10.1007/s00253-018-9484-5

Liu, X., Zhuo, S., Rensing, C., and Zhou, J. (2018). Syntrophic growth with direct interspecies electron transfer between pili-free Geobacter species. *ISME J.* 12, 2142–2151. doi: 10.1038/s41396-018-0193-y

Logan, B. E., Rossi, R., Ragab, A., and Saikaly, P. E. (2019). Electroactive microorganisms in bioelectrochemical systems. *Nat. Rev. Microbiol.* 17, 307–319. doi: 10.1038/s41579-019-0173-x

Lovley, D. R., and Holmes, D. E. (2020). Protein nanowires: the electrification of the microbial world and maybe our own. *J. Bacteriol.* 202, e00331–20. doi: 10.1128/JB.00331-20

Lovley, D. R., and Holmes, D. E. (2022). Electromicrobiology: the ecophysiology of phylogenetically diverse electroactive microorganisms. *Nat. Rev. Microbiol.* 20, 5–19. doi: 10.1038/s41579-021-00597-6

Lovley, D. R., Ueki, T., Zhang, T., Malvankar, N. S., Shrestha, P. M., Flanagan, K., et al. (2011). Geobacter: the microbe electric's physiology, ecology, and practical applications. *Adv. Microb. Physiol.* 59, 1–100. doi: 10.1016/B978-0-12-387661-4.00004-5

Lovley, D. R., and Yao, J. (2021). Intrinsically conductive microbial nanowires for "green" electronics with novel functions. *Trends Biotechnol.* 39, 940–952. doi: 10.1016/j.tibtech.2020.12.005

Reguera, G., and Kashefi, K. (2019). The electrifying physiology of Geobacter bacteria, 30 years on. *Adv. Microb. Physiol.* 74, 1–95. doi: 10.1016/bs.ampbs.2019.02.007

Reguera, G., Mccarthy, K. D., Mehta, T., Nicoll, J. S., Tuominen, M. T., and Lovley, D. R. (2005). Extracellular electron transfer *via* microbial nanowires. *Nature.* 435, 1098–1101. doi: 10.1038/nature03661

Roy, S., Xie, O., and Dorval Courchesne, N.-M. (2020). Challenges in engineering conductive protein fibres: Disentangling the knowledge. *Canadian J. Chem. Engin.* 98, 2081–2095. doi: 10.1002/cjce.23836

Shi, L., Dong, H., Reguera, G., Beyenal, H., Lu, A., Liu, J., et al. (2016). Extracellular electron transfer mechanisms between microorganisms and minerals. *Nat. Rev. Microbiol.* 14, 651–662. doi: 10.1038/nrmicro.2016.93

Smith, A. F., Liu, X., Woodard, T. L., Emrick, T., J.M., J., et al. (2020). Bioelectronic protein nanowire sensors for ammonia detection. *Nano Res.* 13, 1479–1484. doi: 10.1007/s12274-020-2825-6

Steidl, R. J., Lampa-Pastirk, S., and Reguera, G. (2016). Mechanistic stratification in electroactive biofilms of Geobacter sulfurreducens mediated by pilus nanowires. *Nature Commun.* 7, 12217. doi: 10.1038/ncomms12217

Tan, H.-Y., Adhikari, R. Y., Malvankar, N. S., Ward, J. E., Woodard, T. L., Nevin, K. P., et al. (2017). Expressing the Geobacter metallireducens PilA in Geobacter sulfurreducens yields pili with exceptional conductivity. *mBio.* 8, e02203–16. doi: 10.1128/mBio.02203-16

Tan, Y., Adhikari, R. Y., Malvankar, N. S., Ward, J. E., Nevin, K. P., Woodard, T. L., et al. (2016). The low conductivity of Geobacter uraniireducens pili suggests a diversity of extracellular electron transfer mechanisms in the genus Geobacter. *Front. Microbiol.* 7, 980. doi: 10.3389/fmicb.2016.00980

Ueki, T., Nevin, K. P., Rotaru, A.-E., Wang, L.-Y., Ward, J. E., Woodard, T. L., et al. (2018). Geobacter strains expressing poorly conductive pili reveal constraints on direct interspecies electron transfer mechanisms. *mBio.* 9, e01273–18. doi: 10.1128/mBio.01273-18

Ueki, T., Walker, D. J. F., Tremblay, P.-L., Nevin, K. P., Ward, J. E., Woodard, T. L., et al. (2019). Decorating the outer surface of microbially produced protein nanowires with peptides. *ACS Synth. Biol.* 8, 1809–1817. doi: 10.1021/acssynbio.9b00131

Ueki, T., Walker, D. J. F., Woodard, T. L., Nevin, K. P., Nonnenmann, S., and Lovley, D. R. (2020). An *Escherichia coli* chassis for production of electrically conductive protein nanowires. *ACS Synth. Biol.* 9, 647–654. doi: 10.1021/acssynbio.9b00506

Vargas, M., Malvankar, N. S., Tremblay, P.-L., Leang, C., Smith, J. A., Patel, P., et al. (2013). Aromatic amino acids required for pili conductivity and long-range extracellular electron transport in Geobacter sulfurreducens. *mBio.* 4:e00105–13. doi: 10.1128/mBio.00210-13

Walker, D. J. F., Adhikari, R. Y., Holmes, D. E., Ward, J. E., Woodard, T. L., Nevin, K. P., et al. (2018). Electrically conductive pili from genes of phylogenetically diverse microorganisms. *ISME J.* 12, 48–58. doi: 10.1038/ismej.2017.141

Walker, D. J. F., Martz, E., Holmes, D. E., Zhou, Z., Nonnenmann, S. S., and Lovley, D. R. (2019). The archaellum of Methanospirillum hungatei is electrically conductive. *mBio.* 10, e00579–19. doi: 10.1128/mBio.00579-19

Walker, D. J. F., Nevin, K. P., Nonnenmann, S. S., Holmes, D. E., Woodard, T. L., Ward, J. E., et al. (2020). Syntrophus conductive pili demonstrate that common hydrogen-donating syntrophs can have a direct electron transfer option. *ISME J.* 14, 837–846. doi: 10.1038/s41396-019-0575-9

Wang, F., Gu, Y., O'brien, J. P., Yi, S. M., Yalcin, S. E., Srikanth, V., et al. (2019). Structure of microbial nanowires reveals stacked hemes that transport electrons over micrometers. *Cell.* 177, 361–369. doi: 10.1016/j.cell.2019.03.029

Zhao, Z., Li, Y., Zhang, Y., and Lovley, D. R. (2020). Sparking anaerobic digestion: promoting direct interspecies electron transfer to enhance methane production. *IScience.* 23, 101794. doi: 10.1016/j.isci.2020.101794

Conflict of Interest: The author declares that the research was conducted in the absence of any commercial or financial relationships that could be construed as a potential conflict of interest.

frontiers | Frontiers in Microbiology

MINI REVIEW
published: 10 June 2022
doi: 10.3389/fmicb.2022.906363

Biomaterials and Electroactive Bacteria for Biodegradable Electronics

Robin Bonné[1]†, Koen Wouters[2]†, Jamie J. M. Lustermans[1] and Jean V. Manca[2]*

[1] *Center for Electromicrobiology, Department of Biology, Aarhus University, Aarhus, Denmark,* [2] *X-LAB, UHasselt, Diepenbeek, Belgium*

The global production of unrecycled electronic waste is extensively growing each year, urging the search for alternatives in biodegradable electronic materials. Electroactive bacteria and their nanowires have emerged as a new route toward electronic biological materials (e-biologics). Recent studies on electron transport in cable bacteria—filamentous, multicellular electroactive bacteria—showed centimeter long electron transport in an organized conductive fiber structure with high conductivities and remarkable intrinsic electrical properties. In this work we give a brief overview of the recent advances in biodegradable electronics with a focus on the use of biomaterials and electroactive bacteria, and with special attention for cable bacteria. We investigate the potential of cable bacteria in this field, as we compare the intrinsic electrical properties of cable bacteria to organic and inorganic electronic materials. Based on their intrinsic electrical properties, we show cable bacteria filaments to have great potential as for instance interconnects and transistor channels in a new generation of bioelectronics. Together with other biomaterials and electroactive bacteria they open electrifying routes toward a new generation of biodegradable electronics.

Keywords: cable bacteria, long-range electron transport, bioelectronics, organic electronics, e-waste, e-biologics, microbial nanowires, biological semiconductor

Edited by:
Amelia-Elena Rotaru,
University of Southern Denmark,
Denmark

Reviewed by:
Kengo Inoue,
University of Miyazaki, Japan
Annette Ruth Rowe,
University of Cincinnati, United States
Joshua T. Atkinson,
University of Southern California,
United States

***Correspondence:**
Robin Bonné
robin.bonne@bio.au.dk

†*These authors have contributed equally to this work*

Specialty section:
This article was submitted to
Microbiological Chemistry
and Geomicrobiology,
a section of the journal
Frontiers in Microbiology

Received: *28 March 2022*
Accepted: *20 May 2022*
Published: *10 June 2022*

Citation:
Bonné R, Wouters K,
Lustermans JJM and Manca JV
(2022) Biomaterials and Electroactive
Bacteria for Biodegradable
Electronics.
Front. Microbiol. 13:906363.
doi: 10.3389/fmicb.2022.906363

INTRODUCTION: E-WASTE AS A GLOBAL PROBLEM

The use of electronic devices is creating the world's fastest-growing waste-stream, with currently 50 million tons of e-waste produced each year (Ryder and Zhao Houlin, 2019). This not only causes $62.5 billion in material value of resources in our spent devices to be dumped into landfill (Ryder and Zhao Houlin, 2019), but exposure to this e-waste has a plethora of negative effects on humans, even *in utero* (Grant et al., 2013). Thus, electronic waste forms a substantial problem for environmental and human wellbeing, for which alternatives should be found on a short term (Kang et al., 2020). Biodegradable electronics is a new field that aims to replace the harmful non-durable materials used in electronics with biodegradable alternatives. In this review we will discuss the recent advances of using biomaterials for biodegradable electronics and the possible role of electroactive bacteria and in particular cable bacteria, of which an overview is given in **Figure 1**.

ADVANCES IN BIODEGRADABLE ELECTRONICS

Biodegradability might seem like a broad term since all materials will be degraded when left in nature after enough time. We will focus on so-called transient electronics: materials that have limited lifetimes before they disappear with the ultimate goal being bioresorption: the complete degradation of a device when immersed in biofluids. The kinetics of biodegradable materials depend on their chemical and morphological properties and the environmental conditions, such as temperature and pH and ionic content when in a solution (Kang et al., 2014). The lifetime of these devices can be accurately controlled by encapsulating the device with biodegradable material or by actively triggering the degradation reaction (Hwang et al., 2012; Kang et al., 2014, 2020). The number of defects through which water/vapor—which degrade the device—could leak can be tuned multiple ways, for example, by using multiple layers (Kang et al., 2014). Another option is doping materials to hinder their electrolysis (Seidel et al., 1990).

Biodegradable electronics can be found among inorganic, organic, and biological materials. Transience by bioresorption has for example been simulated for (semi-) conductors such as Silicon (Si), Germanium (Ge), SiGe and amorphous indium gallium zinc oxide (a-IGZO) in aqueous media. Some proposed non-biological transient dielectric materials include metal or semiconductor oxides and nitrides such as MgO, SiO_2, and SiN_x (Hwang et al., 2012). For example, the silicon and SiO_2 undergo hydrolysis to form either harmless $Si(OH)_4$ and H_2, or $Si(OH)_4$ and water (Seidel et al., 1990). This is a surface level effect, which allows for silicon's use as encapsulation layer. Nevertheless, layers of SiO_2 have defects through which water can permeate rapidly (<10 min), making it ineffective for such use (Lee et al., 2017). In this paper the focus will be on biodegradable materials originating from nature. They have the advantage that high-scale low-cost production is possible (Kang et al., 2020), because they are often solution based and allow low-temperature processing steps (Stadler et al., 2007). Furthermore, they have a high chemical compatibility with many other materials, and their properties can be tuned for their lifetime and morphology (Kang et al., 2020). Besides, organic monolayers can be combined with metals and plastics to create flexible electronics (Sekitani et al., 2009).

For biological biodegradable semiconductors, we will focus on materials that have proven conduction at least in the micrometer range, thereby excluding possible candidates like single peptides/proteins (Ing et al., 2018) and DNA (Beratan, 2019). A first interesting group of biological semiconductors are naturally occurring molecules such as indigo, which originates from several species of plants (Zollinger, 2003), but nowadays has become the most mass-produced industrial dye (Glowacki et al., 2011). These are planar molecules, which are connected through hydrogen bonding, resulting in tight π-stacking between neighboring molecules (Irimia-Vladu et al., 2012). This means that the orbitals which are not used in the intermolecular binding of the elements overlap and form conductive pathways. Despite having a high melting point, and low solubility, indigo can be degraded by enzymes (Campos et al., 2001), bacteria (Valdez-Vazquez et al., 2020), oxidizing agents (Prado et al., 2008) and light (in water) in timeframes down to a single day (Vautier et al., 2001), with a reported rate of 0.90 μmol L^{-1} min^{-1} (Vautier et al., 2001). In donor-acceptor solar cells, indigo acts like a good acceptor material (Glowacki et al., 2011). Another naturally occurring semiconductor is the pigment β-carotene, which can act as an electron donor in e.g., dye sensitized solar cells (Glowacki et al., 2011). However, this material is highly soluble in organic solvents, which makes certain measurements such as cyclic voltammetry challenging (Glowacki et al., 2011). Once dissolved it degrades with a reaction rate of 0.621 h^{-1} (Chen et al., 2014). The photo-to-electric conversion efficiency is very low when used in a dye sensitized solar cell (Suryana et al., 2013a). Eumelanins are a subclass of melanin which is found in skin pigment, which are natural semiconductors (Feig et al., 2018). Upon the absorption of water, a reaction occurs where free electrons and protons are released, self-doping the eumelanins. In 8 days, *in vivo* melanin implants can be nearly completely eroded and resorbed (Feig et al., 2018).

Instead of just considering naturally occurring biomolecules, it is interesting to look at their derivates to obtain organic semiconductors which are based on naturally occurring molecules as is reviewed by Glowacki et al. (2011). For example, indanthrene yellow G and indanthrene brilliant orange RK, are man-made pigments used in dyes that act as wide-bandgap semiconductors with high electron affinity. Other pigments can be derived from different sources to function as p-type electron donors like Quinacridone and Cibalakrot, with a larger bandgap (Glowacki et al., 2011). In 115 days, the conductivity of the former degraded to 80% of its original value (Daniel Głowacki et al., 2013). Gelatin is a conductive polymer obtained from collagen, of which the conductivity can be increased even further by combining it with conducting polymers such as Polyaniline (PANI) (Harrington and von Hippel, 1962; Li et al., 2006). Other biodegradable semiconductors which are neither natural nor nature-inspired include Poly(p-phenylene vinylene) (PPV), ambipolar polyselenophene, Buckminster fullerene, pentacene, and 5,50-bis-(7-dodecyl-9H-fluoren-2-yl)-2,20-bithiophene (DDFTTF).

Next to the biodegradable (semi) conducting materials, there is a much larger variety in isolating biomaterials that can be used as underlying substrates for the electronic circuitry, as described in Irimia-vladu et al. (2010b). The cheapest yet very familiar biodegradable substrate is paper. Despite its roughness, low-voltage active circuits can be realized on top of it using gravure and flexographic printing techniques. Hard gelatin capsules and caramelized glucose can be ingested and therefore used in bio-metabolizable electronics (Irimia-vladu et al., 2010b). Caramelized glucose is sensitive to moisture but has a smoothness close to that of glass. Poly(L-lactide-co-glycolide) (PLGA) are other sugar-based biopolymers obtained from pure L lactide, which can be used as substrate (Bettinger and Bao, 2010; Chanfreau et al., 2010). Though water can permeate through PLGA, which causes rapid failure (< 10 min) when they are used as encapsulation layer (Lee et al., 2017). Another familiar substrate is silk, a polypeptide polymer made up of fibroin and sericin, which have interchain hydrogen bonds, leading to the mechanical robustness of the silk fibers (Irimia-Vladu et al., 2012). Silk elicits no immune response and it safely dissolves and resorbs completely, making it safe to be implanted into the body. Furthermore, silk can be engineered to degrade under the desired conditions (Wang et al., 2008; Hu et al., 2011; Irimia-Vladu et al., 2012). A less common natural

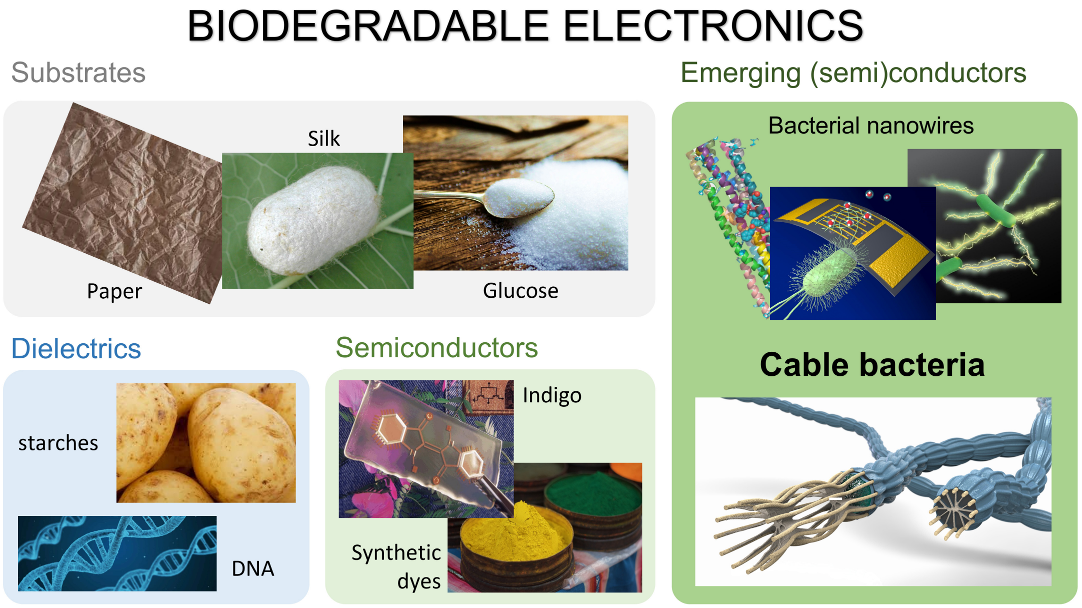

FIGURE 1 | Several biomaterials that have potential in biodegradable electronics, electroactive bacteria and in particular cable bacteria are interesting upcoming candidates.

TABLE 1 | An overview for different (semi) conducting materials and substrate materials for biodegradable electronics with their relevant characteristics measured in dry conditions. Bacterial nanowires stand out against the known biodegradable semiconductors for their high conductivity and mobility values. Cable bacteria top other nanowires for their excessive conduction length and n-type transistor behavior.

(Semi) Conducting materials

Material		Cond. length (nanowires)	Conductivity (S/cm)	Transistor properties	Mobility (cm^2/Vs)	References
Biodegradable semiconductor	Indigo		10^{-6}	n-type	0.01	Vautier et al., 2001; Bouzidi et al., 2017
	B-carotene		10^{-3}	p-type	0.0004	Suryana et al., 2013b
	Eumelanin		10^{-5}	n-type	0.01	Ambrico et al., 2011; di Mauro et al., 2021
	Quinacridone		10^{-4}	p-type	0.001	Inokuchi and Akamatu, 1961; Enengl et al., 2015
	Perylene diimide		10^{-1} (Doped, redox cond.)	n-type	0.01	Gregg and Cormier, 1998
Polymer nanowire	P3HT	10 µm	10 (Doped)	p-type	0.1	Briseno et al., 2008; Paterson et al., 2018
	PEDOT:PSS	10 µm	10	p-type	10	Groenendaal et al., 2000; Wei et al., 2013
Bacterial nanowire (wild type)	*Geobacter sulfurreducens*	10 µm	5	p-type	0.03	Reguera et al., 2005; Lampa-Pastirk et al., 2016
	Shewanella oneidensis	10 µm	1	p-type	0.1	El-Naggar et al., 2010; Leung et al., 2013
	Cable bacteria	1 cm	10	n-type	0.1	Meysman et al., 2019; Bonné et al., 2020

Substrate materials

Material	Dielectric constant	Breakdown field (MV/cm)	References
Paper (with oil)	2.3	0.3	Feng et al., 2020
Caramelized glucose	6.4	1.5	Irimia-vladu et al., 2010a
Silk	2.7	2.5	Townsend et al., 1997
Silk (treated)	4.6	4.0	Dickerson et al., 2013
Shellac	3.1	8	Irimia-Vladu et al., 2013
Ecoflex®	2.2	0.2	Siegenthaler et al., 2012b

polymeric material produced by insects is shellac, a natural polyester copolymer, which can also be synthetically produced in multiple different grades and shades that can easily be cast to produce substrate foils (Irimia-Vladu et al., 2012). Of the mentioned substrates, glucose silk and shellac have very good surface smoothness. However, in general, biodegradable substrates need a smoothing layer to allow the fabrication of electronic components on top of them (Irimia-vladu et al., 2010b). An example of a material used for such a layer is polydimethylsiloxane (PDMS), which binds specific regions of the circuit to the substrate and provides strain isolation (Kim et al., 2009). The substrates described here are summarized with their dielectric constants and breakdown fields in **Table 1**.

After looking at plant and animal based biodegradable organic substrates, one can look for substrates originating from microorganisms, an example of which is poly(4hydroxybutyrate) (P4HB), as described by Martin and Williams (2003) and Bettinger and Bao (2010). This material is produced by genetically engineered microorganisms, usually *Escherichia coli* K12, since it is very difficult to produce polymers fit for most applications through chemical synthesis (Martin and Williams, 2003). P4HB is strong, with a tensile strength comparable to high molecular weight polyethylene, yet flexible, with an elongation to break of 1,000% and is often extremely well tolerated *in vivo* (Martin and Williams, 2003). As for the semiconductors, there are biodegradable substrates which are neither naturally occurring nor nature inspired. For example, Ecoflex® is a completely biodegradable aliphatic-aromatic polyester which combines excellent mechanical properties, such as its tear-resistance, flexibility, and its resistance to fluctuations in water and humidity, with good processability of synthetic thermoplastics (Siegenthaler et al., 2012a). It is certified worldwide as compostable and approved for contact with food, however, this is only compostable in an industrial composter. A distinction is made between Ecoflex® F, based on fossil monomers, and Ecoflex® FS, a compound with poly(lactic acid) that has a higher rate of biodegradation. The material can also be blended with poly(lactic acid) (PLA), to obtain a blend called Ecovio.

Other materials crucial in the production of capacitors and advanced electrical components like Field-Effect Transistors (FETs) are dielectrics. These are electrical insulators which can be polarized by electric fields such as the previously mentioned biodegradable substrates, but also less sturdy materials. An abundant example is DNA, which can be obtained for example as waste material from the fishing industry and processed from water-based solutions (Irimia-Vladu et al., 2012). When DNA is used in an Organic Field-Effect Transistor (OFET), it displays significant hysteresis in the transfer characteristics, because of its high permittivity (Stadler et al., 2007). The separate nucleobases which compose DNA, adenine, cytosine, guanine, thymine, and uracil (which replaces thymine in RNA) could be used instead. These molecules are abundant and have low toxicity and cost (Irimia-vladu et al., 2010b). Another kind of biodegradable dielectric material are starches (Siegenthaler et al., 2012a). They consist of amylose and amylopectin polymers, forming a multilayer structure through hydrogen bonding. Starches obtained from different types of plants, such as corn or potato, differ, having an influence on the particle size and moisture absorption. Pure starch has multiple properties which makes it difficult to process and does not give it many applications. However, it is possible to chemically modify the starch to overcome these problems, though not enough to use it as substrate (Siegenthaler et al., 2012a). However, it can be used as such if the starch is blended with a hydrophobic polymer such as Ecoflex®.

ELECTROACTIVE BACTERIA FOR BIOELECTRONICS

In the last decades, other extraordinary electronic materials were found in the world of microbiology: electroactive bacteria that make their own conductive wires. These electroactive microbes developed the ability to respire through minerals or other organisms (Summers et al., 2010; Shi et al., 2016; Sure et al., 2016), either through electron shuttles or as direct contact through self-made nanowires that form an electrical bridge between the bacterium and the mineral. When studying these bacteria in a bioelectrochemical system (BES), they were found to also respire through electrodes. The chosen conditions of the BES, like available substrates and electric potential of the electrode, can be tuned to enhance the nanowire production (Liu and Li, 2020; Yalcin et al., 2020). These bacterial nanowires are found in many forms and debate is still going on about its exact function and chemical structure (Creasey et al., 2018). Below we give an overview of nanowires that were found to be electrically conductive after isolation, both in wet and dry environments (Ing et al., 2018).

One organism intensively studied for its protein nanowires is *Geobacter sulfurreducens* (Reguera et al., 2005). Nanowires are often found in the form of c-type cytochromes: a heme containing protein with a Fe atom at its core. The prominent example is a nanowire made of a coiling stack of the cytochrome OmcS that consists of 6 heme groups (Wang et al., 2019) with measured conductivities in the order of 5 mS cm^{-1} (Malvankar et al., 2011; Yalcin et al., 2020). Another cytochrome nanowire made from 8-heme OmcZ proteins even reaches conductivities that are 1,000-fold higher (Yalcin et al., 2020). Next to cytochrome nanowires, a nanowire based on PilA proteins (nicknamed e-pili) have been described in many works (Reguera et al., 2005). Although controversy persists, there is ample evidence of these nanowires conducting electricity with conductivities in the range of 50–200 mS cm^{-1}, respectively, for pH 7 and pH 2 (Adhikari et al., 2016). Another study found conductivities in the range of 1–5 S cm^{-1} with estimated mobilities in the range of 0.02 cm^2 V^{-1} s^{-1} (Lampa-Pastirk et al., 2016). In another well-studied organism called *Shewanella oneidensis,* nanowires are found in the form of extensions of the outer membrane (Gorby et al., 2006; Pirbadian et al., 2014) that are packed with 20-heme protein complexes made of MtrA, MtrB, MtrC and OmcA cytochromes. These nanowires reach values of up to 1 S cm^{-1} (El-Naggar et al., 2010) and appear to have p-type transistor behavior with mobility values in the range of 0.1 cm^2 V^{-1} s^{-1} (Leung et al., 2013). Besides these organisms a whole zoo of over 100 different electroactive bacteria (Logan et al., 2019) and their nanowires are either confirmed to have similar properties (Walker et al., 2018, 2019) or are waiting to be tested for their electronic potential.

Even though we can find some very good electrical characteristics for these nanowires, modifications to the wild-type nanowires can boost the conductivity values even further. The introduction of the *PilA* gene from *Geobacter metallireducens* in *G. sulfurreducens*, e.g., produces e-pili with conductivities in the order of 300 S cm^{-1} (Tan et al., 2017), while the inclusion of more aromatic rings like tryptophan in e-pili increased the conductivities to 100 S cm^{-1} at pH 7 and 1,000 S cm^{-1} at pH 2 (Tan et al., 2016). When thinking about applying these bacterial nanowires in biodegradable electronics, one might assume an intensive and costly process, but the recent discovery of nanowire production through genetic manipulation of *Escherichia coli* (Ueki et al., 2020) and the development of bottom-up fabrication of e-pili (Cosert et al., 2019) suggest a means of easier and cheaper production in the long term. Functionalization and adhesion of different substrates is also made easier with the possibility of decorating nanowires with peptides (Ueki et al., 2019). First proof-of-principle applications are developed as sensors (Smith et al., 2020), (limited) electricity production (Liu et al., 2020) and they are expected to play a role as conductors in bioelectronics (Lovley and Yao, 2021).

A SPECIAL CASE: CABLE BACTERIA FOR BIODEGRADABLE ELECTRONICS

The main drawback for bacterial nanowires is the relatively short range of conduction, as they were only constructed over micrometer distances for now (Ing et al., 2018). Ten years ago, a new bacterium with the ability of transporting electrons over centimeter distances was discovered in the sea sediment: Cable bacteria (Pfeffer et al., 2012). They developed this mechanism to reach for both H_2S in the deeper layer of the sediment and the O_2 that is only available at the surface. Coupling the redox reactions of sulfide oxidation and oxygen reduction (Nielsen et al., 2010), it was hypothesized that cable bacteria could transport electrical currents over their centimeter long bodies (Pfeffer et al., 2012). This hypothesis appeared true when Meysman et al. (2019) measured conduction through dry filaments of cable bacteria and found it to be highly conductive with conductivities ranging in the order of 0.01–10 S cm^{-1}, with one measurement even reaching 79 S cm^{-1}. The current was shown to be flowing in an organized structure of around 10–60 parallel wires of each 50 nm in diameter that are present just under the outer membrane of the bacterium (Cornelissen et al., 2018) and that are interconnected at cell junctions (Thiruvallur Eachambadi et al., 2020).

The results presented in previous works show cable bacteria can overcome the micrometer range conduction previously present in electromicrobiology, as conduction has been shown over more than 1 cm, thereby proving by far the longest electron transport in a single biological structure (Meysman et al., 2019). One use of the conductive fibers in cable bacteria could be as an interconnector in a circuit, as they show low contact resistance (Bonné et al., 2020) and conductivities exceeding 10 S cm^{-1} (Meysman et al., 2019). The typical currents found *in vivo* are in the order of 0.1–1 nA for a single filament (Pfeffer et al., 2012; Schauer et al., 2014), but measurements on the conductive fiber sheaths show that single filaments can bear currents up to 0.3 μA at a DC bias of 1V (Bonné et al., 2020), and even higher values could be expected. This corresponds with a current density of 3 A mm^{-2}, comparable to the typical allowed density in household copper wires (5–20 A mm^{-2}). Next to its interconnection properties, it was shown that cable bacteria could work as transistors with FET mobilities in the range of 0.1 cm^2 V^{-1} s^{-1} (Bonné et al., 2020), giving them a potential role in future computational circuits. Finally, next to direct current (DC), alternating current (AC) signals have been shown to pass through cable bacteria (Bonné et al., 2020). Showing visible degradation after 9–30 days in its near-natural environment during which time it has been exposed to mainly (micro-) oxic conditions (**Supplementary Figure 1**), this suggests that cable bacterium could be an interesting biodegradable material for bioelectronics.

To put the values found for cable bacteria in perspective, in **Table 1** their initial electronic properties are compared to the previously discussed biodegradable semiconductors. Conductivity, mobility, and transistor properties for these materials were obtained by dry solid-state measurements like current-voltage-analysis, atomic force microscopy and field-effect transistor measurements (doped perylene diimide, treated in an electrochemical setup, being the only exception). It is clear that cable bacteria stand out with their high mobility values and conductivities that are a few orders of magnitude larger. Next to that, **Table 1** also shows the state-of-the-art characteristics of the model (wild type) microbial nanowires of *G. sulfurreducens* and *S. oneidensis* and well-studied organic nanowires P3HT and PEDOT:PSS, also resulting from dry solid state measurements. It is apparent that already after a few years of measurements, cable bacteria can easily compete with materials that are studied for one or a few decades. Conductivity and mobility values of cable bacteria fibers can be found in the same range as organic electronics and wild type nanowires, with PEDOT:PSS outrunning alternatives in terms of mobility. However, cable bacteria really stand out for their n-type transistor behavior that is uncommon for biological materials and even more for the conduction length that is a few orders of magnitude higher than typical lengths for other biological and organic nanowires.

CONCLUSION, CHALLENGES, AND OUTLOOK

The increasing amount of e-waste that is created worldwide has put an urge on the search for biodegradable electronics. In the mini-review presented in this work, we found that important progress was made in finding more sustainable materials in electronics, but their limited applicability in modern day devices shows they have a long way to go. An important element missing in most studies so far is a common and quantitative study on the rate and conditions of biodegradability of the different materials, which is crucial for their further investigation as bioelectronic materials. In the search for biological materials that could function as conductors or transistors in biodegradable electronics, interesting candidates are found in the world of electromicrobiology (Lovley, 2012), where electroactive bacteria like *Geobacter* and *Shewanella* species produce nanowires as electron transport conduits. Recent progress in the study of different proteins (Yalcin et al., 2020) and genetic manipulation has ramped up the conductivity values (Tan et al., 2016, 2017); modification of *Escherichia coli* has made PilA based nanowires easy to produce (Ueki et al., 2020). Yet, conduction lengths exceeding micrometers are yet to be shown, as well as the implementation in biodegradable electronic circuitry. An answer to this shortcoming might be cable bacteria that create nanowire networks that show electron transport over centimeters with high conductivities and electron mobility values.

Although the characteristics in **Table 1** seem promising, research on cable bacteria is only in a young stage, and some limitations must be overcome to meet industrial requirements. Firstly, values for the conductivity can vary a few orders of magnitude among experiments, with **Table 1** only displaying the order or magnitude of the highest measured values. This might be because all measurements were done on different species of cable bacteria taken from natural sediments that come from different field sites (Kjeldsen et al., 2019) and the variability found among cells within one organism (Bonné et al., 2020). Moreover, the measurement conditions were different for all filaments. As current through a bacterium decays exponentially in ambient air, a sample preparation time that takes 1 min longer (before placing the sample in a nitrogen environment or vacuum) might change the conductivity by a factor of 2. Although the true conductivity of the conductive fibers in cable bacteria is expected to be close to and possibly higher than the maximally reported value of 79 S cm^{-1}, a more consistent set of values of the electronic properties is needed for the different species of cable bacteria. As a second limitation, all species of cable bacteria lack a pure culture so far, making upscaling difficult. Although some attempts have been made toward it, only a single-strain sediment culture was achieved until this point (Thorup et al., 2021). Finally, the conductive periplasmic fibers are yet to be extracted properly from cable bacteria, as it is expected that the pure fibers rather than the full filaments will be used in future electronics (Cosert et al., 2019). An easy and cheap method must be developed to either fully extract the fibers or produce them in a laboratory environment. It has to be emphasized that the chemical nature of the conductive fibers in cable bacteria is not yet discovered (Kjeldsen et al., 2019; Boschker et al., 2021; Thiruvallur Eachambadi et al., 2021), making it difficult to describe the electron transport mechanism, quantify the biodegradability of the material, and create a detailed forecast of the applicability in bioelectronics.

As a general conclusion, it can be stated that significant progress is being made toward biodegradable electronics, in terms of the usage and development of biomaterials and electroactive bacteria. Within the class of electroactive bacteria, cable bacteria show some very interesting features that could make them a potential long-range biodegradable interconnector or transistor in future durable electronics. Although the research field needs to overcome a few challenges before being able to get scaled up, the bacteria were only discovered 10 years ago and only in 2019 the first direct electrical measurements were made. If this blooming trend continues as it did for bacterial nanowires (Lovley and Walker, 2019), the road is open for cable bacteria fibers or cable bacteria inspired materials to be integrated together with a variety of complementary biomaterials and electroactive bacteria in our electronics in another 10 years from now. This new generation of electronics—being biodegradable—will dissolve in time together with the global e-waste problem.

AUTHOR CONTRIBUTIONS

JM conceived the study. RB and KW wrote the manuscript with equal contribution. JL made **Supplementary Figure 1**. All authors did editing and proofreading.

FUNDING

This research was financially supported by the Research Foundation-Flanders (FWO project grant G013922N to JM) and Danish National Research Foundation (grant DNRF136 to JL).

ACKNOWLEDGMENTS

We thank the colleagues from X-LAB and PHYSXLAB from Hasselt University and for discussions.

SUPPLEMENTARY MATERIAL

The Supplementary Material for this article can be found online at: https://www.frontiersin.org/articles/10.3389/fmicb.2022.906363/full#supplementary-material

REFERENCES

Adhikari, R. Y., Malvankar, N. S., Tuominen, M. T., and Lovley, D. R. (2016). Conductivity of individual Geobacter pili. *RSC Adv.* 6, 8354–8357. doi: 10.1039/c5ra28092c

Ambrico, M., Ambrico, P. F., Cardone, A., Ligonzo, T., Cicco, S. R., di Mundo, R., et al. (2011). Melanin layer on silicon: An attractive structure for a possible exploitation in bio-polymer based metal-insulator-silicon devices. *Adv. Mat.* 23, 3332–3336. doi: 10.1002/ADMA.201101358

Beratan, D. N. (2019). Why Are DNA and Protein Electron Transfer So Different? *Ann. Rev. Phys. Chem.* 70, 71–97. doi: 10.1146/annurev-physchem-042018-052353

Bettinger, C. J., and Bao, Z. (2010). Organic thin-film transistors fabricated on resorbable biomaterial substrates. *Adv. Mat.* 22, 651–655. doi: 10.1002/adma.200902322

Bonné, R., Hou, J. L., Hustings, J., Wouters, K., Meert, M., Hidalgo-Martinez, S., et al. (2020). Intrinsic electrical properties of cable bacteria reveal an Arrhenius temperature dependence. *Sci. Rep.* 1:19798. doi: 10.1038/s41598-020-76671-5

Boschker, H. T. S., Cook, P. L. M., Polerecky, L., Eachambadi, R. T., Lozano, H., Hidalgo-Martinez, S., et al. (2021). Efficient long-range conduction in cable bacteria through nickel protein wires. *Nat. Commun.* 12:3996. doi: 10.1038/s41467-021-24312-4

Bouzidi, A., Yahia, I. S., and El-Sadek, M. S. A. (2017). Novel and highly stable indigo (C.I. Vat Blue I) organic semiconductor dye: Crystal structure, optically diffused reflectance and the electrical conductivity/dielectric behaviors. *Dyes Pigments* 146, 66–72. doi: 10.1016/J.DYEPIG.2017.06.046

Briseno, A. L., Mannsfeld, S. C. B., Jenekhe, S. A., Bao, Z., and Xia, Y. (2008). Introducing organic nanowire transistors. *Materials Today* 11, 38–47. doi: 10.1016/S1369-7021(08)70055-5

Campos, R., Kandelbauer, A., Robra, K. H., Cavaco-Paulo, A., and Gübitz, G. M. (2001). Indigo degradation with purified laccases from Trametes hirsuta and Sclerotium rolfsii. *J. Biotechnol.* 89 131-9. doi: 10.1016/S0168-1656(01)00303-0

Chanfreau, S., Mena, M., Porras-Domínguez, J. R., Ramírez-Gilly, M., Gimeno, M., Roquero, P., et al. (2010). Enzymatic synthesis of poly-L-lactide and poly-L-lactide-co-glycolide in an ionic liquid. *Bioproc. Biosyst. Eng.* 33, 629–638. doi: 10.1007/s00449-009-0388-8

Chen, L., Bai, G., Yang, R., Zang, J., Zhou, T., and Zhao, G. (2014). Encapsulation of β-carotene within ferritin nanocages greatly increases its water-solubility and thermal stability. *Food Chem.* 149, 307–312. doi: 10.1016/J.FOODCHEM.2013.10.115

Cornelissen, R., Bøggild, A., Thiruvallur Eachambadi, R., Koning, R. I., Kremer, A., Hidalgo-Martinez, S., et al. (2018). The Cell Envelope Structure of Cable Bacteria. *Front. Microbiol.* 9:3044. doi: 10.3389/fmicb.2018.03044

Cosert, K. M., Castro-Forero, A., Steidl, R. J., Worden, R. M., and Reguera, G. (2019). Bottom-up fabrication of protein nanowires *via* controlled self-assembly of recombinant Geobacter pilins. *mBio* 10:e02721–19 doi: 10.1128/mBio.02721-19

Creasey, R. C. G., Mostert, A. B., Nguyen, T. A. H., Virdis, B., Freguia, S., and Laycock, B. (2018). Microbial nanowires – Electron transport and the role of synthetic analogues. *Acta Biomat.* 69, 1–30. doi: 10.1016/j.actbio.2018.01.007

Daniel Głowacki, E., Irimia-Vladu, M., Kaltenbrunner, M., Ga, J., White, M. S., Monkowius, U., et al. (2013). Hydrogen-Bonded Semiconducting Pigments for Air-Stable Field-Effect Transistors. *Adv. Materials* 25, 1563–1569. doi: 10.1002/ADMA.201204039

di Mauro, E., Rho, D., and Santato, C. (2021). Biodegradation of bio-sourced and synthetic organic electronic materials towards green organic electronics. *Nat. Commun.* 1:3167. doi: 10.1038/s41467-021-23227-4

Dickerson, M. B., Fillery, S. P., Koerner, H., Singh, K. M., Martinick, K., Drummy, L. F., et al. (2013). Dielectric breakdown strength of regenerated silk fibroin films as a function of protein conformation. *Biomacromolecules* 14, 3509–3514. doi: 10.1021/BM4008452

El-Naggar, M. Y., Wanger, G., Leung, K. M., Yuzvinsky, T. D., Southam, G., Yang, J., et al. (2010). Electrical transport along bacterial nanowires from Shewanella oneidensis MR-1. *Proc. Natl. Acad. Sci.* 107, 18127–18131. doi: 10.1073/pnas.1004880107

Enengl, C., Enengl, S., Havlicek, M., Stadler, P., Glowacki, E. D., Scharber, M. C., et al. (2015). The Role of Heteroatoms Leading to Hydrogen Bonds in View of Extended Chemical Stability of Organic Semiconductors. *Adv. Funct. Mat.* 25, 6679–6688. doi: 10.1002/ADFM.201503241

Feig, V. R., Tran, H., and Bao, Z. (2018). Biodegradable Polymeric Materials in Degradable Electronic Devices. *ACS Central Sci.* 4, 337–348. doi: 10.1021/acscentsci.7b00595

Feng, D., Hao, J., Yang, L., Liao, R., Chen, X., and Li, J. (2020). Comparison of AC breakdown characteristics on insulation paper (pressboard) immersed by three-element mixed insulation oil and mineral oil. *High Volt.* 5, 298–305. doi: 10.1049/HVE.2019.0103

Glowacki, E. D., Leonat, L., Voss, G., Bodea, M., Bozkurt, Z., Irimia-Vladu, M., et al. (2011). Natural and nature-inspired semiconductors for organic electronics. *Organic Semiconductors in Sensors and Bioelectronics IV* (Bellingham:SPIE) M1–M81180. doi: 10.1117/12.892467

Gorby, Y. A., Yanina, S., McLean, J. S., Rosso, K. M., Moyles, D., Dohnalkova, A., et al. (2006). Electrically conductive bacterial nanowires produced by Shewanella oneidensis strain MR-1 and other microorganisms. *Proc. Natl. Acad. Sci. U.S.A.* 103, 11358–11363. doi: 10.1073/pnas.0604517103

Grant, K., Goldizen, F. C., Sly, P. D., Brune, M. N., Neira, M., van den Berg, M., et al. (2013). Health consequences of exposure to e-waste: A systematic review. *Lancet Glob. Health* 1, e350–e361. doi: 10.1016/S2214-109X(13)70101-3

Gregg, B. A., and Cormier, R. A. (1998). Liquid Crystal Perylene Diimide Films Characterized by Electrochemical, Spectroelectrochemical, and Conductivity versus Potential Measurements. *J. Phys. Chem. B* 102, 9952–9957. doi: 10.1021/JP982842E

Groenendaal, L., Jonas, F., Freitag, D., Pielartzik, H., and Reynolds, J. R. (2000). Poly(3,4-ethylenedioxythiophene) and Its Derivatives: Past, Present, and Future. *Adv. Mat.* 12, 481–494. doi: 10.1002/(SICI)1521-4095(200004)12:7<481::AID-ADMA481<3.0.CO;2-C

Harrington, W. F., and von Hippel, P. H. (1962). The Structure Of Collagen And Gelatin. *Adv. Protein Chem.* 16, 1–138. doi: 10.1016/S0065-3233(08)60028-5

Hu, X., Shmelev, K., Sun, L., Gil, E. S., Park, S. H., Cebe, P., et al. (2011). Regulation of silk material structure by temperature-controlled water vapor annealing. *Biomacromolecules* 12, 1686–1696. doi: 10.1021/bm200062a

Hwang, S.-W., Tao, H., Kim, D.-H., Cheng, H., Song, J.-K., Rill, E., et al. (2012). A Physically Transient Form of Silicon Electronics. *Science* 337, 1640–1644. doi: 10.1126/science.1226325

Ing, N. L., El-Naggar, M. Y., and Hochbaum, A. I. (2018). Going the Distance: Long-Range Conductivity in Protein and Peptide Bioelectronic Materials. *J. Phys. Chem. B* 122, 10403–10423. doi: 10.1021/acs.jpcb.8b07431

Inokuchi, H., and Akamatu, H. (1961). Electrical Conductivity of Organic Semiconductors. *Solid State Phys.Adv. Res. Appl.* 12, 93–148. doi: 10.1016/S0081-1947(08)60653-0

Irimia-vladu, B. M., Troshin, P. A., Reisinger, M., Shmygleva, L., Kanbur, Y., Schwabegger, G., et al. (2010a). Biocompatible and Biodegradable Materials for Organic Field-Effect Transistors. 4069–4076. doi: 10.1002/adfm.201001031

Irimia-vladu, M., Troshin, P. A., Reisinger, M., Schwabegger, G., Ullah, M., Schwoediauer, R., et al. (2010b). Environmentally sustainable organic field effect transistors. *Organic Elect.* 11, 1974–1990. doi: 10.1016/j.orgel.2010.09.007

Irimia-Vladu, M., Głowacki, E. D., Schwabegger, G., Leonat, L., Akpinar, H. Z., Sitter, H., et al. (2013). Natural resin shellac as a substrate and a dielectric layer for organic field-effect transistors. *Green Chem.* 15, 1473–1476. doi: 10.1039/C3GC40388B

Irimia-Vladu, M., Głowacki, E. D., Voss, G., Bauer, S., and Sariciftci, N. S. (2012). Green and biodegradable electronics. *Materials Today* 15, 340–346. doi: 10.1016/S1369-7021(12)70139-6

Kang, S. K., Hwang, S. W., Cheng, H., Yu, S., Kim, B. H., Kim, J. H., et al. (2014). Dissolution behaviors and applications of silicon oxides and nitrides in transient electronics. *Adv. Funct. Materials* 24, 4427–4434. doi: 10.1002/adfm.201304293

Kang, S. K., Yin, L., and Bettinger, C. (2020). The emergence of transient electronic devices. *MRS Bull.* 45, 87–95. doi: 10.1557/mrs.2020.19

Kim, D. H., Kim, Y. S., Wu, J., Liu, Z., Song, J., Kim, H. S., et al. (2009). Ultrathin silicon circuits with strain-isolation layers and mesh layouts for high-performance electronics on fabric, vinyl, leather, and paper. *Adv. Materials* 21, 3703–3707. doi: 10.1002/adma.200900405

Kjeldsen, K. U., Schreiber, L., Thorup, C. A., Boesen, T., Bjerg, J. T., Yang, T., et al. (2019). On the evolution and physiology of cable bacteria. *Proc. Natl. Acad. Sci.* 116:201903514. doi: 10.1073/pnas.1903514116

Lampa-Pastirk, S., Veazey, J. P., Walsh, K. A., Feliciano, G. T., Steidl, R. J., Tessmer, S. H., et al. (2016). Thermally activated charge transport in microbial protein nanowires. *Sci. Rep.* 6:23517. doi: 10.1038/srep23517

Lee, Y. K., Yu, K. J., Song, E., Barati Farimani, A., Vitale, F., Xie, Z., et al. (2017). Dissolution of Monocrystalline Silicon Nanomembranes and Their Use as Encapsulation Layers and Electrical Interfaces in Water-Soluble Electronics. *ACS Nano* 11, 12562–12572. doi: 10.1021/acsnano.7b06697

Leung, K. M., Wanger, G., El-Naggar, M. Y., Gorby, Y., Southam, G., Lau, W. M., et al. (2013). Shewanella oneidensis MR-1 Bacterial Nanowires Exhibit p-Type, Tunable Electronic Behavior. *Nano Lett.* 13, 2407–2411. doi: 10.1021/nl400237p

Li, M., Guo, Y., Wei, Y., MacDiarmid, A. G., and Lelkes, P. I. (2006). Electrospinning polyaniline-contained gelatin nanofibers for tissue engineering applications. *Biomaterials* 27, 2705–2715. doi: 10.1016/J.BIOMATERIALS.2005.11.037

Liu, D. F., and Li, W. W. (2020). Potential-dependent extracellular electron transfer pathways of exoelectrogens. *Curr. Opin. Chem. Biol.* 59, 140–146. doi: 10.1016/J.CBPA.2020.06.005

Liu, X., Gao, H., Ward, J. E., Liu, X., Yin, B., Fu, T., et al. (2020). Power generation from ambient humidity using protein nanowires. *Nature* 578, 550–554. doi: 10.1038/s41586-020-2010-9

Logan, B. E., Rossi, R., Ragab, A., and Saikaly, P. E. (2019). Electroactive microorganisms in bioelectrochemical systems. *Nat. Rev. Microbiol.* 17, 307–319. doi: 10.1038/s41579-019-0173-x

Lovley, D. R. (2012). Electromicrobiology. *Annu. Rev. Microbiol.* 66, 391–409 doi: 10.1146/annurev-micro-092611-150104

Lovley, D. R., and Walker, D. J. F. (2019). Geobacter Protein Nanowires. *Front. Microbiol.* 10:2078. doi: 10.3389/fmicb.2019.02078

Lovley, D. R., and Yao, J. (2021). Intrinsically Conductive Microbial Nanowires for 'Green' Electronics with Novel Functions. *Trends Biotechnol.* 39, 940–952. doi: 10.1016/J.TIBTECH.2020.12.005

Malvankar, N. S., Vargas, M., Nevin, K. P., Franks, A. E., Leang, C., Kim, B. C., et al. (2011). Tunable metallic-like conductivity in microbial nanowire networks. *Nat. Nanotechnol.* 6, 573–579. doi: 10.1038/nnano.2011.119

Martin, D. P., and Williams, S. F. (2003). Medical applications of poly-4-hydroxybutyrate: A strong flexible absorbable biomaterial. *Biochem. Eng. J.* 16, 97–105. doi: 10.1016/S1369-703X(03)00040-8

Meysman, F. J. R., Cornelissen, R., Trashin, S., Bonné, R., Hidalgo-Martinez, S., van der Veen, J., et al. (2019). A highly conductive fibre network enables centimetre-scale electron transport in multicellular cable bacteria. *Nat. Commun.* 10:4120. doi: 10.1038/s41467-019-12115-7

Nielsen, L. P., Risgaard-Petersen, N., Fossing, H., Christensen, P. B., and Sayama, M. (2010). Electric currents couple spatially separated biogeochemical processes in marine sediment. *Nature* 463, 1071–1074. doi: 10.1038/nature08790

Paterson, A. F., Singh, S., Fallon, K. J., Hodsden, T., Han, Y., Schroeder, B. C., et al. (2018). Recent Progress in High-Mobility Organic Transistors: A Reality Check. *Adv. Materials* 30:e1801079. doi: 10.1002/adma.201801079

Pfeffer, C., Larsen, S., Song, J., Dong, M., Besenbacher, F., Meyer, R. L., et al. (2012). Filamentous bacteria transport electrons over centimetre distances. *Nature* 491, 218–221. doi: 10.1038/nature11586

Pirbadian, S., Barchinger, S. E., Leung, K. M., Byun, H. S., Jangir, Y., Bouhenni, R. A., et al. (2014). Shewanella oneidensis MR-1 nanowires are outer membrane and periplasmic extensions of the extracellular electron transport components. *Proc. Natl. Acad. Sci. U.S.A.* 111, 12883–12888. doi: 10.1073/pnas.1410551111

Prado, A. G. S., Bolzon, L. B., Pedroso, C. P., Moura, A. O., and Costa, L. L. (2008). Nb2O5 as efficient and recyclable photocatalyst for indigo carmine degradation. *Appl. Catalysis B* 82, 219–224. doi: 10.1016/j.apcatb.2008.01.024

Reguera, G., McCarthy, K. D., Mehta, T., Nicoll, J. S., Tuominen, M. T., and Lovley, D. R. (2005). Extracellular electron transfer *via* microbial nanowires. *Nature* 435, 1098–1101. doi: 10.1038/nature03661

Ryder, G., and Zhao Houlin, H. (2019). *The world's e-waste is a huge problem. It's also a golden opportunity. World Economic Forum Annual Meeting*. Available online at : https://www.weforum.org/agenda/2019/01/how-a-circular-approach-can-turn-e-waste-into-a-golden-opportunity/. (Accessed on Feb 8 2021)

Schauer, R., Risgaard-Petersen, N., Kjeldsen, K. U., Tataru Bjerg, J. J., Jørgensen, B., Schramm, A., et al. (2014). Succession of cable bacteria and electric currents in marine sediment. *ISME J.* 8, 1314–1322. doi: 10.1038/ismej.2013.239

Seidel, H., Csepregi, L., Heuberger, A., and Baumgärtel, H. (1990). Anisotropic Etching of Crystalline Silicon in Alkaline Solutions: II . Influence of Dopants. *J.Electrochem. Soc.* 137, 3626–3632. doi: 10.1149/1.2086278

Sekitani, T., Yokota, T., Zschieschang, U., Klauk, H., Bauer, S., Takeuchi, K., et al. (2009). Organic nonvolatile memory transistors for flexible sensor arrays. *Science* 326, 1516–1519. doi: 10.1126/science.1179963

Shi, L., Dong, H., Reguera, G., Beyenal, H., Lu, A., Liu, J., et al. (2016). Extracellular electron transfer mechanisms between microorganisms and minerals. *Nat. Rev. Microbiol.* 10, 651–662. doi: 10.1038/nrmicro.2016.93

Siegenthaler, K. O., Künkel, A., Skupin, G., and Yamamoto, M. (2012a). Ecoflex® and ecovio®: Biodegradable, performance-enabling plastics. *Adv. Polymer Sci.* 245, 91–136. doi: 10.1007/12-2010-106

Siegenthaler, K. O., Künkel, A., Skupin, G., and Yamamoto, M. (2012b). Ecoflex® and ecovio®: Biodegradable, performance-enabling plastics. *Adv. Polymer Sci.* 245, 91–136.

Smith, A. F., Liu, X., Woodard, T. L., Fu, T., Emrick, T., Jiménez, J. M., et al. (2020). Bioelectronic protein nanowire sensors for ammonia detection. *Nano Res.* 5, 1479–1484. doi: 10.1007/S12274-020-2825-6

Stadler, P., Oppelt, K., Singh, T. B., Grote, J. G., Schwödiauer, R., Bauer, S., et al. (2007). Organic field-effect transistors and memory elements using deoxyribonucleic acid (DNA) gate dielectric. *Organic Elect.* 8, 648–654. doi: 10.1016/j.orgel.2007.05.003

Summers, Z. M., Fogarty, H. E., Leang, C., Franks, A. E., Malvankar, N. S., and Lovley, D. R. (2010). Direct exchange of electrons within aggregates of an evolved syntrophic coculture of anaerobic bacteria. *Science* 330, 1413–1415. doi: 10.1126/SCIENCE.1196526

Sure, S., Ackland, M. L., Torriero, A. A. J., Adholeya, A., and Kochar, M. (2016). Microbial nanowires: An electrifying tale. *Microbiology* 162, 2017–2028. doi: 10.1099/mic.0.000382

Suryana, R., Khoiruddin, and Supriyanto, A. (2013a). Beta-carotene dye of daucus carota as sensitizer on dye-sensitized solar cell. *Materials Sci. Forum* 737, 15–19. doi: 10.4028/www.scientific.net/MSF.737.15

Suryana, R., Khoiruddin, and Supriyanto, A. (2013b). Beta-carotene dye of daucus carota as sensitizer on dye-sensitized solar cell. *Materials Sci. Forum* 737, 15–19. doi: 10.4028/WWW.SCIENTIFIC.NET/MSF.737.15

Tan, Y., Adhikari, R. Y., Malvankar, N. S., Pi, S., Ward, J. E., Woodard, T. L., et al. (2016). Synthetic Biological Protein Nanowires with High Conductivity. *Small* 12, 4481–4485. doi: 10.1002/smll.201601112

Tan, Y., Adhikari, R. Y., Malvankar, N. S., War, J. E., Woodard, T. L., Nevin, K. P., et al. (2017). Expressing the geobacter metallireducens pila in geobacter sulfurreducens yields pili with exceptional conductivity. *mBio* 8, e02203–16. doi: 10.1128/mBio.02203-16

Thiruvallur Eachambadi, R., Bonné, R., Cornelissen, R., Hidalgo-Martinez, S., Vangronsveld, J., Meysman, F. J. R., et al. (2020). An Ordered and Fail-Safe Electrical Network in Cable Bacteria. *Adv. Biosyst.*4:2000006. doi: 10.1002/adbi.202000006

Thiruvallur Eachambadi, R., Boschker, H. T. S., Franquet, A., Spampinato, V., Hidalgo-Martinez, S., Valcke, R., et al. (2021). Enhanced Laterally Resolved ToF-SIMS and AFM Imaging of the Electrically Conductive Structures in Cable Bacteria. *Analytical Chem.* 93, 7226–7234. doi: 10.1021/ACS.ANALCHEM.1C00298

Thorup, C., Petro, C., Bøggild, A., Ebsen, T. S., Brokjær, S., Nielsen, L. P., et al. (2021). How to grow your cable bacteria: Establishment of a stable single-strain culture in sediment and proposal of Candidatus Electronema aureum GS. *Syst. Appl. Microbiol.* 44:126236. doi: 10.1016/J.SYAPM.2021.126236

Townsend, P. H., Martin, S. J., Godschalx, J., Romer, D. R., Smith, D. W., Castillo, D., et al. (1997). Silk Polymer Coating with Low Dielectric Constant and High Thermal Stability for Ulsi Interlayer Dielectric. *MRS Online Proc. Library* 1, 9–17. doi: 10.1557/PROC-476-9

Ueki, T., Walker, D. J. F., Tremblay, P. L., Nevin, K. P., Ward, J. E., Woodard, T. L., et al. (2019). Decorating the Outer Surface of Microbially Produced Protein Nanowires with Peptides. *ACS Synthetic Biol.* 8, 1809–1817. doi: 10.1021/ACSSYNBIO.9B00131/SUPPL_FILE/SB9B00131_SI_001.PDF

Ueki, T., Walker, D. J. F., Woodard, T. L., Nevin, K. P., Nonnenmann, S. S., and Lovley, D. R. (2020). An *Escherichia coli* Chassis for Production of Electrically Conductive Protein Nanowires. *ACS Synthetic Biol.* 9, 647–654. doi: 10.1021/ACSSYNBIO.9B00506/SUPPL_FILE/SB9B00506_SI_001.PDF

Valdez-Vazquez, I., Robledo-Rizo, J. G., Muñoz-Páez, K. M., Pérez-Rangel, M., and de la Luz Ruiz-Aguilar, G. M. (2020). Simultaneous hydrogen production and decolorization of denim textile wastewater: kinetics of decolorizing of indigo dye by bacterial and fungal strains. *Braz. J. Microbiol.* 51, 701–709. doi: 10.1007/s42770-019-00157-4

Vautier, M., Guillard, C., and Herrmann, J. M. (2001). Photocatalytic Degradation of Dyes in Water: Case Study of Indigo and of Indigo Carmine. *J. Catalysis* 201, 46–59. doi: 10.1006/JCAT.2001.3232

Walker, D. J., Adhikari, R. Y., Holmes, D. E., Ward, J. E., Woodard, T. L., Nevin, K. P., et al. (2018). Electrically conductive pili from pilin genes of phylogenetically diverse microorganisms. *ISME J.* 12, 48–58. doi: 10.1038/ismej.2017.141

Walker, D. J. F., Martz, E., Holmes, D. E., Zhou, Z., Nonnenmann, S. S., and Lovley, D. R. (2019). The archaellum of methanospirillum hungatei is electrically conductive. *mBio* 10, e00579–19. doi: 10.1128/mBio.00579-19

Wang, F., Gu, Y., O'Brien, J. P., Yi, S. M., Yalcin, S. E., Srikanth, V., et al. (2019). Structure of Microbial Nanowires Reveals Stacked Hemes that Transport Electrons over Micrometers. *Cell* 177, 361.e–369.e. doi: 10.1016/j.cell.2019.03.029

Wang, Y., Rudym, D. D., Walsh, A., Abrahamsen, L., Kim, H. J., Kim, H. S., et al. (2008). *In vivo* degradation of three-dimensional silk fibroin scaffolds. *Biomaterials* 29, 3415–3428. doi: 10.1016/j.biomaterials.2008.05.002

Wei, Q., Mukaida, M., Naitoh, Y., and Ishida, T. (2013). Morphological Change and Mobility Enhancement in PEDOT:PSS by Adding Co-solvents. *Adv. Materials* 25, 2831–2836. doi: 10.1002/adma.201205158

Yalcin, S. E., O'Brien, J. P., Gu, Y., Reiss, K., Yi, S. M., Jain, R., et al. (2020). Electric field stimulates production of highly conductive microbial OmcZ nanowires. *Nat. Chem. Biol.*10, 1136–1142. doi: 10.1038/s41589-020-0623-9

Zollinger, H. (2003). Color Chemistry Syntheses, Properties, and Applications of Organic Dyes and Pigments: Von H. Zollinger; Weinheim, Basel, Cambridge, New York, VCH Verlagsgesellschaft, 1987; XII, 367 Seiten mit 40 Bildern und 16 Tabellen; Format 17 cm × 24 cm, Pappband DM. 3rd revise. Zeitschrift fü Chemie 29, 259–268. doi: 10.1002/zfch.19890291016

Conflict of Interest: The authors declare that the research was conducted in the absence of any commercial or financial relationships that could be construed as a potential conflict of interest.

frontiers | Frontiers in Microbiology

ORIGINAL RESEARCH
published: 10 June 2022
doi: 10.3389/fmicb.2022.909824

Genome-Scale Mutational Analysis of Cathode-Oxidizing *Thioclava electrotropha* ElOx9^T

Joshua D. Sackett*[1]*, *Nitin Kamble*[1], *Edmund Leach*[1], *Taruna Schuelke*[2], *Elizabeth Wilbanks*[2] and *Annette R. Rowe*[1]

[1] Department of Biological Sciences, University of Cincinnati, Cincinnati, OH, United States, [2] Department of Ecology, Evolution, and Marine Biology, University of California, Santa Barbara, Santa Barbara, CA, United States

Extracellular electron transfer (EET) – the process by which microorganisms transfer electrons across their membrane(s) to/from solid-phase materials – has implications for a wide range of biogeochemically important processes in marine environments. Though EET is thought to play an important role in the oxidation of inorganic minerals by lithotrophic organisms, the mechanisms involved in the oxidation of solid particles are poorly understood. To explore the genetic basis of oxidative EET, we utilized genomic analyses and transposon insertion mutagenesis screens (Tn-seq) in the metabolically flexible, lithotrophic Alphaproteobacterium *Thioclava electrotropha* ElOx9^T. The finished genome of this strain is 4.3 MB, and consists of 4,139 predicted ORFs, 54 contain heme binding motifs, and 33 of those 54 are predicted to localize to the cell envelope or have unknown localizations. To begin to understand the genetic basis of oxidative EET in ElOx9^T, we constructed a transposon mutant library in semi-rich media which was comprised of >91,000 individual mutants encompassing >69,000 unique TA dinucleotide insertion sites. The library was subjected to heterotrophic growth on minimal media with acetate and autotrophic oxidative EET conditions on indium tin oxide coated glass electrodes poised at –278 mV vs. SHE or un-poised in an open circuit condition. We identified 528 genes classified as essential under these growth conditions. With respect to electrochemical conditions, 25 genes were essential under oxidative EET conditions, and 29 genes were essential in both the open circuit control and oxidative EET conditions. Though many of the genes identified under electrochemical conditions are predicted to be localized in the cytoplasm and lack heme binding motifs and/or homology to known EET proteins, we identified several hypothetical proteins and poorly characterized oxidoreductases that implicate a novel mechanism(s) for EET that warrants further study. Our results provide a starting point to explore the genetic basis of novel oxidative EET in this marine sediment microbe.

Keywords: extracellular electron transfer (EET), lithotrophy, Tn-seq, marine bacterium, marine sediment, electrotroph, genomics

Edited by:
Nils Risgaard-Petersen,
Aarhus University, Denmark

Reviewed by:
Chi Ho Chan,
University of Minnesota Twin Cities,
United States
Sarah Glaven,
United States Naval Research
Laboratory, United States

****Correspondence:***
Joshua D. Sackett
Joshua.Sackett@uc.edu
Annette R. Rowe
Annette.Rowe@uc.edu

Specialty section:
This article was submitted to
Microbiological Chemistry
and Geomicrobiology,
a section of the journal
Frontiers in Microbiology

Received: *31 March 2022*
Accepted: *17 May 2022*
Published: *10 June 2022*

Citation:
Sackett JD, Kamble N, Leach E,
Schuelke T, Wilbanks E and Rowe AR
(2022) Genome-Scale Mutational
Analysis of Cathode-Oxidizing
Thioclava electrotropha ElOx9^T.
Front. Microbiol. 13:909824.
doi: 10.3389/fmicb.2022.909824

INTRODUCTION

The discovery of extracellular electron transfer (EET) – the process by which microorganisms transfer electrons across their membrane(s) to/from solid-phase materials – has important implications for a wide range of biogeochemically important processes (Gralnick and Newman, 2007; Richter et al., 2012). Though our understanding of EET mechanisms is limited to just a few model mineral-reducing microbes [such as *Shewanella oneidensis* MR-1 (Lies et al., 2005; Nevin and Lovley, 2010), *Geobacter metallireducens* (Reguera et al., 2005; Reguera and Kashefi, 2019), *Pseudomonas aeruginosa* (Shen et al., 2014)], there is a growing diversity of microorganisms and physiologies that are thought to be capable of extracellular electron transfer, including phototrophs (Bose et al., 2014; Guzman et al., 2019; Gupta et al., 2020), sulfur and iron oxidizing microorganisms (Myers and Nealson, 1988; Bond and Lovley, 2003; Reguera et al., 2005; Rowe et al., 2015), anerobic ammonia oxidizers (Qu et al., 2014; Shaw et al., 2020) and consortia such as anaerobic methane oxidizers (Villano et al., 2010; Scheller et al., 2016; Gao et al., 2017) and syntrophic ethanol oxidizers (Rotaru et al., 2014). These observations span marine and freshwater systems and suggest that we are barely scratching the surface of the role EET plays in microbial metabolisms and the role of these processes in many environmental systems.

Though the role of EET in iron oxidation has recently been identified (Jiao and Newman, 2007; Liu et al., 2012; Summers et al., 2013; Bose et al., 2014; Barco et al., 2015), the mechanisms of *oxidation* of other inorganic and often insoluble materials, such as sulfur minerals, are poorly understood (Emerson, 2012). As the proteins involved in these reactions remain unknown, many omics-based studies fail to identify them in datasets, leaving them to accumulate among the conserved/hypothetical genes of unknown function, which are prevalent in environmental omics surveys. Coupled with the fact that these physiologies are difficult to detect in nature via chemistry alone (whether due to low substrate concentrations, the transient nature of reactants and/or products, or competition with abiotic or geochemical reactions), our understanding of the role these processes play in many environmental systems is severely limited (Ilbert and Bonnefoy, 2013). This is especially true for subseafloor marine sediments, which account for an estimated 2.9×10^{29} microbial cells and ~0.6% of Earth's total biomass (Kallmeyer et al., 2012). Currently, direct measurements of microbial metabolism in the "deep" and "dark" oceans far exceed the expected models based on the influx of organic carbon into the system (Burd et al., 2010). Metabolisms, such as lithotrophy and/or lithoautrophy, which depend less on organic carbon and may actually act as a source for organic carbon, may account for at least some of the missing carbon in current global carbon budgets (Swan et al., 2011). Therefore, the identification of genes to aid in understanding and detection of these processes in nature is crucial.

A growing number of studies over the past decade have expanded our knowledge of the diversity of marine microorganisms that engage in EET in marine sediments (Rowe et al., 2015; Chang et al., 2018; Lam et al., 2018, 2019). *Thioclava electrotropha* ElOx9^T, originally isolated from marine sediment bioelectrochemical enrichments from Catalina Island, California, is one such bacterium (Rowe et al., 2015; Chang et al., 2018). Species of *Thioclava* are widespread in marine sediments and surface waters (Sorokin et al., 2005; Rowe et al., 2015; Liu et al., 2017; Chang et al., 2018; Karbelkar et al., 2019), and several strains are known lithoautotrophs capable of sulfur oxidation. Strain ElOx9^T is metabolically flexible, capable of oxygen or nitrate respiration, heterotrophic growth with acetate or glucose, and autotrophic growth with H_2 or reduced sulfur substrates (S^{2-}, S^0, or $S_2O_3{}^{2-}$) as energy sources (Chang et al., 2018). Recent bioelectrochemical investigations into the EET phenotype in *T. electrotropha* ElOx9^T indicate that biofilms that form on poised cathodes are electrochemically active (Rowe et al., 2015; Karbelkar et al., 2019) and that electron transfer is facilitated by direct contact – not mediated by soluble electron carriers – between the biofilm and the electrode surface under both aerobic (Rowe et al., 2015) and anaerobic conditions (Karbelkar et al., 2019). However, our preliminary genomic investigations failed to identify highly probable candidate genes that could be involved in EET, and consequently, the genetic basis of this process has yet to be determined.

Transposon saturation mutagenesis sequencing methods, collectively termed Tn-seq, have emerged as powerful, high-throughput tools to generate and test genome-scale mutant libraries and define gene essentiality under various growth conditions (Jacobs et al., 2003; Cameron et al., 2008; van Opijnen et al., 2009). These methods rely on the generation and pooling of a dense transposon library in the organism of interest in which the total number of mutants generated approximates the number of theoretically possible transposon insertion sites (Freed, 2017). This pooled mutant library (parent library) is then subjected to a growth condition of interest. Genomic DNA from the parent library and from all experimental growth conditions is isolated, transposon-genome junctions are sequenced, and the location and frequency of transposon insertions throughout the genome are determined. Essentiality and fitness determinations can be made based on the frequency of gene insertions in a particular library or by comparing insertion frequencies between differential growth conditions (i.e., comparing before and after a growth selection). This method has been employed to identify essential genes in diverse microorganisms, such as *Mycoplasma genitalium* (Glass et al., 2006), *Vibrio cholerae* (Cameron et al., 2008), *Rhodopseudomonas palustris* (Pechter et al., 2016), *G. sulfurreducens* (Rollefson et al., 2009; Chan et al., 2017), and *S. oneidensis* MR-1 (Bouhenni et al., 2005; Brutinel and Gralnick, 2012; Yang et al., 2014; Baym et al., 2016; Rowe et al., 2021). From Tn-seq experiments conducted in *G. sulfurreducens*, Chan et al. (2017) identified a putative methyl-accepting chemotaxis-cyclic dinucleotide sensing network (*esnABCD*) required for electrode colonization and a putative porin-cytochrome conduit complex (*extABCD*) required for growth with electrodes. In *S. oneidensis* MR-1, Rowe et al. (2021) identified and bioelectrochemically characterized five genes involved in EET: a putative diguanylate cyclase involved in both reductive and oxidative EET, and four other genes that play significant roles just in oxidative EET. These studies highlight the utility of Tn-seq experiments in identifying genes involved in physiologic processes on a genome scale and in an efficient, high-throughput manner.

To investigate the genetic basis of oxidative EET in ElOx9^T, we coupled comprehensive genomic analysis with genome-scale transposon insertion mutagenesis sequencing screens to identify genes deemed essential for (1) heterotrophic growth in semi-rich media, (2) heterotrophic growth in minimal media with acetate (also used for electrode pre-growth), and (3) autotrophic oxidative EET conditions on an indium tin oxide (ITO) coated glass electrode poised at –278 mV vs. SHE or un-poised for open circuit conditions for comparative analysis.

MATERIALS AND METHODS

Bacterial Strains and Culture Conditions

All cultures used in this work were stored in 40% glycerol at –80°C unless otherwise stated. Prior to each experiment, *T. electrotropha* ElOx9^T cultures were grown from a single colony isolated on either Difco^{TM} Marine (DM) broth or Luria-Bertani (LB) broth with added NaCl and other ions (LBS + Ions) as described previously (Chang et al., 2018), with the addition of 1.5% agar. *E. coli* WM3064, a diaminopimelic acid (DAP) auxotroph, was utilized as a donor for conjugation and routinely grown on LB with the addition of 300 μM DAP. Kanamycin (100 mg/L) was routinely used to select for plasmid or transposon insertions in respective strains. All cultures were grown at 30°C in liquid media unless otherwise stated. Though ElOx9^T strains were grown in the enriched media DM and LBS + Ions for maintenance, a low-sulfate saltwater base (SWB) minimal medium (Rowe et al., 2015) was used for the majority of growth and electrochemical experiments. For heterotrophic growth, 5 mM sodium acetate was added as an electron donor.

Genomic DNA Isolation, Sequencing, and Analysis

Genomic DNA was isolated from turbid cultures with the DNeasy PowerSoil Kit (Qiagen, Germantown, MD) according to the manufacturer's instructions. DNA libraries were prepared for Illumina sequencing as described previously (Chang et al., 2018). DNA for long read sequencing was extracted using the Qiagen Blood and Tissue Kit (Qiagen, Germantown, MD). The DNA extract was barcoded using the Native Barcoding Kit 1D (Oxford Nanopore, United Kingdom) and prepared for sequencing using the Ligation Sequencing Kit 1D. NanoPore libraries were demultiplexed and base called with MinKNOW software (V.2). The genome was first assembled with Flye v. 2.7 (Kolmogorov et al., 2019) using the NanoPore long-read sequences. Illumina reads were aligned to the genome using Burrows–Wheeler aligner (Li and Durbin, 2010) and subsequently used to polish the long-read assembly using Pilon v. 1.23 (Walker et al., 2014) using default parameters.

Genome statistics were determined with QUAST v4.4 (Gurevich et al., 2013), and assembly quality was assessed with CheckM v.1.0.18 (Parks et al., 2015). The genome was annotated using the NCBI Prokaryotic Genome Annotation Pipeline (PGAP). Potential metabolic pathways were identified using KEGG's BlastKOALA functional characterization tool (Kanehisa et al., 2016). Protein-encoding genes were analyzed for the presence of carbohydrate-active enzymes (CAZymes; Lombard et al., 2014) using the dbCAN2 automated carbohydrate-active enzyme annotation server (Yin et al., 2012; Zhang et al., 2018). Proteins annotated as CAZymes by a minimum of two independent methods (any combination of pHMMER [hidden Markov model-based annotation], DIAMOND (Buchfink et al., 2014) [sequence alignment-based annotation], or Hotpep (Busk et al., 2017)[peptide pattern recognition-based annotation]) were considered positive hits. Putative heme-binding proteins were identified by creating a searchable database of ElOx9^T's genome in Prosite (Hulo et al., 2006) and searching the database for c-type cytochrome heme-binding motifs ($CX_{2-4}CH$). PSORTb v 3.0.3 (Yu et al., 2010) was subsequently used to predict the localization of those proteins. The nearest neighboring genomes were identified with the Genome Taxonomy Database (GTDB-tk v 1.7.0; Chaumeil et al., 2020). Whole genome average nucleotide identity (ANI) values between ElOx9^T and neighbors identified by GTDB-tk were calculated with the Kostas lab ANI calculator (Rodriguez-R and Konstantinidis, 2016).

Transposon Mutant Library Generation and Selection

Transposon mutagenesis was performed by conjugal transfer of the modified *mariner* transposon pEB001 (Brutinel and Gralnick, 2012) to ElOx9^T from *Escherichia coli* WM3064 as described previously (Chan et al., 2017). In brief, this involved conjugation of the WM3064 donor strain containing pEB001 with ElOx9^T on the permissive media LBS + Ions agar containing 300 μM DAP. Pre-conjugation cultures of *E. coli* and ElOx9^T were grown at 30°C for 12–16 h and washed 3 × with LBS + Ions via centrifugation and resuspension. ElOx9^T cells were heat shocked in a pre-heated water bath (45°C for 5 min) and conjugation was performed by combining WM3064 and ElOx9^T to a final OD_{600} ratio of 1:0.65 in 100 μl of LBS + Ions and spotted in 10 μl aliquots onto permissive media. Negative controls were performed using LBS + Ions (DAP-) plates for WM3064 and LBS + Ions + Kan plates for ElOx9^T. Conjugation plates were incubated for 12–16 h. These conjugation spots were collected using a nichrome wire loop washed 3X in 1X phosphate buffer and diluted onto large (200 mm diameter) LBS + Ions + Kan agar plates. Plates were incubated at 30°C for 16–24 h. until visible colonies formed. Successful conjugation was determined using colony PCR on select colonies, targeting the mechanosensitive conductance channel mscL in ElOx9^T (absent in WM3064, primers mscL_Fwd and mscL_Rev) and the inserted transposon (primers ARR_Tn_Fwd and ARR_Tn_Rev). Primer sequences are listed in **Supplementary Table 1**. Approximately 9.1×10^4 colonies were generated, pooled in approximately 10 mL of LBS + Ions with 10% glycerol, and 1 mL aliquots were stored at –80°C for use in Tn-seq selection experiments.

ElOx9^T library transconjugants (containing a viable insertion of the *mariner* transposon) from these frozen stocks were sequenced directly (hereafter referred to as the LBS + Ions parent library). Triplicate libraries were grown in SWB + acetate for 16 h and growth was monitored by OD_{600} to ensure at least six doublings occurred. Cells from SWB + acetate were harvested for sequencing. Pre-growth for the electrochemical systems (hereafter referred to as "Pre-Electrochemistry") was treated in the same way, however, aliquots of the cultures (10–20% of total culture volume) were added to bioelectrochemical systems at an OD_{600} of 0.2 for both poised potential and open circuit conditions as described below. The remaining cells from Pre-Electrochemistry growth were collected for sequencing. Electrochemical "growth" was calculated to be an average of 6 generations after 6 days. This was calculated from an autotrophic hydrogen growth curve of ElOx9^T that consumes 2.1 C based on cell yields per electron. For current ranging from 3 to 6 μA, the range of coulombs consumed at ∼6 days is between 1.5 and 3 C. This was in the desired range for the lowest current consuming experiments.

Bioelectrochemical Measurements

The electrochemical analysis of the ElOx9^T library was performed in standard three-electrode bioreactors as described previously (Rowe et al., 2015). An ITO coated glass (Delta Technologies, Loveland, CO) with a 10.68 cm^2 surface area was used as a working electrode, platinum wire (Sigma-Aldrich, St. Louis, MO) as a counter electrode, and Ag/AgCl (1M KCl; CH Instruments, Austin, TX, United States) as a reference electrode. The reactors were inoculated with 30 ml of SWB media and constantly purged with 0.2 μm-filtered ambient air to provide O_2. Chronoamperometry and cyclic voltammetry (CV) analyses were performed using a 16-channel potentiostat (Biologic, Seyssinet-Pariset, France). For Chronoamperometry studies, the working electrode was poised at –278 mV vs. SHE to act as the electron donor for the cells. For CV, the working potential was cycled between –378 and 622 mV vs. SHE at a scan rate of 1 mV/s. The reactors were inoculated with a resuspended cell culture from the pre-growth to a final OD_{600} of 0.2 once a stable baseline current was achieved. Analysis of the electrode-attached biofilms was performed after the cathodic current in the bioreactor maximized and a CV was recorded. As kill controls were not permissible due to the need to outgrow electrode-attached cells, CVs were compared to separate experiments with wild-type ElOx9^T in which CVs were recorded before and after the addition of the ubiquinone mimic Antimycin A (50 μM final concentration) to discern biologically mediated EET processes from abiotic processes. The addition of Antimycin A results in a strong reduction in current consumption and reduced catalytic activity as seen in the CVs (**Supplementary Figure 4**). Open circuit conditions were run identically to poised potential conditions; however, no voltage was applied. Following electrochemical experiments, planktonic cells and spent cathode media were removed from all reactors, and libraries were outgrown on SWB + acetate at 30°C prior to collection of biomass for sequencing. All planktonic- and biofilm-associated cells (recovered via scraping) from the outgrowths were collected for sequencing.

Transposon Library Sequencing

Genomic DNA from Tn-seq selection conditions and parent libraries was isolated with the Wizard Genomic DNA Purification Kit (Promega, Madison, WI). To isolate transposon insertion sites, up to 3 μg of genomic DNA was digested with *Mme*I (New England Biolabs, Ipswich, MA), heat inactivated and treated with Antarctic phosphatase (New England Biolabs, Ipswich, MA). The *Mme*I digested and Antarctic phosphatase-treated genomic DNA fragments were end repaired and dA-tailed with the NEBNext Ultra II End Repair/dA-Tailing Module (New England Biolabs, Ipswich, MA). Illumina adaptors (NEBNext Multiplex Oligos for Illumina Dual Index Primers Set 1, New England Biolabs, Ipswich, MA) were then ligated to these fragments with the NEBNext Ultra II Ligation Module (New England Biolabs, Ipswich, MA). These reactions were treated with USER enzyme (New England Biolabs, Ipswich, MA) and purified using the GeneJET Gel Extraction Kit (Thermo Fisher Scientific, Waltham, MA) and eluted in 50 μl prior to quantification using the Qubit dsDNA BR Assay Kit and a Qubit 4 Fluorometer (Thermo Fisher Scientific, Waltham, MA).

Approximately 50 ng of purified transposon-genome junction DNA was used in PCR enrichments using Phusion High-Fidelity DNA polymerase with GC buffer master mix (Thermo Fisher Scientific, Waltham, MA), custom forward primer ARR_Read1_TnF, and NEBNext Index reverse primers from the NEBNext Multiplex Oligos for Illumina Dual Index Primers Set 1 kit (New England Biolabs, Ipswich, MA) that anneal to the inverted repeat of the transposon and the ligated Illumina adaptor, respectively. Primer sequences are shown in **Supplementary Table 1**. PCR reactions were then run on 2% agarose gel. Expected PCR bands of ∼174 bp were excised from the gel cleaned using the GeneJET Gel Extraction kit (Thermo Fisher Scientific, Waltham, MA). PCR products were sent to Novogene (Sacramento, CA) for sequencing, following a quality control test using Bioanalyser traces. Individually barcoded libraries were pooled following the scheme in **Supplementary Table 1** and sequenced in two lanes on an Illumina HiSeq 2500 with 2 × 150 paired-end chemistry. Manufacturers' protocols were followed for all steps outlined above unless otherwise stated.

Transposon Insertion Mutagenesis Screens Data Analysis

Analysis of Tn-seq data was performed using high performance computing resources provided by the Ohio Supercomputer Center (Ohio Supercomputer Center, 1987). Forward reads were truncated at the start of the NEBNext adaptor using Trimmomatic v. 0.36 (Bolger et al., 2014) allowing for up to two mismatches over the length of the adaptor sequence, reverse complemented using FASTX-Toolkit (Gordon and Hannon, 2010), reverse complements were truncated at the beginning of the *Mme*I recognition site endogenous to the transposon with Trimmomatic v. 0.36 (allowing for two mismatches over the length of the inverted repeat – *Mme*I sequence), and reverse complemented back to + sense. Upon removal of four bases belonging to the transposon's inverted repeat (between *Mme*I recognition site and genomic DNA) and considering the end repair step removes the two bp 5' overhang following *Mme*I digestion, the expected genomic DNA insert size was 14 bp. Reads were then filtered to retain genomic DNA inserts beginning with "TA" and ranging from 14 to 18 bp using awk. Remaining reads were then quality filtered using Trimmomatic with the following options: SLIDINGWINDOW:1:20 and MINLEN:14. Reverse reads were excluded from the analysis due to ambiguous base calls in the genomic DNA insert that, when removed, resulted in insert lengths < 14 bp.

Subsequent steps were conducted using a combination of publicly available programs and scripts from https://github.com/jbadomics/tnseq. Filtered reads were mapped to the ElOx9^T genome and plasmid with Bowtie1 v. 1.1.2 (Langmead et al., 2009), discarding reads without 100% identity to a unique position in the genome. Insertion sites were formatted using bioawk and insertions per gene were tabulated with the tabulate_insertions.py python script. Further, insertion events that occurred in the last 5% of the gene sequence were omitted as Yang et al. (2014) found higher transposon insertion frequencies in essential genes within the last ∼2% of the gene sequence, suggesting that insertions at the end of the gene may not be as effective in disrupting gene function. Genes lacking TA sites and genes for which less than half of the total number of TA sites within the gene are unique were excluded from our analysis. To account for differences in sequencing depth, reads per kilobase (RpK) values were normalized to 10^7 reads per sample based on the total number of reads that mapped to a single TA site in the genome and plasmid, as described previously (Pechter et al., 2016).

Determination of Gene Essentiality

Gene essentiality calls were determined following a similar statistical approach reported previously (Pechter et al., 2016). For each replicate, $\log_2$[normalized RpK] values were analyzed via histogram. Outliers were removed, the mean and standard deviation of the distribution were calculated, and a normal distribution curve was fitted to the data using the mean and SD. Essential genes were those with $\log_2$[normalized RpK] values less than 3 SD below the mean; that is, falling below the interval that encompasses 99.7% of the data in a normal distribution in all replicates. Genes with reduced insertion frequency (IF; growth defect) were those that fell between 2 and 3 SD below the mean (95–99.7% of data). Genes with $\log_2$[normalized RpK] within 2 SD of the mean were considered non-essential. Those with increased IF (growth advantage) were those genes with $\log_2$[normalized RpK] greater than 2 SD above the mean. As transposon insertion in essential genes may be lethal, genes that lacked transposon insertions were considered essential. Genes with different essentiality calls between replicates were designated "Uncertain."

Data Availability

The raw genome sequencing reads (Illumina and NanoPore) have been deposited in the NCBI Sequence Read Archive (SRR18508951 and SRR18508952). The accession number for the genome assembly is GCA_002085925.2. Tn-Seq raw reads for each library are available from BioProject PRJNA821218.

RESULTS AND DISCUSSION

Genomics

General Features of the Genome

ElOx9^T was isolated from Catalina Harbor (California, United States) sediments via enrichments on artificial saltwater agar plates supplemented with elemental sulfur/thiosulfate and nitrate as electron donor and acceptor, respectively, and was established as the type strain of *T. electrotropha* sp. nov. (Chang et al., 2018). ElOx9^T's genome encodes a 4.27 Mb chromosome and 128 kb plasmid (summary statistics are shown in **Table 1**). The chromosome has a GC content of 63.87% and encodes 4,014 genes, 52 tRNAs comprising all 20 amino acids, and three rRNA operons. The plasmid has a GC content of 59.98% and encodes 125 genes, including 30 hypothetical proteins and 26 predicted transposases.

Taxonomically, the 16S rRNA gene of ElOx9^T is most similar to that of *T. nitratireducens* strain 25B10_4 (100% query coverage, > 99% identity, accession no. CP019437.1). Comparisons at the genome level demonstrate greater genetic diversity across the sequenced representatives than is seen at the 16S rRNA level. Whole genome ANI comparisons were made between ElOx9^T and closely related draft and complete genomes as identified by GTDB (**Supplementary Figure 1**). ElOx9^T shares 76.2–95.6% ANI with neighboring organisms' genomes and was most similar to *T. sediminum* TAW_CT$_{134}^{T}$ (accession no. GCF_002020355.1), a nitrate-reducing marine bacterium isolated from coastal sediments around Xiamen Island, Fujian province, China (Liu et al., 2017).

TABLE 1 | Genome assembly and quality statistics for *Thioclava electrotropha* ElOx9^T.

	Chromosome	Plasmid
Genome completeness (%)[a]	99.39	N/A
Est. contamination (%)[a]	0.15	N/A
Quality[b]		
# contigs	1	1
Largest contig (bps)	4,267,812	127,662
Total length (bps)	4,267,812	127,662
GC (%)	63.87	59.98
# Mismatches (N characters)	0	0
Features[c]		
CDS	4,014	125
With assigned function	3,470	95
Hypothetical	544	30
tRNAs	52[d]	0
rRNA operons	3	0
ncRNA	3	0
CRISPR arrays	0	0
Pseudogenes	72	18
Signal Peptides[e]		
Genes with Sec/SPI signal peptides[f]	383	7
Genes with Sec/SPII signal peptides[g]	89	2
Genes with Tat/SPI signal peptides[h]	72	1

[a] *Determined with CheckM v1.0.18 (Parks et al., 2015).*

[b] *Determined with QUAST v4.4 (Gurevich et al., 2013).*

[c] *Determined with the NCBI Prokaryotic Genome Annotation Pipeline (Tatusova et al., 2016; Haft et al., 2018).*

[d] *Comprises all 20 amino acids.*

[e] *Determined with SignalP 5.0 (Almagro Armenteros et al., 2019).*

[f] *Sec/SPI denotes signal peptides transported by the Sec translocon and cleaved by Signal Peptidase I (Lep).*

[g] *Sec/SPII denotes lipoprotein signal peptides transported by the Sec translocon and cleaved by Signal Peptidase II (Lsp).*

[h] *Tat/SPI denotes Tat signal peptides transported by the Tat translocon and cleaved by Signal Peptidase I (Lep).*

Metabolic Potential of ElOx9^T

ElOx9^T is capable of heterotrophic growth on acetate and glucose with either oxygen or nitrate as the terminal electron acceptor, and autotrophic growth with the oxidation of elemental sulfur, thiosulfate, or hydrogen (Chang et al., 2018). Metabolic pathways reconstructed from the genome with BLASTKoala (Kanehisa et al., 2016) corroborate these observations. The genome encodes complete pathways for the Embden–Meyerhof–Parnas (glycolysis), gluconeogenesis, the Entner–Doudoroff pathway, the pentose phosphate pathway, the citric acid cycle, and the reductive pentose phosphate pathway (Calvin Benson Bassham cycle). ElOx9^T's genome lacks isocitrate lyase but encodes malate synthase. Thus, this organism may be incapable of bypassing the decarboxylation steps of the TCA cycle via the glyoxylate shunt and may form malate from glyoxylate. ElOx9^T has demonstrated growth with acetate as the sole carbon source, likely via conversion to acetyl-CoA by acetyl-CoA synthase, rather than via the glyoxylate cycle. A complete pathway for oxidative phosphorylation and an incomplete denitrification pathway – lacking nitrous oxide reductase *nosZ* – were annotated. Genomic evidence for lithotrophic metabolisms includes the complete sulfur oxidation pathway (*soxABCDXYZ*) and [NiFe] hydrogenase gene clusters (metabolic potential overview in **Figure 1** and **Supplementary Table 2**).

Complete amino acid biosynthesis pathways for all 20 amino acids were identified, thus auxotrophies are not predicted and have not been observed in culture (Chang et al., 2018). The genome encodes 76 putative carbohydrate-active enzymes (**Supplementary Figure 2**), primarily glycosyl transferases and glycoside hydrolases. Some of these proteins include mannitol 2-dehydrogenase, phosphomannomutase, α- and β-glucosidases, α-galactosidase, in addition to several proteins putatively involved in the degradation of cell wall components. The genome encoded 231 peptidases and 86 non-peptidase homologs, and 12 peptidase inhibitors (**Supplementary Table 3**). The most numerous peptidase families were: family S33 prolyl aminopeptidases, which preferably cleave N-terminal proline residues, thus providing the organism with proline-rich substrates; family U69 self-processing peptidases, such as some adhesins, that may autocatalytically cleave the extracellular portion of the protein upon translocation to the outer membrane, which aids in adhesion to surfaces; family M23B [8] beta-lytic metallopeptidases, such as lysostaphin, which act on cell wall peptidoglycan and are often used in defense or feeding; family M20 and subfamily M20D exopeptidases, including carboxypeptidases and dipeptidases that primarily function in facilitating intracellular protein degradation and recycling; and family C26 gamma-glutamyl hydrolases that act on gamma-linked glutamate bonds in peptides. These predictions suggest that ElOx9^T is metabolically versatile with respect to autotrophic and heterotrophic growth, but also may be capable of metabolizing a variety of organic substrates.

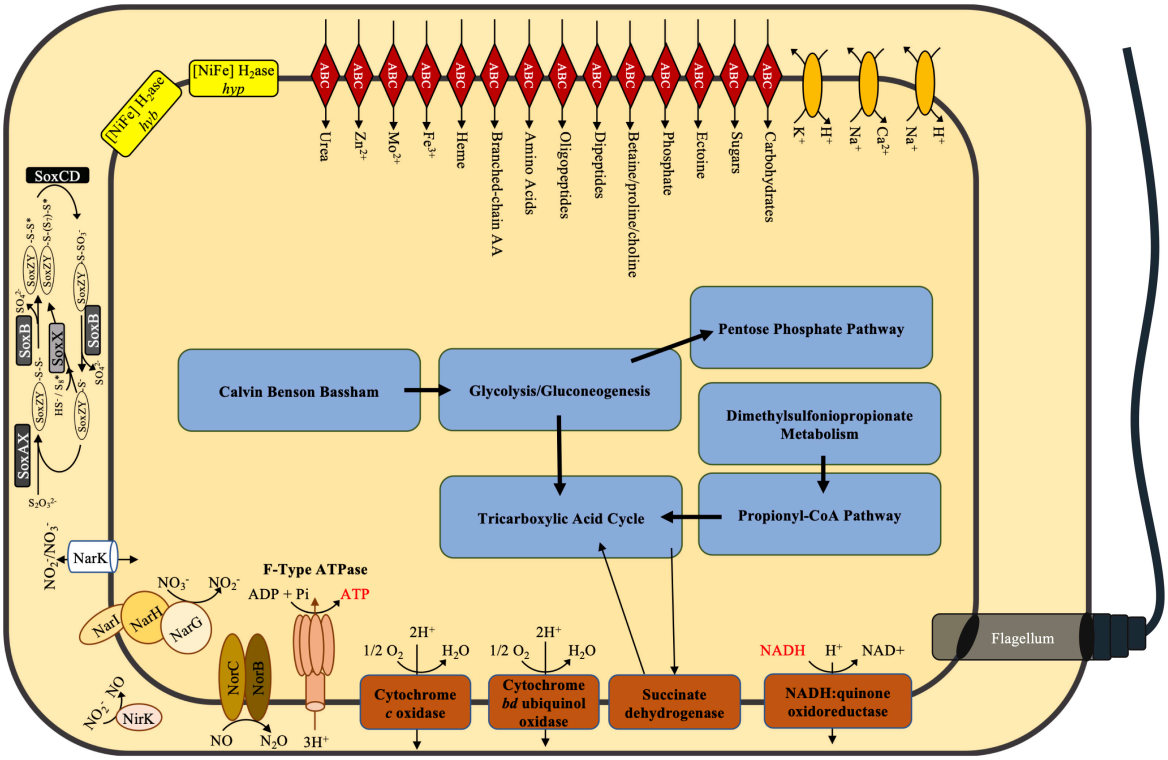

FIGURE 1 | Simplified genome-resolved central metabolic model for *Thioclava electrotropha* ElOx9^T. See **Supplementary Table 2** for a list of genes comprising central metabolic pathways.

ABC transporters for the following compounds were predicted from the genome sequence: rhamnose, D-ribose, c4-dicarboxylate, and other sugars and carbohydrates, ectoin/hydroxyectoin, glycine betaine/L-proline, choline, taurine, thiamine, lipoprotein, oligopeptides, phosphate, phosphonate, urea, heme, molybdenum, zinc, and other metals. The several glycine-betaine/L-proline ABC transporters present in the genome are of particular interest as they have been known to transport dimethylsulfoniopropionate (DMSP; Cosquer et al., 1999), a major organic sulfur compound produced by marine phytoplankton (Yoch, 2002). A metagenomic study of seawater and sediment samples collected along a 10.9 km depth profile in the Mariana Trench identified high abundances of cells containing DMSP catabolic genes belonging primarily to several genera of Actinobacteria, Gammaproteobacteria, and Alphaproteobacteria, including *Thioclava* (Zheng et al., 2020). ElOx9^T has the genomic potential to utilize DMSP as a carbon and energy source, in a process that would release the greenhouse gas dimethylsulfide (Lovelock et al., 1972).

Identification of Putative Redox-Active Proteins in the Cell Envelope

Though ElOx9^T has demonstrated capacity for oxidative EET, the genes responsible for conferring this capacity have yet to be identified. The primary characterized mechanism of direct extracellular electron transfer in model organisms such as *S. oneidensis* MR-1 and *Geobacter* species – both primarily known for their mineral reduction metabolisms – entail the use of outer membrane multiheme *c*-type cytochromes (Paquete et al., 2022). ElOx9^T lacks genes with homology to either the Mtr pathway in MR-1 or the outer membrane cytochromes in *G. sulfurreducens.* As ElOx9^T lacks genes canonically involved in anode respiration in model organisms, we sought to identify putative redox active proteins that contain heme-binding motifs ($CX_{2-4}CH$). Of the 54 heme-binding-motif-containing proteins identified, 33 were predicted to localize to the cell envelope, including 7 to the cytoplasmic membrane, 10 to the periplasm, and 16 with unknown localizations (**Supplementary Table 4**). The majority of these proteins contain a single heme-binding motif and the maximum number of motifs identified was 8 in a tetrathionate reductase family octaheme *c*-type cytochrome (AKL02_08055). Complicating the analysis of putative heme-binding-motif-containing proteins is the absence of distinct functional annotations. Therefore, to determine if any of these proteins are involved in oxidative EET, we employed Tn-seq methods to identify essential genes under electrotrophic conditions.

Essential Gene Analysis via Transposon Insertion Mutagenesis Screens

Construction and Selection of Complex Transposon Mutant Library in ElOx9^T

To create a transposon mutant library, the mini*Himar1* transposon from an *E. coli* WM3064 strain harboring the pMini*Himar* RB1 transposon delivery vector (Bouhenni et al., 2005) was conjugated into ElOx9^T (Chang et al., 2018) as outlined in Methods. This parent library was outgrown in LBS + Ions semi-rich media under aerobic conditions, which generated in excess of 91,000 transposon insertion mutants covering > 69,000 individual TA dinucleotide sites throughout the genome. This parent library was then subjected to differential growth conditions, including aerobic heterotrophic growth in minimal media (SWB) with acetate, and autotrophic oxidative EET conditions (SWB), with electrochemistry pre-growth (Pre-Electrochemistry) and open circuit conditions serving as controls for growth on minimal media and attachment phenotypes, respectively. All conditions were tested in at least triplicate (quadruplicate for oxidative EET). Heterotrophic conditions were monitored by measurement of optical density, ensuring a minimum outgrowth of six generations in each replicate. Cells from overnight growth in SWB + acetate, monitored by taking OD_{600} measurements, were used to inoculate bioelectrochemical reactors and aliquots were taken for the Pre-Electrochemistry Tn-seq control condition. Electrochemistry replicates were monitored for maximal current production during chronoamperometry at −278 mV vs. SHE (approximately 5 days, **Supplementary Figure 4**). Cyclic voltammetry was performed on all replicates to verify the current generation was consistent with previously characterized ElOx9^T electrochemistry, as kill controls were not feasible with this experimental design (**Supplementary Figure 4**).

Transposon Insertion Mutagenesis Screens Sequencing Library Statistics

In all libraries, most quality-controlled sequencing reads aligned to the genome a single time (73.9–90.4% mapping frequency, **Supplementary Table 5**). Greater than 90% of the unique insertion sites identified in each technical replicate (LBS + Ions parent library) were identified in all replicates of the same growth condition, suggesting that insertion sites identified by our approach are primarily authentic. In fact, we observed high concordance among all replicates within each growth condition supporting the reproducibility of our approach (**Supplementary Table 5**).

The mini*Himar1* transposon preferentially inserts at TA dinucleotide sequences (Lampe et al., 1998; Yang et al., 2014). *in silico* analysis identified 129,162 potential mini*HimarI* transposon insertion sites within ElOx9^T's genome. Individual library coverage percentages ranged from 45.7 to 56.7% of total TA sites (**Supplementary Table 5**). While insertion densities below 100% are not unexpected, other investigations employing *mariner* transposon-based Tn-seq methods calculated an insertion density of 83% (Perry and Yost, 2014). It is conceivable that our lower transposon insertion frequency may be due to sequencing reads mapping to non-unique TA sites throughout the genome. In each library, approximately 5–7% of quality-controlled reads are aligned to multiple TA dinucleotide sites. Considering the expected genomic DNA insert length was 14 base pairs given our experimental design and the average genomic DNA insert length was ∼14.5 bp for all libraries (**Supplementary Table 5**), we calculated the number of duplicated TA sites (14bp), which equated to 11,864 sites throughout the genome. Despite this caveat, sequencing reads mapped to 4,024 genes in ElOx9^T's genome. After exclusion of 33 genes lacking TA sites entirely (**Supplementary Table 6**), 10 genes lacking TA sites when ignoring insertion sites in the last 5% of the gene sequence (**Supplementary Table 7**), and 35 genes lacking unique TA sites in the first 95% of the gene (**Supplementary Table 8**), gene coverage is estimated at 98.8%.

Identification of Essential Genes

Pairwise comparisons of $\log_2$[normalized RpK] values for all replicates within a growth condition (**Supplementary Table 9**) revealed strong correlations between replicates ($R^2 > 0.97$ for most comparisons). For each replicate, $\log_2$[normalized RpK] values were analyzed via histogram. Outliers were removed and the mean and standard deviation of the distribution was calculated. A normal distribution curve was fitted to the data using the mean and SD (**Supplementary Figure 3**). Essential genes were those with $\log_2$[normalized RpK] values less than 3 SD below the mean in all replicates; genes with a growth defect had reduced insertion frequency that fell 2–3 SD below the mean; genes considered non-essential fell within 2 SD of the mean, and genes with a growth advantage had increased insertion frequency that was greater than 2 SD above the mean (**Supplementary Tables 10–15**). Insertions in rRNAs and tRNAs, genes lacking insertions in unique TA sites, and genes for which essentiality calls differed among all replicates in a growth condition were excluded from our analysis. It is important to note that this stringent statistical method for defining essentiality may result in the misidentification of a small proportion of genes as non-essential. Nonetheless, we believe our approach, rigorous analysis, and demonstrated replicability provide an accurate and conservative prediction of gene essentiality.

Core Essential Genome

The distribution of gene essentiality calls for all libraries is shown in **Table 2**. Most of the essential genes identified in each library were classified as essential in all libraries (**Figure 2** and **Supplementary Table 16**). These 528 essential genes comprise the *core essential genome* of ElOx9^T and represent 12.7% of the genome. Previous Tn-Seq studies in Bacteria show the percentage of open reading frames deemed essential ranges from just 5% in *Burkholderia cenocepacia* (Wong et al., 2016; 8.06 Mb genome) to 80% in *M. genitalium* (Glass et al., 2006; 0.58 Mb genome). The majority of the essential genes (82%) have KEGG ontology (KO) annotations and are predicted to be involved in many functional categories, including carbohydrate metabolism (primarily glycolysis, TCA cycle, and PPP); oxidative phosphorylation; biosynthesis of lipids, nucleotides, amino acids, aminoacyl-tRNAs, peptidoglycan, cofactors, vitamins, and porphyrin; genetic information processing (DNA replication and repair, transcription, translation, and protein folding and sorting), environmental sensing (transport and secretion[*sec* and *tat*]), and cellular processes (cell cycle and division). The remaining essential genes without KO annotations were comprised primarily of hypothetical proteins (40 in total), proteins containing domains of unknown function, other proteins with poorly characterized function, transcriptional regulators, and stress response. Unsurprisingly, a similar set of essential genes was identified via Tn-seq in the metabolically versatile Alphaproteobacterium *Rhodopseudomonas palustris* (Pechter et al., 2016).

Ten of the 528 essential genes were located on ElOx9T's 128kb plasmid and encoded three transposases, two proteins in the type II toxin/antitoxin system, a transcriptional regulator, *repABC* operon involved in plasmid replication and segregation, and several hypothetical proteins. *repABC* plasmids are common among the Alphaproteobacteria (Cevallos et al., 2008). The presence of these features in the essential genome suggests that the plasmid is an indispensable genetic element, however, the role of plasmid-encoded genes in the growth and survival of ElOx9^T is not immediately clear and warrants further study.

Essential Genes Under Heterotrophic Conditions

The essential gene profiles for growth under heterotrophic conditions (LBS + Ions, SWB + acetate, and Pre-Electrochemistry) were remarkably similar. Eight genes were identified as essential in LBS + Ions only, eight in all conditions except LBS + Ions, 6 solely in SWB + acetate, and 4 in Pre-Electrochemistry (**Figure 2** and **Supplementary Table 16**). Most of these essential genes, regardless of growth condition, are predicted to be involved in major carbon metabolism pathways, such as the TCA cycle, glycolysis, and biosynthetic pathways. Despite seemingly incongruent essentiality calls for these genes in libraries grown under aerobic heterotrophic conditions, all but one of the genes identified as essential in one condition were designated essential, growth defect, or uncertain in all other conditions. That is, for all the genes deemed essential in at least one heterotrophic growth condition, only one of these genes was classified as non-essential in another growth condition. This gene, a DUF1643 domain-containing hypothetical protein (AKL02_18975), was essential or uncertain in all conditions except in LBS + Ions, where it was designated non-essential. BLASTP searches show that this protein is found in a variety of *Thioclava* species and organisms in closely related genera, although the role of DUF1643 remains unknown (Mir-Sanchis et al., 2016).

Oxidative Extracellular Electron Transfer in ElOx9^T Does Not Use the Sox System or Hydrogenases

Chemolithoautotrophic growth with thiosulfate, S^0, and H_2 serving as electron donors has been demonstrated in ElOx9^T

TABLE 2 | Distribution of gene essentiality calls for all libraries.

	Essential	Growth defect	Non-essential	Growth advantage	Uncertain
LBS + Ions	563	105	3,270	15	108
SWB + Acetate	584	105	3,249	10	113
Pre-Electrochemistry	580	99	3,250	11	121
Open Circuit	598	73	3,188	6	196
Electrochemistry	618	37	3,059	1	346

The "Uncertain" category represents the number of genes that had discrepancies in essentiality calls between all replicates.

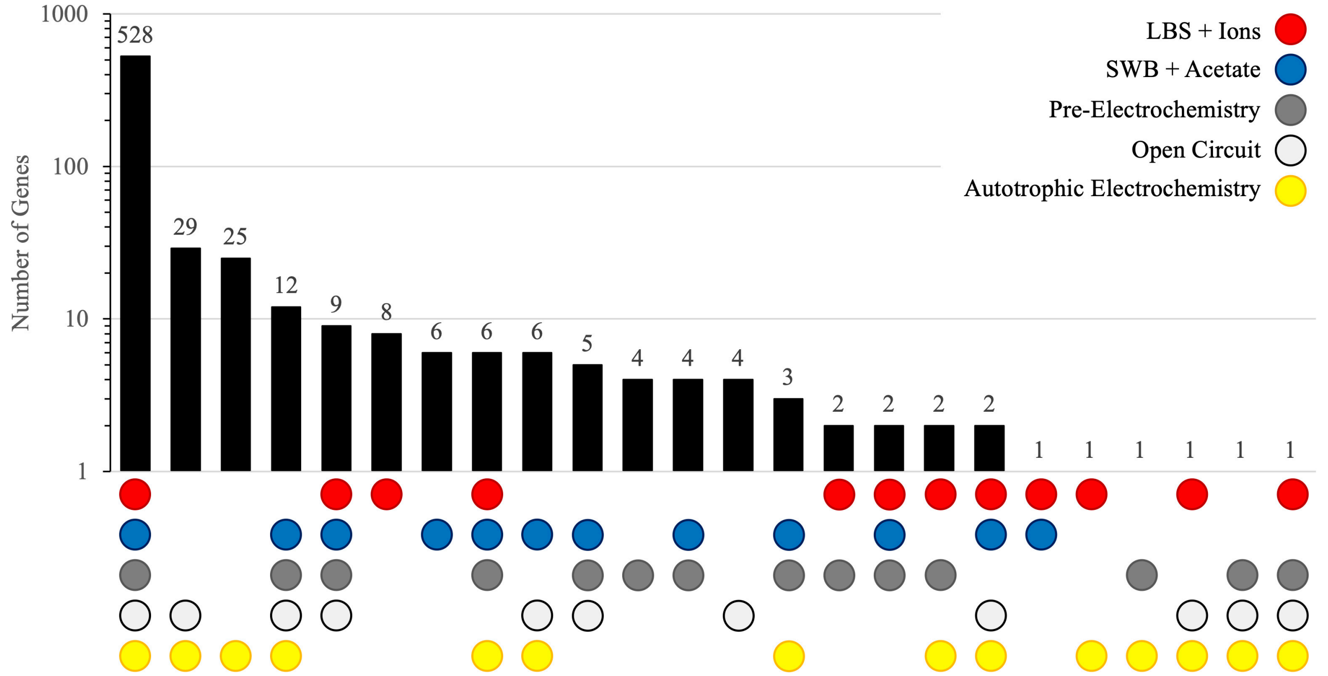

FIGURE 2 | UpSet plot showing the distribution of essential genes identified by Tn-seq under all five growth conditions (LBS + Ions – red circle, SWB + Acetate – blue circle, Pre-Electrochemistry (pre-growth in SWB + Acetate) – gray circle, Autotrophic Open Circuit condition – white circle, and Autotrophic Electrotrophy – yellow circle). Note: y-axis is log scale.

(Rowe et al., 2015; Chang et al., 2018). In bioelectrochemical investigations, electrodes are often poised at environmentally relevant redox potentials to mimic those of solid-phase minerals, effectively serving as non-corrodible proxies for minerals. In the present experiment, the working electrode was poised at –278 mV vs. SHE, just below the calculated redox potential for S^0 oxidation in artificial SWB at pH 8 (Rowe et al., 2015), which should provide the organisms with even more reducing power compared to S^0. To our surprise, Tn-seq revealed that *soxA*, *soxB*, *soxC*, *soxD*, *soxX*, *soxY*, and *soxZ* were non-essential for growth under any of the conditions tested. Similarly, with a single exception – a HypC/HybG/HupF family hydrogenase formation chaperone AKL02_15805 that was essential under all conditions tested – genes involved in hydrogenase biosynthesis were non-essential. This may seem unexpected, as the Mtr pathway in *S. oneidensis* MR-1 is required for both Fe^{3+} and Mn^{4+} reduction and anode reduction (Beliaev and Saffarini, 1998; Beliaev et al., 2001; Bretschger et al., 2007). This indicates that neither the *sox* system nor hydrogenases are essential for oxidative EET in ElOx9^T under the conditions tested. Interestingly, another *Thioclava* species, *T. dalianensis* DLFJ1-1^T (Zhang et al., 2013) has the capacity for electrode oxidation (Chang et al., 2018) but lacks the ability to oxidize reduced sulfur compounds (Liu et al., 2015). If electrode oxidation is a common feature among this genus and is evolutionarily conserved, these observations suggest that it is not unexpected that the *sox* system is not essential for oxidative EET and indicates some other mechanism is responsible for this phenotype.

Essential Genes for Extracellular Electron Transfer

Initially, open circuit control conditions were included to differentiate genes required for biofilm formation and attachment from those directly involved in EET. However, recent evidence has shown that microbial colonization on non-corrodible conductive materials (electrodes used in bioelectrochemical investigations) by organisms with EET capacity was responsible for a shift in open circuit potential by up to 150 mV, suggesting that conductive materials may be serving as conduits for EET even without an applied potential (Bird et al., 2021). Although open circuit potentials were not measured for our open circuit conditions, given the observation that some electroautotrophs are capable of catalyzing a shift in open-circuit potential, we chose to consider the 29 essential genes found in both open circuit and electrochemical conditions as putatively essential for EET in ElOx9^T alongside the 25 genes deemed essential under oxidative EET conditions alone. Nearly all genes deemed essential for oxidative EET were non-essential in all other conditions (excluding open circuit) and only five genes essential for both oxidative EET and open circuit were non-essential in all other conditions (**Supplementary Table 16**).

Unexpectedly, just one of these genes contains a putative heme-binding motif: AKL02_00085, a NAD(P)-dependent oxidoreductase predicted to localize in the cytoplasm. Known direct electron transfer mechanisms involve multiheme cytochromes localized to the outer membrane, in pili or nanowires, or contained in outer membrane vesicles [reviewed in (Paquete et al., 2022)]. To that end, just fourteen of the essential genes were predicted to localize to the cell envelope (**Table 3**). As we are most interested in genes involved in extracellular electron transfer, we focus our discussion on a few of these proteins predicted to facilitate potentially relevant redox reactions. Rubrerythrin family proteins (AKL_00835) are non-heme diiron proteins commonly found in anaerobic bacteria, some of which use electrons from NAD(P)H to reduce H_2O_2 to H_2O and alleviate oxidative stress (Caldas Nogueira et al., 2021). AKL02_16390 encodes a quinone-dependent dihydroorotate dehydrogenase. Dihydroorotate dehydrogenases are involved in pyrimidine biosynthesis but are also involved in energy metabolism. These flavin mononucleotide-containing enzymes facilitate the oxidation of dihydroorotate to orotate and transfer those electrons to quinones (Sousa et al., 2021). AKL02_07710 is annotated as a DUF59 domain-containing protein and BLASTP indicated this protein in ElOx9^T has nearly 100% homology to SUF system Fe-S cluster assembly proteins found in a variety of *Thioclava* species. Although the function of many DUF59 domain-containing proteins has yet to be determined, DUF59-containing SufT in *S. aureus* and *Sinorhizobium meliloti* have roles in iron-sulfur cluster assembly [reviewed in (Mashruwala and Boyd, 2018)]. Hypothetical protein AKL02_14895 lacks any biochemically characterized homologs, but pSORTb predicted a cytoplasmic membrane localization and InterProScan predicted a non-cytoplasmic region flanked by an N-terminal transmembrane helix and a C-terminal transmembrane region. Finally, AKL02_06520 is annotated as NADH:ubiquinone oxidoreductase subunit NDUFA12, a component of the mitochondrial respiratory chain complex I. In ElOx9^T, this gene is located in an operon with outer membrane lipid asymmetry maintenance protein mlaD (AKL02_06525, non-essential) and a DUF2155 domain-containing protein (AKL02_06530, non-essential). NDUFA12 is commonly found either in a domain fusion or a gene neighborhood with mlaD in the Alphaproteobacteria (Isom et al., 2017) and is theorized to form a supramolecular complex spanning both inner and outer membranes (Ekiert et al., 2017). The role of these proteins in EET cannot be directly discerned from Tn-seq data. In this instance, the utility of the Tn-seq approach was to identify genes which, when disrupted by transposon insertion, caused a significant deleterious effect on growth. Tn-seq successfully identified a short list of genes for investigating the mechanism of oxidative extracellular electron transfer in ElOx9^T.

Putative Genes Essential for Extracellular Electron Transfer in ElOx9^T Are Found in Other Electroactive *Thioclava* Species

Chang et al. (2018) demonstrated that three previously characterized species of *Thioclava* are also capable of electrode oxidation: *T. atlantica* 13D2W-2^T (Lai et al., 2014), *T. dalianensis* DLFJ1-1^T (Zhang et al., 2013), and *T. indica* DT-234^T (Liu et al., 2015). To evaluate the phylogenetic breadth of putative extracellular electron uptake pathways in *Thioclava* species, we used BLASTP to search the genomes of these three organisms for homologs to the essential EET genes identified in our Tn-Seq screen predicted to localize to the cellular envelope (**Table 3**).

TABLE 3 | Essential genes in electrochemistry or electrochemistry/open circuit conditions predicted to localize to the cell membrane or of unknown localization.

Locus tag	Product	KEGG Orthology	Localization (Score)	Homologs identified in other electrotrophic *Thioclava* species[1]
AKL02_09955	HlyC/CorC family transporter	–	Cytoplasmic Membrane (10)	A, B, C
AKL02_00835	rubrerythrin family protein	K22737	Cytoplasmic Membrane (10)	A, B, C
AKL02_02090	Na^+/H^+ antiporter subunit G	K05564	Cytoplasmic Membrane (10)	A, B, C
AKL02_12420	CDP-diacylglycerol–serine O-phosphatidyltransferase	K17103	Cytoplasmic Membrane (10)	A, B, C
AKL02_06280	ribosome biogenesis GTPase Der	K03977	Cytoplasmic Membrane (7.88)	A, B, C
AKL02_20245	ParA family protein	K03496	Cytoplasmic Membrane (7.88)	A, B, C
AKL02_00700	flagellar basal body-associated FliL family protein	K02415	Cytoplasmic Membrane (9.82)	A*, C*
AKL02_16390	quinone-dependent dihydroorotate dehydrogenase	K00254	Cytoplasmic Membrane (9.82)	A, B*, C
AKL02_11895	ABC transporter ATP-binding protein	K02013	Cytoplasmic Membrane (9.82)	A, B, C
AKL02_14895	hypothetical protein	–	Cytoplasmic Membrane (9.86)	Aˆ, Bˆ, Cˆ
AKL02_10975	PAS domain-containing sensor histidine kinase	K13598	Cytoplasmic Membrane (9.99)	A, B, C
AKL02_06725	biopolymer transporter ExbD	K03559	Unknown (2.5)	A*, C*
AKL02_06520	NADH:ubiquinone oxidoreductase subunit NDUFA12	–	Unknown (2)	A, B, C
AKL02_07710	DUF59 domain-containing protein	–	Unknown (2)	A, B, C

[1] *Electrotrophic Thioclava species: A, T. atlantica 13D2W-2^T; B, T. dalianensis DLFJ1-1^T; C, T. indica DT-234^T. Proteins are considered conserved if BLASTP results indicate > 80% AAI and > 80% query coverage.*

**60–80% AAI with > 80% query coverage.*

ˆ60–80% query coverage with > 80% AAI.

Homologs for all genes were found in 13D2W-2^T and DT-234^T, and homologs for all but two genes were found in DLFJ1-1^T. The presence of nearly all the essential EET genes in ElOx9^T that localize to the cellular envelope in other electroactive *Thioclava* species (**Table 3**) may hint at a conserved mechanism of oxidative EET in this clade of organisms. Further investigation into the involvement of these genes in oxidative EET and the phylogeny of these proteins will help shed light on this outstanding question.

Genes Implicated in Oxidative Extracellular Electron Transfer in *S. oneidensis* MR-1 Are Found in ElOx9^T, but Are Non-essential

A recent study into the genetic basis of oxidative EET in MR-1 has shed light on the genetic basis of oxidative EET in this organism. Rowe et al. (2021) identified five proteins that, while not essential for oxidative EET, their deletion results in a statistically significant reduction in electron uptake. Given the lack of knowledge on oxidative EET mechanisms, we searched for homologs of the oxidative EET proteins identified in MR-1 in the genome of ElOx9^T. Four of the five proteins newly identified in the electron uptake pathway in MR-1 have putative homologs in ElOx9^T (**Supplementary Table 17**). AKL02_11685, AKL02_17145, and AKL02_17885 were all deemed non-essential under the growth conditions tested. The essentiality of AKL02_15595 was deemed uncertain under electrotrophic conditions and non-essential under all others; however, this gene was non-essential in three of the four electrochemistry replicates and was classified as a growth defect in the fourth. These data suggest that the oxidative EET genes identified in ElOx9^T are non-essential under all conditions tested, but this does not indicate that they do not play a role in oxidative EET. In fact, these five genes were identified in MR-1 by specifically targeting non-essential genes in the genome; they are not essential for oxidative EET in MR-1. This same phenomenon may be true in ElOx9^T and the identification of these genes in ElOx9^T provides a starting place for investigating the role of non-essential genes in oxidative EET and expanding our knowledge of the diversity of EET mechanisms among Bacteria.

CONCLUSION

We employed the Tn-seq approach to glean information on the genetic underpinnings of oxidative extracellular electron transfer in the metabolically versatile Alphaproteobacterium *T. electrotropha* ElOx9^T and identified 54 proteins not previously implicated in this process. While the majority of EET essential proteins are predicted to localize to the cytoplasm, a subset localizes to the cell envelope or has unknown localizations. To our surprise, none of the genes identified are multiheme cytochromes. The lack of heme-binding-motif-containing proteins essential for EET may be due to redundant or overlapping functions of multiple proteins involved in the EET pathway or could be due to ElOx9^T employing multiple EET pathways altogether. For example, *G. sulfurreducens* employs a variety of mechanisms to transfer electrons to/from the extracellular environment, including conductive pili and periplasmic, inner-, and outer-membrane-bound *c*-type cytochromes, all of which have multiple homologs encoded in the genome (Reguera et al., 2005; Shi et al., 2009; Chan et al., 2017; Uekia, 2021). If ElOx9^T employs multiple mechanisms for EET, Tn-seq may not aid in identifying EET genes. Another possibility is that disruption of certain genes involved in EET does not result in a loss of function. Rowe et al. (2021) identified five proteins involved in oxidative EET that were deemed non-essential in Tn-seq screens. All these genes, when individually deleted, resulted in reduced capacity for electron uptake but did not knock out EET capacity entirely. Thus, it is conceivable that genes involved in EET may not be identified as essential unless their disruption results in a highly deleterious or lethal effect on growth. These investigations highlight the potential complexities to be aware of while investigating EET mechanisms in non-model organisms.

DATA AVAILABILITY STATEMENT

The data presented in the study are deposited in the NCBI Sequence Read Archive repository, accession numbers SRR18508951, SRR18508952, GCA_002085925.2, and PRJNA821218.

AUTHOR CONTRIBUTIONS

AR conceived and designed the work. AR and NK contributed to methods development. AR, NK, EL, and JS executed the experiments. JS, AR, TS, and EW analyzed the data. JS drafted the manuscript. All authors revised the manuscript and approved the submitted version.

FUNDING

This work was supported by Center for Deep Energy Biosphere Investigations small research grant (NSF-STC-OCE0939564) awarded to AR. This work was C-DEBI contribution to 595. JS was supported by a National Science Foundation Postdoctoral Research Fellowship (NSF OCE-PRF 2126677).

ACKNOWLEDGMENTS

We thank J. Gralnick and D. Bond for the pEB001 plasmid. We also thank the reviewers for comments and suggestions that improved the manuscript.

SUPPLEMENTARY MATERIAL

The Supplementary Material for this article can be found online at: https://www.frontiersin.org/articles/10.3389/fmicb.2022.909824/full#supplementary-material

REFERENCES

Almagro Armenteros, J. J., Tsirigos, K. D., Sønderby, C. K., Petersen, T. N., Winther, O., Brunak, S., et al. (2019). SignalP 5.0 improves signal peptide predictions using deep neural networks. *Nat. Biotechnol.* 374, 420–423. doi: 10.1038/s41587-019-0036-z

Barco, R. A., Emerson, D., Sylvan, J. B., Orcutt, B. N., Jacobson Meyers, M. E., Ramírez, G. A., et al. (2015). New insight into microbial iron oxidation as revealed by the proteomic profile of an obligate iron-oxidizing chemolithoautotroph. *Appl. Environ. Microbiol.* 81, 5927–5937. doi: 10.1128/AEM.01374-15

Baym, M., Shaket, L., Anzai, I. A., Adesina, O., and Barstow, B. (2016). Rapid construction of a whole-genome transposon insertion collection for Shewanella oneidensis by Knockout Sudoku. *Nat. Commun.* 71:13270. doi: 10.1038/ncomms13270

Beliaev, A. S., and Saffarini, D. A. (1998). Shewanella putrefaciens mtrB Encodes an Outer Membrane Protein Required for Fe(III) and Mn(IV) Reduction. *J. Bacteriol.* 180, 6292–6297. doi: 10.1128/JB.180.23.6292-6297.1998

Beliaev, A. S., Saffarini, D. A., McLaughlin, J. L., and Hunnicutt, D. (2001). MtrC, an outer membrane decahaem c cytochrome required for metal reduction in Shewanella putrefaciens MR-1. *Mol. Microbiol.* 39, 722–730. doi: 10.1046/J.1365-2958.2001.02257.X

Bird, L. J., Tender, L. M., Eddie, B., Oh, E., Phillips, D. A., and Glaven, S. M. (2021). Microbial survival and growth on non-corrodible conductive materials. *Environ. Microbiol.* 23, 7231–7244. doi: 10.1111/1462-2920.15810

Bolger, A. M., Lohse, M., and Usadel, B. (2014). Trimmomatic: a flexible trimmer for Illumina sequence data. *Bioinformatics* 30, 2114–2120. doi: 10.1093/BIOINFORMATICS/BTU170

Bond, D. R., and Lovley, D. R. (2003). Electricity production by Geobacter sulfurreducens attached to electrodes. *Appl. Environ. Microbiol.* 69, 1548–1555. doi: 10.1128/AEM.69.3.1548-1555.2003

Bose, A., Gardel, E. J., Vidoudez, C., Parra, E. A., and Girguis, P. R. (2014). Electron uptake by iron-oxidizing phototrophic bacteria. *Nat. Commun.* 5:3391. doi: 10.1038/ncomms4391

Bouhenni, R., Gehrke, A., and Saffarini, D. (2005). Identification of genes involved in cytochrome c biogenesis in Shewanella oneidensis, using a modified mariner transposon. *Appl. Environ. Microbiol.* 71, 4935–4937. doi: 10.1128/AEM.71.8.4935-4937.2005

Bretschger, O., Obraztsova, A., Sturm, C. A., In, S. C., Gorby, Y. A., Reed, S. B., et al. (2007). Current production and metal oxide reduction by Shewanella oneidensis MR-1 wild type and mutants. *Appl. Environ. Microbiol.* 73, 7003–7012. doi: 10.1128/AEM.01087-07

Brutinel, E. D., and Gralnick, J. A. (2012). Anomalies of the anaerobic tricarboxylic acid cycle in Shewanella oneidensis revealed by Tn-seq. *Mol. Microbiol.* 86, 273–283. doi: 10.1111/J.1365-2958.2012.08196.X

Buchfink, B., Xie, C., and Huson, D. H. (2014). Fast and sensitive protein alignment using DIAMOND. *Nat. Methods* 121, 59–60. doi: 10.1038/nmeth.3176

Burd, A. B., Hansell, D. A., Steinberg, D. K., Anderson, T. R., Arístegui, J., Baltar, F., et al. (2010). Assessing the apparent imbalance between geochemical and biochemical indicators of meso- and bathypelagic biological activity: what the @$#! is wrong with present calculations of carbon budgets? *Deep Sea Res. Part II Top. Stud. Oceanogr.* 57, 1557–1571. doi: 10.1016/J.DSR2.2010.02.022

Busk, P. K., Pilgaard, B., Lezyk, M. J., Meyer, A. S., and Lange, L. (2017). Homology to peptide pattern for annotation of carbohydrate-active enzymes and prediction of function. *BMC Bioinforma.* 18:214. doi: 10.1186/S12859-017-1625-9

Caldas Nogueira, M. L., Pastore, A. J., and Davidson, V. L. (2021). Diversity of structures and functions of oxo-bridged non-heme diiron proteins. *Arch. Biochem. Biophys.* 705:108917. doi: 10.1016/J.ABB.2021.108917

Cameron, D. E., Urbach, J. M., and Mekalanos, J. J. (2008). A defined transposon mutant library and its use in identifying motility genes in *Vibrio cholerae*. *Proc. Natl. Acad. Sci. U. S. A.* 105, 8736–8741. doi: 10.1073/PNAS.0803281105

Cevallos, M. A., Cervantes-Rivera, R., and Gutiérrez-Ríos, R. M. (2008). The repABC plasmid family. *Plasmid* 60, 19–37. doi: 10.1016/J.PLASMID.2008.03.001

Chan, C. H., Levar, C. E., Jiménez-Otero, F., and Bond, D. R. (2017). Genome scale mutational analysis of Geobacter sulfurreducens reveals distinct molecular mechanisms for respiration and sensing of poised electrodes versus Fe(III) oxides. *J. Bacteriol.* 199, e340–e317. doi: 10.1128/JB.00340-17

Chang, R., Bird, L., Barr, C., Osburn, M., Wilbanks, E., Nealson, K., et al. (2018). Thioclava electrotropha sp. Nov., a versatile electrode and sulfur-oxidizing bacterium from marine sediments. *Int. J. Syst. Evol. Microbiol.* 68, 1652–1658. doi: 10.1099/ijsem.0.002723

Chaumeil, P.-A., Mussig, A. J., Hugenholtz, P., and Parks, D. H. (2020). GTDB-Tk: a toolkit to classify genomes with the Genome Taxonomy Database. *Bioinformatics* 36, 1925–1927. doi: 10.1093/BIOINFORMATICS/BTZ848

Cosquer, A., Pichereau, V., Pocard, J. A., Minet, J., Cormier, M., and Bernard, T. (1999). Nanomolar levels of dimethylsulfoniopropionate, dimethylsulfonioacetate, and glycine betaine are sufficient to confer osmoprotection to *Escherichia coli*. *Appl. Environ. Microbiol.* 65, 3304–3311. doi: 10.1128/AEM.65.8.3304-3311.1999

Ekiert, D. C., Bhabha, G., Isom, G. L., Greenan, G., Ovchinnikov, S., Henderson, I. R., et al. (2017). Architectures of Lipid Transport Systems for the Bacterial Outer Membrane. *Cell* 169, 273–285.e17. doi: 10.1016/J.CELL.2017.03.019

Emerson, D. (2012). Biogeochemistry and microbiology of microaerobic Fe(II) oxidation. *Biochem. Soc. Trans.* 40, 1211–1216. doi: 10.1042/BST20120154

Freed, N. E. (2017). Creation of a Dense Transposon Insertion Library Using Bacterial Conjugation in Enterobacterial Strains Such As *Escherichia Coli* or *Shigella* flexneri. *J. Vis. Exp.* 23:56216. doi: 10.3791/56216

Gao, Y., Lee, J., Neufeld, J. D., Park, J., Rittmann, B. E., and Lee, H. S. (2017). Anaerobic oxidation of methane coupled with extracellular electron transfer to electrodes. *Sci. Reports* 7:5099. doi: 10.1038/s41598-017-05180-9

Glass, J. I., Assad-Garcia, N., Alperovich, N., Yooseph, S., Lewis, M. R., Maruf, M., et al. (2006). Essential genes of a minimal bacterium. *Proc. Natl. Acad. Sci.U. S. A.* 103, 425–430. doi: 10.1073/PNAS.0510013103

Gordon, A., and Hannon, G. J. (2010). *Fastx-Toolkit. FASTQ/A Short-Reads Preprocessing Tools (unpublished)*. Available online at: http://hannonlab.cshl.edu/fastx_toolkit. (accessed April 6, 2020).

Gralnick, J. A., and Newman, D. K. (2007). Extracellular respiration. *Mol. Microbiol.* 65, 1–11. doi: 10.1111/J.1365-2958.2007.05778.X

Gupta, D., Guzman, M. S., and Bose, A. (2020). Extracellular electron uptake by autotrophic microbes: physiological, ecological, and evolutionary implications. *J. Ind. Microbiol. Biotechnol.* 47, 863–876. doi: 10.1007/S10295-020-02309-0

Gurevich, A., Saveliev, V., Vyahhi, N., and Tesler, G. (2013). QUAST: quality assessment tool for genome assemblies. *Bioinformatics* 29, 1072–1075. doi: 10.1093/bioinformatics/btt086

Guzman, M. S., Rengasamy, K., Binkley, M. M., Jones, C., Ranaivoarisoa, T. O., Singh, R., et al. (2019). Phototrophic extracellular electron uptake is linked to carbon dioxide fixation in the bacterium Rhodopseudomonas palustris. *Nat. Commun.* 10:1355. doi: 10.1038/s41467-019-09377-6

Haft, D. H., DiCuccio, M., Badretdin, A., Brover, V., Chetvernin, V., O'Neill, K., et al. (2018). RefSeq: an update on prokaryotic genome annotation and curation. *Nucleic Acids Res.* 46, D851–D860. doi: 10.1093/NAR/GKX1068

Hulo, N., Bairoch, A., Bulliard, V., Cerutti, L., De Castro, E., Langendijk-Genevaux, P. S., et al. (2006). The PROSITE database. *Nucleic. Acids Res.* 34, D227–D230. doi: 10.1093/nar/gkj063

Ilbert, M., and Bonnefoy, V. (2013). Insight into the evolution of the iron oxidation pathways. *Biochim. Biophys. Acta Bioenerg.* 1827, 161–175. doi: 10.1016/J.BBABIO.2012.10.001

Isom, G. L., Davies, N. J., Chong, Z. S., Bryant, J. A., Jamshad, M., Sharif, M., et al. (2017). MCE domain proteins: conserved inner membrane lipid-binding proteins required for outer membrane homeostasis. *Sci. Rep.* 7:8608. doi: 10.1038/s41598-017-09111-6

Jacobs, M. A., Alwood, A., Thaipisuttikul, I., Spencer, D., Haugen, E., Ernst, S., et al. (2003). Comprehensive transposon mutant library of *Pseudomonas aeruginosa*. *Proc. Natl. Acad. Sci. U. S. A.* 100, 14339–14344. doi: 10.1073/PNAS.2036282100

Jiao, Y., and Newman, D. K. (2007). The pio operon is essential for phototrophic Fe(II) oxidation in Rhodopseudomonas palustris TIE-1. *J. Bacteriol.* 189, 1765–1773. doi: 10.1128/JB.00776-06

Kallmeyer, J., Pockalny, R., Adhikari, R. R., Smith, D. C., and D'Hondt, S. (2012). Global distribution of microbial abundance and biomass in subseafloor sediment. *Proc. Natl. Acad. Sci.U. S. A.* 109, 16213–16216. doi: 10.1073/PNAS.1203849109

Kanehisa, M., Sato, Y., and Morishima, K. (2016). BlastKOALA and GhostKOALA: KEGG Tools for Functional Characterization of Genome and Metagenome Sequences. *J. Mol. Biol.* 428, 726–731. doi: 10.1016/j.jmb.2015.11.006

Karbelkar, A. A., Rowe, A. R., and El-Naggar, M. Y. (2019). An electrochemical investigation of interfacial electron uptake by the sulfur oxidizing bacterium Thioclava electrotropha ElOx9. *Electrochim. Acta* 324:134838. doi: 10.1016/j.electacta.2019.134838

Kolmogorov, M., Yuan, J., Lin, Y., and Pevzner, P. A. (2019). Assembly of long, error-prone reads using repeat graphs. *Nat. Biotechnol.* 37, 540–546. doi: 10.1038/s41587-019-0072-8

Lai, Q., Li, S., Xu, H., Jiang, L., Zhang, R., and Shao, Z. (2014). Thioclava atlantica sp. nov., isolated from deep sea sediment of the Atlantic Ocean. *Antonie Van Leeuwenhoek* 106, 919–925. doi: 10.1007/S10482-014-0261-X

Lam, B. R., Barr, C. R., Rowe, A. R., and Nealson, K. H. (2019). Differences in Applied Redox Potential on Cathodes Enrich for Diverse Electrochemically Active Microbial Isolates From a Marine Sediment. *Front. Microbiol.* 10:1979. doi: 10.3389/fmicb.2019.01979

Lam, B. R., Rowe, A. R., and Nealson, K. H. (2018). Variation in electrode redox potential selects for different microorganisms under cathodic current flow from electrodes in marine sediments. *Environ. Microbiol.* 20, 2270–2287. doi: 10.1111/1462-2920.14275

Lampe, D. J., Grant, T. E., and Robertson, H. M. (1998). Factors Affecting Transposition of the Himar1 mariner Transposon in Vitro. *Genetics* 149, 179–187. doi: 10.1093/GENETICS/149.1.179

Langmead, B., Trapnell, C., Pop, M., and Salzberg, S. L. (2009). Ultrafast and memory-efficient alignment of short DNA sequences to the human genome. *Genome Biol.* 10:R25. doi: 10.1186/GB-2009-10-3-R25

Li, H., and Durbin, R. (2010). Fast and accurate long-read alignment with Burrows-Wheeler transform. *Bioinformatics* 26, 589–595. doi: 10.1093/bioinformatics/btp698

Lies, D. P., Hernandez, M. E., Kappler, A., Mielke, R. E., Gralnick, J. A., and Newman, D. K. (2005). Shewanella oneidensis MR-1 uses overlapping pathways for iron reduction at a distance and by direct contact under conditions relevant for biofilms. *Appl. Environ. Microbiol.* 71, 4414–4426. doi: 10.1128/AEM.71.8.4414-4426.2005

Liu, J., Wang, Z., Belchik, S. M., Edwards, M. J., Liu, C., Kennedy, D. W., et al. (2012). Identification and characterization of M to A: a decaheme c-type cytochrome of the neutrophilic Fe(ll)-oxidizing bacterium Sideroxydans lithotrophicus ES-1. *Front. Microbiol.* 3:37. doi: 10.3389/FMICB.2012.00037

Liu, Y., Lai, Q., Du, J., Xu, H., Jiang, L., and Shao, Z. (2015). Thioclava indica sp. nov., isolated from surface seawater of the Indian Ocean. *Antonie Van Leeuwenhoek* 107, 297–304. doi: 10.1007/S10482-014-0320-3

Liu, Y., Lai, Q., and Shao, Z. (2017). A Multilocus Sequence Analysis Scheme for Phylogeny of Thioclava Bacteria and Proposal of Two Novel Species. *Front. Microbiol.* 8:1321. doi: 10.3389/FMICB.2017.01321

Lombard, V., Golaconda Ramulu, H., Drula, E., Coutinho, P. M., and Henrissat, B. (2014). The carbohydrate-active enzymes database (CAZy) in 2013. *Nucleic Acids Res.* 42, D490–D495. doi: 10.1093/NAR/GKT1178

Lovelock, J. E., Maggs, R. J., and Rasmussen, R. A. (1972). Atmospheric Dimethyl Sulphide and the Natural Sulphur Cycle. *Nature* 237, 452–453. doi: 10.1038/237452a0

Mashruwala, A. A., and Boyd, J. M. (2018). Investigating the role(s) of SufT and the domain of unknown function 59 (DUF59) in the maturation of iron–sulfur proteins. *Curr. Genet.* 64, 9–16. doi: 10.1007/S00294-017-0716-5

Mir-Sanchis, I., Roman, C. A., Misiura, A., Pigli, Y. Z., Boyle-Vavra, S., and Rice, P. A. (2016). Staphylococcal SCCmec elements encode an active MCM-like helicase and thus may be replicative. *Nat. Struct. Mol. Biol.* 2310, 891–898. doi: 10.1038/nsmb.3286

Myers, C. R., and Nealson, K. H. (1988). Microbial reduction of manganese oxides: interactions with iron and sulfur. *Geochim. Cosmochim. Acta* 52, 2727–2732. doi: 10.1016/0016-7037(88)90041-5

Nevin, K. P., and Lovley, D. R. (2010). Mechanisms for Fe(III) Oxide Reduction in Sedimentary Environments. *Geomicrobiology* 19, 141–159. doi: 10.1080/01490450252864253

Ohio Supercomputer Center (1987). *Ohio Supercomputer Center. Columbus OH: Ohio Supercomputer Center*. Ohio: Ohio Supercomputer Center.

Paquete, C. M., Rosenbaum, M. A., Bañeras, L., Rotaru, A. E., and Puig, S. (2022). Let's chat: communication between electroactive microorganisms. *Bioresour. Technol.* 347:126705. doi: 10.1016/J.BIORTECH.2022.126705

Parks, D. H., Imelfort, M., Skennerton, C. T., Hugenholtz, P., and Tyson, G. W. (2015). CheckM: assessing the quality of microbial genomes recovered from isolates, single cells, and metagenomes. *Genome Res.* 25, 1043–1055. doi: 10.1101/gr.186072.114

Pechter, K. B., Gallagher, L., Pyles, H., Manoil, C. S., and Harwood, C. S. (2016). Essential genome of the metabolically versatile alphaproteobacterium Rhodopseudomonas palustris. *J. Bacteriol.* 198, 867–876. doi: 10.1128/JB.00771-15

Perry, B. J., and Yost, C. K. (2014). Construction of a mariner-based transposon vector for use in insertion sequence mutagenesis in selected members of the Rhizobiaceae. *BMC Microbiol.* 14:298. doi: 10.1186/S12866-014-0298-Z

Qu, B., Fan, B., Zhu, S., and Zheng, Y. (2014). Anaerobic ammonium oxidation with an anode as the electron acceptor. *Environ. Microbiol. Rep.* 6, 100–105. doi: 10.1111/1758-2229.12113

Reguera, G., and Kashefi, K. (2019). The electrifying physiology of Geobacter bacteria, 30 years on. *Adv. Microb. Physiol.* 74, 1–96. doi: 10.1016/BS.AMPBS.2019.02.007

Reguera, G., McCarthy, K. D., Mehta, T., Nicoll, J. S., Tuominen, M. T., and Lovley, D. R. (2005). Extracellular electron transfer via microbial nanowires. *Nature* 435, 1098–1101. doi: 10.1038/nature03661

Richter, K., Schicklberger, M., and Gescher, J. (2012). Dissimilatory reduction of extracellular electron acceptors in anaerobic respiration. *Appl. Environ. Microbiol.* 78, 913–921. doi: 10.1128/AEM.06803-11

Rodriguez-R, L. M., and Konstantinidis, K. T. (2016). The enveomics collection: a toolbox for specialized analyses of microbial genomes and metagenomes. *PeerJ Preprints.* 4:e1900v1. doi: 10.7287/PEERJ.PREPRINTS.1900V1

Rollefson, J. B., Levar, C. E., and Bond, D. R. (2009). Identification of genes involved in biofilm formation and respiration via mini-Himar transposon mutagenesis of Geobacter sulfurreducens. *J. Bacteriol.* 191, 4207–4217. doi: 10.1128/JB.00057-09

Rotaru, A. E., Shrestha, P. M., Liu, F., Markovaite, B., Chen, S., Nevin, K. P., et al. (2014). Direct interspecies electron transfer between Geobacter metallireducens and Methanosarcina barkeri. *Appl. Environ. Microbiol.* 80, 4599–4605. doi: 10.1128/AEM.00895-14

Rowe, A. R., Chellamuthu, P., Lam, B., Okamoto, A., and Nealson, K. H. (2015). Marine sediments microbes capable of electrode oxidation as a surrogate for lithotrophic insoluble substrate metabolism. *Front. Microbiol.* 6:784. doi: 10.3389/fmicb.2014.00784

Rowe, A. R., Salimijazi, F., Trutschel, L., Sackett, J., Adesina, O., Anzai, I., et al. (2021). Identification of a pathway for electron uptake in Shewanella oneidensis. *Commun. Biol.* 4:957. doi: 10.1038/s42003-021-02454-x

Scheller, S., Yu, H., Chadwick, G. L., McGlynn, S. E., and Orphan, V. J. (2016). Artificial electron acceptors decouple archaeal methane oxidation from sulfate reduction. *Science* 351, 703–707. doi: 10.1126/SCIENCE.AAD7154

Shaw, D. R., Ali, M., Katuri, K. P., Gralnick, J. A., Reimann, J., Mesman, R., et al. (2020). Extracellular electron transfer-dependent anaerobic oxidation of ammonium by anammox bacteria. *Nat. Commun.* 11, 2058–2070. doi: 10.1038/s41467-020-16016-y

Shen, H. B., Yong, X. Y., Chen, Y. L., Liao, Z. H., Si, R. W., Zhou, J., et al. (2014). Enhanced bioelectricity generation by improving pyocyanin production and membrane permeability through sophorolipid addition in *Pseudomonas aeruginosa*-inoculated microbial fuel cells. *Bioresour. Technol.* 167, 490–494. doi: 10.1016/J.BIORTECH.2014.05.093

Shi, L., Richardson, D. J., Wang, Z., Kerisit, S. N., Rosso, K. M., Zachara, J. M., et al. (2009). The roles of outer membrane cytochromes of Shewanella and Geobacter in extracellular electron transfer. *Environ. Microbiol. Rep.* 1, 220–227. doi: 10.1111/j.1758-2229.2009.00035.x

Sorokin, D. Y., Tourova, T. P., Spiridonova, E. M., Rainey, F. A., and Muyzer, G. (2005). Thioclava pacifica gen. nov., sp. nov., a novel facultatively autotrophic, marine, sulfur-oxidizing bacterium from a near-shore sulfidic hydrothermal area. *Int. J. Syst. Evol. Microbiol.* 55, 1069–1075. doi: 10.1099/IJS.0.63415-0

Sousa, F. M., Refojo, P. N., and Pereira, M. M. (2021). Investigating the amino acid sequences of membrane bound dihydroorotate:quinone oxidoreductases (DHOQOs): structural and functional implications. *Biochim. Biophys. Acta Bioenerg.* 1862:148321. doi: 10.1016/J.BBABIO.2020.148321

Summers, Z. M., Gralnick, J. A., and Bond, D. R. (2013). Cultivation of an obligate Fe(II)-oxidizing lithoautotrophic bacterium using electrodes. *MBio* 4, 420–432. doi: 10.1128/MBIO.00420-12

Swan, B. K., Martinez-Garcia, M., Preston, C. M., Sczyrba, A., Woyke, T., Lamy, D., et al. (2011). Potential for chemolithoautotrophy among ubiquitous bacteria lineages in the dark ocean. *Science* 333, 1296–1300. doi: 10.1126/SCIENCE.1203690

Tatusova, T., DiCuccio, M., Badretdin, A., Chetvernin, V., Nawrocki, E. P., Zaslavsky, L., et al. (2016). NCBI prokaryotic genome annotation pipeline. *Nucleic Acids Res.* 44, 6614–6624. doi: 10.1093/NAR/GKW569

Uekia, T. (2021). Cytochromes in Extracellular Electron Transfer in Geobacter. *Appl. Environ. Microbiol.* 87, e3109–e3120. doi: 10.1128/AEM.03109-20

van Opijnen, T., Bodi, K. L., and Camilli, A. (2009). Tn-seq: high-throughput parallel sequencing for fitness and genetic interaction studies in microorganisms. *Nat. Methods* 610, 767–772. doi: 10.1038/nmeth.1377

Villano, M., Aulenta, F., Ciucci, C., Ferri, T., Giuliano, A., and Majone, M. (2010). Bioelectrochemical reduction of CO2 to CH4 via direct and indirect extracellular electron transfer by a hydrogenophilic methanogenic culture. *Bioresour. Technol.* 101, 3085–3090. doi: 10.1016/J.BIORTECH.2009.12.077

Walker, B. J., Abeel, T., Shea, T., Priest, M., Abouelliel, A., Sakthikumar, S., et al. (2014). Pilon: an integrated tool for comprehensive microbial variant detection and genome assembly improvement. *PLoS One* 9:e112963. doi: 10.1371/journal.pone.0112963

Wong, Y. C., El Ghany, M. A., Naeem, R., Lee, K. W., Tan, Y. C., Pain, A., et al. (2016). Candidate essential genes in Burkholderia cenocepacia J2315 identified by genome-wide TraDIS. *Front. Microbiol.* 7:1288. doi: 10.3389/fmicb.2016.01288

Yang, H., Krumholz, E. W., Brutinel, E. D., Palani, N. P., Sadowsky, M. J., Odlyzko, A. M., et al. (2014). Genome-Scale Metabolic Network Validation of Shewanella oneidensis Using Transposon Insertion Frequency Analysis. *PLoS Comput. Biol.* 10:e1003848. doi: 10.1371/JOURNAL.PCBI.1003848

Yin, Y., Mao, X., Yang, J., Chen, X., Mao, F., and Xu, Y. (2012). dbCAN: a web resource for automated carbohydrate-active enzyme annotation. *Nucleic Acids Res.* 40, W445–W451. doi: 10.1093/NAR/GKS479

Yoch, D. C. (2002). Dimethylsulfoniopropionate: its Sources, Role in the Marine Food Web, and Biological Degradation to Dimethylsulfide. *Appl. Environ. Microbiol.* 68:5804. doi: 10.1128/AEM.68.12.5804-5815.2002

Yu, N. Y., Wagner, J. R., Laird, M. R., Melli, G., Rey, S., Lo, R., et al. (2010). PSORTb 3.0: improved protein subcellular localization prediction with refined localization subcategories and predictive capabilities for all prokaryotes. *Bioinformatics* 26, 1608–1615. doi: 10.1093/bioinformatics/btq249

Zhang, H., Yohe, T., Huang, L., Entwistle, S., Wu, P., Yang, Z., et al. (2018). dbCAN2: a meta server for automated carbohydrate-active enzyme annotation. *Nucleic Acids Res.* 46, W95–W101. doi: 10.1093/NAR/GKY418

Zhang, R., Lai, Q., Wang, W., Li, S., and Shao, Z. (2013). Thioclava dalianensis sp. nov., isolated from surface seawater. *Int. J. Syst. Evol. Microbiol.* 63, 2981–2985. doi: 10.1099/IJS.0.046094-0

Zheng, Y., Wang, J., Zhou, S., Zhang, Y., Liu, J., Xue, C.-X. X., et al. (2020). Bacteria are important dimethylsulfoniopropionate producers in marine aphotic and high-pressure environments. *Nat. Commun.* 11:4658. doi: 10.1038/s41467-020-18434-4

Conflict of Interest: The authors declare that the research was conducted in the absence of any commercial or financial relationships that could be construed as a potential conflict of interest.

frontiers | Frontiers in Microbiology

ORIGINAL RESEARCH
published: 17 June 2022
doi: 10.3389/fmicb.2022.909109

Reduction Kinetic of Water Soluble Metal Salts by *Geobacter sulfurreducens*: Fe^{2+}/Hemes Stabilize and Regulate Electron Flux Rates

Maksym Karamash*[1], *Michael Stumpe*[2], *Jörn Dengjel*[2], *Carlos A. Salgueiro*[3,4], *Bernd Giese*[1]* and *Katharina M. Fromm*[1]

[1] Department of Chemistry, University of Fribourg, Fribourg, Switzerland, [2] Department of Biology, University of Fribourg, Fribourg, Switzerland, [3] Associate Laboratory i4HB – Institute for Health and Bioeconomy, School of Science and Technology, NOVA University Lisbon, Costa da Caparica, Portugal, [4] UCIBIO – Applied Molecular Biosciences Unit, Chemistry Department, School of Science and Technology, NOVA University Lisbon, Costa da Caparica, Portugal

OPEN ACCESS

Edited by:
Amelia-Elena Rotaru,
University of Southern Denmark,
Denmark

Reviewed by:
Yonggang Yang,
Guangdong Academy of Science,
China
Alessandro Carmona,
Research Centre for Energy
Resources and Consumption, Spain

****Correspondence:***
Bernd Giese
bernd.giese@unifr.ch
Katharina M. Fromm
katharina.fromm@unifr.ch

Specialty section:
This article was submitted to
Microbiological Chemistry
and Geomicrobiology,
a section of the journal
Frontiers in Microbiology

Received: *31 March 2022*
Accepted: *20 May 2022*
Published: *17 June 2022*

Citation:
Karamash M, Stumpe M, Dengjel J, Salgueiro CA, Giese B and Fromm KM (2022) Reduction Kinetic of Water Soluble Metal Salts by Geobacter sulfurreducens: Fe^{2+}/Hemes Stabilize and Regulate Electron Flux Rates. Front. Microbiol. 13:909109. doi: 10.3389/fmicb.2022.909109

Geobacter sulfurreducens is a widely applied microorganism for the reduction of toxic metal salts, as an electron source for bioelectrochemical devices, and as a reagent for the synthesis of nanoparticles. In order to understand the influence of metal salts, and of electron transporting, multiheme *c*-cytochromes on the electron flux during respiration of *G. sulfurreducens*, the reduction kinetic of Fe^{3+}, Co^{3+}, V^{5+}, Cr^{6+}, and Mn^{7+} containing complexes were measured. Starting from the resting phase, each *G. sulfurreducens* cell produced an electron flux of 3.7×10^5 electrons per second during the respiration process. Reduction rates were within ± 30% the same for the 6 different metal salts, and reaction kinetics were of zero order. Decrease of *c*-cytochrome concentrations by downregulation and mutation demonstrated that *c*-cytochromes stabilized respiration rates by variation of their redox states. Increasing Fe^{2+}/heme levels increased electron flux rates, and induced respiration flexibility. The kinetic effects parallel electrochemical results of *G. sulfurreducens* biofilms on electrodes, and might help to optimize bioelectrochemical devices.

Keywords: reaction kinetic, *c*-cytochrome, *Geobacter sulfurreducens*, remediation, bioelectrochemistry

INTRODUCTION

Geobacter sulfurreducens has found important applications in remediation of oxidizing and toxic metal salts (Lovley et al., 2011; Pushkar et al., 2021), as an electron source of microbial fuel cells (Bond and Lovley, 2003; Slate et al., 2019), as well as a reagent for the synthesis of nanoparticles (Lloyd et al., 2011; Khan et al., 2020; Egan-Morriss et al., 2022). This microorganism, first discovered and isolated by Lovley et al. (1987) and Caccavo et al. (1994) relies on different extracellular minerals (Lovley and Phillips, 1988; Shi et al., 2016) and metal salts as electron acceptors (Ding et al., 2008; Lloyd et al., 2011; Lovley et al., 2011; Levar et al., 2014). Respiration experiments on insoluble minerals, and electrochemical studies on solid electrodes have shown that the electron donor NADH in the cytoplasm and the extracellular electron acceptors are separated from each other by the periplasm, delimited, respectively, by the inner and by the outer cell membranes. Electron transport occurs *via* multi-heme-bearing cytochromes (Ueki, 2021), some of which are soluble in the periplasm (Ppc), while others are attached to the inner (Imc) or the outer cell membrane (Omc). Cytochromes of *G. sulfurreducens,* which are involved in the respiration process, exist in many varieties and contain on average 7.5 iron-hemes (Ueki, 2021), and the total number of iron-hemes per cell is about 10^7 (Esteve-Núñez et al., 2008). Electron transfer through the periplasm is mainly based on triheme cytochromes (Ppc), some of them as protein clusters (Santos et al., 2015). During the stationary phase of the bacteria, all iron/hemes are in the Fe^{2+} state. They become rapidly oxidized to Fe^{3+}/hemes (Chabert et al., 2020) upon addition of metal salts with appropriate redox potentials (Santos et al., 2015; Levar et al., 2017). Fe^{3+}/hemes then oxidize NADH *via* the menaquinol/menaquinone pool, and the resulting proton gradient catalyzes ATP synthesis. In a recent study on the formation of Ag nanoparticles (AgNPs) by *G. sulfurreducens* respiration with water soluble $AgNO_3$, we have demonstrated that Ag^+ ions are bound by outer membrane cytochromes with high complexation constants (Chabert et al., 2020). Subsequent electron transfer in the Ag^+/Omc complexes triggered a fast electron flux through *G. sulfurreducens*, leading to AgNPs at the outer cell membrane (**Figure 1**). The constant electron flux rate of $3{\cdot}10^5\ e^-{\cdot}s^{-1}$ per cell was independent of the Ag^+ ion concentration, and agreed well with electrochemical measurements on single cells of *G. sulfurreducens* (Jiang et al., 2013), as well as *Shewanella oneidensis* (Gross and El-Naggar, 2015). We have now measured reduction rates, and kinetic orders of additional water-soluble metal salts by *G. sulfurreducens*. $[Fe(edta)]^-$, $[Fe(CN)_6]^{3-}$, $Co[(bpy)_2CO_3]^+$, $[VO_2(edta)]^{3-}$, $CrO_4{}^{2-}$, and $MnO_4{}^-$ ions were chosen as oxidants, because their concentrations, and the redox changes of *c*-cytochromes could be exactly determined during the fast respiration processes by time resolved experiments. *G. sulfurreducens* cells in the resting and the exponential growth phases were used. Their *c*-cytochrome concentrations were changed by downregulation and mutation.

MATERIALS AND METHODS

Preparation of *Geobacter sulfurreducens* Solutions

G. sulfurreducens (DSM-12127) was received from the Leibniz Institute DSMZ. Preparation of standard *G. sulfurreducens* solutions in growth medium A: 5 ml of the purchased bacteria solution were solved in 50 ml of growth medium A (**Supplementary Figure 1**), which contained in the first growth round 10 mM KCl and 100 μM $FeSO_4$. After 5 days of growing, 5 ml of this bacterial solution was added into 50 ml of a growth medium A that contained 2 μM KCI and 25 μM $FeSO_4$. This growing procedure with 25 μM $FeSO_4$ took about 3–5 days until the fumarate was consumed, and was repeated 4 times. Inductively coupled plasma optical emission spectroscopy (ICP-OES) showed that after this growth process, the bacterial solution of *G. sulfurreducens* contained $\leq$ 10 μM iron ion concentrations. These standard solutions in medium A without fumarate, which contained *G. sulfurreducens* in the resting state (lag phase) and acetate as carbon source (Estevez-Canales et al., 2015), were directly used for the reduction of the water-soluble metal salts. Preparation of *G. sulfurreducens* solutions in growth medium B: 5 ml of a standard *G. sulfurreducens* solution, which was prepared in growth medium A, and contained 10 μM Fe^{2+}, was added to 50 ml of growth medium B lacking $FeSO_4$ (Estevez-Canales et al., 2015; **Supplementary Figure 1**). After 5 days, these solutions in growth medium B, which contained *G. sulfurreducens* in the resting state and acetate as a carbon source (Estevez-Canales et al., 2015), were directly used for the reduction of the water soluble metal salts. The decrease of *c*-cytochrome amounts in *G. sulfurreducens* by growth in medium B compared to medium A was determined by mass spectrometric proteome analysis: disruption of cells and protein extraction were done in a sample homogenizer after adding a lysis buffer (8 M urea, 50 mM Tris-Cl, pH 8) and glass beads (0.18 mm). The same protein amount for each sample was further processed as described in Stekovic et al. (2020). MS raw files were analyzed using the Spectronaut software version 15.7 (Bruderer et al., 2015) with standard settings (without data imputation) in direct DIA mode using reference proteome of *G. sulfurreducens* (UniProt, UP000000577) and common contaminants. Further data processing and statistical analysis used the Perseus software version 1.6. The results are shown in **Supplementary Figure 2** and **Table 1**. The mutant lacking OmcBEST of *G. sulfurreducens* (PCA) was provided by Derek R. Lovley (University of Massachusetts, Amherst, United States). One ml was cultured in 10 ml of NBAF medium under anaerobic conditions as described in Coppi et al. (2001). After 5 days of growing, when *G. sulfurreducens* was again in the lag phase, 5 ml were solved in 50 ml of growth medium A, and reacted for 5 days until *G. sulfurreducens* was again in the lag phase. This growing procedure was repeated 4 times, and the solutions were used directly for the kinetic experiments with water-soluble metal salts.

Analysis of Oxidizing Metal Salts

$Na[Fe(edta)]$, $K_3[Fe(CN)_6]$, K_2CrO_4, and $KMnO_4$ were purchased from Sigma-Aldrich. $Na_3[VO_2(edta)]$ was synthesized according to Komarova et al. (1991). $[Co(bpy)_2CO_3]Cl$ was generated from $[Co(bpy)_3]Cl_3$, which was solved in growth medium A without fumarate and acetate. O_2 was exchanged by N_2/CO_2 (80/20) and the solution was heated to 125°C for 20 min at 1.25 bar. The structure of $[Co(bpy)_2CO_3]Cl$ was confirmed by single crystal X-ray diffraction (SC-XRD) and electrospray ionization mass spectrometry (ESI-MS). Concentration decrease of the Fe^{3+}, Co^{3+}, V^{5+}, Cr^{6+}, and Mn^{7+} salts, which were reduced by *G. sulfurreducens* to Fe^{2+}, Co^{2+}, V^{4+}, Cr^{3+}, and Mn^{4+} salts, respectively, was analyzed by UV/Vis spectroscopy at wavelengths shown in **Figure 2A** and **Supplementary Figure 3**. In order to determine the location of the oxidizing metal salts after *G. sulfurreducens* respiration, solutions of 4.65 mM $Na[Fe(edta)]$, $K_3[Fe(CN)_6]$, $[Co(bpy)_2CO_3]Cl$, $Na_3[VO_2(edta)]$, as well as 1.55 mM K_2CrO_4 and $KMnO_4$, respectively, were treated for 20 min with N_2/CO_2 (80/20) at ambient temperature. Then, 0.2 ml of them were added to 6 ml of a standard *G. sulfurreducens* solution. After 1 h reaction time (30°C) 0.35 ml of a 37% HCl solution were added, mixed with a vortex for about 1 min, and centrifuged at 10,000 rpm at 20°C for 10 min.

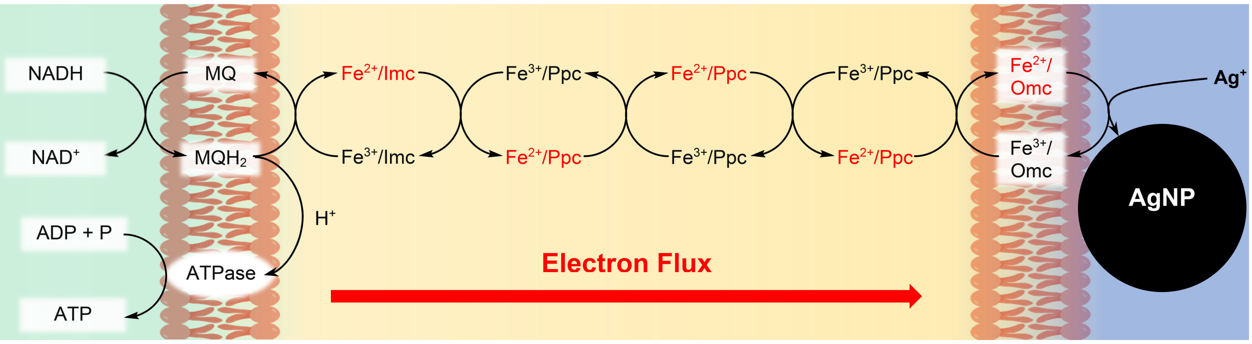

FIGURE 1 | Synthesis of Ag nanoparticles (AgNPs) during respiration of *G. sulfurreducens* with water soluble Ag^+ ions. The *c*-type cytochromes at the inner cell membrane (Imc), in the periplasm (Ppc), and at the outer cell membrane (Omc) transport electrons from intracellular electron donors like NADH to Ag^+/Omc complexes, which leads to AgNPs, attached to the outer cell membrane (Chabert et al., 2020). In recent cell growth experiments with $CrO_4{}^{2-}$ (Gong et al., 2018), Cr^{3+} reduction products could be detected within the cells, if the bacteria reacted for several hours with the chromium salts. Therefore, our reduction experiments of $CrO_4{}^{2-}$ might also occur partly inside of the cells, although the reaction conditions are different.

TABLE 1 | Functions and remaining percentages of *c*-cytochromes that were downregulated by at least 50% during fumarate-respiring growth of *G. sulfurreducens* in medium B compared to growth in medium A (100%).

c-cytochrome	Medium B, %	EET	Predicted cellular location
PpcE (GSU1760)	50	Only found in cultures with Fe^{3+} citrate vs. Fe^{3+} oxides (Ding et al., 2008)	Periplasm
PpcF (GSU2201)	47	Upregulated in cells grown on Fe^{3+} and Mn^{4+} oxide compared to Fe^{3+} citrate (Aklujkar et al., 2013)	Periplasm
GSU3332	47	Gene knockout deficient in the reduction of U^{6+} and Fe^{3+} hydroxide (Shelobolina et al., 2007)	IM (Predicted by Loctree)
CccA (GSU2811)	43	Upregulated by growth on Fe^{3+} and Mn^{4+} oxide compared to Fe^{3+} citrate (Aklujkar et al., 2013)	Periplasm
CoxB (GSU0222)	43	Upregulated by growth on Mn^{4+} oxide compared to Fe^{3+} citrate (Aklujkar et al., 2013)	Periplasm
GSU1740	43	Upregulated by growth on Fe^{3+} and Mn^{4+} oxide compared to Fe^{3+} citrate (Aklujkar et al., 2013)	Periplasm
GSU2210	42		
CcpA (GSU2813)	42		
OmcI (GSU1228)	42	Deletion mutant affected growth in Fe^{3+} citrate and on Fe oxides (Aklujkar et al., 2013)	Periplasm, OM-bounded (Predicted by Loctree)
OmcX (GSU0670)	42	Required for Fe^{3+} reduction (Butler et al., 2010). Downregulated in Fe oxides (Kato et al., 2013)	
OmcA (GSU2884)	40	Upregulated by growth on Fe^{3+} oxides (Aklujkar et al., 2013)	
GSU2743	38	Not involved in EET (Embree et al., 2014)	Periplasm
ppcA (GSU0612)	38	Upregulated by growth on Mn^{4+} oxide (Aklujkar et al., 2013)	Periplasm
ExtG (GSU2724)	33	ExtEFG deletion mutant presented lower levels of Fe^{3+} citrate reduction (Otero et al., 2018)	OM complex ExtEFG
MacA (GSU0466)	29	Upregulated on Mn oxides. Knockout mutant: slow growth on Fe citrate or oxide (Aklujkar et al., 2013)	IM/Periplasm
OmaC (GSU2732)	28	Essential for iron reduction together with OmabcB (Otero et al., 2018)	OM complex OmabcC
PpcD (GSU1024)	25	Upregulated by growth on Fe^{3+} oxide compared to Fe^{3+} citrate (Ding et al., 2008)	Periplasm
PccJ (GSU2494)	23	Upregulated by growth on Fe^{3+} oxides. Mutant had phenotype as wild type (Aklujkar et al., 2013)	Periplasm

The annotation number for each c-cytochrome encoding gene is given in parenthesis. IM is the abbreviation for inner membrane, and OM for outer membrane.

Inductively coupled plasma optical emission spectroscopy (ICP-OES) demonstrated that about 90% of the metal salts were observed outside of the cells, and analysis of the Cr^{3+} distribution (Gong et al., 2018) showed that up to 93% of the

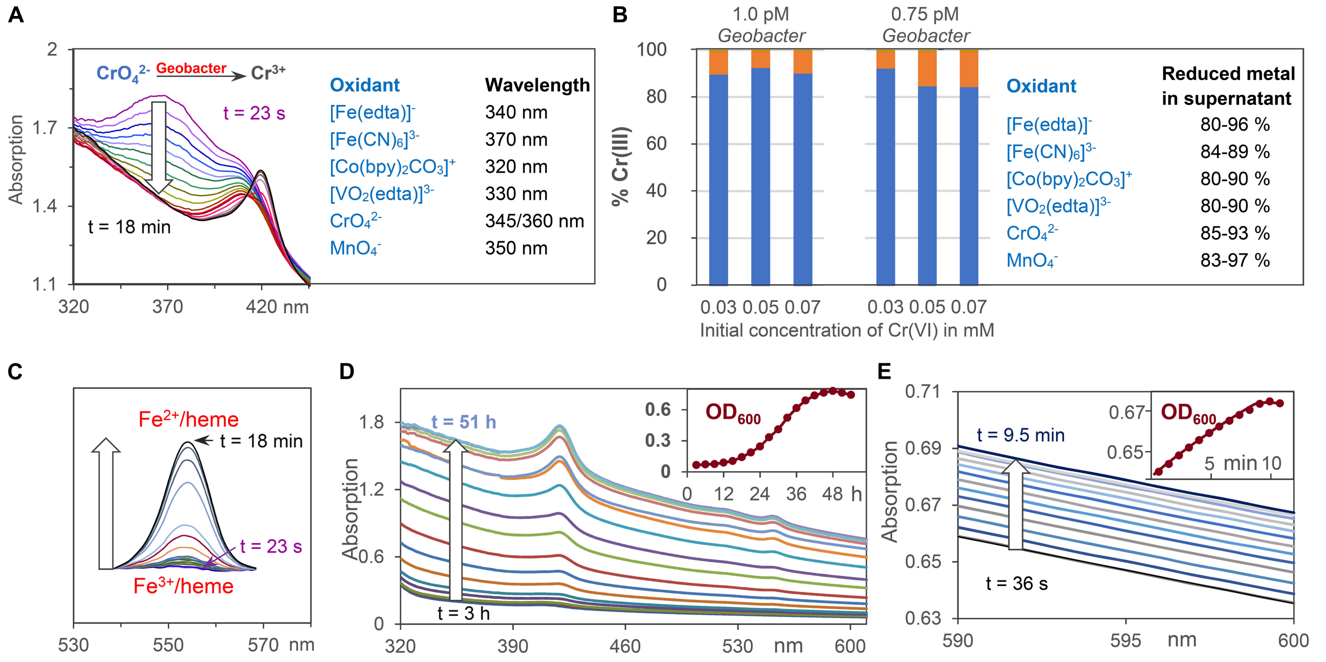

FIGURE 2 | Analytical tools for the analysis of extracellular metal ion, Fe^{2+}/heme, and cell concentrations. **(A)** Reduction of oxidizing metals salts by *G. sulfurreducens* by time dependent UV/Vis spectroscopy at wavelengths where product absorptions are negligible. CrO_4^{2-} respiration is shown as an example. **(B)** ICP analysis of Cr^{3+} ions outside of the cell (blue) and at the cell membrane (orange) after reduction of CrO_4^{2-}. Percentage data for reduced metal salts in the supernatant are given. **(C)** Changes of Fe^{2+}/heme concentration during respiration using the areas of Q-bands. **(D)** Increase of UV/Vis absorptions during bacteria growth with fumarate as intracellular oxidant. The insert shows scattering increases at 600 nm (OD_{600}) during 2 days of cell growth. **(E)** UV/Vis absorptions during cell growth using low chromate concentrations for *G. sulfurreducens* respiration, starting from the resting state.

chromium ions were found in the supernatant, about 6% at the cell membrane, and less than 1% was detected inside of the cells (**Figure 2B**).

Analysis of Fe^{2+}/Hemes

Concentrations of Fe^{2+}/hemes were analyzed by their Q-band areas between 540 and 570 nm (**Figure 2C**), and in some cases also by their Soret band at 420 nm (**Figure 2A**). Ultrasound treatment, which destroyed the cell membranes of *G. sulfurreducens*, did not increase the total UV/Vis absorption of iron-hemes. This demonstrates that *G. sulfurreducens* cells are transparent enough to detect all iron-hemes of the bacteria. Filtration of *G. sulfurreducens* solutions gave a tiny peak ($\leq$5%) of iron hemes in the supernatant (**Supplementary Figure 4**). With about 10^7 iron hemes per cell (Esteve-Núñez et al., 2008) and 10^{-12} M cell concentrations of our experiments, these 5% lead to less than 1 μM Fe^{2+}/heme solutions outside of the cell, which could at best reduce less than 1% of 0.1 mM extracellular metal ion salt solutions.

Analysis of Cell Growth

Cell growth was analyzed by spectroscopy at 600 nm (Muhamadali et al., 2015). *G. sulfurreducens* cells are about 1–2 μm large, thus a concentration increase raised the light scattering effect on the UV/Vis spectra (**Figure 2D**). Test experiments with 40 mM fumarate as an internal oxidant for the cell growth proved that OD_{600} data followed the same exponential increase as experiments, where cell growth in solution was determined by increase of the cell weight (Engel et al., 2020). Dilution of clear cell solutions changed the OD_{600} values in a linear way, and an OD_{600} value of 0.54 corresponds to 0.7 pM *G. sulfurreducens* (Vasylevskyi et al., 2017). The change of OD_{600} values during respiration was detected with high accuracy, so that it could also be used to follow cell growth in experiments with low oxidant concentrations (**Figure 2E**). Rates of metal salt induced cell growth were measured at 30°C under anaerobic conditions: 0.1 ml of a $K_3[Fe(CN)_6]$ solution was added to 3 ml of a standard *G. sulfurreducens* solution. The initial concentration of the oxidant in the reaction mixture was 0.15 mM, and the cell growth was analyzed at OD_{600}. Analogous experiments with K_2CrO_4 were carried out with reaction mixture concentrations of 0.03 and 0.05 mM.

Kinetic Experiments of Metal Salt Reduction by *Geobacter sulfurreducens* Starting From the Resting (Lag) Phase

Kinetic measurements were carried out in standard *G. sulfurreducens* solutions in the lag phase (see above) with 0.15 mM $Na[Fe(edta)]$, $K_3[Fe(CN)_6]$, $Co[(bpy)_2CO_3]Cl$, $Na_3[VO_2(edta)]$, and 0.05 mM K_2CrO_4 and $KMnO_4$ solutions, respectively. Under these conditions, the oxidizing metal salts did not kill the bacterial cells, and the reaction mixtures

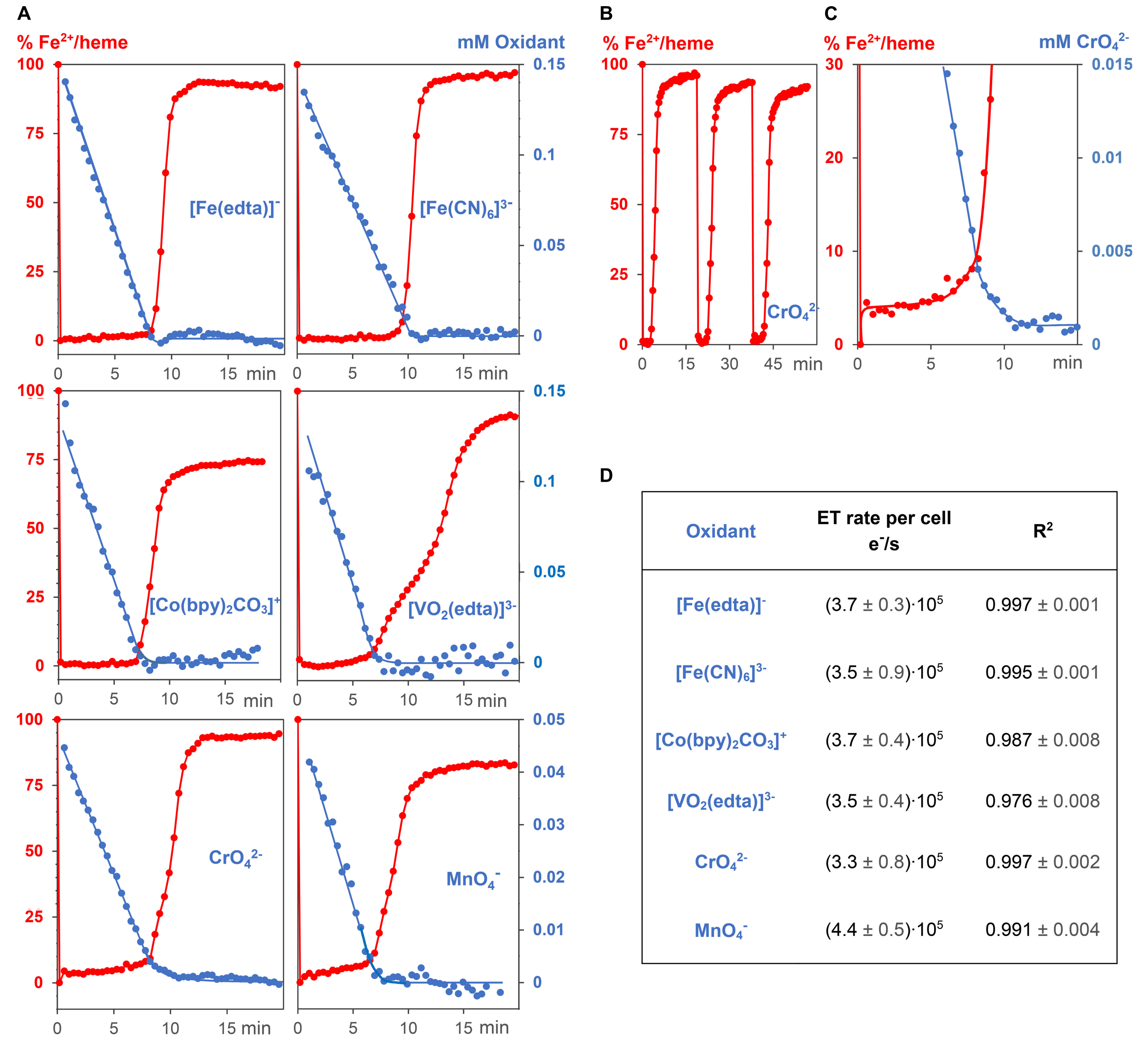

Oxidant	ET rate per cell e^-/s	R^2
$[Fe(edta)]^-$	$(3.7 \pm 0.3)\cdot10^5$	0.997 ± 0.001
$[Fe(CN)_6]^{3-}$	$(3.5 \pm 0.9)\cdot10^5$	0.995 ± 0.001
$[Co(bpy)_2CO_3]^+$	$(3.7 \pm 0.4)\cdot10^5$	0.987 ± 0.008
$[VO_2(edta)]^{3-}$	$(3.5 \pm 0.4)\cdot10^5$	0.976 ± 0.008
CrO_4^{2-}	$(3.3 \pm 0.8)\cdot10^5$	0.997 ± 0.002
MnO_4^-	$(4.4 \pm 0.5)\cdot10^5$	0.991 ± 0.004

FIGURE 3 | Kinetic experiments of *G. sulfurreducens* with extracellular metal salts. **(A)** Reduction of 6 different oxidizing metal salt solutions (blue, 0.05–0.15 mM) with *G. sulfurreducens* solutions in the resting state (8.9 ± 0.3 pM). Their linear time dependences of the metal salt concentrations demonstrate zero kinetic order of the reduction process. At the start of the experiments, all iron ions of the bacterial multiheme cytochromes were in the Fe^{2+} state (red). They were rapidly oxidized upon addition of extracellular metal salts, their levels remained low during reduction of the metal salts, and increased again after major consumption of the oxidants. **(B)** Experiments could be repeated several times. Shown are Fe^{2+}/heme levels upon three consecutive additions of $CrO_4{}^{2-}$. **(C)** A closer look at the Fe^{2+}/heme (red) and $CrO_4{}^{2-}$ (blue) concentrations. The Fe^{2+} /heme levels increased after major part of $CrO_4{}^{2-}$ was reduced, which obviously stabilized EET rates at low concentrations of the extracellular metal salts. **(D)** Zero order reduction rates per cell for the 6 different metal salts at 30°C and pH = 7.4.

remained homogeneous. All experiments were repeated 3 times at 30°C under N_2/CO_2 (80/20). Addition of 0.05 or 0.1 ml metal salt solutions to 3 ml standard *G. sulfurreducens* in the lag phase occurred by injection through a sealing plug with needles that had been sterilized with a Bunsen burner. Oxidants were used in such amounts that their initial concentrations in the reaction mixtures were 0.05 mM for Cr^{6+} or Mn^{7+}, and 0.15 mM for Fe^{3+}, Co^{3+}, and V^{5+}, respectively. The concentrations of *G. sulfurreducens* were calculated from the OD_{600} data. UV/Vis spectra were recorded between 610 and 320 nm. Each run took 25.3 s. Concentration changes of metal salts were analyzed at wavelengths that are listed in **Figure 2A** and **Supplementary Figure 3**. Concentration changes of Fe^{2+}/hemes were determined by the areas of the Q-bands (540, 570 nm) if $Na[Fe(edta)]$, $K_3[Fe(CN)_6]$, $KMnO_4$, and K_2CrO_4 were used as oxidants (**Figure 2C**). Because Co^{2+} and V^{4+} salts absorb at the Q-bands wavelengths, the differences of Soret bands at 420 nm (Fe^{2+}/heme) and 410 nm (Fe^{3+}/heme) were used. The determined concentrations of oxidizing metal salts and Fe^{2+}/hemes were plotted against reaction times. The linear time dependences of the metal salt concentrations (**Figure 3A**) are the electron flux rates, and division by *G. sulfurreducens* concentrations led to the electron flux rate per cell (**Figure 3D**).

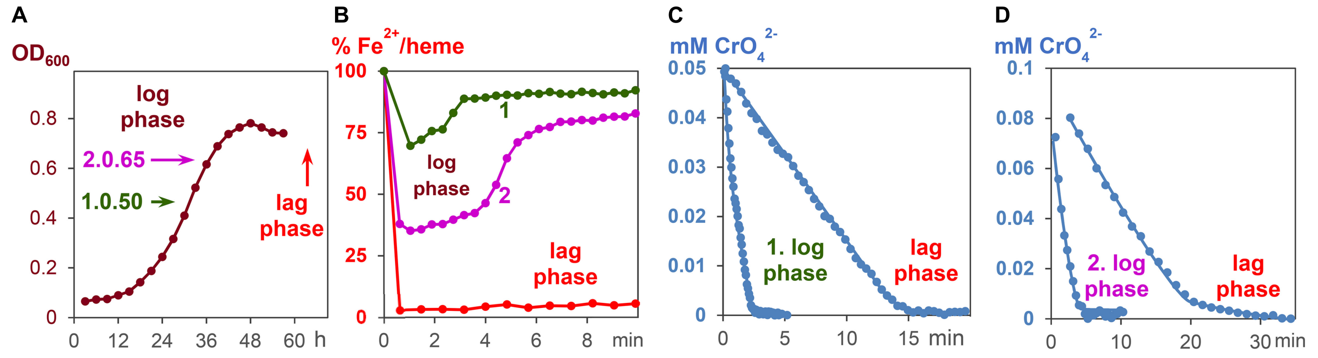

FIGURE 4 | CrO_4^{2-} induce respiration of *G. sulfurreducens*, starting from the log phase. **(A)** Fumarate- respiring growth of *G. sulfurreducens*. Bacteria after 30 and 36 h growth, respectively, were used for metal induced respiration of *G. sulfurreducens* in the log phase. **(B)** Fe^{2+}/heme levels during CrO_4^{2-} induced respiration of bacteria starting from log phases 1 and 2, as well as the resting (lag) phase. **(C)** Reduction of CrO_4^{2-} (0.05 mM) by bacteria (0.63 ± 0.2 pM) in the log phase 1 and the lag phase. **(D)** Reduction of CrO_4^{2-} (0.1 mM) by bacteria (0.83 ± 0.2 pM) in the log phase 2 and the lag phase.

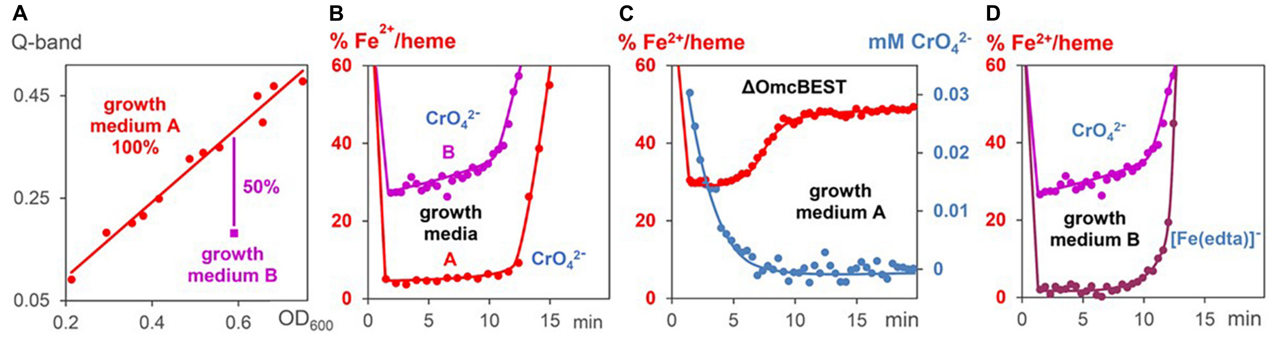

FIGURE 5 | Changes of Fe^{2+}/heme levels during metal induced respiration of *G. sulfurreducens*. **(A)** Linear correlation (red line) between Fe^{2+}/heme concentrations (Q-bands) and *G. sulfurreducens* concentrations (OD_{600} data). The data (red points) were gained by dilution and different cell growth experiments in medium A. Measurement (magenta point) with *G. sulfurreducens*, grown in medium B, where *c*-cytochromes are downregulated. **(B)** Fe^{2+}/heme levels during CrO_4^{2-} induced respiration (0.05 mM) of cells grown in media A (0.63 pM) and B (0.73 pM). **(C)** Fe^{2+}/heme levels (red) and CrO_4^{2-} concentrations (blue) during CrO_4^{2-} induced respiration (0.05 mM) of mutants lacking OmcBEST (0.76 pM) grown in medium A. **(D)** Fe^{2+}/heme levels of experiments with *G. sulfurreducens* (0.74 pM), grown in medium B, with $[Fe(edta)]^-$ (0.15 mM) and CrO_4^{2-} (0.05 mM), respectively.

Kinetic Experiments of Metal Salt Reduction by *Geobacter sulfurreducens* Starting From the Growth (Log) Phase

All experiments were carried out under strictly anaerobic conditions at 30°C. To start the growth process with fumarate as an oxidant, 5 ml of the standard *G. sulfurreducens* solution were added to 50 ml of growth medium A. The growing process was analyzed by taking probes every 3 h and measuring the OD_{600} values (**Figure 4A**). After about 30 h, 3 ml of a *G. sulfurreducens* solution, which was then in the exponential growth (log) phase, was injected with a sterilized needle through a sealing plug into an UV cuvette. The OD_{600} values of *G. sulfurreducens* were about 0.50. To this *G. sulfurreducens* solution, which contained all iron-hemes in the Fe^{2+} oxidation state, 0.05 ml of a K_2CrO_4 solution was added, so that the initial concentration of CrO_4^{2-} was 0.05 mM (experiment 1, **Figures 4B,C**). Another experiment with *G. sulfurreducens* (OD_{600} = 0.65), which had continued its growth with fumarate as oxidant, was carried out about 6 h later: 3 ml of *G. sulfurreducens* in the exponential growth (log) phase were injected into an UV cuvette, and 0.1 ml of a CrO_4^{2-} solution was added, so that the reaction mixture was at the start 0.1 mM in CrO_4^{2-} (experiment 2, **Figures 4B,D**). Concentration changes of CrO_4^{2-} and Fe^{2+}/hemes were analyzed from the UV/Vis spectra at 345 nm and the Q-band, respectively.

RESULTS

Influence of Extracellular Metal Salts on Reduction Rates

Reactions of 0.15 mM Na[Fe(edta)], $K_3[Fe(CN)_6]$, $Co[(bpy)_2CO_3]Cl$, $Na_3[VO_2(edta)]$, and 0.05 mM K_2CrO_4 as well as $KMnO_4$ solutions with 0.89 pM *G. sulfurreducens* in the resting phase, solved in media as described above, oxidized the Fe^{2+}/hemes of cytochromes to Fe^{3+}/hemes within a few seconds, and a steady metal salt reduction occurred over 10 min (**Figure 3A**). The concentration of the electron transporting Fe^{2+}/hemes remained nearly constant at a low level until up to

80% of the metal salt reductions were completed (**Figures 3A,C**). After about 7–9 min, when most of metal salts had been reduced, Fe^{2+}/hemes were regenerated by cellular processes, and the bacteria are ready for a second round of the metal ion reduction process (**Figure 3B**). The electron flux did not change although concentrations of metal salts decreased. Their linear time dependences are the overall reduction rates, and division by *G. sulfurreducens* concentrations yielded electron flux rates per single cell. Data for $CrO_4{}^{2-}$ and $MnO_4{}^{-}$ were furthermore multiplied by the stoichiometric factor of 3, considering a three electron transfer. All six metal salts led to the fast electron flux rate of $3.7 \cdot 10^5$ $e^- \cdot s^{-1}$ per cell with a reproducibility of $\pm$ $1.2 \cdot 10^5$ $e^- \cdot s^{-1}$ (**Figure 3D**). Thus, reduction rates were not only independent of metal salt concentrations, but also of the metal salt types. The variation of bacteria or initial metal salt concentrations by a factor of 2 did not change reduction rates per cell (**Supplementary Figure 5**). A fivefold increase of extracellular metal salts started to deactivate cells, which led to a slowdown of the reduction, indicated by a curvature of the time dependent metal salt reduction, and a lower regeneration of the Fe^{2+}/hemes. Additional experiments showed that reduction of metal salts could neither be detected with dead *G. sulfurreducens* cells nor with the supernatant of living cells, and $Cr_2(SO_4)_3$ or $K_3[Co(CN)_6]$, which cannot oxidize Fe^{2+}/hemes of cytochromes, did not drive the respiration.

Influence of Fe^{2+}/Hemes on Reduction Rates

Experiments were carried out with bacteria, which contained either lower *c*-cytochrome concentrations, or reacted faster with the metal salts. A downregulation of *c*-cytochromes was carried out by preparation of *G. sulfurreducens* cells in a growth medium of low Fe^{2+} concentration (medium B). Mass spectrometric proteome analysis detected 2,579 proteins after growth in medium A as well as in medium B, from which 64 are *c*-cytochromes (**Supplementary Figure 2**). Two thirds of them were downregulated by cell growth in medium B, 18 by more than 50% (**Table 1**). Comparison with literature data demonstrated that 17 of these 18 cytochromes are involved in the EET process. Most of them are located in the periplasm, from which three are predicted to be bound to the outer membrane, two to the inner membrane, and two cytochromes are outer membrane complexes. As a consequence, the total iron heme concentrations decreased by 50% in the downregulated cells (**Figure 5A**). Reduction experiments of these bacteria with metal salts showed that electron flux rates remained constant, whereas the Fe^{2+}/heme levels increased considerably (**Figure 5B**). Obviously, constant rates could be maintained in cells of lower *c*-cytochrome concentrations by rising the Fe^{2+}/heme levels. A similar effect was observed with a mutant, where outer membrane cytochromes OmcB, OmcE, OmcS, and OmcT were deleted (**Figure 5C**).

An increase of electron flux rates was achieved by experiments starting with *G. sulfurreducens* in the exponential growth phase (log phase). In order to carry out these measurements, cells were prepared under fumarate-respiring conditions (Butler et al., 2006). The log phase started after several hours, reached a rate maximum at about 30 h, then slowed down, and stopped during the third day (**Figure 4A**). In the first hours of this growth process, Fe^{2+}/hemes were partly oxidized but became reduced again during the log phase (**Supplementary Figure 6**). Once all iron hemes of *G. sulfurreducens* were in the Fe^{2+} state, K_2CrO_4 was added to the growing *G. sulfurreducens* solution, and the $CrO_4{}^{2-}$ reduction rate was measured (**Figures 4C,D**). Experiments at different growth times showed that electron flux was 4–6 times faster in the log phase than with cells starting from the lag phase. Cells in the exponential growth demands faster ATP production, which can be achieved by an increase of the electron flux rate. This was made possible by an increase of the Fe^{2+}/heme levels in the *c*-cytochromes from 5% (lag phase) to up to 75% (log phase) during the metal salt reduction (**Figure 4B**).

Influence of Extracellular Metal Salts on Cell Growth Rates

Respiration induces the formation of ATP, which leads to bacterial growth in ATP dependent processes (Brown, 1992; Velten et al., 2007; Bochdansky et al., 2021). To elucidate whether ATP formation and ATP consumption occur with the same rates, the decrease of the metal salts, and the increase of cell growth were measured. Reactions started with *G. sulfurreducens* in the resting state and medium A as solvent, which lacks fumarate as oxidant. Respiration was induced by addition of 0.03–0.05 mM $CrO_4{}^{2-}$ or 0.15 mM $[Fe(CN)_6]^{3-}$ solutions. **Figures 6A–C** demonstrate that cell growth increased linearly, and required the same reaction times as the respiration process. The OD_{600} increase during respiration revealed that a 0.15 mM electron flux generated 4.5 ± 0.5% cell increase from 0.81 pM *G. sulfurreducens* solutions. Hence, a flow of 0.15 mM electrons produced 0.036 pM cell growth, so that $4 \cdot 10^9$ electrons were needed to synthesize enough ATP for one cell division, which agrees with the analysis of electrochemical experiments (Levar et al., 2013).

DISCUSSION

Respiration of lag phase *G. sulfurreducens* cells in a growth medium, which lacks the oxidant fumarate, reduced Fe^{3+}, Co^{3+}, V^{5+}, Cr^{6+}, and Mn^{7+} ions of the 6 different metal salts with electron flux rates of $3.7 \cdot 10^5$ $e^- \cdot s^{-1}$ per cell at 30°C, a pH of 7.4 and a reproducibility of ± 30% (**Figures 3A,D**). The nearly constant Fe^{2+}/heme levels demonstrated that the oxidation of Fe^{2+}/hemes by the metal salts, and the reduction of Fe^{3+}/hemes by the menaquinole pool occurred with the same rates, leading to a constant electron flux. Rates and kinetic orders agree well with our earlier reduction experiments of Ag^+ ions by *G. sulfurreducens* (Chabert et al., 2020), which led to Ag nanoparticles (AgNPs), as reaction products (**Figure 1**). We had measured high binding constants of Ag^+ ions to Met and His of outer membrane cytochromes, and observed the formation of AgNPs at the outer cell membrane. In recent cell growth experiments with $CrO_4{}^{2-}$ (Gong et al., 2018), Cr^{3+} reduction products could also be

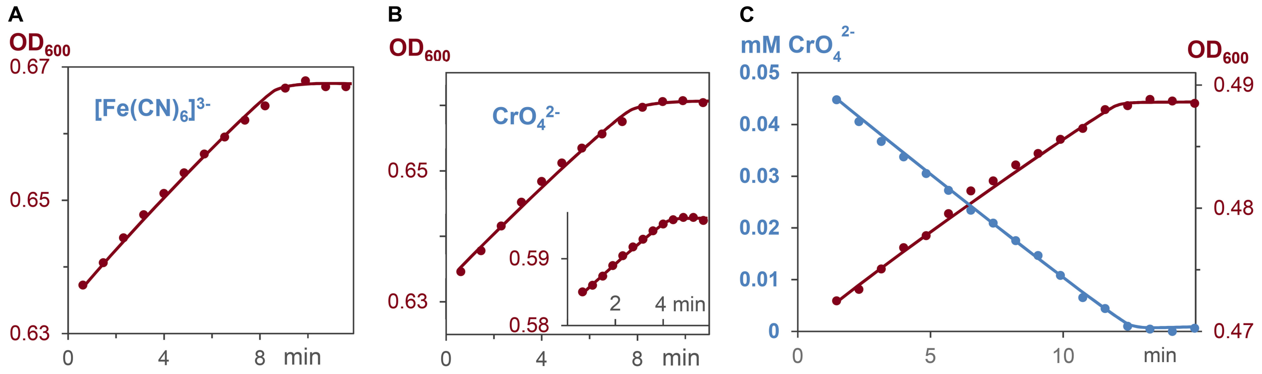

FIGURE 6 | Increase of cell concentration and decrease of oxidants $[Fe(CN)_6]^{3-}$ and $CrO_4{}^{2-}$ during *G. sulfurreducens* respiration in grow medium A, lacking fumarate, and stating from the lag phase. **(A)** Linear increase of the bacterial growth with 0.15 mM $[Fe(CN)_6]^{3-}$, $R^2 = 0.98$. **(B)** Linear increase of the bacterial growth with 0.05 and 0.03 mM $CrO_4{}^{2-}$ (insert), $R^2 = 0.98$. **(C)** Linear $CrO_4{}^{2-}$ decrease (blue, $R^2 = 0.99$), and linear bacterial growth (brown, $R^2 = 0.98$) of the same respiration experiment.

detected within the cells, if the bacteria were treated for several hours with metal salts. Our experiments were finished within 10–20 min, and we never observed Cr^{3+} within the cells (**Figure 2B**), but to avoid overinterpretation, we don't exclude the possibility that some of the $CrO_4{}^{2-}$ was reduced inside of the cells even under our different reaction conditions. This obviously did not change the electron flux rate (**Figure 3A**), which is driven by the need for a constant ATP production (Velten et al., 2007; Bochdansky et al., 2021; Wilson and Matschinsky, 2021) during *G. sulfurreducens* respiration (**Figures 6A–C**). Interestingly, the same electron flux rates were also measured in electrochemical experiments on single cells of *G. sulfurreducens* (Jiang et al., 2013) as well as *Shewanella oneidensis* (Gross and El-Naggar, 2015).

The influence of Fe^{2+}/hemes on electron flux rates was studied (a) with *G. sulfurreducens* cells of downregulated *c*-cytochromes, (b) with cells in the exponential growth phase, and (c) with *G. sulfurreducens* mutants. Decrease of *c*-cytochrome concentrations (**Figure 5A** and **Table 1**) was observed in microorganisms that were prepared under fumarate-respiring conditions at very low $FeSO_4$ concentrations (medium B). Addition of $CrO_4{}^{2-}$ ions to these downregulated cells induced nearly the same reaction rates as experiments with *G. sulfurreducens*, grown in medium A (**Figure 5B**). This was surprising, as *c*-cytochromes are the electron transporting carriers and their decrease should slow down the electron flux. Obviously, the observed rise of Fe^{2+}/heme levels from ≤ 5 to 30% compensated the downregulation of *c*-cytochromes. Electron flux rates of metal salt induced respiration, which used *G. sulfurreducens* cells in the exponential growth phase, were 4–6 times faster compared to experiments starting from *G. sulfurreducens* in the resting phase (**Figures 4C,D**). Such an acceleration is reasonable as the ATP demand increases in the exponential growth phase, requiring at the same time a faster electron flux, which was achieved by an increase of Fe^{2+}:/heme levels in the cytochromes from 5% *via* 40 to 75% (**Figure 4B**). Such a rise of the Fe^{2+}/heme level augments the reductive power of multiheme cytochromes (Quian et al., 2011; Liu and Bond, 2012; Santos et al., 2015), and increases electron transfer rates by the Marcus theory (Marcus, 1993). It demonstrates the importance of the electron storing capacities of multiheme cytochromes (Esteve-Núñez et al., 2008), which can regulate respiration by their redox states. Our observations are again in accord with electrochemical experiments, where the redox status of *c*-cytochromes in *G. sulfurreducens* biofilms changed with the applied potential (Liu et al., 2011). Thus, the Fe^{2+}/heme level is an important parameter for the optimization of *G. sulfurreducens* as an electron-producing source.

The analogous effects of our metal salt induced electron flux measurements with electrochemical current production of biofilms at the anode inititated us to measure the reduction rate of $CrO_4{}^{2-}$ by *G. sulfurreducens* mutants, in which OmcBEST was deleted. Electrochemical measurements on biofilms had shown (Nevin et al., 2009) that "deletion of OmcS, OmcB and OmcE had nearly no impact on maximum current production." This is in strong contrast to Fe^{3+} oxide and Fe^{3+} citrate induced cell growth experiments. *G. sulfurreducens* mutants, in which OmcB, OmcE, or OmcS were mutated out (Leang et al., 2003; Richter et al., 2011) reduced the cell growth rates dramatically. Our rate measurements with water-soluble $CrO_4{}^{2-}$ ions are again in accord with electrochemical results. **Figure 5C** demonstrates that the mutant, in which OmcBEST was deleted, hardly changed the $CrO_4{}^{2-}$ reduction time, but the missing outer membrane cytochromes induced a drastic increase of the Fe^{2+}/hemes level during the metal salt reduction. It demonstrates that the effect of decreasing outer membrane cytochromes on the respiration rate was compensated by an increase of the Fe^{2+}/heme level. Thus, Fe^{2+}/hemes play a central role in the regulation of electron flux rates. These measurements stimulate studies to elucidate the effects of *G. sulfurreducens* mutations on electron flux rates in bioelectrochemical measurements compared to cell growth experiments. An obvious difference between these two techniques is that in cell growth experiments the cells are several hours in contact to the oxidizing minerals and the reduced metal ions.

In contrast, electrochemical experiments with *G. sulfurreducens* biofilms on electrodes, as well as the metal salt induced electron flux measurements, presented in this publication, take only some minutes. We will check in future work, whether the sensitivity of mutated cells against strong oxidants is one of the reasons for the differences between long time cell growth and short time bioelectrochemical experiments.

DATA AVAILABILITY STATEMENT

The datasets presented in this study can be found in online repositories. The names of the repository/repositories and accession number(s) can be found below: ProteomeXchange, PXD032892.

AUTHOR CONTRIBUTIONS

MK designed and carried out the kinetic experiments. MK and BG analyzed the data and calculated reaction kinetics. MS carried out the proteomic experiments. MS, JD, and CS discussed the proteomic experiments. MK, BG, and KF discussed all data and suggested the reaction mechanism. All authors contributed to the article and approved the submitted version.

FUNDING

We thank the Swiss National Science Foundation for support *via* the grant 178827, as well as the University of Fribourg and the NCCR Bioinspired Materials.

ACKNOWLEDGMENTS

We thank D. R. Lovley and T. L. Woodward for the *G. sulfurreducens* mutant lacking OmcBEST.

SUPPLEMENTARY MATERIAL

The Supplementary Material for this article can be found online at: https://www.frontiersin.org/articles/10.3389/fmicb.2022.909109/full#supplementary-material

REFERENCES

Aklujkar, M., Coppi, M. V., Leang, C., Kim, B. C., Chavan, M. A., Perpetua, L. A., et al. (2013). Proteins involved in electron transfer to Fe(III) and Mn(IV) oxides by *Geobacter sulfurreducens* and *Geobacter uraniireducens*. *Microbiology* 159, 515–535. doi: 10.1099/mic.0.064089-0

Bochdansky, A. B., Stouffer, A. N., and Washington, N. N. (2021). Adenosine triphosphate (ATP) as a metric of microbial biomass in aquatic systems: new simplified protocols, laboratory validation, and a reflection on data from the literature. *Limnol. Oceanogr. Methods* 19, 115–131. doi: 10.1002/lom3.10409

Bond, D. R., and Lovley, D. R. (2003). Electricity production by geobacter sulfurreducens attached to electrodes. *Appl. Environ. Microbiol.* 69, 1548–1555. doi: 10.1128/AEM.69.3.1548-1555.2003

Brown, G. C. (1992). Control of respiration and ATP synthesis in mammalian mitochondria and cells. *Biochem. J.* 284, 1–13. doi: 10.1042/bj2840001

Bruderer, R., Bernhardt, O. M., Gandhi, T., Miladinović, S. M., and Cheng, L. Y. (2015). Extending the limits of quantitative proteome profiling with data-independent acquisition and application to acetaminophen-treated three-dimensional liver microtissues. *Mol. Cell. Proteomics* 14, 1400–1410. doi: 10.1074/mcp.M114.044305

Butler, J. E., Glaven, R. H., Esteve-Nuìnþez, A., Nuìnþez, C., Shelobolina, E. S., Bond, D. R., et al. (2006). Genetic characterization of a single bifunctional enzyme for fumarate reduction and succinate oxidation in *Geobacter sulfurreducens* and engineering of fumarate reduction in *Geobacter metallireducens*. *J. Bacteriol.* 188, 450–455. doi: 10.1128/JB.188.2.450-455.2006

Butler, J. E., Young, N. D., and Lovley, D. R. (2010). Evolution of electron transfer out of the cell: comparative genomics of six *Geobacter genomes*. *BMC Genom.* 11:40. doi: 10.1186/1471-2164-11-40

Caccavo, F., Lonergan, D. J., Lovley, D. R., Davis, M., Stoiz, J. F., and McInerney, M. J. (1994). Geobacter sulfurreducens sp. nov., a hydrogen- and acetate-oxidizing dissimilatory metal-reducing microorganism. *Appl. Environ. Microbiol.* 60, 3752–3759. doi: 10.1128/aem.60.10.3752-3759.1994

Chabert, V., Babel, L., Füeg, M. P., Karamash, M., Madivoli, E. S., Herault, N., et al. (2020). Kinetics and mechanism of mineral respiration: how iron hemes synchronize electron transfer rates. *Angew. Chem. Int. Ed.* 59, 12331–12336. doi: 10.1002/anie.201914873

Coppi, M. V., Leang, C., Sandler, S. J., and Lovley, D. R. (2001). Development of a genetic system for *Geobacter sulfurreducens*. *Appl. Environ. Microbiol.* 67, 3180–3187. doi: 10.1128/AEM.67.7.3180-3187.2001

Ding, Y.-H. R., Hixson, K. K., Aklujkar, M. A., Lipton, M. S., Smith, R. D., Lovley, D. R., et al. (2008). Proteome of *Geobacter sulfurreducens* grown with Fe(III) oxide or Fe(III) citrate as the electron acceptor. *Biochim. Biophys. Acta* 1784, 1935–1941. doi: 10.1016/j.bbapap.2008.06.011

Egan-Morriss, C., Kimber, R. L., Powell, N. A., and Lloyd, J. R. (2022). Biotechnological syntheses of Pd-based nanoparticle catalysis. *Nanoscale Adv.* 4, 654–679. doi: 10.1039/D1NA00686J

Embree, M., Qiu, Y., Shieu, W., Nagarajan, H., O'Neil, R., Lovley, D., et al. (2014). The iron stimulon and fur regulon of *Geobacter sulfurreducens* and their role in energy metabolism. *Appl. Environ. Microbiol.* 80, 2918–2927. doi: 10.1128/AEM.03916-13

Engel, C. E. A., Vorländer, D., Biedendieck, R., Krull, R., and Dohnt, K. (2020). Quantification of microaerobic growth of *Geobacter sulfurreducens*. *PLoS One* 15:e0215341. doi: 10.1371/journal.pone.0215341

Esteve-Núñez, A., Sosnik, J., Visconti, P., and Lovley, D. R. (2008). Fluorescent properties of c-type cytochromes reveal their potential role as an extracytoplasmic electron sink in *Geobacter sulfurreducens*. *Environ. Microbiol.* 10, 497–505. doi: 10.1111/j.1462-2920.2007.01470.x

Estevez-Canales, M., Kuzume, A., Borjas, Z., Füeg, M., Lovley, D., Wandlowski, T., et al. (2015). A severe reduction in the cytochrome c content of *Geobacter sulfurreducens* eliminates its capacity for extracellular electron transfer. *Environ. Microbiol. Rep.* 7, 219–226. doi: 10.1111/1758-2229.12230

Gong, Y., Werth, C. J., He, Y., Su, Y., Zhang, Y., and Zhou, X. (2018). Intracellular versus extracellular accumulation of hexavalent chromium reduction products by *Geobacter sulfurreducens* PCA. *Environ. Pollut.* 240, 485–492. doi: 10.1016/j.envpol.2018.04.046

Gross, B. J., and El-Naggar, M. Y. (2015). A combined electrochemical and optical trapping platform for measuring single cell respiration rates at electrode interfaces. *Rev. Sci. Instrum.* 86:064301.

Jiang, X., Hu, J., Petersen, E. R., Fritzgerald, L. A., Jackan, C. S., Lieber, A. M., et al. (2013). Probing single- to multi-cell level charge transport in *Geobacter sulfurreducens* DL-1. *Nat. Commun.* 4:2751. doi: 10.1038/ncomms3751

Kato, S., Hashimoto, K., and Watanabe, K. (2013). Iron-oxide minerals affect extracellular electron-transfer paths of geobacter spp. *Microbes Environ.* 28, 141–148. doi: 10.1264/jsme2.ME12161

Khan, M. R., Fromm, K. M., Rizvi, T. F., Giese, B., Ahamad, F., Turner, R. J., et al. (2020). Metal nanoparticle–microbe interactions: synthesis and antimicrobial effects. *Part. Syst. Charact.* 37:1900419. doi: 10.1002/ppsc.201900419

Komarova, T. V., Obrezkov, O. N., and Shpigun, O. A. (1991). Ion chromatographic behaviour of anionic EDTA complexes of vanadium(IV) and vanadium(V). *Anal. Chim. Acta* 254:63. doi: 10.1016/0003-2670(91)90009-T

Leang, C., Coppi, M. V., and Lovley, D. R. (2003). OmcB, a c-type polyheme cytochrome, involved in fe(III) reduction in *Geobacter sulfurreducens*. *J. Bacteriol.* 185, 2096–2103. doi: 10.1128/JB.185.7.2096-2103.2003

Levar, C. E., Chan, C. H., Mehta-Kolte, M. G., and Bond, D. R. (2014). An inner membrane cytochrome required only for reduction of high redox potential extracellular electron acceptors. *mBio* 5:e2034. doi: 10.1128/mBio.02034-14

Levar, C. E., Hoffman, C. L., Dunshee, A. J., Toner, B. M., and Bond, D. R. (2017). Redox potential as a master variable controlling pathways of metal reduction by *Geobacter sulfurreducens*. *ISME J.* 11, 741–752. doi: 10.1038/ismej.2016.146

Levar, C. E., Rollefson, J. B., and Bond, D. R. (2013). "Energetic and molecular constraints on the mechanism of environmental fe(III) reduction by geobacter," in *Microbial Metal Respiration*, eds J. Gescher and A. Kappler (Berlin, Heidelberg: Springer), 29–48. doi: 10.1007/978-3-642-32867-1_2

Liu, Y., and Bond, D. R. (2012). Long-distance electron transfer by g. sulfurreducens biofilms results in accumulation of reduced c-type cytochromes. *ChemSusChem* 5, 1047–1053. doi: 10.1002/cssc.201100734

Liu, Y., Kim, H., Franklin, R. R., and Bond, D. R. (2011). Linking spectral and electrochemical analysis to monitor c-type cytochrome redox states in living *Geobacter sulfurreducens* biofilms. *ChemPhysChem* 12, 2235–2241. doi: 10.1002/cphc.201100246

Lloyd, J. R., Byrne, J. M., and Coker, V. S. (2011). Biotechnological synthesis of functional nanomaterials. *Curr. Opin. Biotechnol.* 22, 509–515. doi: 10.1016/j.copbio.2011.06.008

Lovley, D. R., and Phillips, E. J. (1988). Novel mode of microbial energy metabolism: organic carbon oxidation coupled to dissimilatory reduction of iron or manganese. *Appl. Environ. Microbiol.* 54:1480. doi: 10.1128/aem.54.6.1472-1480.1988

Lovley, D. R., Stolz, J. F., Nord, G. L., and Phillips, E. J. P. (1987). Anaerobic production of magnetite by a dissimilatory iron-reducing microorganism. *Nature* 330, 252–254. doi: 10.1038/330252a0

Lovley, D. R., Ueki, T., Zhang, T., Malvankar, N. S., Shrestha, P. M., Flanagan, K. A., et al. (2011). Geobacter: the microbe electric's physiology, ecology, and practical applications. *Adv. Microb. Physiol.* 59, 1–100. doi: 10.1016/B978-0-12-387661-4.00004-5

Marcus, R. A. (1993). Electron transfer reactions in chemistry: theory and experiment. *Angew. Chem. Int. Ed.* 32, 1111–1222. doi: 10.1002/anie.199311113

Muhamadali, H., Xu, Y., Ellis, D. I., Allwood, J. W., Rattray, N. J. W., Correa, E., et al. (2015). Metabolic profiling of *Geobacter sulfurreducens* during industrial bioprocess scale-up. *Appl. Environ. Microbiol.* 81, 3288–3298. doi: 10.1128/AEM.00294-15

Nevin, K. P., Kim, B.-C., Glaven, R. H., Johnson, J. P., Woodward, T. L., Methé, B. A., et al. (2009). Anode biofilm transcriptomics reveals outer surface components essential for high density current production in *Geobacter sulfurreducens* fuel cells. *PLoS One* 4:e5628. doi: 10.1371/journal.phone.0005628

Otero, F. J., Chan, C. H., and Bond, D. R. (2018). Identification of different putative outer membrane electron conduits necessary for Fe(III) citrate, Fe(III) oxide, Mn(IV) oxide, or electrode reduction by *Geobacter sulfurreducens*. *J. Bacteriol.* 200:e347. doi: 10.1128/JB.00347-18

Pushkar, B., Sevak, P., Parab, J., and Nikanth, N. (2021). Chromium pollution and its bioremediation mechanisms in bacteria: a review. *Environ. Polution* 240, 483–492. doi: 10.1016/j.envpol.2018.04.046

Quian, X., Mester, T., Morgado, L., Arakawa, T., Sharma, M. L., Inoue, K., et al. (2011). Biochemical characterization of purified OmcS, a c-type cytochrome required for insoluble Fe(III) reduction in *Geobacter sulfurreducens*. *Biochim. Biophys. Acta* 1807, 404–412. doi: 10.1016/j.bbabio.2011.01.003

Richter, K., Schickberger, M., and Gescher, J. (2011). Dissimilatory Reduction of Extracellular Electron Acceptors in Anaerobic Respiration. *Appl. Environ. Microbiol.* 78, 913–921. doi: 10.1128/AEM.06803-11

Santos, T. C., Silva, M. A., Morgado, L., Dantas, J. M., and Salgueiro, C. A. (2015). Diving into the redox properties of *Geobacter sulfurreducens* cytochromes: a model for extracellular electron transfer. *Dalton Trans.* 44, 9335–9344. doi: 10.1039/C5DT00556F

Shelobolina, E. S., Coppi, M. V., Korenevsky, A. A., DiDonato, L. N., Sullivan, S. A., Konishi, H., et al. (2007). Importance of c-type cytochromes for U(VI) reduction by *Geobacter sulfurreducens*. *BMC Microbiol.* 7:16. doi: 10.1186/1471-2180-7-16

Shi, L., Dong, H., Reguera, G., Beyenal, H., Lu, A., Liu, J., et al. (2016). Extracellular electron transfer mechanisms between microorganisms and minerals. *Nat. Rev. Microbiol.* 14, 651–662. doi: 10.1038/nrmicro.2016.93

Slate, A. J., Whitehead, K. A., Brownson, D. A. C., and Banks, C. E. (2019). Microbial fuel cells: an overview of current technology. *Renew. Sustain. Energy Rev.* 101, 60–81. doi: 10.1016/j.rser.2018.09.044

Stekovic, S., Hofer, S. J., Tripolt, N., Aon, M. A., Royer, P., Pein, L., et al. (2020). Alternate day fasting improves physiological and molecular markers of aging in healthy, non-obese humans. *Cell Metab* 30, 462–476.e6. doi: 10.1016/j.cmet.2019.07.016

Ueki, T. (2021). Cytochromes in extracellular electron transfer in geobacter. *Appl. Environ. Microbiol.* 87, e3109–e3120. doi: 10.1128/AEM.03109-20

Vasylevskyi, S. I., Kracht, S., Corcosa, P., Fromm, K. M., Giese, B., and Füeg, M. (2017). Formation of silver nanoparticles by electron transfer in peptides and c-cytochromes. *Angew. Chem. Int. Ed.* 56, 5926–5930. doi: 10.1002/anie.201702621

Velten, S., Hammes, F., Boller, M., and Egli, T. (2007). Rapid and direct estimation of active biomass on granular activated carbon through adenosine tri-phosphate (ATP) determination. *Water Res.* 41, 1973–1983. doi: 10.1016/j.watres.2007.01.021

Wilson, D. F., and Matschinsky, F. M. (2021). Metabolic homeostasis: its origin and thermodynamic basis. *Front. Physiol.* 12:658997. doi: 10.3389/fphys.2021.658997

Conflict of Interest: The authors declare that the research was conducted in the absence of any commercial or financial relationships that could be construed as a potential conflict of interest.

frontiers | Frontiers in Microbiology

ORIGINAL RESEARCH
published: 13 July 2022
doi: 10.3389/fmicb.2022.907976

Cable Bacteria Activity Modulates Arsenic Release From Sediments in a Seasonally Hypoxic Marine Basin

Sebastiaan J. van de Velde[1,2]*, *Laurine D. W. Burdorf*[3], *Silvia Hidalgo-Martinez*[3], *Martine Leermakers*[4] *and Filip J. R. Meysman*[3,5]*

[1] Department of Geoscience, Environment and Society, Université Libre de Bruxelles, Brussels, Belgium, [2] Operational Directorate Natural Environment, Royal Belgian Institute of Natural Sciences, Brussels, Belgium, [3] Microbial Systems Technology, Department of Biology, University of Antwerp, Antwerp, Belgium, [4] Analytical, Environmental and Geo-Chemistry, Department of Chemistry, Vrije Universiteit Brussel, Brussels, Belgium, [5] Department of Biotechnology, Delft University of Technology, Delft, Netherlands

Edited by:
Amelia-Elena Rotaru,
University of Southern Denmark, Denmark

Reviewed by:
Jens Harder,
Max Planck Society, Germany
Susan Childers,
Colby College, United States

***Correspondence:**
Sebastiaan J. van de Velde
sebastiaan.van.de.velde@ulb.be
Filip J. R. Meysman
f.j.r.meysman@tudelft.nl

Specialty section:
This article was submitted to Microbiological Chemistry and Geomicrobiology, a section of the journal Frontiers in Microbiology

Received: 30 March 2022
Accepted: 30 May 2022
Published: 13 July 2022

Citation:
van de Velde SJ, Burdorf LDW, Hidalgo-Martinez S, Leermakers M and Meysman FJR (2022) Cable Bacteria Activity Modulates Arsenic Release From Sediments in a Seasonally Hypoxic Marine Basin. Front. Microbiol. 13:907976. doi: 10.3389/fmicb.2022.907976

Eutrophication and global change are increasing the occurrence of seasonal hypoxia (bottom-water oxygen concentration $<63\ \mu M$) in coastal systems worldwide. In extreme cases, the bottom water can become completely anoxic, allowing sulfide to escape from the sediments and leading to the development of bottom-water euxinia. In seasonally hypoxic coastal basins, electrogenic sulfur oxidation by long, filamentous cable bacteria has been shown to stimulate the formation of an iron oxide layer near the sediment-water interface, while the bottom waters are oxygenated. Upon the development of bottom-water anoxia, this iron oxide "firewall" prevents the sedimentary release of sulfide. Iron oxides also act as an adsorption trap for elements such as arsenic. Arsenic is a toxic trace metal, and its release from sediments can have a negative impact on marine ecosystems. Yet, it is currently unknown how electrogenic sulfur oxidation impacts arsenic cycling in seasonally hypoxic basins. In this study, we presented results from a seasonal field study of an uncontaminated marine lake, complemented with a long-term sediment core incubation experiment, which reveals that cable bacteria have a strong impact on the arsenic cycle in a seasonally hypoxic system. Electrogenic sulfur oxidation significantly modulates the arsenic fluxes over a seasonal time scale by enriching arsenic in the iron oxide layer near the sediment-water interface in the oxic period and pulse-releasing arsenic during the anoxic period. Fluxes as large as 20 μmol m^{-2} day^{-1} were measured, which are comparable to As fluxes reported from highly contaminated sediments. Since cable bacteria are recognized as active components of the microbial community in seasonally hypoxic systems worldwide, this seasonal amplification of arsenic fluxes is likely a widespread phenomenon.

Keywords: electrogenic sulfur oxidation, marine sediments, long-distance electron transport, cable bacteria, arsenic, euxinia

INTRODUCTION

The global prevalence of seasonal hypoxia in coastal systems is increasing as a result of climate change and increased delivery of nutrients to the coastal ocean (Diaz and Rosenberg, 2008; Breitburg et al., 2018). Stratification coupled to high primary production leads to low oxygen concentrations in the bottom water of coastal water bodies in summer ["hypoxia," defined as (O_2)

$< 63\ \mu M$]. In some cases, the bottom water may become entirely devoid of oxygen ("anoxic") and allows the escape of dissolved sulfide from the sediment, which can lead to the accumulation of sulfide in the bottom waters (named "euxinia"). At the same time, bottom-water oxygen limits the efflux of trace metals such as arsenic (As) from marine sediments by sustaining an iron oxide layer near the sediment-water interface (SWI), which acts as an efficient adsorption trap for trace metal(loid)s (Riedel et al., 1999). As the prevalence and frequency of hypoxia increase, trace metal(loid)s release from marine sediments is expected to increase (Banks et al., 2012). For a toxic trace metalloid like As, such an enhanced sedimentary efflux may harm the local marine ecosystem. Exposure to micromolar levels of As (both As^{III} and As^{V}) is toxic to plants and animals, and the inorganic forms of As are also known carcinogens in humans (Sharma and Sohn, 2009).

In seasonally hypoxic Lake Grevelingen, the metabolic activity of cable bacteria during the oxic period in winter and spring limits sedimentary sulfide release during the anoxic period in summer by developing a "firewall" for dissolved sulfide (Burdorf et al., submitted; Seitaj et al., 2015). Cable bacteria are sulfur-oxidizing bacteria that perform electrogenic sulfur oxidation (e-SOx), which couples the oxidation of sulfide at depth to the reduction of oxygen near the SWI through electrical currents that run along the centimeter-long axis of these filamentous bacteria (Nielsen et al., 2010; Meysman et al., 2019). This centimeter-scale decoupling of redox half-reactions generates large characteristic pH excursions, inducing a broad and acidic zone at depth and a narrow and alkaline zone near the SWI (Nielsen and Risgaard-Petersen, 2014; Meysman et al., 2015; Meysman, 2017). The low pH at depth dissolves iron sulfides and releases dissolved iron in the pore water, of which part diffuses toward the oxic zone and precipitates as iron oxide (Risgaard-Petersen et al., 2012; Rao et al., 2016). This upward transport of reduced iron builds up a disproportionally large iron oxide layer during the oxic months, which subsequently provides an efficient cap (referred to as a "firewall") for dissolved sulfide during the hypoxic and anoxic period (Burdorf et al., submitted; Seitaj et al., 2015). Active cable bacteria populations are also found in other seasonally hypoxic sites (Burdorf et al., 2017), which makes this possibly a global feature.

The As cycle in marine sediments is closely coupled to the iron cycle due to strong interactions between As and various iron minerals, such as iron (oxyhydr)oxides (further referred to as iron oxides) and iron-sulfide minerals (Mucci et al., 2000; Bostick and Fendorf, 2003; Chaillou et al., 2003; Wolthers et al., 2005; Couture et al., 2010). Under oxic bottom water conditions, As enters the sediment adsorbed onto iron oxides in settling particles. When these iron oxides are buried below the oxic zone, As is co-released with ferrous iron to the pore water during dissimilatory iron reduction (Edenborn et al., 1986; Peterson and Carpenter, 1986; Chaillou et al., 2003; Gao and Mucci, 2003). Consequently, the concentrations of dissolved As in the pore water are much higher than in the overlying water. The release of As from the sediment is generally small, as long as the water column is sufficiently oxygenated to sustain an iron oxide layer near the SWI. Only a limited fraction of As ($0.02–0.9\ \mu mol\ m^{-2}\ day^{-1}$) is generally able to diffuse through the oxic zone and into the overlying water (Peterson and Carpenter, 1986; Martin and Pedersen, 2002; Chaillou et al., 2003; Senn et al., 2007) because of the fast adsorption of As on the iron oxide oxides in the oxic zone (Couture et al., 2010). When oxygen concentrations in the overlying water decrease, the As efflux from sediments can become much higher ($1.6–4.8\ \mu mol\ m^{-2}\ day^{-1}$) (Riedel et al., 1999; Banks et al., 2012), as the iron oxide layer is no longer sustained.

The high affinity of As for iron oxides, together with the iron firewall mechanism induced by the cable bacteria, suggests that seasonally hypoxic systems may experience an amplified seasonal As cycle. Preliminary evidence indeed indicates that during the dissolution of iron sulfide minerals in the electro-active zone (the zone where e-SOx is active), As is released to the pore water (van de Velde et al., 2017). However, the evolution of the As cycle in coastal systems experiencing seasonal hypoxia remains poorly understood, and the impact of the iron firewall mechanism on As effluxes has not been examined. In this study, we presented *in-situ* pore-water and solid-phase data from three time points (i.e., March, May, and September 2015) in the seasonal cycle of Lake Grevelingen. These data are combined with results from a long-term core incubation experiment, where we monitored As release over several weeks after induction of anoxia. Our results demonstrated that the e-SOx metabolism of cable bacteria seasonally modulates the As release from the sediment, by limiting the As efflux in spring and stimulating the As efflux at the onset of hypoxia.

MATERIALS AND METHODS

Field Site

Lake Grevelingen (N 51°44′, E 3°52′) is a saline coastal water body (area: 115 km^2) in the Netherlands that is part of the former Rhine-Meuse-Scheldt estuary. Water exchange takes place via a sluice connection with the North Sea, and so a relative constant salinity (29–32) is maintained throughout the year. The study site was station "S1" in the Den Osse basin (23 m depth), which rapidly accumulates organic-rich sediments ($\sim 2\ cm\ year^{-1}$) (Malkin et al., 2014). Seasonal oxygen depletion is a yearly occurring phenomenon at this site (Wetsteijn, 2011). In 2012, an extensive year-long sampling campaign has revealed the importance of e-SOx for sedimentary Fe, Mn, S, P, and Mo cycling in response to seasonally changing oxygen conditions (Seitaj et al., 2015; Sulu-Gambari et al., 2016a,b; Sulu-gambari et al., 2017). This dataset forms the background for this study.

Water-Column and Sediment Core Sampling

Bottom water and sediment cores were collected on three different occasions (i.e., March, May, and August 2015). During each sampling campaign, water column depth profiles of temperature (T), salinity (S), and oxygen (O_2) saturation were recorded with a CTD instrument (YSI 6600, YSI inc., USA). Bottom water was sampled with a 12 L NISKIN bottle, which was held stationary at 20 m depth for at least 10 min before retrieval. The bottom water was analyzed for O_2, dissolved iron, and dissolved As. Afterwards, sediment cores were collected using a single core gravity corer (UWITEC, Austria) and transparent PVC core liners (inner diameter: 6 cm; length: 60 cm). Upon retrieval, sediment cores were carefully inspected and only cores with an apparent undisturbed SWI were kept for further analysis. Sediment cores were investigated with microsensor depth profiling at *in-situ* temperature in a temperature-controlled shipboard laboratory within 6 h from sampling. Subsequently, the sediment cores were transported back to a shore-based laboratory (NIOZ, Yerseke, The Netherlands) in a thermally insulated container for further analysis and experiments.

Sediment Incubations

Whole-core sediment incubations were initiated the day after sediment core collection. Two cores were sectioned immediately before the incubation to determine the initial pore-water and solid-phase conditions. Three replicate cores were subsequently incubated, and the sediment levels of these cores were adjusted to have comparable volumes of overlying water (∼15 cm). At the start of the incubation, about 75% of the overlying water in these cores was replaced with deoxygenated artificial seawater (salinity = 30); the cores were closed off with custom-built airtight polyoxymethylene lids equipped with a central stirrer and incubated in the dark in a temperature-controlled incubator (LT650 Elbanton, The Netherlands, 4°C—the *in-situ* temperature of the bottom water in March). Oxygen concentrations were continuously monitored (sampling frequency $\sim 0.1\ \text{min}^{-1}$) during the whole incubation using Oxygen Spot Sensors (OXPSP5; Pyroscience, Germany). Each week, the overlying water in the incubations was discretely sampled *via* two sampling ports in the lid, which allowed water sampling without O_2 introduction. The water sample was analyzed for dissolved iron, dissolved sulfide, and dissolved As. To this end, glass syringes (Hamilton, USA) were connected to the sampling ports with tygon tubing. After sample collection, ∼75% of the overlying water was removed and replaced with freshly prepared artificial seawater (salinity = 30), which was deoxygenated beforehand *via* nitrogen bubbling. The new artificial seawater was added carefully by placing a piece of bubble wrap on the top of the remaining water, which minimized disturbance of the sediment surface. Subsequently, the lid was replaced, and any remaining bubbles were removed by injecting anoxic water. Incubations continued for a few weeks after sulfide was detected in the overlying water (March: 23 weeks, May: 15 weeks, August: 7 weeks). In August, sulfide was detected after only 1 week of incubation, and thus the incubation time was much shorter for this month. At the end of the long-term incubation, duplicate cores were sectioned, and pore water and solid phase were analyzed (see below).

Sediment and Pore Water Collection

Cores were sectioned for pore-water collection in an anaerobic glove box (N_2 atmosphere with 3–5% H_2; Coy lab products, USA). Cores were sectioned at 0.5 cm resolution from 0 to 6 cm depth and 1 cm resolution between 6 and 12 cm depth. Sediment slices were collected in 50 ml polypropylene centrifuge tubes (TPP, Switzerland) and centrifuged at 3,000 rpm for 10 min (Sigma 3–18KS, Sigma Laborzentrifugen GmbH, Germany). Subsequently, the centrifuge tubes were opened in the anaerobic glove box, and overlying pore water was transferred into suitable sample containers after filtration through 0.45 μm cellulose filters (Millex-HA filter, Merck Millipore, USA). Pore-water samples were analyzed for dissolved iron and dissolved As. To prevent oxidation, the solid phase that remained after centrifugation was freeze-dried and sealed in an airtight aluminum bag inside the anaerobic glove box and stored anaerobically for later solid-phase analysis.

Microsensor Profiling

Microsensor profiling was carried out for dissolved H_2S (100 μm tip diameter), O_2 (50 μm tip), and pH (200 μm tip) using commercial micro-electrodes (Unisense A.S., Denmark). In each core, 2 replicate profiles were taken for each of the three parameters. Dissolved H_2S was calibrated by making a five-point standard curve using Na_2S standards, which were prepared on the day of analysis. For O_2, a two-point calibration was made using air-saturated seawater (100% saturation) and the anoxic zone of the sediment (0% saturation). pH was calibrated by a 3-point calibration using standard NBS buffers (pH = 4, 7, and 10), followed by a salinity correction with Tris buffer (Dickson et al., 2007). Measurements of pH were performed using an external Ag/AgCl reference electrode, and values are reported on the total pH scale.

Bottom-Water and Pore-Water Analysis

Water samples for dissolved Fe analysis were immediately stabilized with 50 μl of bidistilled HNO_3 (65%) per ml of sample and preserved at 4°C. Before the analysis, samples were diluted 50 times with a standard matrix solution containing 35% artificial seawater and 2% HNO_3 using $0.2\ \text{mg L}^{-1}$ Ytterbium as an internal standard (Crompton, 1989). Samples were subsequently analyzed by inductively coupled plasma-optical emission spectroscopy (ICP-OES, ThermoFisher iCAP6500), precision was <2%. We will refer to concentrations determined by ICP-OES as dissolved Fe (dFe). Note, however, that the sample fraction obtained after filtration does not only consist of aqueous Fe^{2+} and dissolved complexes but potentially also of a fraction of colloidal and nanoparticulate iron (Raiswell and Canfield, 2012).

Samples for As analysis were stabilized and preserved identical as for dFe and were analyzed by high-resolution-inductively coupled plasma-mass spectroscopy (HR-ICP-MS, ThermoScientific Element 2) after 20× dilution with Milli-Q water. Indium (2.5 ppb) containing 2% HNO_3 was injected simultaneously with the sample as an internal standard. Similar to iron, we will refer to As as dissolved As (dAs).

Samples for total free sulfide analysis $[\Sigma H_2S = (H_2S) + (HS^-)]$ were fixed with 100 μl ZnAc (10 %) per ml of sample and analyzed spectrophotometrically following the methylene blue method (Cline, 1969).

Solid-Phase Analysis

To determine the solid-phase speciation of Fe and As within solid sediment phases, two extraction procedures were used (**Supplementary Table 1**). The first extraction uses an ascorbate solution that targets reactive Fe(III) phases, all Mn(III, IV) oxides and oxyhydroxides and associated trace metals (Kostka and Luther, 1994). The second extraction procedure employs a 1 M HCl solution, which extracts acid-volatile sulfides (AVSs), carbonate, amorphous Fe(III) phases, and elements from clay minerals (Kostka and Luther, 1994). In both procedures, 300 μg of dry sediment was extracted with 25 ml of solution (which was purged with N_2 gas for 30 min before) for 24 h at ambient temperature under constant agitation. The addition of the solution was carried out inside an anaerobic chamber, to avoid oxidation artifacts. Afterwards, the solution was centrifuged and the supernatant was filtered (0.45 μm cellulose filters), diluted 20×, stabilized with 1% HNO_3 and stored at 4°C. Analysis was carried out with HR-ICP-MS for Fe and As as described above for bottom- and pore-water analysis. Reproducibility (determined as the relative standard deviation of three replicates) for the ascorbate extraction was 3–7% for Fe and 2–5% for As. For the HCl extraction, reproducibility was 15–20 % for Fe and 20–30% for As.

Solid-phase inventories were calculated as follows:

$$INV = \int_{x_{up}}^{x_{down}} (1-\phi)\rho_s C_{solid} dx \qquad (1)$$

where C_{solid} is the solid-phase concentration (in mol g^{-1} dry weight), φ is the porosity, ρ_s is the density of the solid phase, and x_{up} and x_{down} are the depths over which the inventory was calculated. The porosity φ was determined from water content and solid-phase density measurements, accounting for the salt content of the pore water and averaged for the whole depth interval. The water content was determined as the volume of water removed when wet sediment samples were dried to constant weight at 60°C. Solid-phase density ρ_s at the field site was previously determined at 2.6 g cm^{-3} and assumed to be constant over the whole depth interval (Seitaj et al., 2017).

Flux Calculations

The sediment efflux $F_S(t)$ of a given species S (dAs, dFe, or ΣH_2S) was determined by calculating the solute inventory in the overlying water at the start and end of the weekly incubations. The inventory at the end simply amounts to $V_{OLW}[S]_{end}$, where V_{OLW} is the volume of the overlying water and $[S]_{end} = [S]_t$ is the concentration of species S at time t. The inventory at the start of the incubation needs to account for the water replacement operation and becomes

$$V_{OLW}[S]_{start} = V_{repl}[S]_{repl} + \left(V_{OLW} - V_{repl}\right)[S]_{t-1} \qquad (2)$$

where V_{repl} is the volume of the replaced overlying water, $[S]_{repl}$ is the concentration of species S in the replacing seawater, and $[S]_{t-1}$ is the concentration of S at the previous time point in the overlying water that remained. The efflux then can be calculated as follows:

$$F_S(t) = \frac{V_{OLW}[S]_{end} - V_{OLW}[S]_{start}}{A_{core} t} \qquad (3)$$

where Δt represents the exact duration of the incubation period (always ∼7 days), and A_{core} is the surface area of the sediment (28.3 cm^2).

The cumulative flux represents the total amount of species S that was released into the water column during the whole experiment and was calculated as follows:

$$\int_0^{t_{end}} F_S(t)dt = \sum F_S(t)\Delta t \qquad (4)$$

where t_{end} is the end of the experiment, and $F_S(t)$ is the flux at time t, as calculated by Equation (3).

Diffusive fluxes in the pore water are estimated using the Fick's first law (Fick, 1855) as follows:

$$J_{diff} = -\phi \frac{D_0(S,T)}{\theta^2} \frac{\delta C}{\delta x} \qquad (5)$$

where J_{diff} is the diffusive flux, C is the concentration in the pore water, x is the depth into the sediment, φ represents porosity, and $\theta^2 = 1-2\ln\varphi$ is the correction factor for sediment tortuosity (Boudreau, 1996). The molecular diffusion coefficient (D_0) is calculated for measured salinity and temperature using the R package CRAN:marelac (Soetaert et al., 2010). The concentration gradient (δC/δx) was calculated by fitting a linear regression to the concentration profiles using the custom-made R script FLIPPER (https://github.com/sevdevel/FLIPPER) (van de Velde et al., 2022).

RESULT AND DISCUSSION

Sedimentary Biogeochemical Cycling in a Seasonally Hypoxic System

The combined O_2, H_2S, and pH microsensor profiles suggest a distinct seasonality in the geochemistry of Lake Grevelingen sediments, which are also reflected in the pore-water depth profiles of ferrous iron. This seasonality has been described in detail before and is due to drastic changes in the sedimentary microbial community and metabolism in response to the seasonal variation in bottom water oxygen concentrations in the seasonally hypoxic Lake Grevelingen (Seitaj et al., 2015; Sulu-Gambari et al., 2016a).

In March 2015, the bottom water was fully oxygenated [(O_2) = 329 μM], and microsensor profiling revealed the characteristic geochemical signature of electrogenic sulfur oxidation (e-SOx) by cable bacteria (**Figure 1A**; Nielsen et al., 2010; Meysman et al., 2015). A suboxic zone of ∼40 mm deep was present, in which O_2 and H_2S remained below the detection limit (<1 μM). The pH depth profile showed a subsurface maximum (pH = 8.82 ± 0.03) near the oxygen penetration depth (OPD = 1.4 ± 0.3 mm) due to the proton consumption associated with cathodic reduction of oxygen

$$O_2 + 4e^- + 4H^+ \rightarrow 2H_2O \qquad (6)$$

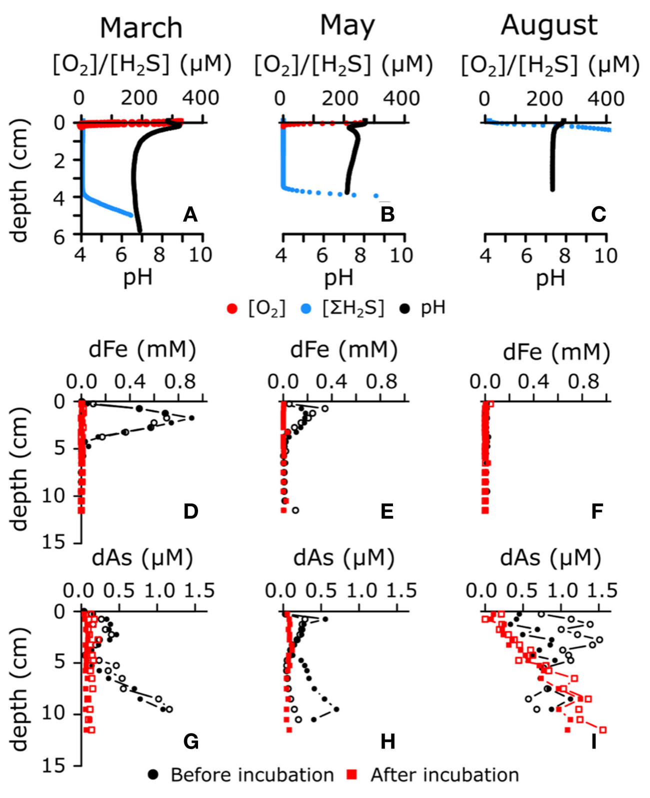

FIGURE 1 | (A–C) Representative microsensor depth profiles of O_2, H_2S, and pH in three different seasons (i.e., March, May, and August 2015) in sediment of seasonally hypoxic Lake Grevelingen. All microsensor profile replicates are shown in **Supplementary Figure 2**. **(D–F)** Pore water depth profiles of dissolved iron in sediment upon core retrieval (denoted in black dots) and after prolonged incubation with anoxic overlying water (denoted in red squares). **(G–I)** Pore water profiles of dissolved arsenic before (denoted in black dots) and after (denoted in red squares) prolonged anoxic incubation. Open and filled symbols represent replicate cores.

while an acidic minimum ($pH = 6.4 \pm 0.1$) was generated near the sulfide appearance depth ($SAD = 41 \pm 2$ mm), resulting from proton production during anodic sulfide oxidation

$$H_2S + 4H_2O \rightarrow SO_4^{2-} + 8e^- + 10H^+ \tag{7}$$

The low pH stimulated the dissolution of acid-sensitive minerals, most notably iron sulfide (Risgaard-Petersen et al., 2012; Rao et al., 2016; van de Velde et al., 2016), thus leading to strong dFe accumulation in the pore water (**Figure 1D**). The rate of FeS dissolution can be estimated by the sum of the diffusive fluxes just above and below the subsurface maximum dFe concentration (2.3 mmol m^{-2} day^{-1}), which is comparable to other sediments with active e-SOx (Rao et al., 2016; van de Velde et al., 2016). Of the ferrous iron released in the pore water, 60% diffused toward the SWI, and the remaining 40% diffused downwards.

In May, bottom water [O_2] was at 60% air saturation (175 μM), and the pH depth profiles revealed a subsurface minimum at the OPD (1.0 ± 0.3 mm), followed by a local maximum in the zone just underneath (**Figure 1B**). This specific type of pH depth profile has been associated with active cycling of iron between oxidized and reduced forms, where sediment mixing transports reduced forms of iron (FeS, adsorbed Fe^{2+}) into the oxic zone and oxidized forms (FeOOH) downwards (Seitaj et al., 2015). This type of iron cycling requires an active form of sediment mixing such as bioturbation (van de Velde and Meysman, 2016; van de Velde et al., 2020), and indeed, we observed small polychaete tubes sticking out of the sediment (Burdorf et al., submitted). Evidence for burrowing fauna in May has also been found during a previous seasonal study of Lake Grevelingen (Seitaj et al., 2015, 2017). The proton production associated with the oxidation of reduced iron (FeS, Fe^{2+} or adsorbed Fe^{2+}) and potential chemolithoautotrophy, led to a pH minimum in the oxic zone ($pH = 7.10 \pm 0.04$)

$$4Fe^{2+} + O_2 + 6H_2O \rightarrow 4FeOOH + 8H^+ \tag{8}$$

whereas below 0.5 cm depth, the recovery of the pH to higher values ($pH = 7.7 \pm 0.2$) is likely driven by the reduction of iron oxides (e.g., *via* sulfide-mediated iron reduction)

$$8FeOOH + H_2S + 14H^+ \rightarrow 8Fe^{2+} + SO_4^{2-} + 12H_2O \tag{9}$$

Bioturbation generated a suboxic zone of 37 ± 7 mm, as the downmixing of iron oxides at depth prevented the accumulation of free sulfide (van de Velde and Meysman, 2016). Even though the redox pathways are likely more complex (e.g., by an intermediate cycle of manganese between oxygen and iron) (Aller, 1990; Sulu-Gambari et al., 2016a,b), iron cycling leads to an overall release of protons within the oxic surface layer and consumption of protons in the deeper suboxic zone (Jourabchi et al., 2005), as seen in the pH depth profile. The reductive dissolution of iron oxide also led to the release of dissolved iron in the pore water (**Figure 1E**), albeit at a lower rate than in March when e-SOx was active (Fe release rate = 1.4 mmol m^{-2} day^{-1}, of which 78% diffuses toward the SWI).

The anoxic bottom water in August [(O_2) < 1 μM] excluded e-SOx by cable bacteria (due to the lack of electron acceptors) and bioturbation (due to faunal mortality), and this is reflected in the microsensor depth profiles (**Figure 1C**). The pH decreased to a minimum of 7.3 ± 0.1 in the first 0.5 cm, after which it remained constant with depth, while ΣH_2S started accumulating immediately at the SWI. This particular combination of pH and ΣH_2S depth profiles is expected when sulfate reduction is the dominant pathway (Jourabchi et al., 2005):

$$2CH_2O + SO_4^{2-} \rightarrow 2HCO_3^- + H_2S \tag{10}$$

Strong sulfide production and the absence of bioturbation and e-SOx prevents the formation of a suboxic zone and inhibits the accumulation of dFe in the pore water through FeS precipitation (**Figure 1F**).

Overall, we found that iron and sulfur cycling in Lake Grevelingen shows a marked seasonality, alternating between dominance of e-SOx in March, bioturbation-driven metal cycling in May and sulfate reduction in August. This seasonal pattern is congruent with previous descriptions of the sediment biogeochemical cycling in Lake Grevelingen (Seitaj et al., 2015; Sulu-Gambari et al., 2016a) and shows that this strong seasonality in iron and sulfur cycling is likely a recurring phenomenon. The upward dFe fluxes were large in both March (1.4 mmol m^{-2} day^{-1}) and May (1.1 mmol m^{-2} day^{-1}), which suggests that substantial iron oxides were formed within the oxic zone, thus leading to the accumulation of iron oxides near the SWI (**Figures 2A,E**). However, there is an important difference between both periods. During e-SOx activity in March, iron is first transferred from reduced FeS to dissolved Fe in the pore water and subsequently precipitates as oxidized FeOOH. This is when a strong iron oxide "firewall" *sensu* Seitaj et al. (2015) is formed, and this engenders a one-way transport of iron from deeper layers to the oxic zone near the sediment surface. In May, when bioturbation is active, iron cycling is fundamentally different. FeOOH and FeS are cycled forth and back within the bioturbated zone, leading to a re-distribution of Fe over reduced and oxidized phases (Burdorf et al., submitted; Seitaj et al., 2015). As shown below, these different modes of iron cycling will differently control the sedimentary As cycle.

Arsenic Cycling in a Seasonally Hypoxic Basin

In March 2015, when the water column was fully oxygenated, e-SOx was active in the sediment (**Figure 1A** and Section Sedimentary Biogeochemical Cycling in a Seasonally Hypoxic System), and a subsurface maximum of dAs was seen over the first 4 cm (coinciding with the suboxic zone; **Figure 1G**). In anoxic sediments, As adsorbs readily onto iron sulfides (Farquhar et al., 2002; Bostick and Fendorf, 2003; Wolthers et al., 2005). During e-SOx-driven dissolution of FeS, As was likely released into the pore water (production rate = 0.85 μmol m^{-2} day^{-1}, of which 45% diffuses upwards), leading to accumulation of dAs in the pore water within the electro-active zone (**Figure 1G**; van de Velde et al., 2017). Alternatively, decreasing pH has been shown to lower the adsorption capacity of As onto iron sulfide minerals (Bostick and Fendorf, 2003; Wolthers et al., 2005). This could be an additional explanation for the As release seen in

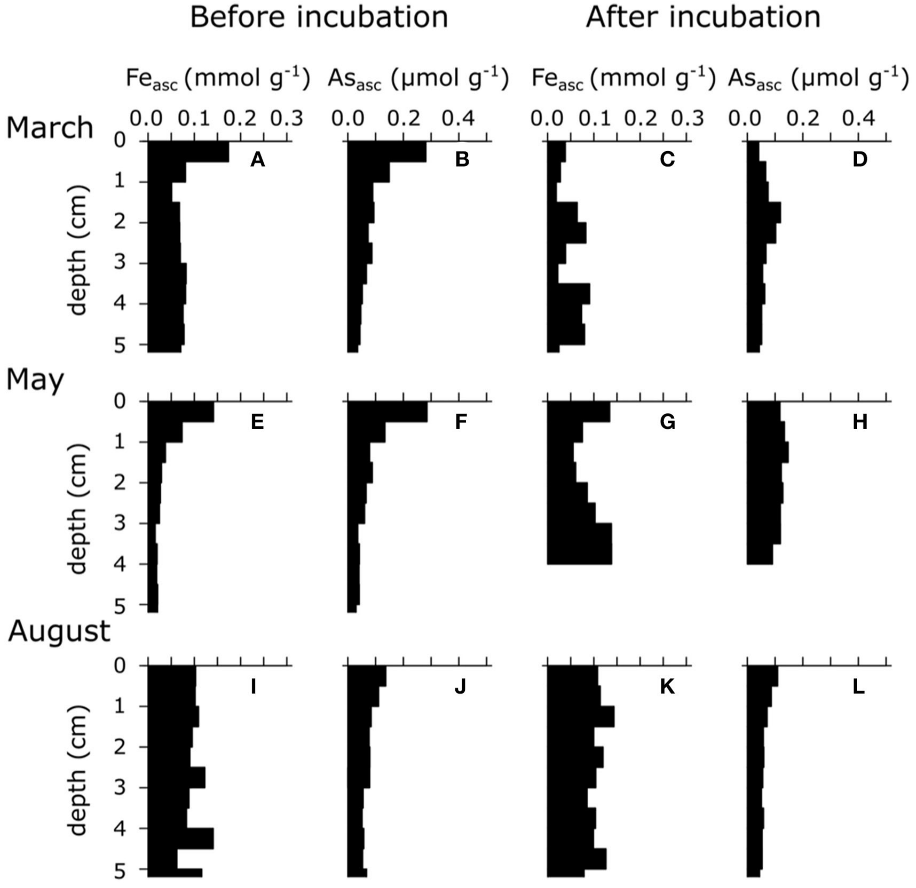

FIGURE 2 | Ascorbate extractable Fe (Fe$_{asc}$) and As (As$_{asc}$) of three different seasons (i.e., March, May, and August 2015) in the sediment of seasonally hypoxic Lake Grevelingen. **(A,E,I)** Solid-phase ascorbate extractable iron depth profile upon core retrieval. **(B,F,J)** Solid-phase ascorbate extractable arsenic depth profile upon core retrieval. **(C,G,K)** Solid-phase ascorbate extractable iron depth profile after prolonged anoxic incubation. **(D,H,L)** Solid-phase ascorbate extractable arsenic depth profile after prolonged anoxic incubation. Results are expressed in μmol g^{-1} dry weight. Note the difference in x-axis for Fe$_{asc}$ and As$_{asc}$.

the electro-active zone. The observed dAs concentrations (0.2–0.5 μM) are comparable to those seen in bioturbated coastal sediments, where the As cycle is driven by iron oxide reduction (0.01–1.2 μM) (Edenborn et al., 1986; Peterson and Carpenter, 1986; Mucci et al., 2000, 2003; Chaillou et al., 2003). However, the dAs concentrations observed here are about four times lower than previously found in North-Sea sediments, where e-SOx was the dominant process (van de Velde et al., 2017). They are also lower than in deltaic sediments that sustain an active iron cycle (Sullivan and Aller, 1996) and contaminated lake sediments (Barrett et al., 2019; Leclerc et al., 2021), where pore water dAs can reach up to 2 μM (and sometimes up to 10 μM). Just below the zone of As release, the pore water showed a zone with strong dAs consumption, which corresponded to the interface between the ferruginous and the sulphidic pore water. This dAs removal is likely caused by intense FeS precipitation due to the supply of dissolved iron from the suboxic zone (**Figure 1D**). As this FeS is newly formed, and thus highly disordered, a lot of adsorption sites for As are created, which enables a strong sink for dAs (and leads to near-zero concentrations of dAs).

Part of the As diffusing upwards adsorbs onto iron oxides that are present near the SWI. Most of the upward diffusing As can be trapped in the oxic layer (0.3 μmol m^{-2} day^{-1}), and only ~0.08 μmol m^{-2} day^{-1} can potentially diffuse into the water column (see As budget in Supporting Information). Trapping of As in the oxic zone leads to As accumulation in the iron oxide layer (up to 0.3 μmol As g^{-1}) near the SWI (**Figure 2B**). Other studies have reported similar concentrations of particulate As in the top layer of coastal sediments (Mucci et al., 2000; Chaillou et al., 2003), higher concentrations are generally found in contaminated marine (0.4–0.7 μmol As g^{-1}; Chaillou et al., 2003) and lake sediments (up to 15 μmol As g^{-1}; Barrett et al., 2019; Leclerc et al., 2021).

Intriguingly, the pore water profiles suggest a strong upward flux of dAs coming from below the sampled depth of 12 cm. This upward flux was present in all cores of all three sampled months (black dots in **Figures 1G–I**) and disappeared after prolonged anoxic incubation (red squares in **Figures 1G–I**), which suggests that there is a deep and continuous source of dAs (below 15 cm depth). Note that the incubation time of the August cores was only 35 days, as compared with >100 days for the other 2 months, so there was less time for dAs to diffuse out of the sediment. This dAs source is possibly coming from crystalline iron oxides that were preserved and slowly dissolved afterwards or As associated with refractory organic matter (Chaillou et al., 2003). Alternatively, the As that was adsorbed on FeS could desorb due to the increase in dissolved sulfide with depth (Bostick and Fendorf, 2003), or As can be released when FeS becomes more ordered, which decreases the available adsorption sites. The affinity of As is a factor 5 lower for pyrite compared with FeS and so the gradual transformation of FeS into FeS_2 in deeper sediments can also lead to As release (Bostick and Fendorf, 2003). Note that the incubated sediment cores only extend to 12 cm and are cut-off from this deeper As source that is present in natural sediments, which explains why dAs decreases at depth over time in the incubations.

In May 2015, the dAs peak was closer to the SWI (0.5 μM at 0.25 cm depth; **Figure 1H**), correlating with the highest As_{asc} concentration (0.3 μmol g^{-1}; **Figure 2F**), which suggests that the As release was now mainly driven by dissimilatory iron reduction (Mucci et al., 2000; Chaillou et al., 2003; Couture et al., 2010). The production rate of As in May was almost two times higher than in March (1.52 μmol m^{-2} day^{-1} vs. 0.85 μmol m^{-2} day^{-1}). In March, the main dAs source was the dissolution of FeS, which has a lower adsorption affinity for dAs than FeOOH. Accordingly, we conjectured that more As was co-released during iron reduction in May, thus explaining the higher release rates compared with those in March.

Below the zone of dAs release, the sink of dAs was less pronounced in May, suggesting that the trapping mechanism from early spring (strong FeS precipitation) was less potent due to lower pore water dFe concentrations (**Figure 1E**). The location of this sink was also higher, corresponding to the upwards migration of the sulfide horizon (**Figure 1H**). As_{asc} concentrations did not vary significantly between March and May (**Figures 2B,F**), suggesting that less dAs was lost from the sediment over that period, likely because the oxygen concentration in the overlying water was still sufficiently high to act as an efficient trap. Hence, sufficient iron oxides were still present (**Figure 2E**) to re-adsorb the dissolved As that was released during dissimilatory iron oxide reduction.

In summer, the whole sediment core was sulphidic (**Figure 1C**), and the concentration of As_{asc} dropped in the top sediment layer (< 0.15 μmol g^{-1}; **Figure 2J**). Dissolved As showed strong accumulation in the upper 5 cm (up to 1.5 μM at 2.5 cm depth; **Figure 1I**). Under high sulfide concentrations, As is known to adsorb onto FeS surfaces (Farquhar et al., 2002; Wolthers et al., 2005) or to form authigenic As sulfides (Mucci et al., 2000, 2003; O'Day et al., 2004), which would lead to low dAs concentrations (in contrast to what we see in this study). However, high sulfide concentrations also inhibit the adsorption capacity of As on iron sulfide mineral surfaces (Bostick and Fendorf, 2003). In the anoxic part of the sediment, iron sulfide minerals are abundant (Seitaj et al., 2015; Sulu-Gambari et al., 2016a; Burdorf et al., submitted), and a fraction of the dAs will be adsorbed onto these minerals (~0.05 μmol g^{-1} in the absence of dissolved sulfide; **Supplementary Material**). The upward migrating ΣH_2S horizon can then lead to a transient increase of dAs by a relatively small decrease in the adsorption capacity of As on iron sulfides (a decrease of ~10% in adsorption capacity can lead to pore water dAs concentrations of >1 μM; **Supplementary Material**).

The combination of solid-phase and pore-water data suggest a strong link between the As cycle and the iron firewall mechanism induced by electrogenic sulfur oxidation (e-SOx), which can be summarized in a conceptual scheme (**Figure 3**). During winter and spring, e-SOx drives the dissolution of FeS and stimulates the formation of an iron oxide layer near the SWI (Seitaj et al., 2015; Sulu-Gambari et al., 2016a,b). Simultaneously, dAs is transferred from FeS in the deeper sediment layers to FeOOH near the SWI, leading to an enrichment of As in the iron oxide layer (**Figures 2B**, **3**). In late spring, the sediment geochemistry changes to a bioturbation-driven iron cycle, which

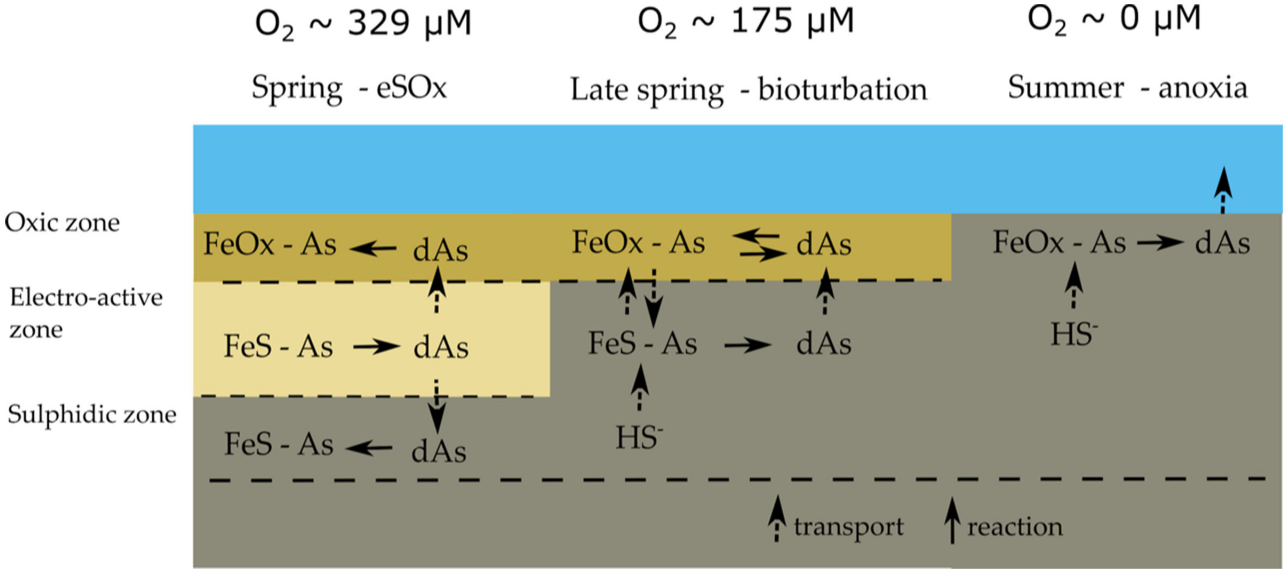

FIGURE 3 | Conceptual model of the sedimentary arsenic cycle in seasonally hypoxic Lake Grevelingen; typical bottom water oxygen concentrations are indicated above. The dominant mode of geochemical cycling alternates between electrogenic sulfur oxidation in spring, bioturbation in late spring and anoxia in summer. See main text for details.

decreases the magnitude of the iron trap by the down-mixing of FeOOH and its subsequent conversion into FeS phases (Burdorf et al., submitted; Seitaj et al., 2015). During this downward mixing, As is released from the reduction of iron oxides and re-adsorbs on the iron oxides still present in the oxic zone, which leads to a constant concentration of dAs concentration in the iron oxide layer (**Figures 2B**, **3**). However, after spring, when oxygen concentrations in the bottom water gradually decrease to eventually result in anoxia, the sulfide-mediated dissolution of the iron oxides will release all the adsorbed As into the overlying water column (**Figures 2J**, **3**).

Benthic-Pelagic Coupling

The fluxes of As, Fe, and ΣH_2S that were recorded weekly during the sediment incubation experiment fully support the above model of the seasonal As cycle in Lake Grevelingen (**Figure 3**). In March, dFe was immediately released upon the introduction of anoxia with a maximum flux of 4 mmol Fe m^{-2} day^{-1} in the first 2 weeks, while in contrast, no detectable ΣH_2S efflux was noted for 50–100 days (**Figures 4A,D**). As was co-released with iron (**Figure 4G**), though with a delay, and its maximum flux was only achieved after 50 days (~3 μmol m^{-2} day^{-1}). This suggests that in the early stages of the incubations, some of the As was re-adsorbed onto the iron oxide layer that was still present. When the sulfide efflux effectively started after 100 days, As still escaped the sediment, though fluxes gradually diminished (~1.5 μmol m^{-2} day^{-1}). This suggests that authigenic As sulfides do not form fast enough to trap all the dAs, and hence, they do not form an efficient sink for As. The measured As fluxes are typical for sediments underlying anoxic bottom waters (1.6–4.8 μmol m^{-2} day^{-1}) (Riedel et al., 1999; Banks et al., 2012).

In May, dFe was also immediately released and quickly increased to a maximum flux (2–3 mmol m^{-2} day^{-1}) that was about half that of March. Due to the presence of iron oxides in the top layer (**Figure 2E**), the ΣH_2S release was also delayed, but now only for 30–50 days (**Figures 4B,E**), revealing that the strength of the iron firewall had diminished (Burdorf et al., submitted). In contrast, the maximum dAs efflux (15–20 μmol m^{-2} day^{-1}) was much higher compared with March, and no delayed response was observed (**Figure 4H**). In August, no detectable dFe or dAs fluxes were measured, and ΣH_2S was immediately released, indicating that the iron oxide layer was exhausted (**Figures 4C,F,I**).

The iron oxide trapping capacity was smaller in May compared with March, likely because part of the FeOOH was transported down by bio-mixing and converted into FeS (Burdorf et al., submitted; Seitaj et al., 2015). This is confirmed by the cumulative Fe flux, which was two times lower in May (69–134 mmol m^{-2}) compared with March (52–60 mmol m^{-2}) (**Table 1**). Cumulative As fluxes strongly correlated with cumulative Fe fluxes in both March and May (**Supplementary Figure 3**). In March, the As/Fe ratio of the cumulative flux was 0.003, while in May, it was 5 times higher (0.014), indicating that ~5 times more As (relative to Fe) was released in May. This suggests that during the initial dissolution stages of the iron oxide layer, a fraction of the As re-adsorbed on the iron oxide layer (consistent with the low As fluxes in the first weeks of the March incubation). In May, the change in solid-phase inventory before and after the experiment, estimated *via* the ascorbate extraction (0.44 mmol As m^{-2}), agreed well with the cumulative As flux (0.32 ± 0.15 mmol As m^{-2}; **Table 1**), indicating that only a small amount of As co-precipitated with sulfide or was adsorbed onto existing iron sulfides. In March, however, there was a larger difference (0.84 vs. 0.17 ±

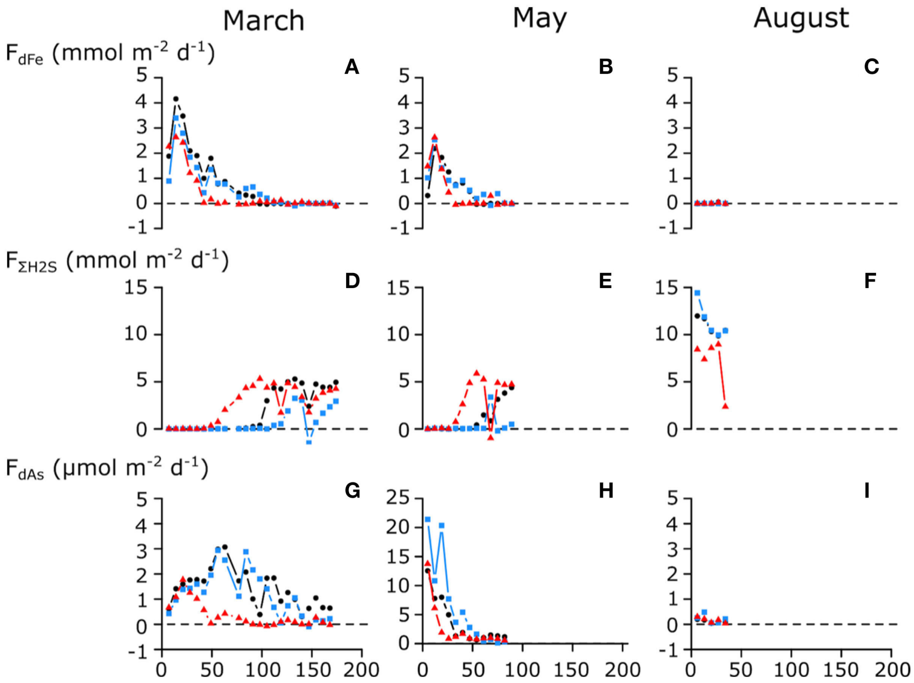

FIGURE 4 | Measured benthic fluxes of **(A–C)** dissolved Fe (dFe); **(D–F)** total free sulfide (ΣH_2S); and **(G–I)** dissolved As (dAs) during the long-term anoxic incubations of cores from seasonally hypoxic Lake Grevelingen. Incubations were stopped when ΣH_2S was detected in the overlying water of all three cores. Cores were collected during different seasons; **(A,D,G)** March 2015; **(B,E,H)** May 2015; and **(C,F,I)** August 2015. Different colors indicate replicate cores. Note the difference in y-axis for the dissolved arsenic flux on **(H)**.

TABLE 1 | Total release of dissolved arsenic (dAs), dissolved iron, and sulfide from the sediment over the course of the incubations (cumulative flux), compared with the inventory change of the ascorbate extraction.

		Cumulative flux (mmol m^{-2})			**Solid-phase inventory change (mmol m^{-2}) in the upper 1 cm**		
		March	**May**	**August**	**March**	**May**	**August**
dAs	Core 1	0.24	0.28	0.004	0.841	0.436	0.135
	Core 2	0.20	0.48	0.005			
	Core 3	0.06	0.18	0.007			
dFe	Core 1	134	52	0.33	491	14.1	−45.4
	Core 2	112	60	0			
	Core 3	69	40	0.21			
ΣH_2S	Core 1	335	100	368			
	Core 2	106	29	385			
	Core 3	450	23	242			

*Positive values indicate net loss; negative values indicate net gain. All units are in mmol m^{-2}. Solid-phase inventory changes were calculated from ascorbate extractable Fe and As concentrations before and after incubation (**Figure 2**).*

0.09 mmol m^{-2}; **Table 1**), which suggests that more As was retained in the sediment (**Figures 4G,H**). Possibly, the constant re-adsorption of As onto the iron oxides retained As in the sediment, which exposed it to sulfide in the pore water for a prolonged time. This could allow the formation and precipitation of authigenic As sulfides in March, which would not have been possible when As immediately diffused into the water column in May.

Impact of the Cable Bacteria Induced Enhanced Seasonality

The iron oxide "firewall" mechanism induced by cable bacteria activity enhances the seasonality of the sedimentary As cycle and its release to the water column. During the oxic season, As is released from the dissolution of iron sulfides and accumulates in the iron oxide layer that is formed at the SWI (**Figure 3**). Subsequently, the sulfide-mediated dissolution of the iron oxide layer during the anoxic period leads to a pulse release, with high benthic As fluxes (up to 20 μmol m^{-2} day^{-1}; **Figure 4H**). This is comparable to As fluxes estimated from pore-water gradients in contaminated lakes with an order of magnitude higher than solid-phase As concentrations (Barrett et al., 2019) and ∼3–4 times higher than previously reported from anoxic sediment incubations (Riedel et al., 1999; Banks et al., 2012). When oxic conditions are subsequently re-stored in autumn and winter, the re-establishment of e-SOx restarts the formation of a new iron oxide layer and the trapping of As restarts. A seasonal study of Lake Grevelingen has shown that this also similarly affects phosphate and molybdenum (Sulu-Gambari et al., 2016b; Sulu-gambari et al., 2017), and it is not unlikely that this mechanism is also active for other elements that have a strong interaction with iron oxides (e.g., silicate and cobalt).

The high As efflux potentially leads to an increased As inventory in the water column. Whether this leads to toxic concentrations depends on the bottom water volume over which the released As is diluted. Water-column profiling (Hagens et al., 2015) shows that the mixed bottom layer in Lake Grevelingen extends over ∼15 m. Using the minimum and maximum cumulative As flux (**Table 1**), this leads to a possible range of As concentrations of 4–32 nM. As a reference, the US EPA guideline for acute exposure of marine animals to arsenite (the reduced form of As, which is stable under anoxic conditions) is 920 nM (Neff, 1997), which suggests that the As release from the sediment of Lake Grevelingen is likely not accumulating up to toxic levels. Yet, in sediment with a low solid-phase As content, we measured high fluxes during the anoxic incubation. In contaminated marine sediments, where sedimentary As concentrations are elevated, even higher fluxes are expected, and the seasonal amplification induced by cable bacteria might pose a previously unknown environmental risk.

DATA AVAILABILITY STATEMENT

The raw data supporting the conclusions of this article will be made available by the authors, without undue reservation.

AUTHOR CONTRIBUTIONS

SV conceived the hypothesis. FM designed the experiment. LB and SH-M performed the field sampling and incubation experiment. SV and LB did the sediment extractions. ML analyzed the arsenic samples. SV and FM wrote the manuscript. All authors contributed to manuscript revision, read, and approved the submitted version.

FUNDING

This research was supported by the Fonds Wetenschappelijk Onderzoek (Grant No. G038819N), the Universiteit Antwerpen (Grant No. TOPBOF), the Netherlands Organization for Scientific Research (Grant No. 016.VICI.170.072), and the Belgian Federal Science Policy Office (Grant No. FED-tWIN2019-prf-008). The HR-ICP-MS instrument was financed by the HERCULES Foundation (Code: UABR/11/010). The experimental work for this manuscript was carried out when SV was supported by a Ph.D. fellowship of the Research Foundation Flanders. SV was currently supported by the Belgian Federal Science Policy Office (Grant No. FED-tWIN2019-prf-008).

ACKNOWLEDGMENTS

The authors would like to thank A. Tramper and P. Van Rijswijk for their help and assistance during the field sampling. The authors thank the crew of the R.V. Navicula for the March and May sampling and the crew of the Bruinvis (Staatsbosbeheer) for the sampling of August.

SUPPLEMENTARY MATERIAL

The Supplementary Material for this article can be found online at: https://www.frontiersin.org/articles/10.3389/fmicb.2022.907976/full#supplementary-material

REFERENCES

Aller, R. C. (1990). Bioturbation and manganese cycling in hemipelagic sediments. *Philos. Trans. R. Soc. London A Math. Phys. Eng. Sci.* 331, 51–68. doi: 10.1098/rsta.1990.0056

Banks, J. L., Ross, D. J., Keough, M. J., Eyre, B. D., and Macleod, C. K. (2012). Measuring hypoxia induced metal release from highly contaminated estuarine sediments during a 40day laboratory incubation experiment. *Sci. Total Environ.* 420, 229–237. doi: 10.1016/j.scitotenv.2012.01.033

Barrett, P. M., Hull, E. A., Burkart, K., Hargrave, O., McLean, J., Taylor, V. F., et al. (2019). Contrasting arsenic cycling in strongly and weakly stratified contaminated lakes: evidence for temperature control on sediment–water arsenic fluxes. *Limnol. Oceanogr.* 64, 1333–1346. doi: 10.1002/lno.11119

Bostick, B. C., and Fendorf, S. (2003). Arsenite sorption on troilite (FeS) and pyrite (FeS2). *Geochim. Cosmochim. Acta* 67, 909–921. doi: 10.1016/S0016-7037(02)01170-5

Boudreau, B. P. (1996). The diffusive tortuosity of fine-grained unlithified sediments. *Geochim. Cosmochim. Acta* 60, 3139–3142. doi: 10.1016/0016-7037(96)00158-5

Breitburg, D., Levin, L. A., Oschlies, A., Grégoire, M., Chavez, F. P., Conley, D. J., et al. (2018). Declining oxygen in the global ocean and coastal waters. *Science* 359, eaam7240. doi: 10.1126/science.aam7240

Burdorf, L. D. W., Tramper, A., Seitaj, D., Meire, L., Hidalgo-Martinez, S., Zetsche, E.-M., et al. (2017). Long-distance electron transport occurs globally in marine sediments. *Biogeosciences* 14, 683–701. doi: 10.5194/bg-14-683-2017

Chaillou, G., Schäfer, J., Anschutz, P., Lavaux, G., and Blanc, G. (2003). The behaviour of arsenic in muddy sediments of The Bay of Biscay (France). *Geochim. Cosmochim. Acta* 67, 2993–3003. doi: 10.1016/S0016-7037(03)00204-7

Cline, J. D. (1969). Spectrophotometric determination of hydrogen sulfide in natural waters. *Limnol. Oceanogr.* 14, 454–458. doi: 10.4319/lo.1969.14.3.0454

Couture, R. M., Gobeil, C., and Tessier, A. (2010). Arsenic, iron and sulfur co-diagenesis in lake sediments. *Geochim. Cosmochim. Acta* 74, 1238–1255. doi: 10.1016/j.gca.2009.11.028

Crompton, T. R. (1989). “Metals,” in *Analysis of Seawater* (Butterworths & Co), 74–215. doi: 10.1016/B978-0-407-01610-1.50007-2

Diaz, R. J., and Rosenberg, R. (2008). Spreading dead zones and consequences for marine ecosystems. *Science* 321, 926–929. doi: 10.1126/science.1156401

Dickson, A. G., Sabine, C. L., and Christian, J. R. (2007). “Guide to best practices for ocean CO2 measurements,” in *PICES Special Publication 3, IOCCP Report No. 8*, eds A. G. Dickson, C. L. Sabine and J. R. Cristian (Sidney, NSW: North Pacific Marine Science Organization), 1–191.

Edenborn, H. M., Belzile, N., Mucci, A., Lebel, J., and Silverberg, N. (1986). Observations on the diagenetic behavior of arsenic in a deep coastal sediment. *Biogeochemistry* 2, 359–376. doi: 10.1007/BF02180326

Farquhar, M. L., Charnock, J. M., Livens, F. R., and Vaughan, D. J. (2002). Mechanisms of arsenic uptake from aqueous solution by interaction with goethite, lepidocrocite, mackinawite, and pyrite: an X-ray absorption spectroscopy study. *Environ. Sci. Technol.* 36, 1757–1762. doi: 10.1021/es010216g

Fick, A. (1855). Uber diffusion. *Ann. Phys.* 94, 59–86. doi: 10.1002/andp.18551700105

Gao, Y., and Mucci, A. (2003). Individual and competitive adsorption of phosphate and arsenate on goethite in artificial seawater. *Chem. Geol.* 199, 91–109. doi: 10.1016/S0009-2541(03)00119-0

Hagens, M., Slomp, C. P., Meysman, F. J. R., Seitaj, D., Harlay, J., Borges, A. V., et al. (2015). Biogeochemical processes and buffering capacity concurrently affect acidification in a seasonally hypoxic coastal marine basin. *Biogeosciences* 12, 1561–1583. doi: 10.5194/bg-12-1561-2015

Jourabchi, P., Van Cappellen, P., and Regnier, P. (2005). Quantitative interpretation of pH distributions in aquatic sediments: a reaction-transport modeling approach. *Am. J. Sci.* 305, 919–956. doi: 10.2475/ajs.305.9.919

Kostka, J. E., and Luther, G. W. III. (1994). Partitioning and speciation of solid phase iron in saltmarsh sediments. *Geochim. Cosmochim. Acta* 58, 1701–1710. doi: 10.1016/0016-7037(94)90531-2

Leclerc, É., Venkiteswaran, J. J., Jasiak, I., Telford, J. V., Schultz, M. D. J., Wolfe, B. B., et al. (2021). Quantifying arsenic post-depositional mobility in lake sediments impacted by gold ore roasting in sub-arctic Canada using inverse diagenetic modelling. *Environ. Pollut.* 288, 117723. doi: 10.1016/j.envpol.2021.117723

Malkin, S. Y., Rao, A. M., Seitaj, D., Vasquez-Cardenas, D., Zetsche, E.-M., Hidalgo-Martinez, S., et al. (2014). Natural occurrence of microbial sulphur oxidation by long-range electron transport in the seafloor. *ISME J.* 8, 1843–1854. doi: 10.1038/ismej.2014.41

Martin, A. J., and Pedersen, T. F. (2002). Seasonal and interannual mobility of arsenic in a Lake impacted by metal mining. *Environ. Sci. Technol.* 36, 1516–1523. doi: 10.1021/es0108537

Meysman, F. J. R. (2017). Cable bacteria take a new breath using long-distance electricity. *Trends Microbiol.* 26, 411–422. doi: 10.1016/j.tim.2017.10.011

Meysman, F. J. R., Cornelissen, R., Trashin, S., Bonn,é, R., Martinez, S. H., van der Veen, J., et al. (2019). A highly conductive fibre network enables centimetre-scale electron transport in multicellular cable bacteria. *Nat. Commun.* 10, 4120. doi: 10.1038/s41467-019-12115-7

Meysman, F. J. R., Risgaard-Petersen, N., Malkin, S. Y., and Nielsen, L. P. (2015). The geochemical fingerprint of microbial long-distance electron transport in the seafloor. *Geochim. Cosmochim. Acta* 152, 122–142. doi: 10.1016/j.gca.2014.12.014

Mucci, A., Boudreau, B., and Guignard, C. (2003). Diagenetic mobility of trace elements in sediments covered by a flash flood deposit: Mn, Fe and As. *Appl. Geochem.* 18, 1011–1026. doi: 10.1016/S0883-2927(02)00207-X

Mucci, A., Richard, L., Lucotte, M., and Guignard, C. (2000). The differential geochemical behavior of arsenic and phosphorus in the water column and sediments of the Saguenay Fjord Estuary, Canada. *Aquat. Geochemistry* 6, 293–324. doi: 10.1023/A:1009632127607

Neff, J. M. (1997). Ecotoxicology of arsenic in the marine environment. *Environ. Toxicol. Chem.* 16, 917–927. doi: 10.1002/etc.5620160511

Nielsen, L. P., and Risgaard-Petersen, N. (2014). Rethinking sediment biogeochemistry after the discovery of electric currents. *Ann. Rev. Mar. Sci.* 7, 425–42. doi: 10.1146/annurev-marine-010814-015708

Nielsen, L. P., Risgaard-Petersen, N., Fossing, H., Christensen, P. B., and Sayama, M. (2010). Electric currents couple spatially separated biogeochemical processes in marine sediment. *Nature* 463, 1071–1074. doi: 10.1038/nature08790

O’Day, P. A., Vlassopoulos, D., Root, R., and Rivera, N. (2004). The influence of sulfur and iron on dissolved arsenic concentrations in the shallow subsurface under changing redox conditions. *Proc. Natl. Acad. Sci. U.S.A.* 101, 13703–13708. doi: 10.1073/pnas.0402775101

Peterson, M. L., and Carpenter, R. (1986). Arsenic distributions in porewaters and sediments of Puget Sound, Lake Washington the Washington coast and Saanich Inlet, B.C. *Geochim. Cosmochim. Acta* 50, 353–369. doi: 10.1016/0016-7037(86)90189-4

Raiswell, R., and Canfield, D. E. (2012). The iron biogeochemical cycle past and present. *Geochem. Perspect.* 1, 1–232. doi: 10.7185/geochempersp.1.1

Rao, A. M. F., Malkin, S. Y., Hidalgo-Martinez, S., and Meysman, F. J. R. (2016). The impact of electrogenic sulfide oxidation on elemental cycling and solute fluxes in coastal sediment. *Geochim. Cosmochim. Acta* 172, 265–286. doi: 10.1016/j.gca.2015.09.014

Riedel, G. F., Sanders, J. G., and Osman, R. W. (1999). Biogeochemical control on the flux of trace elements from estuarine sediments : effects of seasonal and short-term hypoxia. *Mar. Environ. Res.* 47, 349–372. doi: 10.1016/S0141-1136(98)00125-1

Risgaard-Petersen, N., Revil, A., Meister, P., and Nielsen, L. P. (2012). Sulfur, iron-, and calcium cycling associated with natural electric currents running through marine sediment. *Geochim. Cosmochim. Acta* 92, 1–13. doi: 10.1016/j.gca.2012.05.036

Seitaj, D., Schauer, R., Sulu-gambari, F., Hidalgo-martinez, S., Malkin, S. Y., Burdorf, L. D. W., et al. (2015). Cable bacteria generate a firewall against euxinia in seasonally hypoxic basins. *Proc. Natl. Acad. Sci.* 112, 13278–13283. doi: 10.1073/pnas.1510152112

Seitaj, D., Sulu-Gambari, F., Burdorf, L. D. W., Romero-Ramirez, A., Maire, O., Malkin, S. Y., et al. (2017). Sedimentary oxygen dynamics in a seasonally hypoxic basin. *Limnol. Oceanogr.* 62, 452–473. doi: 10.1002/lno.10434

Senn, D. B., Gawel, J. E., Jay, J. A., Hemond, H. F., and Durant, J. L. (2007). Long-term fate of a pulse arsenic input to a eutrophic lake. *Environ. Sci. Technol.* 41, 3062–3068. doi: 10.1021/es062444m

Sharma, V. K., and Sohn, M. (2009). Aquatic arsenic: toxicity, speciation, transformations, and remediation. *Environ. Int.* 35, 743–759. doi: 10.1016/j.envint.2009.01.005

Soetaert, K., Petzoldt, T., and Meysman, F. J. R. (2010). *marelac: Tools for Aquatic Sciences R Package Version 2.1*.

Sullivan, K. A., and Aller, R. C. (1996). Diagenetic cycling of arsenic in Amazon shelf sediments. *Geochim. Cosmochim. Acta* 60, 1465–1477. doi: 10.1016/0016-7037(96)00040-3

Sulu-gambari, F., Roepert, A., Jilbert, T., Hagens, M., Meysman, F. J. R., and Slomp, C. P. (2017). Molybdenum dynamics in sediments of a seasonally hypoxic coastal marine basin. *Chem. Geol.* 466, 627–640. doi: 10.1016/j.chemgeo.2017.07.015

Sulu-Gambari, F., Seitaj, D., Behrends, T., Banerjee, D., Meysman, F. J. R., and Slomp, C. P. (2016a). Impact of cable bacteria on sedimentary iron and manganese dynamics in a seasonally-hypoxic marine basin. *Geochim. Cosmochim. Acta* 192, 49–69. doi: 10.1016/j.gca.2016.07.028

Sulu-Gambari, F., Seitaj, D., Meysman, F. J. R., Schauer, R., Polerecky, L., and Slomp, C. P. (2016b). Cable bacteria control iron-phosphorus dynamics in sediments of a coastal hypoxic basin. *Environ. Sci. Technol.* 50, 1227–1233. doi: 10.1021/acs.est.5b04369

van de Velde, S. J., Burdorf, L. D. W., and Meysman, F. J. R. (2022). FLIPPER - FLexible Interpretation of Porewater Profiles and Estimation of Rates. Zenodo. doi: 10.5281/zenodo.6624982

van de Velde, S. J., Callebaut, I., Gao, Y., and Meysman, F. J. R. (2017). Impact of electrogenic sulfur oxidation on trace metal cycling in a coastal sediment. *Chem. Geol.* 452, 9–23. doi: 10.1016/j.chemgeo.2017.01.028

van de Velde, S. J., Hidalgo-Martinez, S., Callebaut, I., Antler, G., James, R., Leermakers, M., et al. (2020). Burrowing fauna mediate alternative stable states in the redox cycling of salt marsh sediments. *Geochim. Cosmochim. Acta* 276, 31–49. doi: 10.1016/j.gca.2020.02.021

van de Velde, S. J., Lesven, L., Burdorf, L. D. W., Hidalgo-Martinez, S., Geelhoed, J. S., Van Rijswijk, P., et al. (2016). The impact of electrogenic sulfur oxidation on the biogeochemistry of coastal sediments: a field study. *Geochim. Cosmochim. Acta* 194, 211–232. doi: 10.1016/j.gca.2016.08.038

van de Velde, S. J., and Meysman, F. J. R. (2016). The influence of bioturbation on iron and sulphur cycling in marine sediments: a model analysis. *Aquat. Geochem.* 22, 469–504. doi: 10.1007/s10498-016-9301-7

Wetsteijn, L. P. M. (2011). *Grevelingenmeer: Meer Kwetsbaar? Een Beschrijving van de Ecologische Ontwikkelingen Voor de Periode 1999 t/m 2008-2010 in Vergelijking Met de Periode 1990 t/m 1998*. Lelystad. Available onhline at: https://www.zeeweringenwiki.nl/images/5/53/Wetsteijn%2C_L.P.M.J.%2C_2011._Grevelingenmeer_meer_kwetsbaar.pdf

Wolthers, M., Charlet, L., van Der Weijden, C. H., van der Linde, P. R., and Rickard, D. (2005). Arsenic mobility in the ambient sulfidic environment: sorption of arsenic(V) and arsenic(III) onto disordered mackinawite. *Geochim. Cosmochim. Acta* 69, 3483–3492. doi: 10.1016/j.gca.2005.03.003

Conflict of Interest: The authors declare that the research was conducted in the absence of any commercial or financial relationships that could be construed as a potential conflict of interest.

frontiers | Frontiers in Microbiology

TYPE Original Research
PUBLISHED 10 August 2022
DOI 10.3389/fmicb.2022.907703

Tracing and regulating redox homeostasis of model benthic ecosystems for sustainable aquaculture in coastal environments

Nobuaki Shono[1], Mana Ito[2], Akio Umezawa[1], Kenji Sakata[3], Ailong Li[1], Jun Kikuchi[3,4,5], Katsutoshi Ito[2]* and Ryuhei Nakamura[1,6]*

[1]Biofunctional Catalyst Research Team, Center for Sustainable Resource Science, RIKEN, Wako, Japan, [2]Fisheries Technology Institute, Japan Fisheries Research and Education Agency, Hatsukaichi, Japan, [3]RIKEN Center for Sustainable Resource Science, Yokohama, Japan, [4]Graduate School of Medical Life Science, Yokohama City University, Yokohama, Japan, [5]Graduate School of Bioagricultural Sciences, Nagoya University, Nagoya, Japan, [6]Earth-Life Science Institute, Tokyo Institute of Technology, Tokyo, Japan

OPEN ACCESS

EDITED BY
Nils Risgaard-Petersen,
Aarhus University, Denmark

REVIEWED BY
Mayumi Seto,
Nara Women's University, Japan
Masahiro Yamamoto,
Japan Agency for Marine-Earth Science and Technology (JAMSTEC), Japan
Souichiro Kato,
National Institute of Advanced Industrial Science and Technology (AIST), Japan

*CORRESPONDENCE
Katsutoshi Ito
ito_katsutoshi15@fra.go.jp
Ryuhei Nakamura
ryuhei.nakamura@riken.jp

SPECIALTY SECTION
This article was submitted to Microbiological Chemistry and Geomicrobiology, a section of the journal Frontiers in Microbiology

RECEIVED 30 March 2022
ACCEPTED 06 July 2022
PUBLISHED 10 August 2022

CITATION
Shono N, Ito M, Umezawa A, Sakata K, Li A, Kikuchi J, Ito K and Nakamura R (2022) Tracing and regulating redox homeostasis of model benthic ecosystems for sustainable aquaculture in coastal environments.
Front. Microbiol. 13:907703.
doi: 10.3389/fmicb.2022.907703

Aquaculture in coastal environments has an increasingly important role in the world's food supply; however, the accumulation of organic compounds on seafloors due to overfeeding adversely affects benthic ecosystems. To assess the ecological resilience of aquafarms to nutrient influx, we investigated the redox homeostasis of benthic ecosystems using a marine oligochaete as a model benthic organism in aquaculture fields. Real-time monitoring of the redox potential of a model benthic ecosystem constructed in an electrochemical reactor allowed evaluation of the homeostatic response of the system to nutrient addition. Although the detrimental effects of overfeeding were confirmed by irreversible potential changes in the sediment, redox homeostasis was reinforced through a cooperative relationship between oligochaetes and sediment microorganisms. Specifically, the oligochaetes exhibited reversible changes in metabolism and body position in response to dynamic changes in the sediment potential between −300 and 500mV, thereby promoting the decomposition of organic compounds. The potential-dependent changes in metabolism and body position were reproduced by artificially manipulating the sediment potential in electrochemical reactors. Given the importance of benthic animals in sustaining coastal ecosystems, the electrochemical monitoring and physiologic regulation of marine oligochaetes could offer an intriguing approach toward sustainable aquaculture.

KEYWORDS

redox homeostasis, benthic ecosystems, aquaculture, electromicrobiology, benthos

Introduction

The United Nations estimates that the world population will reach 9.8 billion in 2050 and result in an unprecedented food crisis (United Nations, Department of Economic and Social Affairs, Population Division, 2015). To increase food stability, the sustainable use of marine resources, mainly through aquaculture, is considered to be essential (Costello et al., 2020). Currently, half of the fish and shellfish consumed in the world are sourced from aquafarms, which have production rates that are growing faster than those in any other animal production sector (FAO, 2014). In addition, it has been estimated that approximately 15 billion tons of fish can be produced annually in marine coastal areas through aquaculture (Gentry et al., 2017). However, the feeding practices for aquaculture fields located in marine coastal areas often result in overfeeding and the accumulation of organic matter in seafloor sediments, which adversely affects benthic ecosystems (Yokoyama et al., 2006; Holmer et al., 2008a) and leads to eutrophication, algal blooms, and red tides (Sarà, 2007). A recent evaluation of the aquaculture industry using a composite sustainability index comprised of food, energy, water, and carbon, revealed that most aquaculture practices worldwide has low sustainability indices (Jiang et al., 2022). Therefore, there is a need to establish sustainable aquaculture systems that balance productivity and environmental conservation.

Traditionally, the environmental assessment of aquaculture fields uses both chemical indicators and benthic fauna (Holmer et al., 2008b), with the latter serving as bioindicators for collecting diverse information of aquatic environments (Martinez-Crego et al., 2010). However, this approach is not suitable for assessing short-term environmental changes, such as those that occur on the hour- and day-scale. Although chemical indicators, such as oxygen, nitrogen, phosphorus, and sulfur compounds have the potential to instantly respond to changes caused by feeding, this method requires enormous efforts for on-site water and sediment sampling and the comprehensive analysis of complex chemical compounds.

As an alternative approach to bioindicator and chemical analyses, we applied electrochemical techniques for assessing the resilience of benthic ecosystems in aquaculture farms (Ito et al., 2019). The environmental redox potential is a physicochemical value determined by the integration of various factors, including (i) biological parameters, such as gene expression, metabolism, and bacterial flora; (ii) chemical parameters, such as oxygen, sulfide, and nutrient concentrations; and (iii) nutrient influx from rivers and land due to human activities. Therefore, real-time monitoring of the environmental redox potential can be used to evaluate the overall and homeostatic responses of benthic ecosystems associated with aquaculture to feeding.

Redox homeostasis is a common phenomenon in microorganisms and is primarily maintained at the cellular level through the regulation of metabolism and gene expression. At the ecosystem level in aquaculture fields, such homeostasis has the potential to be further strengthened through the cooperative relationship between microorganisms and benthic animals, such as shrimp, polychaetes, and bivalves (Levin et al., 2001; Marinelli and Waldbusser, 2005). As redox homeostasis is disrupted by overfeeding, understanding how the homeostasis is sustained by the interplay between benthic animals and microorganisms is fundamental for developing sustainable aquaculture systems.

As a proof of concept for the use of real-time monitoring of environmental redox potential to assess ecosystem-level homeostasis, here, we reconstructed model benthic ecosystems inside an electrochemical (EC) reactor. A chemically stable and biocompatible conductive glass was used as an electrode within marine sediment containing the marine oligochaete *Thalassodrilides* cf. *briani* (Torii et al., 2016). Aquatic oligochaetes (Annelisda, Clitellata) are found in marine, estuarine, and freshwater environments worldwide (Timm, 1980) and are recognized as ecosystem engineers owing to their bioturbation and organic decomposition activities (Jones et al., 1994; Mermillod-Blondin and Rosenberg, 2006). Using *T.* cf. *briani* as a representative benthos in aquaculture fields, we conducted real-time monitoring of redox homeostasis and analyzed how the redox potential is affected by feeding and the metabolic states and movement of oligochaetes. Utilizing electrochemical techniques, we also artificially manipulated the sediment potential to investigate if the metabolic states and macroscopic movement of oligochaetes could be regulated.

Materials and methods

Sediment sampling and maintenance

Sediment was obtained below a fish culturing raft in the coastal area of Ehime, Japan. The sediment sample was stored in the dark at 19°C with artificial seawater (MARINE ART SF-1; Osaka Yakken Co. Ltd., Osaka, Japan). Prior to experimental use, the sediment was transferred into a beaker at a thickness of approximately 2 cm and covered with approximately 5 cm of artificial sea water.

Preparation of sediment samples

A portion of the sediment being maintained in artificial seawater was collected onto a plate and benthic organisms visible to the naked eye were manually removed. This sediment was considered to contain only microorganisms and a portion of this sample was autoclaved at 121°C for 20 min to prepare sediment without microorganisms or benthos. Finally, forty *T.* cf. *briani* specimens were added to both the autoclaved and microorganisms-only sediment to generate sediment samples that contain only benthos and microorganisms and benthos, respectively.

Electrochemical experiment

A three-electrode electrochemical cell (EC; 8 ml capacity) was assembled using a platinum wire and Ag/AgCl/saturated KCl as counter and reference electrodes, respectively. A fluorine-doped tin oxide (FTO)-coated glass electrode (surface area of 3.14 cm^2; SPD Laboratory, Inc.) was used as a working electrode and was placed at the bottom of the EC reactor. The 3 g of wet sediments and 4 ml of artificial sea water was added in the EC reactor. The temperature of the reactor was maintained at 25°C and no agitation other than that resulting from experimental operation was made during the measurements. The head space of the EC reactor is open to air *via* a membrane filter (0.20 μm pore size; ADVANTEC). Redox potential measurements were conducted using open circuit potential measurements performed with an automatic polarization system (HZ-5000; Hokuto Denko). As nutrients, fish feed (dry pellet; Otohime B1; Marubeni Nisshin Feed, Tokyo, Japan) was pulverized into a powder and suspended in artificial seawater (MARINE ART SF-1; Osaka Yakken Co. Ltd., Osaka, Japan) at a concentration of 20 mg/ml. The amount of fish food in the EC reactor was adjusted by varying the amount of suspension added, and the resulting air-saturated suspension was added to the electrochemical cell. A current vs. time curve was measured under potentiostatic conditions at 400 or 0 mV (vs. SHE) using the automatic polarization system.

NMR analysis

The collected oligochaetes from the EC reactor were gently washed with artificial seawater to remove excess material and transferred to a 2-ml safe lock tube. As much artificial sea water was removed from the tubes as possible by aspiration, and the tubes were allowed to vacuum dry using a GLD-136C rotary vacuum pump (ULVAC), and were then stored at −80°C. Prior to use, 3 mm × 2 mm zirconia beads were added to the tubes and the dried mass of oligochaetes was crushed with a Bead Smash 12 (TOMY) at 3,000 rpm for 5 min. As a calibration standard, 0.1 mM DSS (4,4-dimethyl-4-silapentane-1-sulfonic acid) in D_2O (pH = 7, adjusted with 100 mM potassium phosphate buffer; Yoshida et al., 2014) was added to the samples, which were then incubated at 60°C for 15 min with frequent mixing. The samples were centrifuged at 15,000 rpm for 10 min at room temperature, and the supernatant was transferred to a new tube and stored at either 4°C or frozen. Prior to analysis, the samples were centrifuged at 15,000 rpm for 10 min at room temperature and transferred to 5-mm Φ—nuclear magnetic resonance (NMR) tubes (Shigemi). All oligochaetes samples were subjected to 2D-*J*res NMR analysis for the monitoring of temporal metabolic changes following the electrochemical experiments conducted in sediment. ^{1}H-^{13}C-HSQC and ^{1}H-^{13}C-HSQC-TOCSY NMR was then applied to a standard sample (oligochaetes prior to experimental use) for the NMR signal assignment of metabolites.

Acquisition and analysis of time lapse images

To acquire time lapse images, an electrochemical cell (1 cm × 3.14 cm; same area as used in the electrochemical experiments above) with a flat side was prepared and into which 3 g sediment, 3 ml artificial seawater, and 10 oligochaetes were added. The prepared cell was placed in a box equipped with a mild light source and a time-lapse camera (TLC 200 PRO) in the front, and images were then acquired while conducting potential and current measurements. Image analysis was performed using ImageJ software and a macro program for counting the number of oligochaete tails and quantifying sediment movement.

Results and discussion

Real-time monitoring of redox homeostasis

To construct a miniature benthic ecosystem for real-time monitoring, marine sediments collected approximately 30 m directly beneath an aquaculture raft were placed in an EC reactor equipped a glass electrode on the bottom surface (Figure 1A). The glass working electrode was coated with fluorine-doped tin oxide (FTO), which has high biocompatibility and long-term chemical durability (Ishii et al., 2015), and Ag/AgCl (KCl sat.) was used as the reference electrode (Figure 1B). In this study, the term “redox potential” represents the electrochemical potential measured under open circuit conditions.

The dominant benthic organism in the sediment was a marine annelid identified as *T.* cf. *briani* (Torii et al., 2016), which is a few centimeters in length and a member of the subclass Oligochaeta. *Thalassodrilides* cf. *briani* was selected as a representative benthic invertebrate for this study and other animals, such as polychaetes and amphipods, were removed from the sediment samples (Figure 1C). *Thalassodrilides* cf. *briani* is present at high densities in sediments located in the vicinity of fish farms (Ito et al., 2018), has high tolerance to concentrated sulfide species, and is able to remediate organically polluted sediments (Ito et al., 2016). Cooperative relationships between benthic animals and sediment microorganisms play a fundamental role in maintaining aquaculture environments by accelerating the decomposition of organic matter that accumulates on the seafloor (Andersen and Kristensen, 1992; Nascimento et al., 2012). To examine if this relationship could be monitored electrochemically, we prepared sediment samples containing only microorganisms, only *T.* cf. *briani*, or both *T.* cf. *briani* and microorganisms, and conducted real-time potential monitoring of the three sediments under open circuit conditions for 15 days. The sediment containing only microorganisms was prepared by removing visible benthic organisms, whereas the sediment containing only benthos was generated by adding *T.* cf. *briani* to autoclaved sediments. These two sediment samples exhibited nearly identical profiles for potential, with the potentials ranging from −100 to 100 mV vs. standard hydrogen electrode (SHE) throughout the 15-day experiment (Figures 2A,B). In contrast, the sediments containing both *T.* cf. *briani* and microorganisms showed a steep increase in potential and transient spike-like potential changes of approximately 10 mV, with the

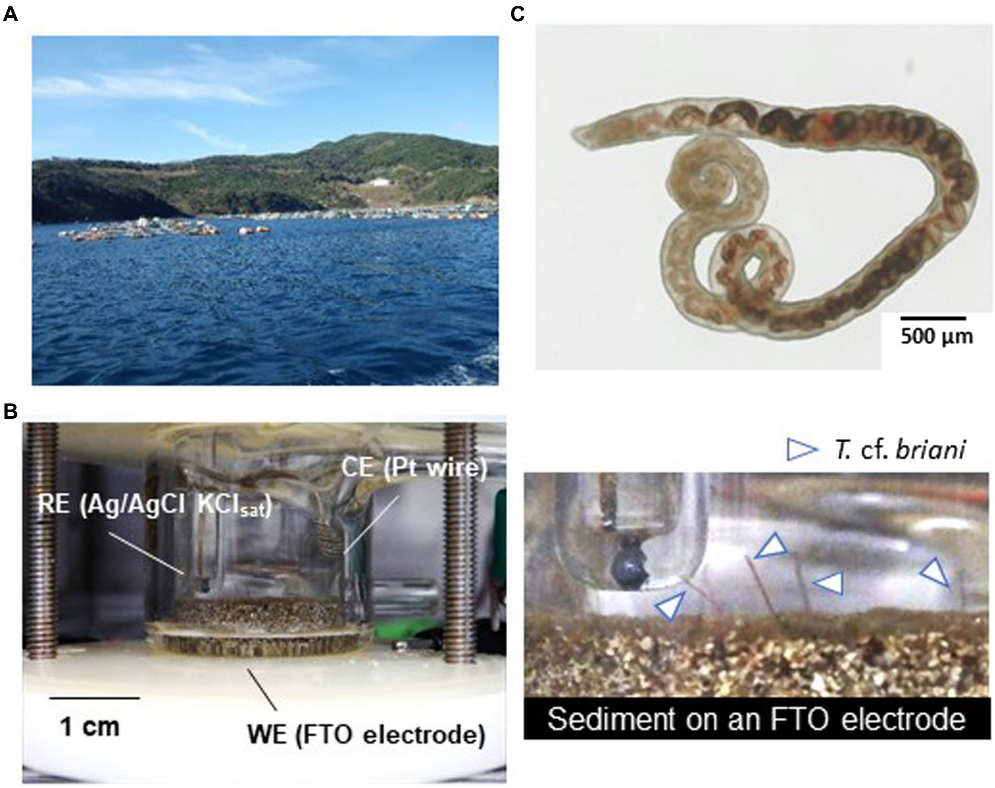

FIGURE 1
(A) Photograph of the fish farm where the sediments used in this study were collected. **(B)** Photographs of the model benthic ecosystem constructed in an electrochemical reactor. RE, WE, and CE denote the reference, working, and counter electrodes, respectively. The objects indicated by the arrows are the tails of oligochaetes protruding from the sediment mounted on the surface of a fluorine-doped tin oxide (FTO)-coated glass electrode. **(C)** Light microscope image of the specimen of the marine oligochaete *Thalassodrilides* cf. *briani*, which was located in sediment samples collected directly beneath the aquaculture raft.

potential reaching approximately 450 mV after 10 days of incubation (Figures 2C,D). The samples lacking either *T.* cf. *briani* or sediment microorganisms did not reach potentials above 100 mV. Therefore, the steep increase in potential up to 450 mV was unique to the marine sediment containing both *T.* cf. *briani* and microorganisms.

Under homeostatic conditions, an ecosystem is expected to reversibly respond to external perturbations such as nutrient influx, which would occur in aquaculture sediments during feeding. However, once an external stress exceeds the resilience limit of the ecosystem, the system can no longer return to the original state. To test if this general homeostatic property is detectable by redox potential measurements, organic matter in the form of fish diet was added into the EC reactor with sediment containing both *T.* cf. *briani* and microorganisms. When 5 mg fish diet was added to the EC reactor, the potential dropped rapidly from 450 to 0 mV; however, the potential increased rapidly in the 24 h following the nutrient addition and then gradually returned to nearly 450 mV level after 1 week of incubation, demonstrating that this model benthic ecosystem functions homeostatically (Figure 2C). Further, when the amount of fish diet added to the EC reactor was increased 4-fold (20 mg), the potential decreased to approximately −300 mV and did not recover to positive values, even after 10 additional days of incubation (Figure 2D; Supplementary Figures 1–3). Such an irreversible change of redox potential indicates that the amount of fish diet added to the reactor exceeded the capacity of this model benthic ecosystems. Consistent with this finding, the sediment in the nutrient-rich system gradually turned black due to the formation of iron sulfides and all of the marine annelids had died under the low potential conditions. Notably, when the experiment was repeated for the sediments lacking either *T.* cf. *briani* or sediment microorganisms, the potential did not recover even after 5 mg feeding, indicating that the cooperation between oligochaetes and sediment microorganisms enhanced the resilience to nutrient influx. This finding, in turn, suggests that the real-time monitoring of redox homeostasis can provide feedback on the feeding practices of aquaculture farms to avoid waste and harm to the surrounding benthic ecosystems.

Potential-dependent movement of benthos

Benthic animals move for a variety of reasons, including nutrient acquisition, locating suitable microhabitats, and the

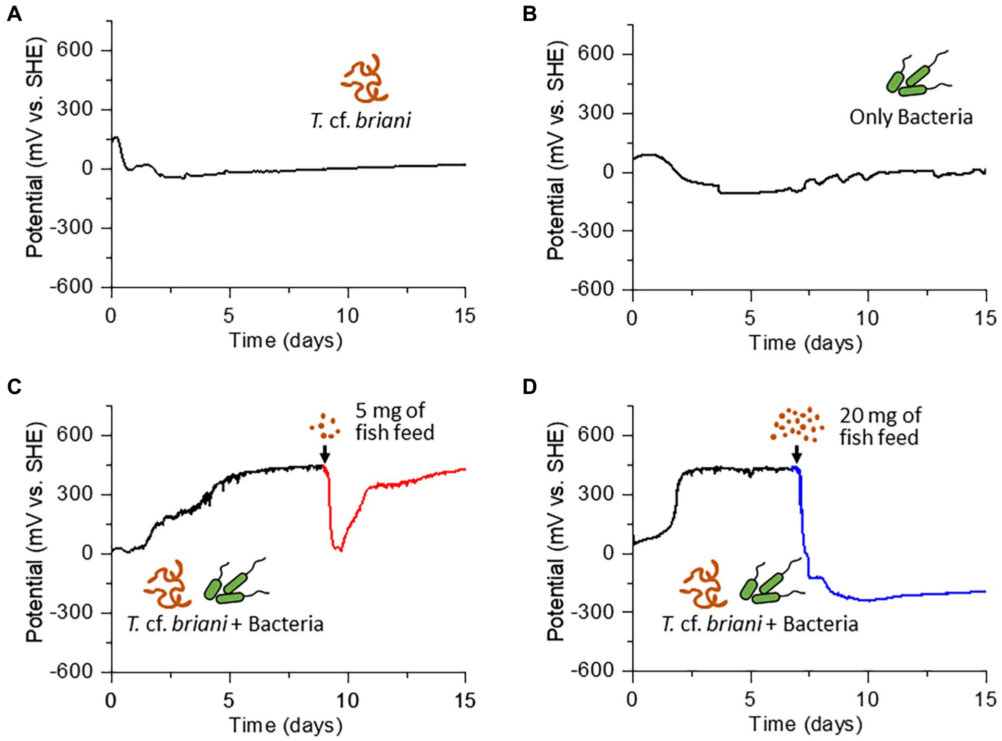

FIGURE 2
Time courses of open circuit potential measurements for **(A)** sediment containing only oligochaetes, **(B)** sediment containing only sediment microorganisms, and **(C,D)** sediment containing both oligochaetes and sediment microorganisms. The arrow in **(C)** and **(D)** indicates the time at which 5 and 20 mg of fish diet, respectively, was added to the electrochemical reactor.

evasion of predators, pollutants, and adverse sediment conditions (Rodriguez and Reynoldson, 2011). As *T.* cf. *briani* is present at the seawater-sediment interface, the movement of this marine annelid is expected to have a significant influence on the redox states of benthic ecosystems. To investigate the correlation between redox potential and the movement of *T.* cf. *briani* in sediment, we developed an EC reactor equipped with an automated photography system (Figure 3A). For this experiment, 10 *T.* cf. *briani* specimens were added to the seafloor sediment on an FTO electrode, and photographs of the seawater-sediment interface were taken every 10 min while simultaneously measuring the electrochemical potential under open circuit conditions. We focused on two body positions: protrusion of the annelid tails from the sediment toward the oxygenated seawater and complete submersion in the sediment. Upon addition of *T.* cf. *briani* to the sediment, the redox potential increased from 0 V to approximately 500 mV, and this high potential value was maintained for 8 days (Figure 3B). The potential then rapidly dropped to −100 V following the addition of 2 mg fish diet, but again increased and had exceeded 400 mV within 24 h. Notably, the change in redox potential was highly synchronized with the macroscopic movement of *T.* cf. *briani*. Specifically, when the potential reached approximately 500 mV, nearly half of the oligochaetes had their tails projecting toward the seawater. Upon feeding, however, the oligochaetes began digging into the sediment until their bodies were completely buried. When the sediment potential recovered to the original state, the oligochaetes again began to stick their tails out into the seawater, demonstrating that the macroscopic movement of this benthos is highly correlated with the homeostatic changes in the redox potential. After prolonged incubation without feeding, the number of oligochaetes with protruding tails gradually decreased from 8 to 2 (Figure 3C), indicating that the “tail upwards” movement is correlated to energy metabolism. This speculation was examined below by the NMR analysis of metabolites.

The bioturbation and burrowing of aquatic oligochaetes is known to alter seawater and sediment fluxes, which could help create an oxidative environment by promoting the influx of oxygen into the sediment (Mermillod-Blondin and Rosenberg, 2006). To estimate the aeration effect caused by the macroscopic movement of *T.* cf. *briani*, the seawater-sediment interface in the EC reactor was mechanically agitated using a microsyringe at an injection rate of 0.2 ml/s, which is much more vigorous than that caused by the movement of *T.* cf. *briani*. A video showing *T.* cf. *briani* digging into the sediment is available in Supplementary Video 1. During the agitation resulting from the pipetting, a significant amount of sediment was displaced into the seawater; however, the potential only increased by approximately 70 mV, and quickly returned to its original level of approximately −20 mV within 3 min (Supplementary Figure 4). Even after

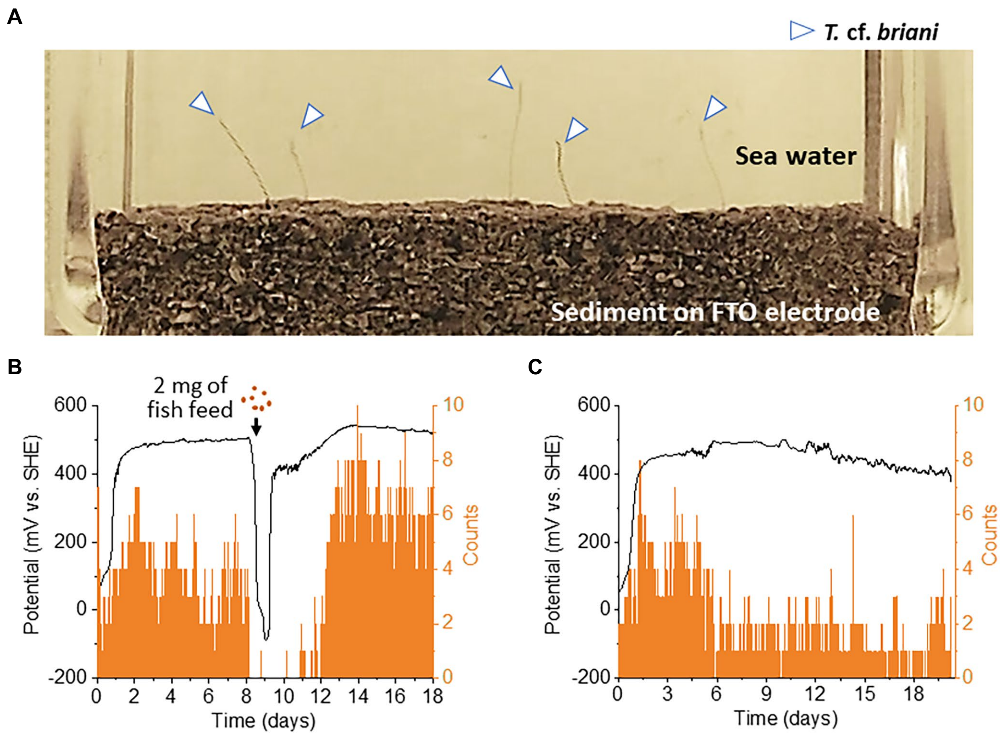

FIGURE 3
(A) Photograph of the seawater-sediment interface taken during open-circuit potential measurements. The arrows show the tail of an oligochaete protruding from the sediment layered on an fluorine-doped tin oxide (FTO)-coated glass electrode. **(B,C)** Correlation between redox potential and the number of tails protruding from the sediment into sea water. On day 8 of the experiment, 2 or 0mg of fish feed (**B,C**, respectively) was added to the reactor.

multiple agitation cycles, we were unable to reproduce the sustained increase in the sediment potential above 400 mV that was observed in the reactor containing both *T.* cf. *briani* and microorganisms. Therefore, the decomposition of organic matter by digestive activity, rather than mechanical aeration effects by the movement of benthos, is the primary reason for the generation of the oxidative environment in our model benthic ecosystem.

Redox-dependent energy metabolism

To investigate the role of the digestive activity of oligochaetes in the observed homeostatic changes in sediment redox potential, we analyzed the metabolites of *T.* cf. *briani* using NMR developed for the analysis of complex environmental samples (Simpson et al., 2011; Komatsu et al., 2015; Kikuchi and Yamada, 2017). Forty *T.* cf. *briani* specimens were collected from EC reactors at four different potential regions: high potential before feeding (region I), low potential after 10-mg feeding (region II), mid-potential during recovery (region III), and high potential after recovery (region IV; Figure 4A). The collected specimens were gently washed with artificial seawater to remove excess material and transferred to 2-ml safe lock tubes for NMR analysis. Twenty metabolites were identified by ^{1}H-^{13}C-Heteronuclear Single Quantum Coherece (HSQC) and ^{1}H-^{13}C-HSQC-Total Correlation Spectroscopy (TOCSY) NMR (Chikayama et al., 2010; Kikuchi et al., 2016; Supplementary Figure 5). In the 2D-*J*res spectra, succinate and fumarate, which are metabolites of tricarboxylic acid cycle (TCA) cycle, showed clear potential-dependent accumulation (Figure 4B). Namely, the amount of succinate increased with decreasing potential in regions I to II; however, the levels returned to the original one as the potential increased in regions III and IV. A positive correlation between fumarate levels and sediment potential was observed. Namely, the amount of fumarate decreased with decreasing potential, but subsequently increased with an increase in the sediment potential.

Fumarate respiration has been found in several benthic organisms, such as mussels, and is thought to sustain cellular functions under hypoxic conditions (Holwerda and De Zwaan, 1980; Van Hellemond and Tielens, 1994). In this mechanism, fumarate serves as an electron acceptor to form succinate, generating a proton motive force for adenosine triphosphate (ATP) synthesis. In the sediment of our model benthic ecosystem, the accumulation of succinate was coupled with a decrease in fumarate under low potential conditions, suggesting that *T.* cf. *briani* gains energy by digesting organic matter *via* fumarate respiration under hypoxic conditions. However, when low-potential conditions last for 15 days or more, most of the *T.* cf. *briani* were found to die.

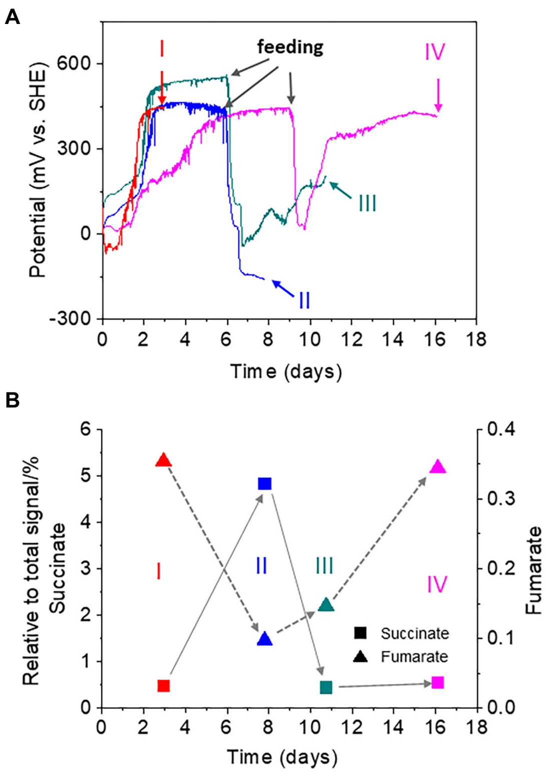

FIGURE 4
(A) Time courses of open circuit potential measurements for the sediment containing oligochaetes and sediment microorganisms. Forty oligochaetes specimens were collected at 4, 8, 11, and 16 h for nuclear magnetic resonance (NMR) analysis. Red line: sample I at a high redox potential before feeding; light blue line: sample II at a low redox potential after feeding; green line: sample III at the mid-redox potential during recovering; and magenta line: sample IV at a high redox potential after recovery. **(B)** Changes in the relative intensity of the NMR signals for succinate (squares) and fumarate (triangles).

Electrochemical regulation of metabolism and movement

The results presented above have demonstrated the effectiveness of real-time potential monitoring to assess the homeostatic function of benthic ecosystems. As a final experiment, the benthic ecosystem containing *T.* cf. *briani* and sediment microorganisms was maintained at electrochemical potentials of 0 or 400 mV to examine if the movement and metabolism of *T.* cf. *briani* could be artificially regulated. Upon applying the potential to the sediment-electrode system, a cathodic current of approximately −3.8 and − 0.5 μA was generated at 0 and 400 mV, respectively (Figure 5A). In addition, the movement of *T.* cf. *briani* clearly differed between 0 and 400 mV, with several oligochaetes extending their tails into the seawater at 400 mV (orange: six of 10 individuals), whereas their entire bodies were buried in the sediment at 0 mV. This potential-dependent regulation of movement is consistent with the change in movement that was observed upon feeding (Figure 3B). After 16 days of electrochemical incubation at 0 and 400 mV, 40 specimens of *T.* cf. *briani* were collected from the sediment and NMR analysis was conducted to examine changes in fumarate and succinate levels at the two sediment potentials. A higher amount of succinate was detected in *T.* cf. *briani* in the sediment with an applied potential of 0 mV relative to those organisms from sediment subjected to 400 mV, whereas fumarate showed the opposite trend (Figures 5B,C). This finding is consistent with the potential-dependent change in metabolite levels that was induced by feeding (Figure 4B), providing strong evidence that the redox homeostasis that observed upon introducing organic matter into the sediment originates from the redox-dependent activity of *T.* cf. *briani.*

Based on the real-time monitoring of redox potential changes upon nutrient addition and the observed electrochemical regulation of metabolism and movement of *T.* cf. *briani*, we propose the following mechanism of redox homeostasis in the model benthic ecosystem. The degradation of organic compounds by *T.* cf. *briani* results in reversible changes in metabolic states and body positions, together leading to changes in the sediment potential. Under high-potential conditions, *T.* cf. *briani* extend its tail into the oxygenated seawater and gains energy by digesting organic compounds *via* aerobic respiration. The introduction of organic compounds into the ecosystem leads to a large drop in the redox potential of the sediment, likely due to the enrichment of anaerobic microorganisms, such as sulfate-reducing bacteria, as inferred from the observed formation of sulfide ions and FeS. In contrast, low-potential conditions were associated with *T.* cf. *briani* embedded in the sediment, a switch from aerobic respiration to the use of fumarate as an electron acceptor. The digestion of organic compounds *via* fumarate respiration leads to an increase in the sediment potential, and the extension of its tail into the seawater-sediment interface facilitates aerobic respiration by *T.* cf. *briani*. This redox-dependent reversible switching in metabolism and movement showcases the high versatility of oligochaetes to adapt to the benthic environment, which can experience dynamic changes in the redox potential between −300 and 500 mV, and is likely a significant factor for maintaining ecosystem-level homeostasis in marine sediments.

Summary

In the present study, we demonstrated that the real-time monitoring of redox homeostasis is a viable method for assessing the resilience of benthic ecosystems, which was reinforced by the cooperative relationships between oligochaetes and sediment microorganisms. In particular, the redox-dependent reversible changes in metabolism and movement of oligochaetes was found to play a crucial role in the homeostatic response of the system to nutrient influx. We also demonstrated that it may be possible to artificially manipulate the metabolism and movement of benthic animals through electrochemical control of sediment potential. Recent advances in electromicrobiology have

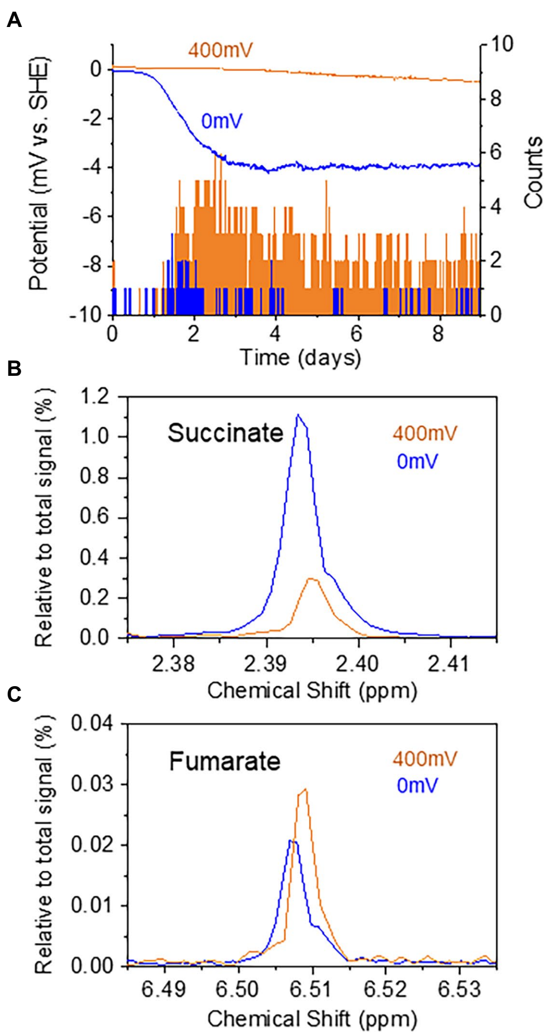

FIGURE 5
(A) Time courses of current generation from the sediment containing oligochaetes and sediment microorganisms at 0 and 400 mV. The number of oligochaetes with tails protruding from the sediment into the sea water at 0 and 400 mV is indicated by orange and blue bars, respectively. **(B,C)** Potential-dependent changes in the relative intensity of the NMR signals for succinate **(B)** and fumarate **(C)**.

demonstrated the application of electrochemical techniques to the monitoring and regulation of bacterial activity, particularly for metal reducing bacteria with the ability of extracellular electron transfer, such as members of the genus *Shewanella* and *Geobacter* (Nealson and Saffarini, 1994; Bond and Lovley, 2003). The electrochemical control of microbial flora has also been reported in mixed-culture systems, in which specific microbial species were enriched by regulating the electrode potential (Torres et al., 2009). To our knowledge, the present study is the first to demonstrate the electrochemical monitoring and physiologic regulation of benthic animals. Future research on the redox-dependent activity of benthic animals, including polychaetes and amphipods, will allow electromicrobiological techniques to be applied to benthic ecosystems and may lead to the development of novel technologies and sustainable aquaculture practices.

Data availability statement

The raw data supporting the conclusions of this article will be made available by the authors, without undue reservation.

Author contributions

NS, KI, and RN conceived and designed the experiments. NS, MI, AU, and KS performed the experiments. NS, MI, KS, AL, JK, KI, and RN analyzed the data. NS and RN wrote the manuscript. All authors contributed to the article and approved the submitted version.

Funding

This work was supported by a grant from commissioned project study on “Technological developments for characterization of harmful plankton in the seawater (Grant Number JP005317),” Ministry of Agriculture, Forestry and Fisheries, Japan.

Acknowledgments

The authors thank Y. Chiba of RIKEN for discussions concerning the metabolism of marine benthos.

Conflict of interest

The authors declare that the research was conducted in the absence of any commercial or financial relationships that could be construed as a potential conflict of interest.

Publisher's note

Supplementary material

The Supplementary Material for this article can be found online at: https://www.frontiersin.org/articles/10.3389/fmicb.2022.907703/full#supplementary-material

References

Andersen, F. O., and Kristensen, E. (1992). The importance of benthic macrofauna in decomposition of microalgae in a coastal marine sediment. *Limnol. Oceanogr.* 37, 1392–1403. doi: 10.4319/lo.1992.37.7.1392

Bond, D. R., and Lovley, D. R. (2003). Electricity production by *Geobacter sulfurreducens* attached to electrodes. *Appl. Environ. Microbiol.* 69, 1548–1555. doi: 10.1128/AEM.69.3.1548-1555.2003

Chikayama, E., Sekiyama, Y., Okamoto, M., Nakanishi, Y., Tsuboi, Y., Akiyama, K., et al. (2010). Statistical indices for simultaneous large-scale metabolite detections for a single NMR spectrum. *Anal. Chem.* 82, 1653–1658. doi: 10.1021/ac9022023

Costello, C., Cao, L., Gelcich, S., Cisneros-Mata, M. A., Free, C. M., Froehlich, H. E., et al. (2020). The future of food from the sea. *Nature* 588, 95–100. doi: 10.1038/s41586-020-2616-y

FAO (2014). The State of World Fisheries and Aquaculture 2014. Rome. 223 pp.

Gentry, R. R., Froehlich, H. E., Grimm, D., Kareiva, P., Parke, M., Rust, M., et al. (2017). Mapping the global potential for marine aquaculture. *Nat. Ecol. Evol.* 1, 1317–1324. doi: 10.1038/s41559-017-0257-9

Holmer, M., Argyrou, M., Dalsgaard, T., Danovaro, R., Diaz-Almela, E., Duarte, C. M., et al. (2008a). Effects of fish farm waste on *Posidonia oceanica* meadows: synthesis and provision of monitoring and management tools. *Mar. Pollut. Bull.* 56, 1618–1629. doi: 10.1016/j.marpolbul.2008.05.020

Holmer, M., Hansen, P. K., Karakassis, I., Borg, J. A., and Schembri, P. J. (2008b). "Monitoring of environmental impacts of marine aquaculture," in *Aquaculture in the Ecosystem*. eds. M. Holmer, K. Black, C. M. Duarte, N. Marbà and I. Karakassis, 47–85.

Holwerda, D. A., and De Zwaan, A. (1980). On the role of fumarate reductase in anaerobic carbohydrate catabolism of *Mytilus edulis* L. *Comp. Biochem. Physiol. B. Biochem.* 67, 447–453. doi: 10.1016/0305-0491(80)90332-6

Ishii, T., Kawaichi, S., Nakagawa, H., Hashimoto, K., and Nakamura, R. (2015). From chemolithoautotrophs to electrolithoautotrophs: CO2 fixation by Fe(II)-oxidizing bacteria coupled with direct uptake of electrons from solid electron sources. *Front. Microbiol.* 6, 994. doi: 10.3389/fmicb.2015.00994

Ito, K., Ito, M., Hano, T., Onduka, T., Mochida, K., Shono, N., et al. (2019). Marine sediment conservation using benthic organisms. *Bull. Jap. Fish. Res. Edu. Agen.* 49, 45–51.

Ito, K., Ito, M., Ohta, K., Hano, T., Ohkubo, N., and Mochida, K. (2018). Seasonal variation of the biomass of the marine oligochaete *Thalassodrilides* cf. *briani* in Fukuura Bay, Japan and its optimal culture conditions. *Jap. J. Benthol.* 73, 57–63. doi: 10.5179/benthos.73.57

Ito, M., Ito, K., Ohta, K., Hano, T., Onduka, T., Mochida, K., et al. (2016). Evaluation of bioremediation potential of three benthic annelids in organically polluted marine sediment. *Chemosphere* 163, 392–399. doi: 10.1016/j.chemosphere.2016.08.046

Jiang, Q., Bhattarai, N., Pahlow, M., and Xu, Z. (2022). Environmental sustainability and footprints of global aquaculture. *Resour. Conserv. Recycl.* 180, 106183. doi: 10.1016/j.resconrec.2022.106183

Jones, C. G., Lawton, J. H., and Shachak, M. (1994). Organisms as ecosystem engineers. *Oikos* 69, 373–386.

Kikuchi, J., Tsuboi, Y., Komatsu, K., Gomi, M., Chikayama, E., and Date, Y. (2016). SpinCouple: development of a web tool for analyzing metabolite mixtures via two-dimensional J-resolved NMR database. *Anal. Chem.* 88, 659–665. doi: 10.1021/acs.analchem.5b02311

Kikuchi, J., and Yamada, S. (2017). NMR window of molecular complexity showing homeostasis in superorganisms. *Analyst* 142, 4161–4172. doi: 10.1039/c7an01019b

Komatsu, T., Kobayashi, T., Hatanaka, M., and Kikuchi, J. (2015). Profiling planktonic biomass using element-specific, multicomponent nuclear magnetic resonance spectroscopy. *Environ. Sci. Technol.* 49, 7056–7062. doi: 10.1021/acs.est.5b00837

Levin, L. A., Boesch, D. F., Covich, A., Dahm, C., Erséus, C., Ewel, K. C., et al. (2001). The function of marine critical transition zones and the importance of sediment biodiversity. *Ecosystems* 4, 430–451. doi: 10.1007/s10021-001-0021-4

Marinelli, R., and Waldbusser, G. (2005). Plant-animal-microbe interactions in coastal sediments: closing the ecological loop. *Coast. Estuar. Stud.* 60, 233–249. doi: 10.1029/CE060p0233

Martinez-Crego, B., Alcoverro, T., and Romero, J. (2010). Biotic indices for assessing the status of coastal waters: a review of strengths and weaknesses. *J. Environ. Monit.* 12, 1013–1028. doi: 10.1039/b920937a

Mermillod-Blondin, F., and Rosenberg, R. (2006). Ecosystem engineering: the impact of bioturbation on biogeochemical processes in marine and freshwater benthic habitats. *Aquat. Sci.* 68, 434–442. doi: 10.1007/s00027-006-0858-x

Nascimento, F. J. A., Naslund, J., and Elmgren, R. (2012). Meiofauna enhances organic matter mineralization in soft sediment ecosystems. *Limnol. Oceanogr.* 57, 338–346. doi: 10.4319/lo.2012.57.1.0338

Nealson, K. H., and Saffarini, D. (1994). Iron and manganese in anaerobic respiration: environmental significance, physiology, and regulation. *Annu. Rev. Microbiol.* 48, 311–343. doi: 10.1146/annurev.mi.48.100194.001523

Rodriguez, P., and Reynoldson, T. B. (2011). *The Pollution Biology of Aquatic Oligochaetes*. Dordrecht: Springer.

Sarà, G. (2007). Ecological effects of aquaculture on living and non-living suspended fractions of the water column: a meta-analysis. *Water Res.* 41, 3187–3200. doi: 10.1016/j.watres.2007.05.013

Simpson, A. J., McNally, D. J., and Simpson, M. J. (2011). NMR spectroscopy in environmental research: from molecular interactions to global processes. *Prog. Nucl. Magn. Reson. Spectrosc.* 58, 97–175. doi: 10.1016/j.pnmrs.2010.09.001

Timm, T. (1980). "Distribution of aquatic oligochaetes," in *Aquatic Oligochaete Biology*. eds. R. O. Brinkhurst and D. G. Cook (Boston, MA: Springer), 55–77.

Torii, T., Erséus, C., Martinsson, S., and Ito, M. (2016). Morphological and genetic characterization of the first species of *Thalassodrilides* (Annelida: Clitellata: Naididae: Limnodriloidinae) from Japan. *Spec. Diver.* 21, 117–125. doi: 10.12782/sd.21.2.117

Torres, C. I., Krajmalnik-Brown, R., Parameswaran, P., Marcus, A. K., Wanger, G., Gorby, Y. A., et al. (2009). Selecting anode-respiring bacteria based on anode potential: phylogenetic, electrochemical, and microscopic characterization. *Environ. Sci. Technol.* 43, 9519–9524. doi: 10.1021/es902165y

United Nations, Department of Economic and Social Affairs, Population Division (2015). World Population Prospects: The 2015 Revision, Key Findings and Advance Tables. Working Paper No. ESA/P/WP.241.

Van Hellemond, J. J., and Tielens, A. G. (1994). Expression and functional properties of fumarate reductase. *Biochem. J.* 304, 321–331. doi: 10.1042/bj3040321

Yokoyama, H., Abo, K., and Ishihi, Y. (2006). Quantifying aquaculture-derived organic matter in the sediment in and around a coastal fish farm using stable carbon and nitrogen isotope ratios. *Aquaculture* 254, 411–425. doi: 10.1016/j.aquaculture.2005.10.024

Yoshida, S., Date, Y., Akama, M., and Kikuchi, J. (2014). Comparative metabolomic and ionomic approach for abundant fishes in estuarine environments of Japan. *Sci. Rep.* 4, 7005. doi: 10.1038/srep07005

frontiers | Frontiers in Microbiology

TYPE Original Research
PUBLISHED 22 December 2022
DOI 10.3389/fmicb.2022.1034401

Biogeochemical impacts of fish farming on coastal sediments: Insights into the functional role of cable bacteria

Diana Vasquez-Cardenas[1,2]*, Silvia Hidalgo-Martinez[2], Lucas Hulst[1], Thorgerdur Thorleifsdottir[3], Gudmundur Vidir Helgason[3], Thorleifur Eiriksson[3], Jeanine S. Geelhoed[2], Thorleifur Agustsson[4], Leon Moodley[4] and Filip J. R. Meysman[1,2]

[1]Department of Biotechnology, Delft University of Technology, Delft, Netherlands, [2]Geobiology, Department of Biology, University of Antwerp, Antwerp, Belgium, [3]RORUM ehf, Reykjavík, Iceland, [4]NORCE Norwegian Research Centre, Randaberg, Norway

EDITED BY
Amelia-Elena Rotaru,
University of Southern Denmark,
Denmark

REVIEWED BY
Chris Weisener,
University of Windsor, Canada
Erin Field,
East Carolina University, United States

*CORRESPONDENCE
Diana Vasquez-Cardenas
✉ diana.vasquezcardenas@uantwerpen.be

SPECIALTY SECTION
This article was submitted to Microbiological Chemistry and Geomicrobiology, a section of the journal Frontiers in Microbiology

RECEIVED 01 September 2022
ACCEPTED 05 December 2022
PUBLISHED 22 December 2022

CITATION
Vasquez-Cardenas D, Hidalgo-Martinez S, Hulst L, Thorleifsdottir T, Helgason GV, Eiriksson T, Geelhoed JS, Agustsson T, Moodley L and Meysman FJR (2022) Biogeochemical impacts of fish farming on coastal sediments: Insights into the functional role of cable bacteria. *Front. Microbiol.* 13:1034401. doi: 10.3389/fmicb.2022.1034401

Fish farming in sea cages is a growing component of the global food industry. A prominent ecosystem impact of this industry is the increase in the downward flux of organic matter, which stimulates anaerobic mineralization and sulfide production in underlying sediments. When free sulfide is released to the overlying water, this can have a toxic effect on local marine ecosystems. The microbially-mediated process of sulfide oxidation has the potential to be an important natural mitigation and prevention strategy that has not been studied in fish farm sediments. We examined the microbial community composition (DNA-based 16S rRNA gene) underneath two active fish farms on the Southwestern coast of Iceland and performed laboratory incubations of resident sediment. Field observations confirmed the strong geochemical impact of fish farming on the sediment (up to 150 m away from cages). Sulfide accumulation was evidenced under the cages congruent with a higher supply of degradable organic matter from the cages. Phylogenetically diverse microbes capable of sulfide detoxification were present in the field sediment as well as in lab incubations, including cable bacteria (*Candidatus* Electrothrix), which display a unique metabolism based on long-distance electron transport. Microsensor profiling revealed that the activity of cable bacteria did not exert a dominant impact on the geochemistry of fish farm sediment at the time of sampling. However, laboratory incubations that mimic the recovery process during fallowing, revealed successful enrichment of cable bacteria within weeks, with concomitant high sulfur-oxidizing activity. Overall our results give insight into the role of microbially-mediated sulfide detoxification in aquaculture impacted sediments.

KEYWORDS

electrogenic sulfide oxidation (e-SOx), long-distance electron transport (LDET), aquaculture, sulfur cycling, cable bacteria

1 Introduction

Fish comprises an important source of animal protein to the human population, with the global fish production estimated at 177.8 million tons in 2020 (FAO, 2022). To meet this demand, fish farming has significantly expanded over the past decades, accounting for nearly half of the global production (87.5 million tons). A sizeable fraction of this fish farming (33.1 million tons) occurs in marine waters (FAO, 2022). This intensive aquaculture practice generates large quantities of organic waste that predominantly sinks to the seafloor, which includes both waste products (feces) and undigested fish food (Quiñones et al., 2019; Miranda et al., 2020). The enrichment of organic matter in sediments underneath fish cages promotes anaerobic mineralization, and particularly stimulates sulfate reduction, which generates high concentrations of sulfide in sediments (Holmer and Kristensen, 1996). Free sulfide may diffuse out of the sediment into the overlying water and upon oxidation, it can contribute to the depletion of oxygen in bottom waters (la Rosa et al., 2001; Bissett et al., 2006; Choi et al., 2018). When this situation persists, oxygen becomes fully depleted, and free sulfide accumulates in the water column, in a process called euxinia. Due to the intrinsic toxicity of free sulfide to eukaryotes, euxinia events may induce mass-mortality in both benthic and pelagic fauna (Pearson and Rosenberg, 1978; Holmer et al., 2007). Sedimentation of fecal pellets further serve as a dispersion mechanism for pathogens and fish gut-microbes such as *Pseudomonas*, *Vibrio*, and *Clostridia* both in the water column and sediment near the cages (Kolda et al., 2020; Quero et al., 2020).

The increased sedimentation of organic-rich particles near the fish cages, but also to some extent further away due to transport by currents, has a lasting impact on the local sediment geochemistry, microbiology, and faunal communities (Carroll et al., 2003; Holmer et al., 2007; Ballester-Moltó et al., 2017). To safeguard the environmental quality of local marine coastal areas, environmental standards are enforced upon fish farming activities. One widely enforced remediation measure is fallowing, where farming areas must remain inactive for at least 3 months after each production cycle. This process enables the seabed to partially return to its state prior to the on-set of farming (McGhie et al., 2000; Carroll et al., 2003). However, the complete restoration of fish farm impacted sediments can require multiple years, with only an initial recovery observed in the first and second year. This restoration trajectory depends not only on the fish farming practices but also on the prevalent environmental conditions (Pereira et al., 2004; Keeley et al., 2017; Verhoeven et al., 2018). Other, but less-used remediation techniques include: sediment removal, harrowing, re-suspension, addition of detritivores or polychaetes, and sediment irrigation with oxygenated surface water (Kunihiro et al., 2011; Keeley et al., 2017; Ape et al., 2019). The best course of action to constrain the environmental effects of fish farming remains a subject of debate.

In natural environments with highly organic-enriched sediments, sulfur-oxidizing microbes can act as "ecosystem engineers" that counteract euxinic conditions through highly efficient sulfide oxidation. Off the coast of Namibia, pelagic *Gammaproteobacteria* and *Campylobacterota* (formerly known as *Epsilonproteobacteria*) can fully oxidize sulfide in euxinic bottom waters with nitrate, thus potentially preventing or reducing mass mortality events of the fish community (Lavik et al., 2009). Similarly, high abundances of sulfur-oxidizing microbes from the *Campylobacterota* (*Sulfurimonas* and *Sulfurovum*) and mat-forming *Gammaproteobacteria* are typically observed in fish farm impacted sediments (Kawahara et al., 2009; Verhoeven et al., 2018; Kolda et al., 2020; Quero et al., 2020). However, it is presently unclear to what extent these natural microbial communities can help mitigate the impact of fish farming on the seabed, and accelerate the recovery of ecosystem functions in the seabed. The microbially-mediated process of sulfide oxidation is of critical importance in this matter. Sustainable management of fish farming activities hence calls for a better understanding of microbial sulfide oxidation in the seabed.

A highly efficient form of sulfide detoxification was recently discovered in coastal sediments worldwide, which is conducted by cable bacteria performing electrogenic sulfide oxidation (e-SOx; Pfeffer et al., 2012; Malkin et al., 2014; Burdorf et al., 2017). In this unique bacterial metabolism, sulfide oxidation is supported by long-distance electron transport over centimeters (Nielsen and Risgaard-Petersen, 2015; Meysman, 2018). Cable bacteria activity stimulates various other microbial processes, such as sulfate reduction, denitrification, and chemoautotrophy (Vasquez-Cardenas et al., 2015; Kessler et al., 2019; Sandfeld et al., 2020; Liau et al., 2022) promotes cryptic sulfur cycling, and alters the cycling of phosphorous, manganese and heavy metals in sediment (Rao et al., 2014; van de Velde et al., 2016). e-SOx can also play a crucial role in the prevention of euxinic bottom waters. This process was first demonstrated in the organic-rich sediments of a seasonally hypoxic basin and occurs through a sequence of biogeochemical steps (Seitaj et al., 2015). Firstly, the development of e-SOx strongly decreases the pH in anoxic sediments, which dissolves the ambient pool of iron sulfides. The ferrous iron that is liberated diffuses upward and generates a buffering layer of sedimentary iron oxides just below the oxic surface, which is referred to as an iron firewall (Seitaj et al., 2015). When the bottom water turns anoxic, this iron firewall captures the sulfide diffusing upward and this can prevent/delay the escape of sulfide from the sediment over a period of weeks (Seitaj et al., 2015). In doing so, the detrimental effects of hypoxia and euxinia, both in the benthic and pelagic environments, are alleviated naturally (Marzocchi et al., 2018; Hermans et al., 2020). The reduction of sulfide levels in sediments by e-SOx likely favors the growth of seagrass and mussel beds, and the re-colonization of benthic macro- and meiofauna (Seitaj et al., 2015; Malkin et al., 2017; Martin et al., 2018; Bonaglia et al., 2020).

Here, we hypothesize that a diverse microbial community of sulfur-oxidizers, including cable bacteria, could potentially contribute to sulfide detoxification in fish farm sediments during fallowing, thus enhancing the overall recovery process. To investigate this hypothesis, we studied the *in situ* geochemistry and microbial communities in sediments near fish cages on the East coast of Iceland with different production regimes (short versus long production periods). Accompanying laboratory incubations gave additional insight into the recovery process of fish farm sediments and the potential role of cable bacteria.

2 Materials and methods

2.1 Study area and sample collection

In Iceland, Atlantic salmon (*Salmo salar*) is the most important farmed fish species, and the largest part of its production cycle occurs in sea cages. Our study area was located at two farming sites, Glímeyri and Svarthamarsvik, in Berufjörður, which is a 20 km long and 3–5 km wide fjord on the east coast of Iceland (**Supplementary Figure 1**). Cages have a 160 m circumference, a depth of 32 m and a resulting volume of 47,000 m^3, and are arranged in clusters (7 in Glímeyri and 6 in Svarthamarsvik). Each production cycle lasts up to 36 months, depending on temperature, growth rate, and the size of smolts (young salmon) initially stocked. Harvesting starts when maximum biomass is reached with an average fish weight close to 6 kg. Sampling was conducted on September 24th and 25th 2018 on both locations. The temperature of the bottom water was 4°C and salinity was 33. At the time of sampling, the Glímeyri cluster was early in its production cycle (22nd week), and as a result, it still contained a relatively low biomass (~540 tons divided over 7 cages). In contrast, the Svarthamarsvik cluster was much later in the production cycle (122 weeks) and had already reached the harvesting stage. Hence salmon biomass was much larger (~2,800 tons in 6 cages). The two sampling sites investigated therefore represent two scenarios, the Glímeyri site with low biomass and a short production period (SPP) and the Svarthamarsvik site with high biomass and a long production period (LPP).

In Berufjörður, the tidal current comes into the fjord from the north and exits to the south (**Supplementary Figure 1**). We established a transect in parallel to the tidal current from the south-eastern most cage within each of the two clusters. Three sampling sites were selected along each transect: next to the cage (0 m), 50 and 150 m away from the fish cage (**Supplementary Figure 1** and **Supplementary Table 1**). Intact sediment cores were retrieved with a single-core gravity corer (Uwitec) using polycarbonate core liners (60 mm inner diameter and 60 cm length). Four replicate cores were collected per site. All sediment cores were inspected upon retrieval, and only cores with a visually undisturbed sediment surface, and with overlying water (>5 cm) were retained. Cores were first kept in the shade onboard ship (air temperature 5°C), and within 5 h after collection, they were brought to a climate-controlled room at 0°C for further processing.

Overlying water in each core was aerated via an aquarium air pump and cores were kept at 0°C. Microsensor depth profiles were collected for all replicate cores within 24 h, and two cores per site were subsequently sectioned in six layers (slicing at 0.5, 1.0, 1.5, 2.0, 3.0, and 5.0 cm depth). Sediment slices were collected in petri dishes, homogenized, and immediately transferred to Eppendorf tubes which were either immediately frozen at −20°C for DNA analysis (1.5 ml) or fixed with ethanol 96% at a 1:1 ratio (1 ml) for Fluorescent *in situ* Hybridization (FISH).

2.2 Laboratory sediment incubations

Laboratory sediment incubations were additionally performed to mimic the recovery process of fish farm sediments during fallowing. To this end, the top flocculent layer and big shells were removed from the sediment cores retrieved from the cage site at both the SPP and LPP sites. This removal of organic-rich top sediment simulates a potential remediation technique considered by the fish farming industry, as well as natural dispersion by waves and currents. The subsequent sediment layer (~5 cm thickness) was collected in dark plastic jars (250 ml) and transported to the lab, where it was kept in the fridge (4°C) for up to 2 months. Sediments were sieved (350 μm), homogenized, and repacked into plastic core liners with a stopper at the bottom (diameter 2.5 cm; length 4 cm; 4 replicas per site). Cores were kept submerged in aerated artificial seawater (33 salinity, Instant Ocean Sea Salt), incubated at 18°C, and microsensor depth profiles were collected weekly. A few days after the initial appearance of the fingerprint of electrogenic sulfide oxidation (as confirmed by microsensor profiling), one core for each site was sliced in three layers: 0–0.5, 0.5–1.0, and 1.0–3.0 cm. This occurred on day 15 for SPP and on day 59 for LPP. Sediment was homogenized and subsampled as described above for molecular analysis of the microbial community.

2.3 Microsensor depth profiling

Geochemical characterization of sediments was done via microsensor profiling (O_2, H_2S, and pH) using commercial microelectrodes (Unisense, Denmark). *In situ* cores were measured within 24 h after sediment collection, while laboratory incubations were measured at several time points along the incubation period: 5, 8, 12, 15, 18, 22, 37, 54, and 59 days.

Oxygen depth profiles (tip size, 50 μm) were recorded at 50–100 μm resolution. Depth profiles for H_2S and pH (tip size, 50 and 200 μm, respectively) were recorded at 200 μm resolution in the oxic zone and at 500 μm depth resolution below. Calibration of O_2, pH, and H_2S electrodes was performed as previously described in Malkin et al. (2014). ΣH_2S was calculated from H_2S profiles based on pH measurements at the same depth using the R package AquaEnv (Hofmann et al., 2010). Diffusive oxygen uptake (DOU) was calculating using Fick's first law as follows

$$Ji = \frac{\varphi}{1 - 2ln\varphi} * Di\,(S, T) * \frac{\partial Ci}{\partial x}$$

where φ is the measured porosity (0.8), the term (1–2lnφ) accounts for the tortuosity of the sediment (Boudreau, 1996), D_i is the diffusion coefficient of oxygen at the measured temperature (T_{field} = 0°C, T_{lab} = 18°C) and salinity (S = 33 salinity) using the R package marelac (Soetaert et al., 2014). The maximum concentration gradient ($\frac{\partial Ci}{\partial x}$) was obtained as the linear slope of the concentration profile immediately below the sediment-water interface. Statistical difference between DOU from the different sites was evaluated with ANOVA considering factors such as length of the production period and distance from cage.

2.4 Organic matter

Three proxies were used to trace the impact of aquaculture on the organic matter cycling in the sediment at the field sites: (1) stable isotopic signatures of organic matter ($\delta^{13}C_{TOC}$), under the assumption that feeding pellets, and therefore aquaculture derived organic carbon, have a stable isotope signature distinct from autochthonous marine organic material (McGhie et al., 2000; Holmer et al., 2007); (2) Total organic carbon content (TOC) may be enhanced due to input from the cages depending on prevailing hydrography (Maldonado et al., 2005; Giles, 2008); (3) Biological oxygen demand (BOD) is enhanced by the input of bioavailable aquaculture derived organic matter (Pereira et al., 2004; Piedecausa et al., 2012). To study these three proxies, sediment cores were collected at the cage from each cage cluster, sliced onboard the ship in five distinct layers, and then transported in a cooling box (5°C) to the laboratory for further analysis. For the SPP cage, the surface layer (0–2 cm) and 4 subsurface centimeter-thick layers (5–6, 10–11, 15–16, and 20–21 cm deep) were collected. At the LPP site, the presence of shells only allowed for two-centimeter-thick layers (0–2, 4–6, 8–10, 14–16, and 18–20 cm deep). Measurements of TOC and $\delta^{13}C_{TOC}$ were done in triplicate for the top layer and once for the subsurface sediments. In the lab, sediment was lyophilized, and a subsample was acidified to determine TOC and $\delta^{13}C_{TOC}$ simultaneously on an Element Analyzer-Isotope Ratio Mass Spectrometer (EA-IRMS), as described in Kürten et al. (2013).

The BOD was measured in sediment-seawater slurry incubations in small bottle respirometers, i.e., a 100 ml glass bottle with an optic sensor patch glued on the inside of the bottle (Fibox 4 Oximeter, Presens, Germany). This allows for non-invasive measurement of oxygen concentration in the sediment-seawater slurry. Accurate volumes of sediment were sampled by filling a cut off syringe and transferring surface sediment (0–2 cm) to the BOD respirometer. The weight of the bottle before and after sediment addition was noted for accurate calculation of solid sediment volume and sediment water content. Subsequently, the bottle was half filled with filtered seawater (fjord water from NORCE mesocosm facilities) and aerated (using an aquarium air pump and long sterile needle) for 30 min. This was done to reduce potential artifacts of BOD, including oxidation of reduced compounds in the porewater. After air flushing, bottles were filled with filtered seawater to the brim using a plastic flotation disk to prevent loss of sediment and weighed again (to determine the added water volume). Bottles were then sealed with a cap fitted with a Viton septum (ensuring the absence of air bubbles), vigorously shaken and the time-zero (start) oxygen concentration was measured. Sediment slurries were mixed constantly on a rotator and oxygen concentrations were measured at regular intervals during the incubation period that ranged from 5 to 300 min to obtain a sufficient decrease in oxygen content. The oxygen consumption rate was determined through linear regression. BOD (expressed in μmol O_2 ml sediment^{-1} hr^{-1}) was calculated by multiplying the regression slope (μmol O_2 ml water^{-1} hr^{-1}) by the volume of water added (ml) and dividing by the volume of sediment (ml of sediment). All incubations were conducted at 5°C in the dark.

2.5 Sediment grain size and porosity

Sediment from each site was collected with a Van Veen grab, collected in buckets and transported to the lab. An aliquot of sediment (∼300 g) was submersed in water for a few hours and then sieved through seven different sieves from 4.0 to 0.063 mm, and run off was collected. All eight sediment fractions were then dried to constant weight at 50°C and grain size was determined as described in Folk and Ward (1957). From lab incubations, sediment was collected for porosity determination from water content and dry solid phase density measurements after sediment was dried to constant weight at 70°C.

2.6 DNA extraction and sequencing

Total genomic DNA extraction was performed following the protocol of Zhou et al. (1996) as amended and described in Geelhoed et al. (2020). For field sediments, three depths were selected for DNA extraction: 0–0.5 cm (layer 1), 0.5–1 cm (layer 2), and 3.0–5.0 cm (layer 6). These three layers encompass the organic-rich top layer (top 1 cm), and a deeper anoxic layer, with less organic matter acting as a reference. For the laboratory incubated sediments, only the upper two sediment layers were analyzed as they span the layer in which cable bacteria activity was evident (see below). DNA purity was evaluated via the adsorption ratios at 260/280 nm and 260/230 nm (Ultraspec 2100 spectrophotometer), DNA concentration was assessed with the Qiagen powersoil pro kit on a Qubit 4 fluorometer, and DNA quality was determined on an Implen NP80. DNA concentrations were at least 10 ng/μl. Samples were sent to Novogene Ltd. (Hong Kong, China) for amplicon sequencing of the V3–V4 region of the 16S rRNA gene (position 341–806 bp) using the Illumina paired-end platform with 250 base pair paired-end reads. Primer sequences used were 5′-CCTAYGGGRBGCASCAG-3′ and 5′-GGACTACNNGGGTATCTAAT-3′ (Takahashi et al., 2014).

Raw forward and reverse reads were analyzed using the dada2 R-package (version 1.17.0) that results in a list of Amplicon Sequence Variants (ASVs) with the corresponding counts and taxonomic classification (Callahan et al., 2016). The dada2 pipeline first evaluates the quality of the reads, then filters and trims the reads [trimming parameters: truncLen = (226,223), maxN = 0, truncQ = 2 maxEE = (2,2)]. Forward and reverse reads are merged and chimeras removed using the consensus method. Taxonomy was assigned to ASVs up to genus-level according to the Silva small subunit rRNA reference database v1.38.1 (Quast et al., 2013). Final filtering of the ASV data matrix (dada2 output) was performed by removing singletons, doubletons, and short reads (<400 bp) prior to statistical analysis. Sequences for each sediment layer are available in the NCBI database under BioProject PRNJNA911159, accession numbers SAMN32163971 to SAMN32163991.

2.7 Statistical analysis of amplicon sequence variants

The filtered ASV data matrix was used to analyze the microbial community composition. ASV abundance was treated as compositional data and normalized with the variance stabilization transformation (vst) as part of the DESeq2 R-package (version 1.28.1, Anders and Huber, 2010). To assess the overall effect of the fish farms on the *in situ* microbial community a Principal Coordinate Analysis (PCoA) was performed, followed by an Analysis of Similarities (ANOSIM) of the identified sample clusters with a Bray–Curtis similarity matrix and 999 permutations (vegan R-package version 2.5.7; Clarke, 1993). Quantitative analysis of differential expression (DESeq) of ASVs abundances was then used to identify significantly distinct microbes for the sample clusters obtained in the PCoA (Anders and Huber, 2010). DESeq uses a two-way comparison assuming a negative binomial distribution model that returns the log-fold change (LFC), i.e., (logarithmic) difference in the abundance of each ASV between two factors (Love et al., 2014). ASVs were considered differentially abundant when the LFC was $\geq|4|$ and $p < 0.01$. In addition, a non-parametric Spearman correlation analysis was implemented to compare the microbial communities between *in situ* cage and laboratory sediment (microbiomeSeq R package). Only ASVs that were present in at least 30% of the samples were used for the correlation analysis. Correlation index was calculated at the ASV level and reported as significant for $p < 0.001$.

2.8 Cable bacteria identification and diversity

The presence of cable bacteria in the fish farm sediments was examined via three approaches. First, scanning electron microscopy (SEM) was used to visualize the unique external morphology of cable bacteria (parallel ridges that run continuously along the filament; Pfeffer et al., 2012). To this end, microscopic sediment chambers were prepared as described in Bjerg et al. (2018). After 2 days, long filaments were observed extending from the sediment toward the edge of the microscopic chamber. Filaments were carefully hand-picked from the chambers with glass hooks, rinsed in miliQ to remove salts, transferred onto polycarbonate filters, air-dried and then sputter-coated with gold. SEM images of the filaments were made with a JEOL 5600 Scanning Electron Microscope (SEM) under low vacuum. Average cell length and width were determined with the Fiji-ImageJ software. This technique was applied to the SPP incubation sediment from day 8.

Secondly, the identity of the filamentous bacteria was investigated with Fluorescence *in situ* Hybridization (FISH). The FISH probe DSB706 was used as it targets most members of the *Desulfobulbaceae* family, including the cable bacteria (Lücker et al., 2007). This probe has previously been used to verify the presence of cable bacteria in a diverse range of sediments (Malkin et al., 2014; Schauer et al., 2014; Burdorf et al., 2017). This FISH method was applied to both field and incubated sediments.

Thirdly, the 16S rRNA gene diversity of cable bacteria sequences was assessed in both field and lab samples. All ASVs assigned to either cable bacteria genera (*Candidatus* Electrothrix or *Candidatus* Electronema*;* Trojan et al., 2016) were pre-filtered by removing ASVs that were not present in at least five samples (>20% of samples) with ≥10 total read counts. Remaining ASV sequences were compiled in MEGA-X (Molecular Evolutionary Genetics Analysis software, version 10.2.2) and the sequence similarity to known cable bacteria 16S rRNA gene sequences was confirmed by querying the GenBank repository via BLASTn. Only ASVs sequences with a nucleotide identity ≥94.5% with either cable bacteria genera were retained. To construct a phylogenetic tree for cable bacteria, 16S rRNA gene sequences (>1,000 bp) were retrieved from GenBank including one sequence for each of the 7 known cable bacteria species and 5 *Desulfobulbus* species as reference sequences (**Supplementary Table 2**). Additionally, 2 sequences from a potentially new cable bacteria genera [AR-3 and AR-4 (Dam et al., 2021)] and 2 sequences from uncultured bacterium from coastal sediments, that were closely-related to this potential third cable bacteria genus, were also included. In total 36 sequences were aligned with the Muscle software in MEGA-X (Edgar, 2004) and the alignment was manually inspected. The best-fit phylogenetic tree was estimated by IQ-TREE 2 software using maximum likelihood with 1,000 bootstraps via the ultrafast bootstrap approach (Minh et al., 2020). IQ-Tree output resulted in a General time reversible model (GTR) for base substitution rates, with four Gamma rate categories. The consensus tree was visualized with the FigTree (version 1.4.4) and *Escherichia coli* strain U 5/41 16S rRNA gene was used to root the tree.

3 Results

3.1 Geochemical characterization of fish farm sediments

Two salmon farming sites were investigated: Glímeyri had been in operation for 22 weeks (short production period – SPP), while Svarthamarsvik was already 121 weeks in operation (long production period – LPP). Sediments at all sites were classified as very fine-grain sand and silt (with a median grain diameter <63 μm, **Supplementary Table 3**). Larger particles (>1 cm grain diameter) consisted mainly of shell fragments, and were present at the LPP sites (1.9–6% total weight) and to a lesser degree in SPP sediments (0.3–1.8%). At the SPP sites, the sediment showed a smooth surface, without debris or shells, and active macrofauna was present and increased in number with increasing distance from the cage (**Figure 1**). In contrast, at the LPP sites, the sediment was black and displayed an uneven surface, with particles of waste feed and large shell debris, and no active macrofauna was apparent in the sediment (**Figure 1**). Surface TOC values were statistically different along the transect (ANOVA, $p = 0.004$), also when considering both the distance from the cage and the production period (ANOVA, $p = 0.02$). The surface sediment (0–2 cm) at the LPP cage site had the highest TOC (3.33 ± 0.15%) of all sediments, and this surface value was threefold higher than the subsurface TOC at all LPP stations (range: 0.6–1.0%, **Table 1** and **Supplementary Table 1**). At the SPP cage cluster, TOC values were more similar between sites and sediment depths, and subsurface sediments had a higher TOC than at LPP stations (range: 1.2–1.5%, **Supplementary Table 1**). Stable isotope signatures ($\delta^{13}C_{org}$) of surface sediment (0–2 cm) were generally more depleted below the cages (−23.4 ± 0.2‰ at SPP and −25.9 ± 0.6‰ at LPP), thus more closely resembling the signature of the fish feed (−25.5 ± 0.4‰, **Table 1**). Away from the cages, the $\delta^{13}C_{org}$ signature was closer to that of autochthonous marine organic matter (∼−22.5‰). Significant differences in $\delta^{13}C_{org}$ were found when considering the distance from cage (ANOVA, $p = 0.001$) and the combined effect of distance and production period (ANOVA, $p = 0.02$). Sediment BOD only significantly varied with distance from cage (ANOVA, $p = 0.0007$). Highest values were recorded for the cage sediments (16–18 μmol O_2 ml wet sed^{-1} hr^{-1}), which decreased by one order of magnitude at 50 m distance (1.0 μmol O_2 ml wet sed^{-1} hr^{-1}) and were lowest at 150 m distance (0.3 and 0.4 μmol O_2 ml wet sed^{-1} hr^{-1} for the SPP and LPP transects, respectively, **Table 1**).

Given the shell debris in the sediments at LPP, triplicate H_2S and pH profiling were not possible at 50 and 150 m without damaging the microsensors. The O_2, H_2S, and pH depth profiles showed substantial variability within a given site, likely due to the presence of particle waste, macrofauna, and shell fragments that alter the diffusion of solutes in the sediment. Nevertheless, clear differences in porewater chemistry were observed between the two farming sites and with increasing distance from the cages (**Figure 1**). Sulfide concentrations in sediments underneath the cage were one order of magnitude higher at LPP (5.5 mM) compared to SPP (0.3 mM), and free sulfide was present in the top centimeter of the sediment. However, free sulfide concentrations strongly decreased at 50 m distance for both sites and were below detection limit for the SPP site at 150 m distance. The elevated sulfide concentrations at the LPP cage site were accompanied by more acidic conditions (minimum pH of 6.6 at 3 cm depth). For all other sites pH values remained above 7.2 in the top 5 cm of sediment.

Average diffusive oxygen uptake (DOU) ranged from 10.5 to 44.2 mmol O_2 m^{-2} d^{-1} and mean oxygen penetration depth (OPD) varied from 0.74 to 2.7 mm across all sediments (**Table 1**). ANOVA indicated significant differences in DOU with distance from the cages ($p < 0.0001$) but not with the length of the production period ($p = 0.5$). Highest DOU rates were found next to the cages (21.7–91.0 mmol O_2 m^{-2} d^{-1}) and lowest rates at the 150 m sites (8.0–14.2 mmol O_2 m^{-2} d^{-1}). The OPD statistically differed with distance from the cages (ANOVA, $p < 0.0001$) and in combination with the production period (ANOVA, $p = 0.005$). The shallowest OPD was observed at the cage (0.45–1.20 mm) and deepest OPD was found 150 m away from the cage cluster (1.40–3.25 mm). Overall, the impact of the aquaculture activity resulting from enhanced input of degradable organic matter, was apparent in all geochemical variables, with high porewater H_2S, low subsurface pH, shallow OPD, and high DOU rates near the cages. Although suboxic zones were noted, a clear e-SOx fingerprint (see section

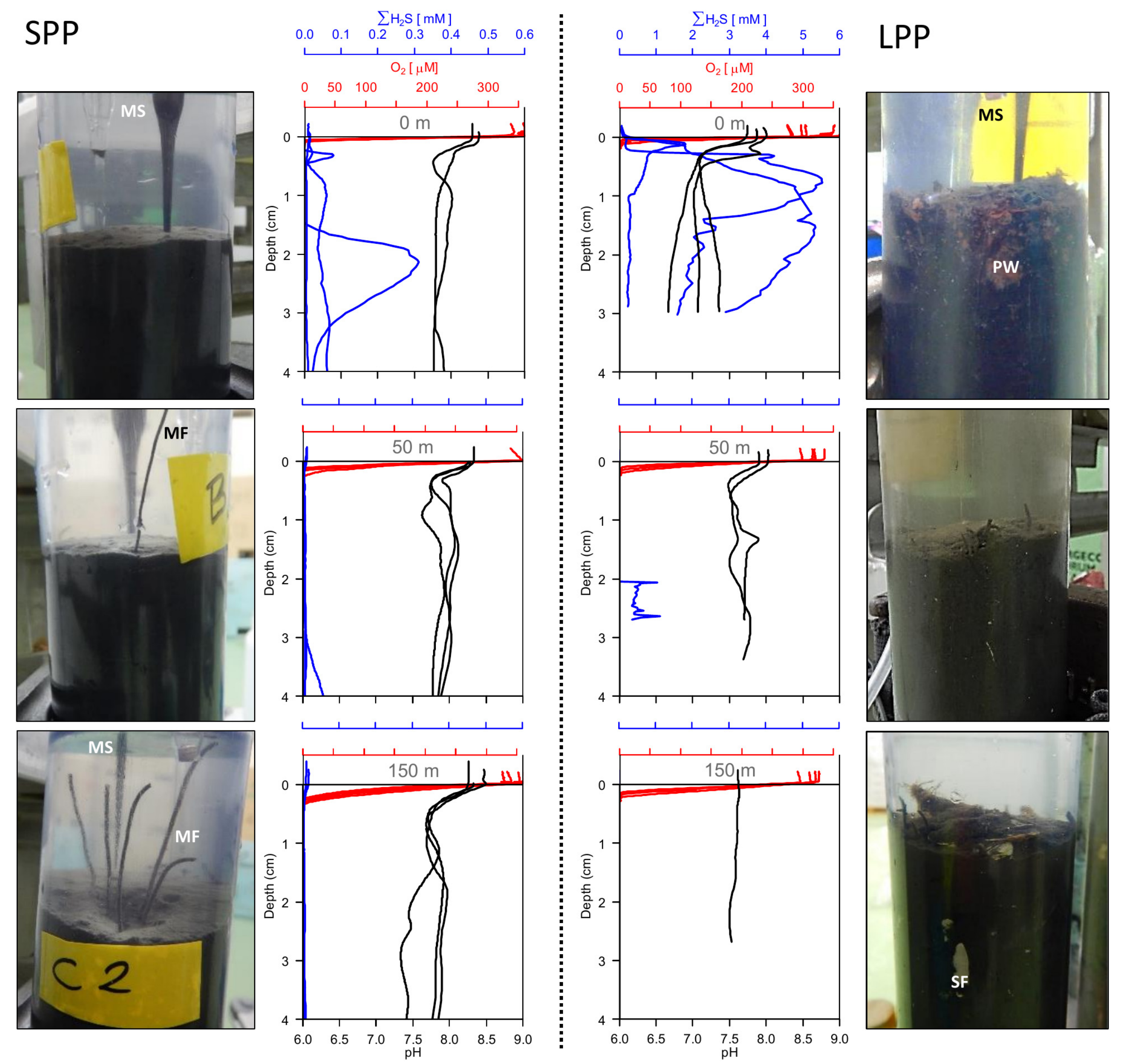

FIGURE 1
Sediment pictures and microsensor sediment profiles retrieved from two fish farming sites (short and long production period) at 0 m **(top row)**, 50 m **(middle row)**, and 150 m **(bottom row)** away from the cage along the transect. SPP, short production period (Left); LPP, long production period (Right). All replicate profiles are plotted for each station; red, oxygen; blue, total sulfide; black, pH. Photos of sediment cores (diameter: 6 cm) indicate microsensor entering the sediment (MS), particle waste (PW), macrofauna (MF), and shell fragments (SF).

"3.3 Geochemical characterization of lab incubations") was not discernible in any of the depth profiles recorded (n = 15; Figure 1).

3.2 Microbial community composition in fish farm sediments

In the 21 fish farm sediment samples analyzed (both field and lab incubations) the number of merged reads per sample (without chimeras, nor singletons) ranged from 92,724 to 115,286, which after filtering (removal of doubletons and minimum read length of 400 bp) ultimately resulted in 6,957–10,174 unique ASVs, and 91,542–1,14,619 total number of reads (Supplementary Table 4 and Supplementary Figure 2). Twenty-three phyla had a relative abundance >0.1% with an average of 90% of the total abundance per sample distributed in only six phyla: *Proteobacteria* (13–55%), *Campylobacterota* (8–43%), *Desulfobacterota* (6–23%), *Bacteroidota* (5–11%), *Actinobacteriota* (2–13%), and *Firmicutes* (1–17%). Within the *Proteobacteria* phylum the most prominent Class was *Gammaproteobacteria* (11–38%) followed by

TABLE 1 Geochemical characteristics of sediments from the field and lab incubations from two fish farm cage clusters: short (SPP) and long (LPP) production period.

	Distance from cage (m)	Conditions	TOC % DW	δ 13C$_{TOC}$ (‰)	BOD µmol O$_2$ ml wet sed^{-1} hr^{-1}	DOU mmol O$_2$ m^{-2} d^{-1}	OPD (mm)
SPP	0	Lab incubation (day 8)	NA	NA	NA	23.0 ± 4.8	1.08 ± 0.25
	0	Field	1.7 ± 0.05	−23.4 ± 0.2	18.2 ± 4.6	35.3 ± 6.5	0.74 ± 0.11
	50	Field	1.8 ± 0.08	−22.7 ± 0.1	1.0 ± 0.3	19.2 ± 2.3	1.56 ± 0.46
	150	Field	1.5 ± 0.07	−22.7 ± 0.1	0.3 ± 0.02	11.6 ± 2.4	2.70 ± 0.38
LPP	0	Lab incubation (day 37)	NA	NA	NA	37.5	0.80
	0	Field	3.3 ± 0.1	−25.9 ± 0.6	16.0 ± 4.2	44.2 ± 24.7	0.74 ± 0.31
	50	Field	1.1 ± 0.04	−22.8 ± 0.3	1.3 ± 0.3	16.7 ± 5.4	1.38 ± 0.44
	150	Field	1.1 ± 0.06	−22.5 ± 0.03	0.4 ± 0.4	10.5 ± 2.0	1.76 ± 0.33

TOC, total organic carbon content in dry weight; BOD, benthic oxygen demand; DOU, diffusive oxygen uptake; OPD, oxygen penetration depth.

Alphaproteobacteria (7–33%). The former was especially dominant in LPP lab incubations (0–0.5 cm: 33%, 0.5–1 cm: 11%) because of the high abundance of *Magnetovibrio*. *Pseudomonas* was the most abundant taxon (1–10%) within the *Gammaproteobacteria* class for all samples except for the SPP lab incubation (0–0.5 cm: 17%) where *Thioalkalispira-Sulfurivermis* showed a higher abundance (**Supplementary Figure 3**). In the *Campylobacterota* phylum, the genus *Sulfurovum* was the most abundant for all sediment samples (5–42%) except for the SPP lab incubation (0–0.5 cm) where *Sulfurimonas* was more abundant (15%, **Supplementary Figure 3**). Within the *Desulfobacterota* phylum, four classes stand out for their higher abundance: *Syntrophobacteria, Desulfobacteria, Desulfuromonadia,* and *Desulfobulbia* (to which the cable bacteria belong). Of the ASVs classified to genus level, the most abundant were *Desulforhopalus* (1–6%, most abundant in LPP cage sediment), *SEEP-SRB4* (1–3%) and *SEEP-SRB1* (1–3%) (**Supplementary Figure 3**). Interestingly, *Ca.* Electrothrix (1.2%) and *Desulfocapsa* (2%) were among the most abundant taxa, in particular for LPP lab incubation (**Supplementary Figure 3**). The most abundant family within the *Bacteroidota* phylum, across all sediment samples, was *Flavobacteriaceae* (1–5%). Within this phylum three families increased in relative abundance in lab sediments compared to field sediment: *Saprospiraceae*, *NS11-12_marine group*, and *Chitinophagaceae* (particular in LPP lab incubations, data not shown). For the *Actinobacteriota*, two orders were dominant, *Actinomarinales* (1–7%) and *Microtrichales* (1–3%). The family *Lachnospiraceae*, of the *Firmicutes* phylum, was especially present in the *in situ* cage sediments (1–8%, 5 out of 6 samples), and *Streptococcaceae* was more abundant in lab incubations (up to 7% for LPP incubation, 0–0.5 cm, data not shown).

To verify the impact of the fish farms on the seabed, differences in the microbial community composition between field sediments were analyzed with PCoA, which explained a total of 51% of the variance in the data. *Distance from the cage* was identified as the main defining factor of the ordination (PC1 = 35%) and differentiated the sediments in two clusters: samples at the fish cages (*Cage*) and samples further away (*≥50 m*) (**Figure 2**). The deepest sediment layer (3–5 cm depth) from the SPP station at the cage, grouped with the ≥50 m sediment samples. ANOSIM analysis confirmed that the microbial communities differed when considering distance from the cage (Cage vs. >50 m; $R = 0.6$; significance = 0.001), whereas the production period (LPP vs. SPP) had a less significant effect ($R = 0.4$; significance = 0.002). The two PCoA clusters (Cage and ≥50 m) were used in a two-way comparison DESeq analysis to identify the microbial taxa that were differentially abundant between the two clusters. DESeq analysis identified 39 differentially abundant taxa for the Cage cluster and 18 taxa for the >50 m cluster (LFC $\geq |4|$ and $p < 0.01$, **Supplementary Table 5** and **Supplementary Figure 4**). Of the 39 differentially abundant taxa for the Cage cluster, the taxa with the highest relative abundance belonged to the genera *Streptococcus* (up to 15.7%), *Silanimonas* (up to 8.7%), *Sulfurimonas* (up to 4.0%), *Desulfocapsa* (up to 1.9%), *Thioalbus* (up to 1.8%), and two unknown genera from the *Saprospiraceae* (up to 4.8%) and *Sedimenticolaceae* (up to 3%) families (**Supplementary Figure 5**). The most abundant taxa for the >50 m cluster within the identified 18 differentially abundant taxa were *Pseudomonas* (up to 3.5%), *Sedimentibacter* (up to 2.6%), and two unknown genera within the *Bacteroidetes vadinHA17* (up to 1.7%) and *Prolixibacteraceae* (up to 2.3%) families (**Supplementary Figure 5**).

3.3 Geochemical characterization of lab incubations

Initially, incubated sediments were characterized by a straight pH depth profile (data not shown), which over the course of weeks developed in to the distinct geochemical

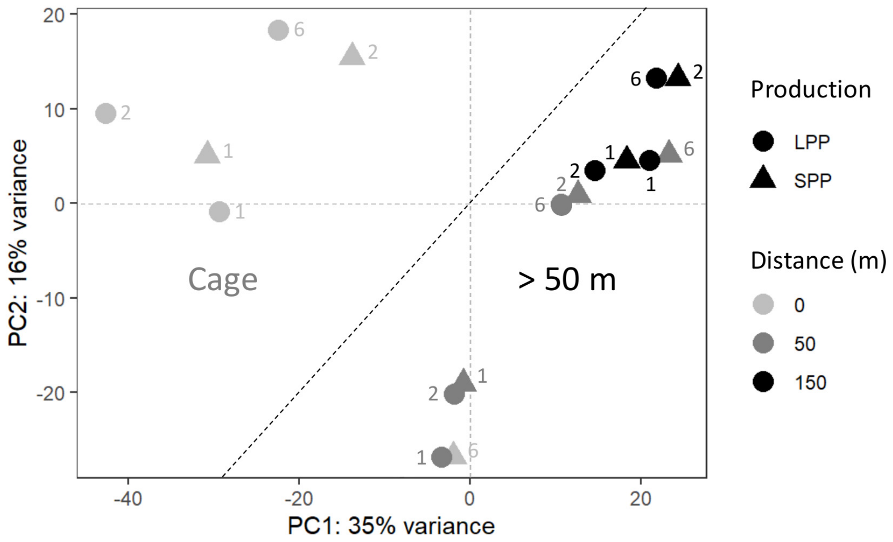

FIGURE 2

Principal coordinate analysis (PCoA) of the microbial community from fish farm sediment (field samples). The compositional nature of the data was considered by applying a variance stabilizing transformation. Two groups were identified, one for microbial communities from sediment at the Cages (Left), and those found >50 m away from cages (Right). SPP, short production period; LPP, long production period. Sediment layer depth intervals are indicated as follows: 1 = 0–0.5 cm, 2 = 0.5– 1.0 cm, 6 = 3.0–5.0 cm.

fingerprint of electrogenic sulfur oxidation (e-SOx) by cable bacteria (Schauer et al., 2014; Meysman et al., 2015). When e-SOx develops, a suboxic zone appears, which separates the oxygen penetration depth (OPD) from the sulfide appearance depth (SAD). At the same time, the pH depth profile shows a maximum in the oxic zone, and then decreases to reach a minimum near the SAD (Nielsen et al., 2010; Meysman et al., 2015). The difference between these two pH values is referred to as ΔpH, and when ΔpH reaches a maximum, it signifies maximum e-SOx activity (Burdorf et al., 2018). Cable bacteria activity was evident in lab incubations from both the SPP and LLP sites yet with a different timing. For the SPP incubations, the maximum ΔpH = 2.3 was reached by day 8 (**Figures 3A, C**). At this point, the OPD was 1.08 ± 0.25 mm, and DOU was 23.0 ± 4.8 mmol O_2 m^{-2} d^{-1} (**Table 1**). In LPP incubations, the e-SOx activity was maximal at 37 days (ΔpH: 2.4, OPD: 0.8 mm, DOU: 37.8 mmol O_2 m^{-2} d^{-1}; **Figures 3B, C** and **Table 1**). No free sulfide was detected in the top 2 cm of sediment, throughout the incubation period for both SPP and LPP incubations.

3.4 Correlation analysis of microbial communities: Field conditions versus lab incubations

Geochemical profiles of cage sediments from the field and lab incubations differed significantly; in the field high sulfide accumulation was present in porewater that resulted in a surface O_2-H_2S interface, whereas a clear e-SOx geochemical signal was obtained in lab incubations (**Figures 1, 3A**). As such we aimed to identify the differences in microbial community composition between these two sediments. To achieve this the Spearman correlation was used, which measures rank relationships between features. The Spearman coefficient identified a total of 64 ASVs ($p < 0.001$) from the Bacteria kingdom, 19 positively correlated to Cage sediments in the field, and 45 positively correlated to lab incubations with e-SOx (**Figure 4**). Four ASVs were present in both Cage and Lab sediment: Ulvibacter ASV 914, an unknown genus from the Order B2M28 ASV 1931, *Desulfocapsa* ASV1197 and an unknown genus of *Anaerolineaceae* ASV1439. The first two had the highest abundance of the ASVs significantly correlated to Cage sediments, whereas Desulfocapsa and Anaerolineacea were 10- to 20-fold higher in lab incubations. Additionally, sulfur oxidizing *Sulfurovum* (ASV2958, ASV4799, ASV5873, and ASV6377) correlated to Cage sediments (**Figure 4**) while *Sulfurimonas* (ASV8, ASV12, and ASV81) and *Thioalbus* (ASV158) correlated to lab incubations ($p < 0.01$, data not shown for $p > 0.001$). All three sulfur oxidizing genera had the highest absolute abundances among the taxa identified with the Spearman's correlation. The most abundant cable bacteria related ASV (ASV88) correlated to lab incubations with a statistical significance of $p = 0.02$. Within the taxa correlated to lab incubations, *Desulfocapsa* (ASV1197) showed the highest abundance, followed by *Acidovorax* (ASV2390 and ASV2339), while the family *Comamonadaceae* showed the largest number of different taxa (eight ASVs classified to the genera *Acidovorax*, *Limnohabitans*, *Piscinibacter*, *Rhodoferax*, and *Simplicispira*).

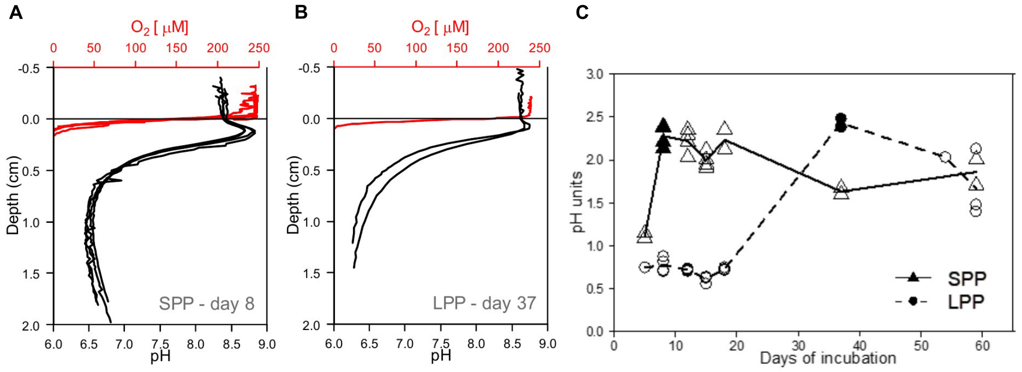

FIGURE 3

Development of e-SOx in lab incubations with fish farm sediments. **(A,B)** Microsensor profiles showing the presence of e-SOx geochemical fingerprint in incubated cage sediment from both short (SPP) and long production period (LPP). Red, oxygen; black, pH, sulfide not detected. **(C)** Plot of the change in Δ pH in time, with maximum Δ pH obtained at day 8 for sediment from SPP (filled triangle) and day 37 for LPP cage sediments (filled circle). All replicates (points) and average (line) Δ pH are plotted.

3.5 Cable bacteria in fish farm sediments

Given the formation of the e-SOx geochemical fingerprint in the laboratory incubations, the associated presence of cable bacteria was verified via three approaches: (1) visualization of handpicked filaments with SEM, (2) taxonomic identification of cable bacteria filaments with FISH, and (3) identification through 16S rRNA gene sequences related to known cable bacteria genera.

Unlike any other microbe, cable bacteria have developed a unique conductive wire structure that allows them to "download" electrons from sulfide deep in the sediment, transport them along the filament, and finally "upload" the electrons onto oxygen at the sediment surface (Meysman et al., 2019). These conductive wires lie underneath the outer membrane and are visible as parallel ridges along the filament (Cornelissen et al., 2018). Examination of SEM images from lab incubations (**Figure 5A**) revealed thin filaments with 10–12 outer membrane ridges (n = 10 cells), which is lower than previously observed (range 15–70) but in accordance with thinner filaments (Cornelissen et al., 2018). Filament diameters varied between very thin (0.5 ± 0.1 µm, 13 filaments, 41 cells) and slightly thicker filaments (0.9 ± 0.1 µm, 7 filaments, 21 cells), with an average cell length of 2.8 ± 0.5 µm (n = 19 cells).

Secondly, FISH analysis confirmed binding of the specific DNA probe for the *Desulfobulbaceae* family (DSB706) to the observed filamentous bacteria (**Figure 5B**). Filaments were, however, only identified in subsurface layers of incubated lab sediments (0.5–1.0 cm) and were not detected in field sediments.

The third approach entailed amplicon sequencing, which produces ASVs that can be assigned to the two known cable bacteria genera (Trojan et al., 2016): *Ca.* Electrothrix (marine) and *Ca.* Electronema (freshwater). Combining data from the field and lab incubations, a total of 23 different ASVs were assigned to *Ca.* Electrothrix and none could be assigned to *Ca.* Electronema. Sequences classified as *Ca.* Electrothrix were present in all sediment samples (field and lab), with 19 ASVs present in at least 5 samples with ≥10 total read counts. Thirteen ASVs clustered with *Ca.* Electrothrix species (**Figure 5C**). The remaining six ASVs clustered outside of the presently known *Ca.* Electrothrix clade but fulfilled the genus-level identity threshold of 94.5% (Yarza et al., 2014) with two other cable bacteria 16S rRNA gene sequences, AR-3 and AR-4, which are described as a potential new cable bacteria genus (Dam et al., 2021, **Figure 5C**). ASV88, clustering with *Ca.* E. communis, was the most dominant cable bacteria taxon across all samples (**Figure 5D**). ASV88 accounted for 71–99% of the total cable bacteria abundance for SPP and LPP lab incubations, and >50% for SPP and LPP cage sediment (0–1 cm, **Supplementary Figure 6**).

Laboratory incubations had the highest relative abundance and sequence counts of cable bacteria related sequences (0.2–1.2%, 229–1,287 sequences) with the highest contributions found in subsurface sediments (0.5–1 cm, **Figure 5D** and **Supplementary Table 4**). For field SPP sediments the relative abundance and counts of cable bacteria related sequences were below the minimum values found in laboratory incubations (<0.1%, 20–96 sequences), except for the cage sediment at 0.5–1 cm depth (0.2%, 177 sequences). The relative abundance of cable bacteria sequences in field LPP sediments, was at the lower range found in lab incubations (0.2–0.5%, 185–369 sequences) with the highest contribution of cable bacteria in subsurface sediments (0.5–1 cm depth) at the 50 m away site (**Figure 5D** and **Supplementary Table 4**). However, sediment at the LPP cage (0–1 cm) had a lower contribution of cable bacteria sequences (0.1%, 74–116 sequences). The diversity of cable bacteria related ASVs was highest (14–19 ASVs) for SPP

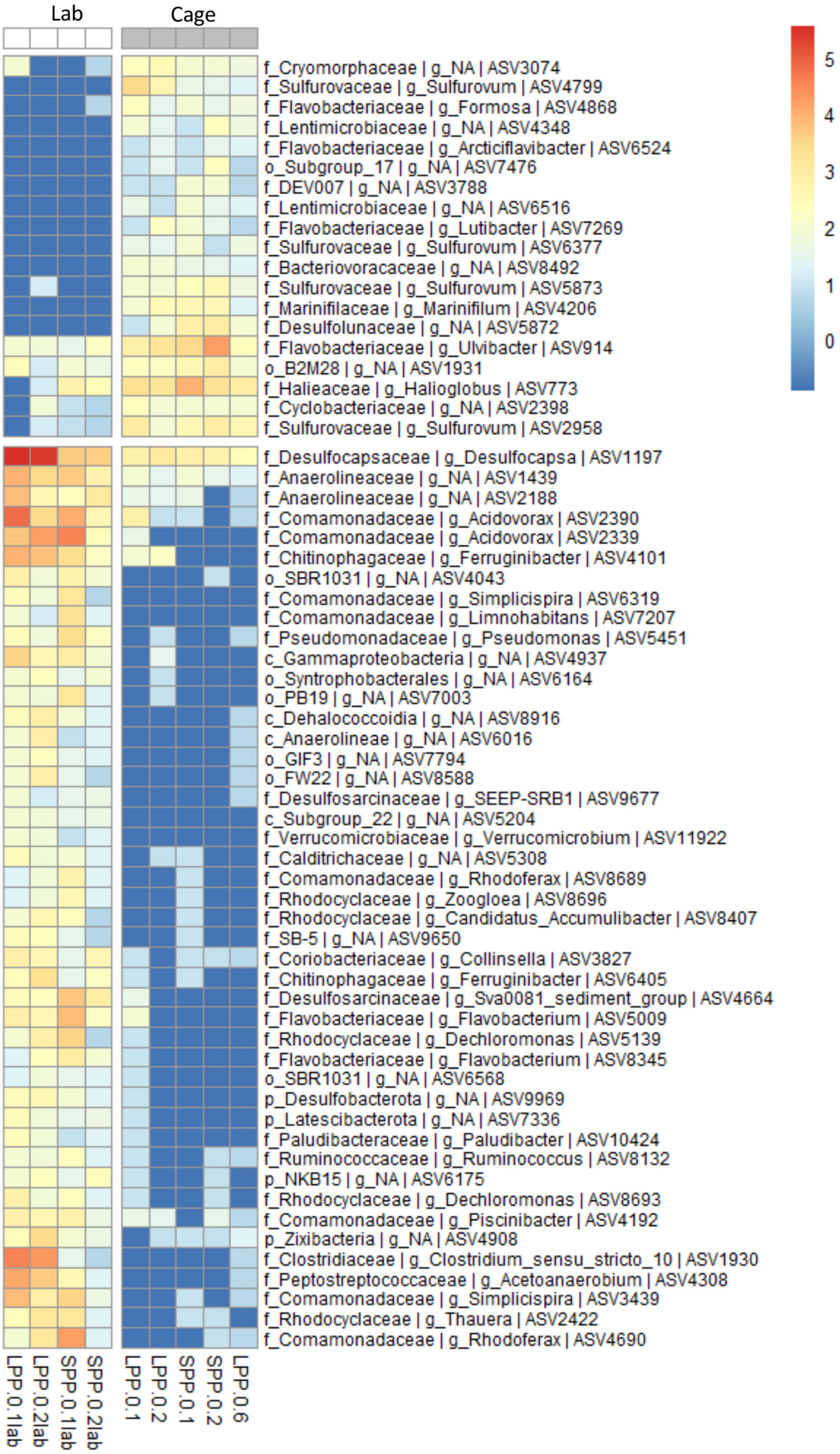

FIGURE 4

Correlation analysis between the microbial communities in cage sediments from the field and from lab incubations (Spearman correlation, $p < 0.001$). ASV abundance is normalized with variance stabilizing transformation (blue to red scale bar). Genus and next known taxonomic level are stated for each ASV (k, Kingdom; p, Phylum; o, Order; c, Class; f, family; g, Genus). Sample code represent production period: LPP, long; SPP, short; distance from: 0 = at cage; and sediment layer: 1 = 0–0.5 cm, 2 = 0.5–1.0 cm, 6 = 3.0–5.0 cm.

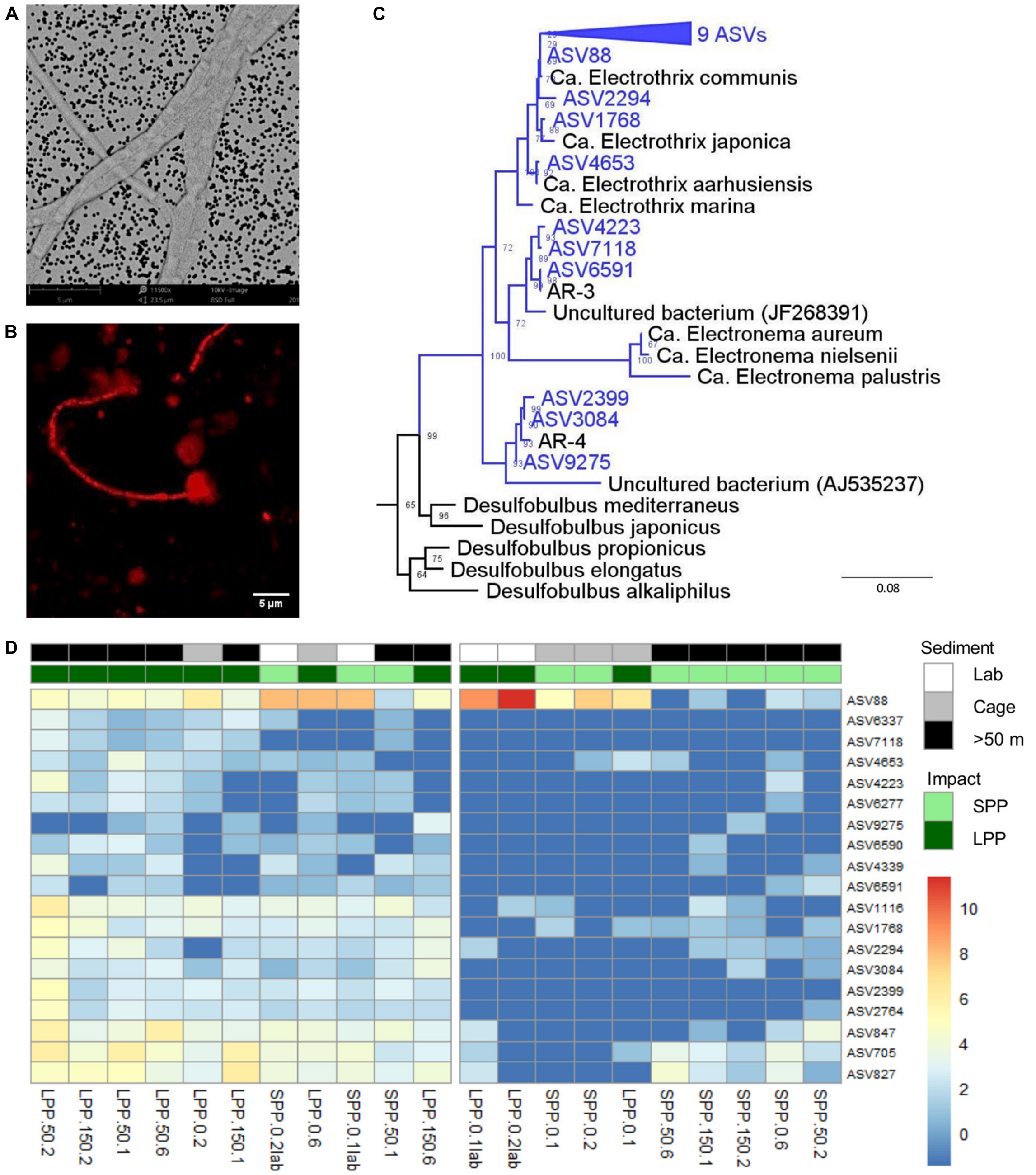

FIGURE 5

Evidence of the presence of cable bacteria in fish farm sediment. **(A)** SEM image of picked cable bacteria filaments from lab incubated sediments. **(B)** Cable bacteria filament from incubated sediments stained with DSB706 probe via FISH technique. **(C)** Phylogenetic (consensus) tree of 19 ASVs (blue) with >94.5% sequence similarity to known cable bacteria genera (*Ca.* Electrothrix, *Ca.* Electronema, AR-3, and AR-4), from both field and lab incubated fish farm sediments. Bootstrap values are stated at the nodes, 4 references sequences from the Desulfobulbia class are included and *E. coli* was used as root. **(D)** Relative abundance of 19 ASVs identified as *Ca. Electrothrix* from all fish farm sediments: Lab incubated sediment (white), field sediment under the Cages (gray), field sediment collected >50 m away from cages (black). Abundances were normalized with variance stabilization transformation (blue to red scale bar). Sample code indicate production period: LPP, long (dark green); SPP, short (light green); distance from cage: 0 = cage, 50 = 50 m, 150 = 150 m; and sediment layer: 1 = 0–0.5 cm, 2 = 0.5–1.0 cm, 6 = 3.0–5.0 cm. Lab incubations are additionally labeled as *lab*.

lab incubated sediment and all but one LPP sediment (Cage 0–0.5 cm with 4 ASVs, Figure 5D and Supplementary Table 4). Fewer cable bacteria related ASVs (2–10 ASVs) were found in LPP lab incubated sediment and SPP sediments (except for surface sediment from 50 m distance, Figure 5D and Supplementary Table 4).

4 Discussion

4.1 Overall impact of fish farms on the seabed

In general, aquaculture activities have a strong impact on the sediment inducing geological, biological and/or chemical changes, with the strongest alteration observed below the cages, extending up to several tens of meters away from the fish cages (Carroll et al., 2003; Giles, 2008). As observed in this study, the most conspicuous changes to the sediment occur below the fish cages at the LPP site, where sediment becomes black, with a top layer of non-ingested fish feed, and little to no signs of fauna or bioturbation (Karakassis et al., 2002; Mulsow et al., 2006). Surface sediments were lighter in coloration and less flocculent, with a higher areal abundance of tube worms with increased distance from the cage (**Figure 1**). An increase in waste particles below the cages, especially at LPP, correlates well with a higher organic carbon content (**Table 1**; McCaig et al., 1999; Maldonado et al., 2005; Keeley et al., 2012; Ballester-Moltó et al., 2017; Hornick and Buschmann, 2018; Verhoeven et al., 2018). The more depleted stable isotope carbon signature found at cage sediments (**Table 1**) reflects the accumulation of leftover fish feed that has a depleted stable isotope signature compared to natural marine organic carbon.

The TOC values we obtained in cage sediments (0.7–3.3%) are within the lower range reported for fish farming sediments (2–48%) as reviewed by Giles (2008). Lower OM content can be associated to lengthy fallowing periods and short production periods (Verhoeven et al., 2018) which could explain the values found in the SPP cage sediment (**Table 1** and **Supplementary Table 1**). The degree and extent of the benthic impact, however, can vary as a function of hydrological factors (e.g., current speed and water depth), sediment type (e.g., fine vs. coarse grains), and production characteristics (e.g., production time and fish density) and thus are particular to each environment (Maldonado et al., 2005; Giles, 2008; Grigorakis and Rigos, 2011; Keeley et al., 2012; Verhoeven et al., 2018). The relatively low TOC values found at the LPP cage therefore suggest that other environmental factors, such as strong local currents or mixing due to storms may wash away part of the surface organic-rich, flocculent layer in Berufjörður. In fact, large shell particles were found in the sediment cores collected from the LPP cluster, up to 150 m away, that might have originated from shell fish growth on the cage structure. The increased input of highly degradable organic matter, as indicated by the highest TOC values in top sediment layers at cages (**Table 1**), may promote the development of chemoorganotrophic microbes such as the differentially abundant *Spirochaete* taxon found in cage sediments (**Supplementary Figures 4**, **5**). *Spirochaete* serve as a bioindicator of highly impacted fish farming sediments (Verhoeven et al., 2018; Quero et al., 2020). Likewise cage sediments were characterized by representatives of the *Cloacimonadales* and *Chitinophagales* orders (up to 1.0 and 4.8% of 16S rRNA sequences, respectively), taxa capable of degrading complex organic compounds and long chain fatty acids such as those present in fish feed and fecal material (Shakeri Yekta et al., 2019).

The observed increase in BOD and DOU at cage sediments relative to sediments further away (**Table 1**) suggests higher oxygen demand for the mineralization of organic matter (Pereira et al., 2004; Piedecausa et al., 2012). Our oxygen consumption rates are comparable to those found in lab incubations with fish farm sediment (~30 mmol O_2 m^{-2} d^{-1}), in shellfish farms in the Mediterranean (27–54 mmol O_2 m^{-2} d^{-1}, Dedieu et al., 2007) and in coastal eutrofied areas in Denmark [~20 mmol O_2 m^{-2} d^{-1}, (Valdemarsen et al., 2014)]. More than 50% of the anaerobic mineralization in active, organic-rich sediments can be accounted for by sulfate reduction which leads to high sulfide production that can accumulate in the porewater of the sediment (Holmer and Kristensen, 1996). Cage sediments at both SPP and LPP sites had the highest concentration of free sulfide in the porewater (**Figure 1**) confirming the higher mineralization rate at these locations. The appearance of sulfide at the sediment surface in concentrations one order of magnitude higher in LPP vs. SPP cage sediments highlights the effect of fish farms on sulfur cycling.

The microbial community structure follows the geochemical trend described, with a clear difference between cage sediments and those more than 50 m away (**Figure 2**). In cage sediments, sulfate reduction is likely the predominant mineralization pathway, and 5 ASVs from the class *Desulfobulbia* (*Desulfocapsa, Desulfotalea, Desulfobulbus, MSBL8,* and one unclassified) known to perform sulfate reduction were identified as differentially abundant taxa (**Supplementary Figures 4**, **5**). In parallel, sulfide oxidizing microbes such as *Sulfurovum* (0.6 – 4.0% of 16S rRNA gene sequences), *Magnetospira* (0.04 – 0.5%), and *Thioalbus* (1.2 – 1.8%) also characterized the sulfidic cage sediments (**Supplementary Figure 3**). All three genera grow (micro)aerobically and oxidize reduced sulfur compounds (sulfide, thiosulfate, tetrathionate and elemental sulfur) in marine environments (Campbell et al., 2006; Takai et al., 2006; Park et al., 2011; Williams et al., 2012; Kojima et al., 2017). In particular, sulfidic fish farm sediments are well-known for an increased presence of *Campylobacterota* (*Sulfurovum* or *Sulfurimonas*) during the production cycle and fallowing periods (Aranda et al., 2015; Verhoeven et al., 2018; Kolda et al., 2020; Miranda et al., 2020; Quero et al., 2020). Thick mats of filamentous microbes from the *Thiotrichaceae* family performing sulfide oxidation are also commonly found in sediments near cages (Aranda et al., 2015; Miranda et al., 2020). However, such microbial mats were not observed at the SPP and LPP field sites upon retrieval of the sediment and taxa assigned to this family contributed less than 0.01% of the 16S rRNA gene sequences. The geochemical fingerprint associated with Beggiatoacea is identified by a decrease pH at the sediment surface and a pH increase at the sulfide appearance depth (Seitaj et al., 2015). This fingerprint was also not observed in sediments from the field nor the lab. Overall, the microbial community in cage sediments had a dominance of sulfate reducing and sulfide oxidizing microbes resembling the community typically found in fish farm sediments (Asami et al., 2005; Kawahara et al., 2009; Choi et al., 2018; Kolda et al., 2020) and in organic-rich marine sediments (Mußmann et al., 2005; Wasmund et al., 2017).

A variety of taxa associated with fish diseases, gut microbiomes and wastewater industry were also found, such as *Streptococcus* in cage sediment, *Pseudomonadales, Bacteroidales, Synergistiales, Cloacimonadales* in sediments >50 m away, and *Pseudomonas, Ruminococcus, Collinsella, Candidatus Accumulibacter,* and *Flavobacterium* in lab incubations (**Supplementary Figures 3**, **5**; Gram et al., 1999; Wexler, 2007; Liu et al., 2015; Møretrø et al., 2016; Ormerod et al., 2016; Martins et al., 2018; Xia et al., 2018). These microbial groups play a key role in anaerobic degradation of organic matter, but due to their pathogenic character, serve as biomarkers for fish farm impacted sediments (Verhoeven et al., 2018; Quero et al., 2020). The presence of potential pathogens and gut-microbiome microbes along the transect studied, highlights the spatial extent of the fish farming activities on the seafloor up to 150 m distance (downstream of prevalent current). The persistence of pathogens surrounding fish farms is one of the main long-term impacts of this industry, that has yet to be resolved (Grigorakis and Rigos, 2011; Martins et al., 2018; Ape et al., 2019).

4.2 Studying the recovery of fish farm sediments

In this study, our aim was to provide insight into the geochemistry and microbial communities in sediments impacted by fish farming activities, but also to focus on the recovery effects through dedicated laboratory incubations. One widely implemented method for fish farm sediment recovery is fallowing, in which the input of organic matter is ceased over a period of months to years. Ceasing fish farm activities at a given location results, over time, in a decreased mineralization of organic matter, and hence a decreased production of sulfide through sulfate reduction. The length of this recovery process varies from months to years depending on the fish farming practices and environmental conditions of a specific area (Pereira et al., 2004; Keeley et al., 2017; Verhoeven et al., 2018). To examine whether this recovery process can be accelerated in the lab, two physical disturbances were implemented to fish farm sediments: (i) removal of the organic-rich top sediment and (ii) mixing of sediments. The removal of the organic-rich surface layer prior to incubation can occur naturally as a result of storms and strong currents. Similarly, sediment mixing has been shown to improve sediment quality by reducing the accumulation of sulfide (Keeley et al., 2017), as mixing causes the pool of reduced metals to become partly oxidized (e.g., FeS or FeS_2 are oxidized to FeOOH). These iron- or manganese (hydr)oxides then become readily available to react with the free sulfide that is being produced via sulfate reduction, thus forming sulfide minerals (e.g., FeOOH combines with H_2S to form FeS or FeS_2). Therefore, our laboratory sediment incubations provide insight in to the potential recovery of fish farm sediments during fallowing (ceasing of organic matter input) or those exposed to strong storms (removal of organic-rich sediment and potential mixing of sediment).

The combined effect of no organic matter input, top layer removal and sediment homogenization in the lab incubated sediments resulted in no measurable accumulation of free sulfide in porewater during the entire incubation period (60 days, **Figures 3A, B**). At the start of the incubation, both SPP and LPP sediments showed a pH depth profile typical for a sediment dominated by anaerobic organic matter mineralization through sulfate reduction (data not shown). Under these conditions there is a constant production of sulfide in subsurface sediments that can lead to the accumulation of sulfide in porewater as observed in *in situ* cage sediments (**Figure 1**).

Interestingly, after a given period of incubation (8 days in SPP and 37 days in LPP), cage sediments developed the geochemical fingerprint of electrogenic sulfur oxidation (e-SOx) by cable bacteria (**Figures 3A, B**). This fingerprint is characterized by a pH maximum at the oxygen penetration depth (OPD) and a pH minimum centimeter(s) deeper in the sediment (Nielsen et al., 2010; Pfeffer et al., 2012). Cable bacteria grow naturally and in lab incubations (under similar conditions as the ones performed in this study) in a broad range of sediments where ample sulfide is produced through sulfate reduction or iron sulfide dissolution (Risgaard-Petersen et al., 2012; Malkin et al., 2014; Schauer et al., 2014; Burdorf et al., 2017). The rapid development of cable bacteria in the lab incubations and the presence of *Ca*. Electrothrix related 16S rRNA gene sequences in all sediment samples (both field and in the lab, **Figure 5**) shows that cable bacteria have the potential to grow in fish farm sediments under conditions that are similar to fallowing. We do note that incubation temperatures in our lab incubations (18°C) were higher than in Icelandic fjords (∼4°C annual average water temperature). Yet, we anticipate that the e-SOx development may still occur within a similar timeframe under field conditions. During incubation of subpolar fjord sediments from Greenland, the e-SOx signature appeared within 26 days of incubation at 0°C (Burdorf et al., 2017), thus demonstrating that low temperatures (∼0°C) do not necessarily delay the development of e-SOx. Under these cold conditions, e-SOx was also sustained for long periods of time (up to 98 days). Thus, the development of e-SOx may still occur within the similar timeframe as in our lab incubations.

Furthermore cable bacteria act as ecosystem engineers by influencing the geochemical cycling in sediments via indirect stimulation of microbial processes such as sulfate reduction, hydrocarbon degradation (toluene, alkanes, and PAHs), iron cycling and denitrification (Müller et al., 2016; Otte et al., 2018; Kessler et al., 2019; Marzocchi et al., 2020; Sandfeld et al., 2020; Liu et al., 2021; Huang et al., 2022; Liau et al., 2022). Indeed, some of the genera that positively correlated to e-SOx activity in our lab incubations (**Figure 4**) may perform sulfate reduction (*Desulfocapsa, SEEP-SRB1*, and *Sva0081*), denitrification (*Thauera, Dechloromonas, Rhodoferex, Zoogloea*, and *Acidovorax*) and iron oxidation (*Acidovorax*). Cable bacteria further displace the oxic-anoxic interface by gliding up and down through the sediment at a microscale while performing e-SOx (Malkin and Meysman, 2015; Bjerg et al., 2016; Scilipoti et al., 2021). Therefore microbes with the ability to move with and sense the changing interface may also be favored in the presence of cable bacteria. Among the genera strongly correlated to e-SOx (**Figure 4**) several are known to be aerobic, and have motility and chemotaxis genes (*Dechloromonas, Thauera, Simplicispira*, and *Flavobacterium*). Additionally, *Magnetovibrio*, a motile, microaerophilic, sulfur oxidizer (Bazylinski et al., 2013), increased 20 times in abundance in the lab incubations compared to field sediments (**Supplementary Figure 3**). Similar positive correlation between *Magnetovibrio* and cable bacteria have been reported in lab incubations, suggesting an adaptive advantage for this microbe potentially linked to the microscale geochemical fluctuations created by cable bacteria activity, in particular related to iron availability (Liau et al., 2022).

The strong O_2-H_2S gradients in the sediment, produced by the activity of cable bacteria (Nielsen and Risgaard-Petersen, 2015; Meysman, 2018) have led to a proposed metabolic link, over centimeter depths, between cable bacteria and other sulfur-oxidizing microbes belonging to the *Campylobacterota* or *Gammaproteobacteria* (Vasquez-Cardenas et al., 2015; Lipsewers et al., 2017). *Campylobacterota* inhabit niches with low oxygen and high sulfide, while sulfur-oxidizing *Gammaproteobacteria* tend toward higher oxygen concentrations in environments such as hydrothermal vents and cave waters (Macalady et al., 2008). Steep redox gradients favor the diversification of species, each with their own narrow niche, plausibly related to sulfide:oxygen ratio and the available reduced sulfur compounds (Macalady et al., 2008; Meier et al., 2017; Pjevac et al., 2018). The activity of cable bacteria may therefore have a cascading effect on sulfur cycling that further drives the niche differentiation and co-occurrence of phylogenetically diverse sulfur oxidizing community. In fact, micro-aerophilic, sulfur-oxidizing taxa [*Sulfurimonas* and *Thioalkalispira-Sulfurivermis,* (Sorokin et al., 2002; Takai et al., 2006)] were found to increase 9 and 18 times (respectively), exhibiting higher average relative abundances (7.3 and 4.7%, respectively) in our lab incubation compared to field sediments (**Supplementary Figure 3**). Likewise, a positive correlation between sulfur-oxidizing Gammaproteobacteria (*Thiogranum* and *Sedimenticola*) and cable bacteria was recently observed in sulfidic sediments from seasonally hypoxic area in Chesapeake bay (Liau et al., 2022). The potential for improved recovery of fish farm sediments, via efficient sulfide removal by a diverse microbial community enhanced by cable bacteria, is evident from our study. However, the nature of the interactions between the species and the intensity of the synergetic effects remain to be resolved.

Overall our laboratory incubations suggest that ceasing the input of organic matter (fallowing) and removing organic-rich surface sediment (storms and current) can accelerate the recovery of sediments in fish farm impacted areas. Mixing of anoxic sediments (storms, currents, and fauna) as well as the development of cable bacteria significantly reduce or even prevent the accumulation of free sulfide in the porewater. Moreover, the rapid development of cable bacteria in SPP sediment lab incubations indicates that the implementation of shorter production periods at one location may result in a faster sulfur-detoxification during fallowing.

4.3 Absence of strong e-SOx in sediments during the production period

The development of cable bacteria in fish farm sediment incubated in the lab raises the question as to why there was no clear e-SOx geochemical fingerprint in the field during the production cycle, and thus what the functional role of cable bacteria is in fish farm sediments. In coastal marine sediments, the e-SOx signal is typically found in sediments with moderately active sites with sulfide concentrations up to 0.3 mM and DOU rates <35 mmol O_2 m^{-2} d^{-1} (Malkin et al., 2014; Burdorf et al., 2016, 2017; van de Velde et al., 2016). However, cable bacteria have also been found in sediments with high sulfide concentration (up to 3 mM), high organic matter content (up to 4.4%), and high mineralization rates (35–126 mmol O_2 m^{-2} d^{-1}) such as mussel bed, oyster reefs, mangroves, and seasonally hypoxic basins (Burdorf et al., 2017; Lipsewers et al., 2017; Malkin et al., 2017). In these environments, e-SOx plays a major role in the oxygen consumption and sulfide oxidation of the sediment (Nielsen and Risgaard-Petersen, 2015). The sulfide concentrations next to the LPP cage exceed the higher limit reported for sediments with an e-SOx signal. Thus development of cable bacteria, or that of their associated microbes, may be impeded in these (highly) sulfidic environments. These environmental conditions may rather favor the rapid colonization by microaerophilic, sulfur oxidizing *Sulfurimonas* and *Sulfurovum* that characterize steep redox-gradient environments, with high sulfide concentration (Campbell et al., 2006; Han and Perner, 2015; Meier et al., 2017), as observed in sediment below the cages (**Figure 4**). The lower sulfide concentrations found in the sediments >50 m away from the cages could therefore potentially allow for the growth of cable bacteria. Indeed, sediments from LPP sites at 50 m distance, and to a lesser degree from SPP, showed a diversity and relative abundance of cable bacteria similar to that found in the lab incubations (**Figure 5D** and **Supplementary Table 4**). In sediments with a clear e-SOx signature, cable bacteria can account for 0.6% up to 7% of the total 16S rRNA gene sequences, and as low as 0.2% in oxic layers or in suboxic sediment when the e-SOx signal is weakening (Klier et al., 2018; Otte et al., 2018; Geelhoed et al., 2020; Dam et al., 2021; Liau et al., 2022). A recent study further shows a 10-fold higher percentage of cable bacteria sequences, when comparing DNA-based to RNA-based 16S rRNA genes in the same sediment sample (Liau et al., 2022). Therefore relative abundances below 1%, as the ones obtained here for DNA-based sequences, could still represent high metabolic activity of cable bacteria. The 16S rRNA gene sequence abundance of cable bacteria in our lab incubations (0.2–1.2%) and in LPP sediments > 50 m away from the cage (0.2–0.5%; **Supplementary Table 4**) therefore suggest that e-SOx may be occurring in sediments, although it does not dominate the geochemistry of the sediment. Interestingly, more than one species of cable bacteria was found in all sediment samples, with the highest variety of cable bacteria related ASVs in SPP lab incubations (with e-SOx) and in the LPP field sediments (without e-SOx **Figure 5D**). The coexistence of several species of cable bacteria at one location has been ascribed to non-exclusive competition between species (Marzocchi et al., 2018). However, apart from salinity, little is known about the factors controlling the diversity patterns of cable bacteria (Trojan et al., 2016; Dam et al., 2021).

The lack of a strong e-SOx geochemical signal in sediments near and surrounding the fish cages may be further attributed to the physical disturbance of the sediment. One of the clearest effects of fish farms is the increase in food particles and fish waste below and around the cages, thus increasing the deposition rate. In addition, the cages themselves serve as artificial surfaces for bivalves and barnacles that need to be regularly removed by divers to ensure good water circulation through the cages. Shell debris is carried by the current downstream where it is deposited on the sediment surface as seen in sediment cores 150 m away from the cages (**Figure 1** and **Supplementary Table 3**). The input of particles (fish feed, fecal pellets, and shells) onto the sediment, disrupts the geochemical gradients and changes the microscale niches available for microbes in the top centimeters of the sediment. Cable bacteria filaments orient and glide vertically in the sediment to maintain a connection between the surface oxygen and the deeper sulfide-horizon (Malkin and Meysman, 2015; Bjerg et al., 2016). However, the rate of particle input in fish farm areas is potentially greater than the speed at which cable bacteria glide or grow, and thus a stable, clear e-SOx signature may be impeded. Moreover, the mixing of sediment by macrofauna bioturbation in the fish farm sediment, as seen in SPP sediments (**Figure 1**) may also break, disorient, or bury cable bacteria filaments, obscuring the e-SOx geochemical fingerprint (Malkin et al., 2014; Burdorf et al., 2016). The presence of cable bacteria related sequences in all our samples and their development in the laboratory incubation (**Figures 3**, **5**) suggests that cable bacteria may be performing e-SOx to some degree in the field, but because of physical perturbations, this processes does not dominate the geochemistry of the sediment. Alternatively, cable bacteria have the complete sulfate reduction pathway encoded in their genome (Kjeldsen et al., 2019), thus they could use this metabolism to live in subsurface sediments until the appropriate conditions arise for them to grow via e-SOx. Nonetheless, the ability for cable bacteria to perform sulfate reduction has not been physiologically demonstrated. The precise environmental requirements and full physiological characterization of cable bacteria remain one of the main fields for further study of this electrogenic microbe (Burdorf et al., 2017; Kjeldsen et al., 2019; Geerlings et al., 2020, 2021; Scilipoti et al., 2021; Malkin et al., 2022).

5 Conclusion

Our study foremost confirms the detrimental geochemical and microbial impacts, both temporal and spatial, of waste particle accumulation on the seabed originating from fish farming activities. A detailed study of the residual organic matter accumulation during repetitive production-fallowing cycles is thus recommended in the SW coast of Iceland to properly constrain the recovery capacity of the benthic system and propose appropriate regulation. Our study suggests that physical manipulation of fish farm sediment such as removal of surface sediment, combined with a period of fallowing (ceased organic matter input) aid in the development of e-SOx by cable bacteria. As a consequence mineralization of organic matter via sulfate reduction may be heightened, as well as the development of potential cooperative interspecies relationships that may further enhance sediment recovery by rapidly consuming sulfide. Therefore we propose that cable bacteria can have a functional role in fish farm sediments, most likely during fallowing periods, resulting in three main remediation processes (1) promotion of efficient sulfur cycling by phylogenetically diverse microbes via interactions with cable bacteria, (2) short-term mitigation of sulfide concentrations via e-SOx due to the rapid consumption of sulfide in the top centimeters of the sediment, thus enabling better colonization conditions for macrofauna, and (3) formation of an iron-firewall which can prevent sulfide build-up in the long-term (Seitaj et al., 2015) once a new production cycle is started at the same location. Our hypothesis awaits *in situ* validation (e.g., occurrence of e-SOx geochemical fingerprint during fallowing) or targeted organic loading experiments in mesocosms. Application of microbial fuel cells has also recently been proposed as an efficient sulfide removal strategy in fish farm sediments (Algar et al., 2020). Interestingly, the use of sediment microbial fuel cells can also induce the appearance of the e-SOx geochemical fingerprint (Reimers et al., 2017; Li et al., 2020; Marzocchi et al., 2020). Potential microbial remediation of sulfidic fish farm sediments may thus be achieved with a combination of physical alterations to sediments, shorter production periods, and microbial fuel cells (if upscaling is feasible, Algar et al., 2020). The synergetic effect of these approaches may lead to more environmentally sustainable practices, with lower long-term adverse impacts, for this growing industry.

Data availability statement

The molecular data presented in this study are available in the NCBI under BioProject PRJNA 911159.

Author contributions

DV-C, SH-M, and FM conceptualized the study and in collaboration with LM, GH, TE, and TA were involved in funding acquisition. DV-C, SH-M, TT, GH, TE, and LM went to the field and collected all the samples. LM and DV-C performed the lab incubations and sediment-slurries. DV-C, SH-M, LH, and JSG obtained and processed all microbial and microsensor data. LM and TA performed the grain size, stable isotope, and organic matter analysis. DV-C performed all statistical analysis and wrote the manuscript with contributions from all co-authors. All authors approved the submitted version.

Funding

This research was possible thanks to the Aquaculture Environmental fund (Reykjavík, Iceland), the Research Foundation Flanders (grants 1275822N and G038819N), and the Netherlands Organization for Scientific Research (VICI grant 016.VICI.170.072).

Acknowledgments

We thank ICE Fish Farm for their logistical support during the sampling campaign at their facilities in Iceland. We also thank the NIOZ for their assistance with TOC and stable isotope analysis, Ben Abbas for his guidance in the lab, Marcel van den Broek and Sairah Malkin for sharing their knowledge on bioinformatics and microbial community analysis.

Conflict of interest

The authors declare that the research was conducted in the absence of any commercial or financial relationships that could be construed as a potential conflict of interest.

Publisher's note

Supplementary material

The Supplementary Material for this article can be found online at: https://www.frontiersin.org/articles/10.3389/fmicb.2022.1034401/full#supplementary-material

References

Algar, C. K., Howard, A., Ward, C., and Wanger, G. (2020). Sediment microbial fuel cells as a barrier to sulfide accumulation and their potential for sediment remediation beneath aquaculture pens. *Sci. Rep.* 10:13087. doi: 10.1038/s41598-020-70002-4

Anders, S., and Huber, W. (2010). Differential expression analysis for sequence count data. *Genome Biol.* 11:R106. doi: 10.1186/gb-2010-11-10-r106

Ape, F., Manini, E., Quero, G. M., Luna, G. M., Sarà, G., Vecchio, P., et al. (2019). Biostimulation of in situ microbial degradation processes in organically-enriched sediments mitigates the impact of aquaculture. *Chemosphere* 226, 715–725. doi: 10.1016/j.chemosphere.2019.03.178

Aranda, C. P., Valenzuela, C., Matamala, Y., Godoy, F. A., and Aranda, N. (2015). Sulphur-cycling bacteria and ciliated protozoans in a Beggiatoaceae mat covering organically enriched sediments beneath a salmon farm in a southern Chilean fjord. *Mar. Pollut. Bull.* 100, 270–278. doi: 10.1016/j.marpolbul.2015.08.040

Asami, H., Aida, M., and Watanabe, K. (2005). Accelerated sulfur cycle in coastal marine sediment beneath areas of intensive shellfish aquaculture. *Appl. Environ. Microbiol.* 71, 2925–2933. doi: 10.1128/AEM.71.6.2925-2933.2005

Ballester-Moltó, M., Sanchez-Jerez, P., Cerezo-Valverde, J., and Aguado-Giménez, F. (2017). Particulate waste outflow from fish-farming cages. How much is uneaten feed? *Mar. Pollut. Bull.* 119, 23–30. doi: 10.1016/j.marpolbul.2017.03.004

Bazylinski, D. A., Williams, T. J., Lefèvre, C. T., Trubitsyn, D., Fang, J., Beveridge, T. J., et al. (2013). *Magnetovibrio blakemorei* gen. nov., sp. nov., a magnetotactic bacterium (Alphaproteobacteria: Rhodospirillaceae) isolated from a salt marsh. *Int. J. Syst. Evol. Microbiol.* 63, 1824–1833. doi: 10.1099/ijs.0.044453-0

Bissett, A., Bowman, J., and Burke, C. (2006). Bacterial diversity in organically-enriched fish farm sediments. *FEMS Microbiol. Ecol.* 55, 48–56. doi: 10.1111/j.1574-6941.2005.00012.x

Bjerg, J. T., Boschker, H. T., Larsen, S., Berry, D., Millo, D., Tataru, P., et al. (2018). Long distance electron transport in individual cable bacteria. *Proc. Natl. Acad. Sci. U.S.A.* 115, 5786–5791.

Bjerg, J. T., Damgaard, L. R., Holm, S. A., Schramm, A., and Nielsen, L. P. (2016). Motility of electric cable bacteria. *Appl. Environ. Microbiol.* 82, 3816–3821. doi: 10.1128/AEM.01038-16

Bonaglia, S., Hedberg, J., Marzocchi, U., Iburg, S., Glud, R. N., and Nascimento, F. J. A. (2020). Meiofauna improve oxygenation and accelerate sulfide removal in the seasonally hypoxic seabed. *Mar. Environ. Res.* 159:104968. doi: 10.1016/j.marenvres.2020.104968

Boudreau, B. P. (1996). The diffusive tortuosity of fine-grained unlithified sediments. *Geochem. Cosmochim. Acta* 60, 3139–3142.

Burdorf, L. D. W., Hidalgo-Martinez, S., Cook, P. L. M., and Meysman, F. J. R. (2016). Long-distance electron transport by cable bacteria in mangrove sediments. *Mar. Ecol. Prog. Ser.* 545, 1–8. doi: 10.3354/meps11635

Burdorf, L. D. W., Malkin, S. Y., Bjerg, J. T., van Rijswijk, P., Criens, F., Tramper, A., et al. (2018). The effect of oxygen availability on long-distance electron transport in marine sediments. *Limnol. Oceanogr.* 63, 1799–1816. doi: 10.1002/lno.10809

Burdorf, L. D. W., Tramper, A., Seitaj, D., Meire, L., Hidalgo-Martinez, S., Zetsche, E. M., et al. (2017). Long-distance electron transport occurs globally in marine sediments. *Biogeosciences* 14, 683–701. doi: 10.5194/bg-14-683-2017

Callahan, B. J., McMurdie, P. J., Rosen, M. J., Han, A. W., Johnson, A. J. A., and Holmes, S. P. (2016). DADA2: High-resolution sample inference from Illumina amplicon data. *Nat. Methods* 13, 581–583. doi: 10.1038/nmeth.3869

Campbell, B. J., Engel, A. S., Porter, M. L., and Takai, K. (2006). The versatile ε-proteobacteria: Key players in sulphidic habitats. *Nat. Rev. Microbiol.* 4, 458–468. doi: 10.1038/nrmicro1414

Carroll, M. L., Cochrane, S., Fieler, R., Velvin, R., and White, P. (2003). Organic enrichment of sediments from salmon farming in Norway: Environmental factors, management practices, and monitoring techniques. *Aquaculture* 226, 165–180. doi: 10.1016/S0044-8486(03)00475-7

Choi, A., Cho, H., Kim, B., Kim, H. C., Jung, R. H., Lee, W. C., et al. (2018). Effects of finfish aquaculture on biogeochemistry and bacterial communities associated with sulfur cycles in highly sulfidic sediments. *Aquac. Environ. Interact.* 10, 413–427. doi: 10.3354/AEI00278

Clarke, K. (1993). Non-parametric multivariate analyses of changes in community structure. *Aust. J. Ecol.* 18, 117–143. doi: 10.1111/j.1442-9993.1993.tb00438.x

Cornelissen, R., Valcke, R., Boschker, H., Geelhoed, J. S., Damgaard, L. R., D'Haen, J., et al. (2018). The cell envelope structure of cable bacteria. *Front. Microbiol.* 9:3044. doi: 10.3389/fmicb.2018.03044

Dam, A. S., Marshall, I. P. G., Risgaard-Petersen, N., Burdorf, L. D. W., and Marzocchi, U. (2021). Effect of salinity on cable bacteria species composition and diversity. *Environ. Microbiol.* 23, 2605–2616. doi: 10.1111/1462-2920.15484

Dedieu, K., Rabouille, C., Gilbert, F., Soetaert, K., Metzger, E., Simonucci, C., et al. (2007). Coupling of carbon, nitrogen and oxygen cycles in sediments from a Mediterranean lagoon: A seasonal perspective. *Mar. Ecol. Prog. Ser.* 346, 45–59. doi: 10.3354/meps07031

Edgar, R. C. (2004). MUSCLE: Multiple sequence alignment with high accuracy and high throughput. *Nucleic Acids Res.* 32, 1792–1797. doi: 10.1093/nar/gkh340

FAO (2022). *The state of world fisheries and aquaculture (SOFIA)*. Rome: FAO. doi: 10.4060/cc0461en

Folk, R. L., and Ward, W. C. (1957). Brazos River bar (Texas): A study in the significance of grain size parameters. *J. Sediment. Res.* 27, 3–26. doi: 10.1306/74D70646-2B21-11D7-8648000102C1865D

Geelhoed, J. S., van de Velde, S. J., and Meysman, F. J. R. (2020). Quantification of cable bacteria in marine sediments via qPCR. *Front. Microbiol.* 11:1506. doi: 10.3389/fmicb.2020.01506

Geerlings, N. M. J., Geelhoed, J. S., Vasquez-Cardenas, D., Kienhuis, M. V. M., Hidalgo-Martinez, S., Boschker, H. T. S., et al. (2021). Cell cycle, filament growth and synchronized cell division in multicellular cable bacteria. *Front. Microbiol.* 12:620807. doi: 10.3389/fmicb.2021.620807

Geerlings, N. M. J., Karman, C., Trashin, S., As, K. S., Kienhuis, M. V. M., Hidalgo-Martinez, S., et al. (2020). Division of labor and growth during electrical cooperation in multicellular cable bacteria. *Proc. Natl. Acad. Sci. U.S.A.* 117, 5478–5485. doi: 10.1073/pnas.1916244117

Giles, H. (2008). Using Bayesian networks to examine consistent trends in fish farm benthic impact studies. *Aquaculture* 274, 181–195. doi: 10.1016/j.aquaculture.2007.11.020

Gram, L., Melchiorsen, J., Spanggaard, B., Huber, I., and Nielsen, T. F. (1999). Inhibition of *Vibrio anguillarum* by *Pseudomonas fluorescens* AH2, a possible probiotic treatment of fish. *Appl. Environ. Microbiol.* 65, 969–973. doi: 10.1128/aem.65.3.969-973.1999

Grigorakis, K., and Rigos, G. (2011). Aquaculture effects on environmental and public welfare–the case of mediterranean mariculture. *Chemosphere* 85, 899–919. doi: 10.1016/j.chemosphere.2011.07.015

Han, Y., and Perner, M. (2015). The globally widespread genus sulfurimonas: Versatile energy metabolisms and adaptations to redox clines. *Front. Microbiol.* 6:989. doi: 10.3389/fmicb.2015.00989

Hermans, M., Risgaard-Petersen, N., Meysman, F. J. R., and Slomp, C. P. (2020). Biogeochemical impact of cable bacteria on coastal Black Sea sediment. *Biogeosciences* 17, 5919–5938. doi: 10.5194/bg-17-5919-2020

Hofmann, A. F., Soetaert, K., Middelburg, J. J., and Meysman, F. J. R. (2010). AquaEnv : An aquatic acid–base modelling environment in R. *Aquat. Geochem.* 16, 507–546. doi: 10.1007/s10498-009-9084-1

Holmer, M., and Kristensen, E. (1996). *Seasonality of sulfate reduction and pore water solutes in a Marine fish farm sediment: The importance of temperature and sedimentary organic matter*. Amsterdam: Kluwer Academic Publishers. doi: 10.1007/BF00001530

Holmer, M., Marba, N., Diaz-Almela, E., Duarte, C. M., Tsapakis, M., and Danovaro, R. (2007). Sedimentation of organic matter from fish farms in oligotrophic Mediterranean assessed through bulk and stable isotope (δ13C and δ15N) analyses. *Aquaculture* 262, 268–280. doi: 10.1016/j.aquaculture.2006.09.033

Hornick, K. M., and Buschmann, A. H. (2018). Insights into the diversity and metabolic function of bacterial communities in sediments from Chilean salmon aquaculture sites. *Ann. Microbiol.* 68, 63–77. doi: 10.1007/s13213-017-1317-8

Huang, Y., Wang, B., Yang, Y., Yang, S., Dong, M., and Xu, M. (2022). Microbial carriers promote and guide pyrene migration in sediments. *J. Hazard. Mater.* 424:127188. doi: 10.1016/j.jhazmat.2021.127188

Karakassis, I., Tsapakis, M., Smith, C. J., and Rumohr, H. (2002). Fish farming impacts in the mediterranean studied through sediment profiling imagery. *Mar. Ecol. Prog. Ser.* 227, 125–133. doi: 10.3354/meps227125

Kawahara, N., Shigematsu, K., Miyadai, T., and Kondo, R. (2009). Comparison of bacterial communities in fish farm sediments along an organic enrichment gradient. *Aquaculture* 287, 107–113. doi: 10.1016/j.aquaculture.2008.10.003

Keeley, N. B., Forrest, B. M., Crawford, C., and MacLeod, C. K. (2012). Exploiting salmon farm benthic enrichment gradients to evaluate the regional performance of biotic indices and environmental indicators. *Ecol. Indic.* 23, 453–466. doi: 10.1016/j.ecolind.2012.04.028

Keeley, N. B., Macleod, C. K., Taylor, D., and Forrest, R. (2017). Comparison of three potential methods for accelerating seabed recovery beneath salmon farms. *Aquaculture* 479, 652–666. doi: 10.1016/j.aquaculture.2017.07.006

Kessler, A. J., Wawryk, M., Marzocchi, U., Roberts, K. L., Wong, W. W., Risgaard-Petersen, N., et al. (2019). Cable bacteria promote DNRA through iron sulfide dissolution. *Limnol. Oceanogr.* 64, 1228–1238. doi: 10.1002/lno.11110

Kjeldsen, K. U., Schreiber, L., Thorup, C. A., Boesen, T., Bjerg, J. T., Yang, T., et al. (2019). On the evolution and physiology of cable bacteria. *Proc. Natl. Acad. Sci. U.S.A.* 116, 19116–19125. doi: 10.1073/pnas.1903514116

Klier, J., Dellwig, O., Leipe, T., Jürgens, K., and Herlemann, D. P. R. (2018). Benthic bacterial community composition in the oligohaline-marine transition of surface sediments in the Baltic Sea based on rRNA analysis. *Front. Microbiol.* 9:236. doi: 10.3389/fmicb.2018.00236

Kojima, H., Watanabe, M., and Fukui, M. (2017). *Sulfurivermis fontis* gen. Nov., sp. nov., a sulfur-oxidizing autotroph, and proposal of Thioprofundaceae fam. nov. *Int. J. Syst. Evol. Microbiol.* 67, 3458–3461. doi: 10.1099/ijsem.0.002137

Kolda, A., Gavrilović, A., Jug-Dujaković, J., Ljubešić, Z., El-Matbouli, M., Lillehaug, A., et al. (2020). Profiling of bacterial assemblages in the marine cage farm environment, with implications on fish, human and ecosystem health. *Ecol. Indic.* 118:106785. doi: 10.1016/j.ecolind.2020.106785

Kunihiro, T., Takasu, H., Miyazaki, T., Uramoto, Y., Kinoshita, K., Yodnarasri, S., et al. (2011). Increase in Alphaproteobacteria in association with a polychaete, *Capitella* sp. I, in the organically enriched sediment. *ISME J.* 5, 1818–1831. doi: 10.1038/ismej.2011.57

Kürten, B., Painting, S. J., Struck, U., Polunin, N. V. C., and Middelburg, J. J. (2013). Tracking seasonal changes in North Sea zooplankton trophic dynamics using stable isotopes. *Biogeochemistry* 113, 167–187. doi: 10.1007/s10533-011-9630-y

la Rosa, T., Mirto, S., Mazzola, A., and Danovaro, R. (2001). Differential responses of benthic microbes and meiofauna to fish-farm disturbance in coastal sediments. *Environ. Pollut.* 112, 427–434. doi: 10.1016/S0269-7491(00)00141-X

Lavik, G., Stührmann, T., Brüchert, V., van der Plas, A., Mohrholz, V., Lam, P., et al. (2009). Detoxification of sulphidic African shelf waters by blooming chemolithotrophs. *Nature* 457, 581–584. doi: 10.1038/nature07588

Li, C., Reimers, C., and Alleau, Y. (2020). Inducing the attachment of cable bacteria on oxidizing electrodes. *Biogeosciences* 17, 597–607. doi: 10.5194/bg-17-597-2020

Liau, P., Kim, C., Saxton, M. A., and Malkin, S. Y. (2022). Microbial succession in a Marine sediment: Inferring interspecific microbial interactions with marine cable bacteria. *Environ. Microbiol.* 1–17. doi: 10.1111/1462-2920.16230

Lipsewers, Y. A., Vasquez-Cardenas, D., Seitaj, D., Schauer, R., Sinninghe Damsté, J. S., Meysman, F. J. R., et al. (2017). Impact of seasonal hypoxia on activity and community structure of chemolithoautotrophic bacteria in a coastal sediment. *Appl. Environ. Microbiol.* 83, e03517–16. doi: 10.1128/AEM.03517-16

Liu, F., Wang, Z., Wu, B., Bjerg, J. T., Hu, W., Guo, X., et al. (2021). Cable bacteria extend the impacts of elevated dissolved oxygen into anoxic sediments. *ISME J.* 15, 1551–1563. doi: 10.1038/s41396-020-00869-8

Liu, Y., Rzeszutek, E., van der Voort, M., Wu, C. H., Thoen, E., Skaar, I., et al. (2015). Diversity of aquatic *Pseudomonas* species and their activity against the fish pathogenic oomycete *Saprolegnia*. *PLoS One* 10:e0136241. doi: 10.1371/journal.pone.0136241

Love, M. I., Huber, W., and Anders, S. (2014). Moderated estimation of fold change and dispersion for RNA-seq data with DESeq2. *Genome Biol.* 15:550. doi: 10.1186/s13059-014-0550-8

Lücker, S., Steger, D., Kjeldsen, K. U., MacGregor, B. J., Wagner, M., and Loy, A. (2007). Improved 16S rRNA-targeted probe set for analysis of sulfate-reducing bacteria by fluorescence in situ hybridization. *J. Microbiol. Methods* 69, 523–528. doi: 10.1016/j.mimet.2007.02.009

Macalady, J. L., Dattagupta, S., Schaperdoth, I., Jones, D. S., Druschel, G. K., and Eastman, D. (2008). Niche differentiation among sulfur-oxidizing bacterial populations in cave waters. *ISME J.* 2, 590–601. doi: 10.1038/ismej.2008.25

Maldonado, M., Carmona, M. C., Echeverría, Y., and Riesgo, A. (2005). The environmental impact of mediterranean cage fish farms at semi-exposed locations: Does it need a re-assessment? *Helgol. Mar. Res.* 59, 121–135. doi: 10.1007/s10152-004-0211-5

Malkin, S. Y., and Meysman, F. J. R. (2015). Rapid redox signal transmission by "cable bacteria" beneath a photosynthetic biofilm. *Appl. Environ. Microbiol.* 81, 948–956. doi: 10.1128/AEM.02682-14

Malkin, S. Y., Liau, P., Kim, C., Hantsoo, K. G., Gomes, M. L., and Song, B. (2022). Contrasting controls on seasonal and spatial distribution of marine cable bacteria (*Candidatus* Electrothrix) and Beggiatoaceae in seasonally hypoxic Chesapeake Bay. *Limnol. Oceanogr.* 67, 1357–1373. doi: 10.1002/lno.12087

Malkin, S. Y., Rao, A. M., Seitaj, D., Vasquez-Cardenas, D., Zetsche, E.-M., Hidalgo-Martinez, S., et al. (2014). Natural occurrence of microbial sulphur oxidation by long-range electron transport in the seafloor. *ISME J.* 8, 1843–1854. doi: 10.1038/ismej.2014.41

Malkin, S. Y., Seitaj, D., Burdorf, L. D. W., Nieuwhof, S., Hidalgo-Martinez, S., Tramper, A., et al. (2017). Electrogenic sulfur oxidation by cable bacteria in bivalve reef sediments. *Front. Mar. Sci.* 4:28. doi: 10.3389/FMARS.2017.00028

Martin, B. C., Bougoure, J., Ryan, M. H., Bennett, W. W., Colmer, T. D., Joyce, N. K., et al. (2018). Oxygen loss from seagrass roots coincides with colonisation of sulphide-oxidising cable bacteria and reduces sulphide stress. *ISME J.* 13, 707–719. doi: 10.1038/s41396-018-0308-5

Martins, P., Coelho, F. J. R. C., Cleary, D. F. R., Pires, A. C. C., Marques, B., Rodrigues, A. M., et al. (2018). Seasonal patterns of bacterioplankton composition in a semi-intensive European seabass (*Dicentrarchus labrax*) aquaculture system. *Aquaculture* 490, 240–250. doi: 10.1016/j.aquaculture.2018.02.038

Marzocchi, U., Bonaglia, S., van de Velde, S., Hall, P. O. J., Schramm, A., Risgaard-Petersen, N., et al. (2018). Transient bottom water oxygenation creates a niche for cable bacteria in long-term anoxic sediments of the Eastern Gotland basin. *Environ. Microbiol.* 20, 3031–3041. doi: 10.1111/1462-2920.14349

Marzocchi, U., Palma, E., Rossetti, S., Aulenta, F., and Scoma, A. (2020). Parallel artificial and biological electric circuits power petroleum decontamination: The case of snorkel and cable bacteria. *Water Res.* 173:115520. doi: 10.1016/j.watres.2020.115520

McCaig, A. E., Phillips, C. J., Stephen, J. R., Kowalchuk, G. A., Harvey, S. M., Herbert, R. A., et al. (1999). Nitrogen cycling and community structure of Proteobacterial-subgroup ammonia-oxidizing bacteria within polluted marine fish farm sediments. *Appl. Environ. Microbiol.* 65, 213–220. doi: 10.1128/aem.65.1.213-220.1999

McGhie, T. K., Crawford, C. M., Mitchell, I. M., and O'Brien, D. (2000). The degradation of fish-cage waste in sediments during fallowing. *Aquaculture* 187, 351–366. doi: 10.1016/S0044-8486(00)00317-3

Meier, D. V., Pjevac, P., Bach, W., Hourdez, S., Girguis, P. R., Vidoudez, C., et al. (2017). Niche partitioning of diverse sulfur-oxidizing bacteria at hydrothermal vents. *ISME J.* 11, 1545–1558. doi: 10.1038/ismej.2017.37

Meysman, F. J. R. (2018). Cable bacteria take a new breath using long-distance electricity. *Trends Microbiol.* 26, 411–422. doi: 10.1016/j.tim.2017.10.011

Meysman, F. J. R., Cornelissen, R., Trashin, S., Bonné, R., Hidalgo-Martinez, S., van der Veen, J., et al. (2019). A highly conductive fibre network enables centimetre-scale electron transport in multicellular cable bacteria. *Nat. Commun.* 10:4120. doi: 10.1038/s41467-019-12115-7

Meysman, F. J. R., Risgaard-Petersen, N., Malkin, S. Y., and Nielsen, L. P. (2015). The geochemical fingerprint of microbial long-distance electron transport in the seafloor. *Geochim. Cosmochim. Acta* 152, 122–142. doi: 10.1016/j.gca.2014.12.014

Minh, B. Q., Schmidt, H. A., Chernomor, O., Schrempf, D., Woodhams, M. D., von Haeseler, A., et al. (2020). IQ-TREE 2: New models and efficient methods for phylogenetic inference in the genomic era. *Mol. Biol. Evol.* 37, 1530–1534. doi: 10.1093/molbev/msaa015

Miranda, R. M., Aguila-torres, P., Maldonado, J., Casado, A., and Aranda, C. P. (2020). Taxonomy and diversity of bacterial communities associated with marine sediments from Chilean salmonid farms. *Aquac. Res.* 52, 1605–1620. doi: 10.1111/are.15014

Møretrø, T., Moen, B., Heir, E., Hansen, A., and Langsrud, S. (2016). Contamination of salmon fillets and processing plants with spoilage bacteria. *Int. J. Food Microbiol.* 237, 98–108. doi: 10.1016/j.ijfoodmicro.2016.08.016

Müller, H., Bosch, J., Griebler, C., Damgaard, L. R., Nielsen, L. P., Lueders, T., et al. (2016). Long-distance electron transfer by cable bacteria in aquifer sediments. *ISME J.* 10, 2010–2019. doi: 10.1038/ismej.2015.250

Mulsow, S., Krieger, Y., and Kennedy, R. (2006). Sediment profile imaging (SPI) and micro-electrode technologies in impact assessment studies: Example from two fjords in southern Chile used for fish farming. *J. Mar. Syst.* 62, 152–163. doi: 10.1016/j.jmarsys.2005.09.012

Mußmann, M., Ishii, K., Rabus, R., and Amann, R. (2005). Diversity and vertical distribution of cultured and uncultured Deltaproteobacteria in an intertidal mud flat of the Wadden Sea. *Environ. Microbiol.* 7, 405–418. doi: 10.1111/j.1462-2920.2005.00708.x

Nielsen, L. P., and Risgaard-Petersen, N. (2015). Rethinking sediment biogeochemistry after the discovery of electric currents. *Ann. Rev. Mar. Sci.* 7, 425–442. doi: 10.1146/annurev-marine-010814-015708

Nielsen, L. P., Risgaard-Petersen, N., Fossing, H., Christensen, P. B., and Sayama, M. (2010). Electric currents couple spatially separated biogeochemical processes in marine sediment. *Nature* 463, 1071–1074. doi: 10.1038/nature08790

Ormerod, K. L., Wood, D. L. A., Lachner, N., Gellatly, S. L., Daly, J. N., Parsons, J. D., et al. (2016). Genomic characterization of the uncultured Bacteroidales family S24-7 inhabiting the guts of homeothermic animals. *Microbiome* 4:30. doi: 10.1186/s40168-016-0181-2

Otte, J. M., Harter, J., Laufer, K., Blackwell, N., Straub, D., Kappler, A., et al. (2018). The distribution of active iron-cycling bacteria in marine and freshwater sediments is decoupled from geochemical gradients. *Environ. Microbiol.* 20, 2483–2499. doi: 10.1111/1462-2920.14260

Park, S.-J., Pham, V. H., Jung, M.-Y., Kim, S.-J., Kim, J.-G., Roh, D.-H., et al. (2011). *Thioalbus denitrificans* gen. nov., sp. nov., a chemolithoautotrophic sulfur-oxidizing gammaproteobacterium, isolated from marine sediment. *Int. J. Syst. Evol. Microbiol.* 61, 2045–2051. doi: 10.1099/ijs.0.024844-0

Pearson, T., and Rosenberg, R. (1978). Macrobenthic succession in relation to organic enrichment and pollution of the marine environment. *Oceanogr. Mar. Biol. Ann. Rev.* 16, 229–311.

Pereira, P. M. F., Black, K. D., McLusky, D. S., and Nickell, T. D. (2004). Recovery of sediments after cessation of marine fish farm production. *Aquaculture* 235, 315–330. doi: 10.1016/j.aquaculture.2003.12.023

Pfeffer, C., Larsen, S., Song, J., Dong, M., Besenbacher, F., Meyer, R. L., et al. (2012). Filamentous bacteria transport electrons over centimetre distances. *Nature* 491, 218–221. doi: 10.1038/nature11586

Piedecausa, M. A., Aguado-Giménez, F., Cerezo Valverde, J., Hernández Llorente, M. D., and García-García, B. (2012). Influence of fish food and faecal pellets on short-term oxygen uptake, ammonium flux and acid volatile sulphide accumulation in sediments impacted by fish farming and non-impacted sediments. *Aquac. Res.* 43, 66–74. doi: 10.1111/j.1365-2109.2011.02801.x

Pjevac, P., Meier, D. V., Markert, S., Hentschker, C., Schweder, T., Becher, D., et al. (2018). Metaproteogenomic profiling of microbial communities colonizing actively venting hydrothermal chimneys. *Front. Microbiol.* 9:680. doi: 10.3389/fmicb.2018.00680

Quast, C., Pruesse, E., Yilmaz, P., Gerken, J., Schweer, T., Yarza, P., et al. (2013). The SILVA ribosomal RNA gene database project: Improved data processing and web-based tools. *Nucleic Acids Res.* 41, D590–D596. doi: 10.1093/nar/gks1219

Quero, G. M., Ape, F., Manini, E., Mirto, S., and Luna, G. M. (2020). Temporal changes in microbial communities beneath fish farm sediments are related to organic enrichment and fish biomass over a production cycle. *Front. Mar. Sci.* 7:524. doi: 10.3389/fmars.2020.00524

Quiñones, R. A., Fuentes, M., Montes, R. M., Soto, D., and León-Muñoz, J. (2019). Environmental issues in Chilean salmon farming: A review. *Rev. Aquac.* 11, 375–402. doi: 10.1111/raq.12337

Rao, A. M. F., Malkin, S. Y., Montserrat, F., and Meysman, F. J. R. (2014). Alkalinity production in intertidal sands intensified by lugworm bioirrigation. *Estuar. Coast. Shelf Sci.* 148, 36–47. doi: 10.1016/j.ecss.2014.06.006

Reimers, C. E., Li, C., Graw, M. F., Schrader, P. S., and Wolf, M. (2017). The identification of cable bacteria attached to the anode of a benthic microbial fuel cell: Evidence of long distance extracellular electron transport to electrodes. *Front. Microbiol.* 8:2055. doi: 10.3389/fmicb.2017.02055

Risgaard-Petersen, N., Revil, A., Meister, P., and Nielsen, L. P. (2012). Sulfur, iron-, and calcium cycling associated with natural electric currents running through marine sediment. *Geochim.* 92, 1–13. doi: 10.1016/j.gca.2012.05.036

Sandfeld, T., Marzocchi, U., Petro, C., Schramm, A., and Risgaard-Petersen, N. (2020). Electrogenic sulfide oxidation mediated by cable bacteria stimulates sulfate reduction in freshwater sediments. *ISME J.* 14, 1233–1246. doi: 10.1038/s41396-020-0607-5

Schauer, R., Risgaard-Petersen, N., Kjeldsen, K. U., Tataru Bjerg, J. J., Jørgensen, B. B., Schramm, A., et al. (2014). Succession of cable bacteria and electric currents in marine sediment. *ISME J.* 8, 1314–1322. doi: 10.1038/ismej.2013.239

Scilipoti, S., Koren, K., Risgaard-Petersen, N., Schramm, A., and Nielsen, L. P. (2021). Oxygen consumption of individual cable bacteria. *Sci. Adv.* 7:eabe1870. doi: 10.1126/sciadv.abe1870

Seitaj, D., Schauer, R., Sulu-Gambari, F., Hidalgo-Martinez, S., Malkin, S. Y., Laurine, D. W., et al. (2015). Cable bacteria in the sediments of seasonally-hypoxic basins : A microbial "firewall" against euxinia. *Proc. Natl. Acad. Sci. U.S.A.* 43, 13278–13283. doi: 10.1073/pnas.1510152112

Shakeri Yekta, S., Liu, T., Axelsson Bjerg, M., Šafarič, L., Karlsson, A., Björn, A., et al. (2019). Sulfide level in municipal sludge digesters affects microbial community response to long-chain fatty acid loads. *Biotechnol. Biofuels* 12:259. doi: 10.1186/s13068-019-1598-1

Soetaert, K., Petzoldt, T., and Meysman, F. J. R. (2014). *marelac: Tools for aquatic sciences R package v2.1.3*.

Sorokin, D. Y., Tourova, T. P., Kolganova, T. V., Sjollema, K. A., and Kuenen, J. G. (2002). *Thioalkalispira microaerophila* gen. nov., sp. nov., a novel lithoautotrophic, sulfur-oxidizing bacterium from a soda lake. *Int. J. Syst. Evol. Microbiol.* 52, 2175–2182. doi: 10.1099/ijs.0.02339-0

Takahashi, S., Tomita, J., Nishioka, K., Hisada, T., and Nishijima, M. (2014). Development of a prokaryotic universal primer for simultaneous analysis of Bacteria and Archaea using next-generation sequencing. *PLoS One* 9:e105592. doi: 10.1371/journal.pone.0105592

Takai, K., Suzuki, M., Nakagawa, S., Miyazaki, M., Suzuki, Y., Inagaki, F., et al. (2006). *Sulfurimonas paralvinellae* sp. nov., a novel mesophilic, hydrogen- and sulfur-oxidizing chemolithoautotroph within the Epsilonproteobacteria isolated from a deep-sea hydrothermal vent polychaete nest, reclassification of *Thiomicrospira denitrificans* as Su. *Int. J. Syst. Evol. Microbiol.* 56, 1725–1733. doi: 10.1099/ijs.0.64255-0

Trojan, D., Schreiber, L., Bjerg, J. T., Bøggild, A., Yang, T., Kjeldsen, K. U., et al. (2016). A taxonomic framework for cable bacteria and proposal of the candidate genera Electrothrix and Electronema. *Syst. Appl. Microbiol.* 39, 297–306. doi: 10.1016/j.syapm.2016.05.006

Valdemarsen, T., Quintana, C., Kristensen, E., and Flindt, M. (2014). Recovery of organic-enriched sediments through microbial degradation: Implications for eutrophic estuaries. *Mar. Ecol. Prog. Ser.* 503, 41–58. doi: 10.3354/meps10747

van de Velde, S., Lesven, L., Burdorf, L. D. W., Hidalgo-Martinez, S., Geelhoed, J. S., van Rijswijk, P., et al. (2016). The impact of electrogenic sulfur oxidation on the biogeochemistry of coastal sediments: A field study. *Geochim. Cosmochim. Acta* 194, 211–232. doi: 10.1016/j.gca.2016.08.038

Vasquez-Cardenas, D., van de Vossenberg, J., Polerecky, L., Malkin, S. Y., Schauer, R., Hidalgo-Martinez, S., et al. (2015). Microbial carbon metabolism associated with electrogenic sulphur oxidation in coastal sediments. *ISME J.* 9, 1966–1978. doi: 10.1038/ismej.2015.10

Verhoeven, J. T. P., Salvo, F., Knight, R., Hamoutene, D., and Dufour, S. C. (2018). Temporal bacterial surveillance of salmon aquaculture sites indicates a long lasting benthic impact with minimal recovery. *Front. Microbiol.* 9:3054. doi: 10.3389/fmicb.2018.03054

Wasmund, K., Mußmann, M., and Loy, A. (2017). The life sulfuric: Microbial ecology of sulfur cycling in marine sediments. *Environ. Microbiol. Rep.* 9, 323–344. doi: 10.1111/1758-2229.12538

Wexler, H. M. (2007). *Bacteroides*: The good, the bad, and the nitty-gritty. *Clin. Microbiol. Rev.* 20, 593–621. doi: 10.1128/CMR.00008-07

Williams, T. J., Lefèvre, C. T., Zhao, W., Beveridge, T. J., and Bazylinski, D. A. (2012). *Magnetospira thiophila* gen. nov., sp. nov., a marine magnetotactic bacterium that represents a novel lineage within the Rhodospirillaceae (Alphaproteobacteria). *Int. J. Syst. Evol. Microbiol.* 62, 2443–2450. doi: 10.1099/ijs.0.037697-0

Xia, J., Ye, L., Ren, H., and Zhang, X. X. (2018). Microbial community structure and function in aerobic granular sludge. *Appl. Microbiol. Biotechnol.* 102, 3967–3979. doi: 10.1007/s00253-018-8905-9

Yarza, P., Yilmaz, P., Pruesse, E., Glöckner, F. O., Ludwig, W., Schleifer, K. H., et al. (2014). Uniting the classification of cultured and uncultured bacteria and archaea using 16S rRNA gene sequences. *Nat. Rev. Microbiol.* 12, 635–645. doi: 10.1038/nrmicro3330

Zhou, J., Bruns, M. A. N. N., and Tiedje, J. M. (1996). DNA recovery from soils of diverse composition. *Appl. Environ. Microbiol.* 62, 316–322. doi: 10.1128/aem.62.2.316-322.1996

frontiers | Frontiers in Microbiology

TYPE Original Research
PUBLISHED 23 February 2023
DOI 10.3389/fmicb.2023.1008293

OPEN ACCESS

EDITED BY
Amelia-Elena Rotaru,
University of Southern Denmark,
Denmark

REVIEWED BY
Adam J. Kessler,
School of Earth, Atmosphere and
Environment, Monash University,
Australia
Yamini Jangir,
California Institute of Technology,
United States

*CORRESPONDENCE
Jamie J. M. Lustermans
✉ jamie.lustermans@gmail.com

SPECIALTY SECTION
This article was submitted to
Microbiological Chemistry and
Geomicrobiology,
a section of the journal
Frontiers in Microbiology

RECEIVED 31 July 2022
ACCEPTED 06 February 2023
PUBLISHED 23 February 2023

CITATION
Lustermans JJM, Bjerg JJ, Burdorf LDW,
Nielsen LP, Schramm A and Marshall IPG (2023)
Persistent flocks of diverse motile bacteria in
long-term incubations of electron-conducting
cable bacteria, *Candidatus* Electronema
aureum.
Front. Microbiol. 14:1008293.
doi: 10.3389/fmicb.2023.1008293

Persistent flocks of diverse motile bacteria in long-term incubations of electron-conducting cable bacteria, *Candidatus* Electronema aureum

Jamie J. M. Lustermans[1]*, Jesper J. Bjerg[1,2],
Laurine D. W. Burdorf[1,2], Lars Peter Nielsen[1], Andreas Schramm[1]
and Ian P. G. Marshall[1]

[1]Section for Microbiology, Department of Biology, Center for Electromicrobiology, Aarhus University, Aarhus, Denmark, [2]Department of Biology, Microbial Systems Technology Excellence Centre, University of Antwerp, Wilrijk, Belgium

Cable bacteria are centimeters-long filamentous bacteria that oxidize sulfide in anoxic sediment layers and reduce oxygen at the oxic-anoxic interface, connecting these reactions *via* electron transport. The ubiquitous cable bacteria have a major impact on sediment geochemistry and microbial communities. This includes diverse bacteria swimming around cable bacteria as dense flocks in the anoxic zone, where the cable bacteria act as chemotactic attractant. We hypothesized that flocking only appears when cable bacteria are highly abundant and active. We set out to discern the timing and drivers of flocking over 81days in an enrichment culture of the freshwater cable bacterium *Candidatus* Electronema aureum GS by measuring sediment microprofiles of pH, oxygen, and electric potential as a proxy of cable bacteria activity. Cable bacterial relative abundance was quantified by 16S rRNA amplicon sequencing, and microscopy observations to determine presence of flocking. Flocking was always observed at some cable bacteria, irrespective of overall cable bacteria rRNA abundance, activity, or sediment pH. Diverse cell morphologies of flockers were observed, suggesting that flocking is not restricted to a specific, single bacterial associate. This, coupled with their consistent presence supports a common mechanism of interaction, likely interspecies electron transfer *via* electron shuttles. Flocking appears exclusively linked to the electron conducting activity of the individual cable bacteria.

KEYWORDS

flocking, cable bacteria, electron conduction, succession, interspecies electron transfer, time series, microprofiles

1. Introduction

Cable bacteria are multi-cellular filaments that can become several centimeters in length and can be found globally in freshwater and marine sediments (Pfeffer et al., 2012; Risgaard-Petersen et al., 2015; Burdorf et al., 2017; Liu et al., 2021; Xu et al., 2021). Electrons are transported upwards through the filament and this results in their ability to physically separate the oxidation of sulfide in the deeper layers from oxygen respiration at the oxic zone.

Cable bacteria have a strong influence on sediment geochemistry including the formation of a gradually widening suboxic zone between the retreating oxygen penetration depth (OPD) and increasing sulfide appearance depth (SAD; Pfeffer et al., 2012; Risgaard-Petersen et al., 2012; Meysman et al., 2015; Liu et al., 2021). This is coupled with a distinctive pH peak, congruent with the cable bacteria's activity and their growth pattern, which is described by a lag phase that rapidly changes into an intense exponential phase and it ends in a trailing decline (Pfeffer et al., 2012; Schauer et al., 2014; Xu et al., 2021).

Besides geochemistry, the activity of cable bacteria has been shown to also influence associated microbial communities, such as iron-cycling bacteria and sulfur-oxidizing Epsilon-and Gammaproteobacteria in marine sediments (Vasquez-Cardenas et al., 2015; Otte et al., 2018). The sulfide oxidizers were found to be active below the oxic zone and were proposed to connect with the cable bacteria's electron transport through the oxidation of sulfide and subsequent transfer of the gained electrons to cable bacteria (Vasquez-Cardenas et al., 2015). Another example of association are flocking bacteria, which were discovered to swim around cable bacteria as a nimbus, in enrichments with the freshwater cable bacteria *Candidatus* Electronema aureum GS (Thorup et al., 2021; Bjerg et al., in press). These flocking bacteria, or flockers, displayed chemotactic behavior toward the cable bacteria, without clearly touching or attaching to the filaments (Bjerg et al., in press). The flockers were only observed around actively electron-conducting cable bacteria, and when the cable bacteria were physically cut (removing the cable bacterium's connection to oxygen and thus stopping electron conduction) the flockers dispersed (Bjerg et al., in press). The flocking bacteria are proposed to be aerobes, yet they were discovered in a hypoxic environment (suboxic/anoxic zone), where most high energy electron acceptors have been depleted (Bjerg et al., in press). The flockers are therefore hypothesized to donate electrons to the cable bacteria through interspecies electron transfer. Cable bacteria could be seen as an alternative electron acceptor (with a direct link to oxygen) for the flocking bacteria.

With this phenomenon's very recent discovery in mind, any study into it is exploratory in nature. Little is currently known about what causes flocking and whether it is related to cable bacteria succession, for example, does it show up at a particular phase of the lifetime of a cable bacteria enrichment, or is it lifetime-unrelated? So far, flocking has only been observed when cable bacteria were very abundant and active, suggesting that the interaction is a consequence of some limitation of cable bacterial growth. To test this hypothesis, we set out to elucidate the occurrence of flocking and its relationship to cable bacteria succession, activity, and geochemical changes. We combined microsensor measurements in sediment cores with sequencing, to describe the biogeochemical succession of a single strain enrichment of *Candidatus* Electronema aureum GS (Thorup et al., 2021), including their activity (inferred from an electric potential (EP) microsensor), changes in pH profile, and relative abundance of cable bacteria. This was compared to microscopy observations of flocking behavior around cable bacteria from the profiled cores, in two replicate time series (TS1 and TS2) each lasting 3 months to resolve how often flocking appears and to determine the amount of flockers and their morphology.

2. Materials and methods

2.1. Sediment preparation, inoculation, and incubation

Black freshwater sediment was retrieved, in June 2019 (TS1) and October 2020 (TS2), from a pond at Aarhus University campus (Vennelyst Park), Denmark (56.164672, 10.207908) at a water depth of 0.5–1 m. The sediment was stored with overlying water at 15°C for 2 weeks.

Before inoculation, sediment was homogenized, sieved (pore size: 0.5 mm) and autoclaved in 2 L bottles for 20 min as described in Thorup et al. (2021) and Marzocchi et al. (2022). Cooled down sediment (15°C) was distributed into 20 and 10 ethanol-cleaned Plexiglas core liners that were closed with a rubber stopper at the bottom. After 24 h settling time, the stoppers were pushed upwards to align the sediment surface with the core liner edge. The cores were inoculated by transferring a clump of sediment from a two-week-old, pre-grown single-strain enrichment culture of *Ca.* Electronema aureum GS (Thorup et al., 2021) and submerged in an aquarium with autoclaved tap water. The aquarium was covered with aluminum foil to prevent algae formation, equipped with aeration and a lid to prevent excessive evaporation, and kept at 15°C. Overlying water was replenished and refreshed several times during the incubation periods.

During the first time series (TS1), O_2, pH, and EP profiles were measured combined with 16S rRNA sequencing and microscopy observations over 80 days, due to technical issues, the videos could not be used for flocking observations. The sequencing and microscopy observations were repeated in the second time series (TS2) with O_2 and EP measurements over 81 days, and additionally the pH was measured on day 81. Following microsensor measurements (of both TS1 and TS2), 1–2 of the measured cores were sliced based on geochemical zone: the oxic layer (determined by the oxygen penetration depth) and the anoxic layer (below the oxygen penetration depth). Samples for light microscopy and 16S rRNA amplicon sequencing were taken from the anoxic layer of each core, of which the latter were frozen at −80°C until RNA extraction.

2.2. Microprofiling and analysis

At each time point, profiles were made of 1–3 randomly chosen core(s). Microprofiles were measured, with the aeration turned off, by moving in-house made O_2, pH and EP microsensors (Revsbech and Jørgensen, 1986; Revsbech, 1989; Damgaard et al., 2014) stepwise (100–500 μm) downwards from ~3,000 μm above the sediment–water interface (SWI) to a depth of ~35,000 μm using a motorized micromanipulator (Unisense A/S, Denmark). At each step there was a 2 s waiting time before measuring a value for 2 s. All profiles were acquired using a four-channel multimeter with built-in A/D converter (Unisense). For the EP and pH sensors an in-house made millivoltmeter (resistance $>10^{14}\,\Omega$,), and for the O_2 sensor a picoamperemeter (Unisense) that was digitized with a 16-bit A/D converter (ADC-216, Unisense), was used. The software SensorTrace PRO (Unisense) was used to control the micromanipulator and acquire measurements.

EP was used as a proxy for cable bacteria activity (Damgaard et al., 2014) and was measured downwards combined with an upwards profile. EP and pH profiles were measured against a general-purpose reference electrode (REF201 Radiometer Analytical, Denmark).

O_2 profiles were calibrated using Na-ascorbate in alkaline anoxic tap water and air-saturated (15°C) overlying water. The pH sensor was calibrated by a 3-point calibration (pH 4.0, 7.0, 10.0) with AVS TITRINORM buffers (VWR Chemicals, Denmark), and pH profiles were always measured in the dark. The reach of the anoxic zones was derived by determining the oxygen penetration depth from the O_2 measurements after the profiles were adjusted to the SWI. Two EP profiles (downwards and upwards) were made for each core, and were drift corrected, using the measurements from the overlying water and the time between the up and down profiles. Current densities were calculated per core and averaged per time point (1–3 profile pairs/cores), as showcased in Risgaard-Petersen et al. (2015), using a sediment conductivity of 0.04 $S\,m^{-1}$ (water conductivity of 0.05 $S\,m^{-1}$ and sediment porosity of 0.87).

The cathodic oxygen consumption (COC) of cable bacteria, which is the contribution of the cable bacterial cathodic cells to the total oxygen consumption performed in the sediment, and the (electric) current density ($mA\,m^{-2}$) in the sediment generated by the cable bacteria, used for this purpose were calculated as described in Risgaard-Petersen et al. (2015) from the EP and O_2 microsensor measurements of the exact cores that were subsequently sampled for flocking observations.

2.3. Cable bacteria rRNA sequencing

Samples from the anoxic zone, in duplicate when possible (at certain time points laboratory access time was limited due to COVID-19 prevention measures), underwent three freeze–thaw cycles increasing from 0.5 to 1.5 h. RNA was extracted using RNeasy Powersoil Total RNA kit (Qiagen), with DNase treatment (Turbo DNA-free kit, Ambion) and confirmation of RNA contents with Qubit (Thermo Fisher Scientific). Reverse transcription and PCR amplification of cDNA was performed with the OneStep RT-PCR kit according to instructions, RNase inhibitor or 5× Q-solution addition were not carried out (Qiagen), using primers Bac341F, Bac805R (Herlemann et al., 2011), 55°C annealing temperature and 30 PCR cycles. The 16S rRNA libraries were prepared according to the manual for 16S Metagenomic Sequencing Library Preparation (Illumina, United States), using AMPure XP Bead 0.8× and 1.12× (Beckman Coulter) for PCR clean-up. The 16S rRNA libraries were 2 × 300 bp paired-end sequenced on the Illumina MiSeq platform following the standard Illumina protocol for MiSeq reagent kit v3 (Illumina, United States).

Data processing started by removing low-read (<500) samples. Amplicon data was primer-trimmed with cutadapt (Martin, 2011). The DADA2 (Callahan et al., 2016) manual was followed with slight deviations; read dereplication after read clustering and read length filtering before chimera removal were added. Trimming was performed based on quality of the sequencing run and paired end merging was done with minimal overlap of 12 bp and 0 mismatch allowance. The Silva 138.1 database (Quast et al., 2012) was used for classification of the ASVs (amplicon sequence variants) to species level. Cable bacteria percentages of *Ca.* Electronema were extracted with Phyloseq (McMurdie and Holmes, 2013). 16S rRNA sequences from both time series experiments can be found under accession number PRJNA837365 in the Sequence Read Archive (SRA) at the NCBI.

Correspondence between the current density and relative abundance of cable bacterial 16S rRNA were determined by calculating the correlation coefficients for these two datasets with Pearson's correlation method in R, on the datasets from TS1 and TS2.

2.4. Microscopy of flocking bacteria and video analysis

During incubation, the population of cable bacteria and the presence of flocking bacteria was followed using phase contrast microscopy. For this, we used in-house made 'trench slides' as described in Thorup et al. (2021). The central trench of the microscopy slide was filled with sediment from the anoxic zone, and the slide was covered with anoxic tap water and a coverslip. In the second time series, the edge of each trench slide coverslip was covered with polydimethylsiloxane (PDMS) as a seal against evaporation and to minimize water movement. The trench slides were kept in an enclosed chamber with a moist paper cloth to prevent dehydration at 15°C for the first day and subsequently at room temperature. These trench slides were then observed for up to 4 days for the presence of flocking bacteria. Microscopy was performed at room temperature using a ZEISS Observer Z1 (Zeiss, Göttingen, Germany) inverted microscope equipped with a phase contrast lens and a PALM automated stage. Images and videos were taken at 100, 200, or 400× magnification, with the Zen Black edition software (Zeiss, Germany) over 1–8 h.

To assess the presence of flocking bacteria, 5 trench slides were prepared per time point during TS2 and observed intermittently over a period of 4 days. Flocking behavior is hard to discern the first day after preparing a trench slide, because gradients of oxygen, sulfide need to establish, so that the cable bacteria can align themselves from sulfidic to oxic zone, and the two zones need to be delineated by a microaerophilic veil (Scilipoti et al., 2021; Bjerg et al., in press). Presence of flocking was therefore, with a few exceptions (days 2, 27, and 32), assessed on the second and fourth day of the trench slides incubation.

Bjerg et al. (in press), clearly describe that the flocking behavior of bacteria occurs around on the anoxic side of the microaerophilic veil of the free-laying cable bacteria spanning the oxic and anoxic zone on trench slides (Supplementary Figure S1). However, sometimes the presence of multiple cable bacteria hinders visual inspection of the flocking behaviors, although a haze of bacteria is often seen (Supplementary Figure S1). The presence of higher bacterial abundance (>100) around a cable bacteria can overcome this shortcoming. Based on the aforementioned previous observations, the following set of criteria was defined to confirm the presence of bacterial flocking behavior: (1) the presence of free-laying cable bacteria spanning from the oxic zone to the anoxic zone, and (2) high bacterial count around the cable bacteria (>100; Supplementary Figure S1). The detection of the phenomenon is therefore a conservative estimate of its prevalence, especially at time points where cable bacteria density on the slides was high. Each slide was inspected by following the microaerophilic veil clockwise around the slide. The microaerophilic veil was discerned by its high visibility as a dense collection of chemotactic bacteria that represent a quivering line of fast swimming bacteria that follow their preferred oxygen concentrations and the shape of the trench slide. A slide would only be marked as having flocking present if any cable bacteria fit both abovementioned criteria.

Videos for counting and morphology were recorded with frames 88 milliseconds apart. Only videos of sufficient quality, length, with a single cable bacterium present, and without major sediment particles, were used for subsequent analysis in FIJI (Schindelin et al., 2012). Videos were processed by removing the median pixel value from each pixel, in essence removing any parts of the video which were not moving. Morphology was assessed by eye, while length and width were measured using the line tool (FIJI). Counts were done by selecting a random 50 µm segment along the length of the cable bacteria filaments and counting all moving bacteria within 50 µm from the cable bacteria filament, i.e., all moving bacteria in a 100 × 50 µm box. For morphology counts, 5 categories were used: spirillum (short spirals with at least one full turn of the helix, and no more than 6), coccus (ovoids, almost as wide as long), spirochaete (at least 20 µm long, and more than 6 helical turns), rod (predominantly large, curved rods at least 4 µm long), and vibrioid (small curved rods with a tapered end), however these cells were mostly below 0.8 µm wide and 1.5 µm long, and the shape was often difficult to make out. As a result, the vibrioid category encompasses any very small bacteria (≤1 × 1.5 µm). Morphology counts were normalized against cable bacteria cells for each video and averaged per time point.

3. Results

3.1. Geochemical development in freshwater sediment

The two time series incubations (TS1, TS2) proved to be comparable in their geochemical developments (Supplementary Figure S2). Differences in the current density (activity), generated by the cable bacteria, between the two time series are visible. Yet, the in-and decreases in cable bacteria activity followed the same trend (Figure 1A; Supplementary Figure S2). The trend described low cable bacteria activity at the start (days 3–11), with no current on day 3 for TS1. From day 6 on, the activity increased to reach the highest current density (79 mA m^{-2}) on day 22, then it appears to vary a little (days 26–40) before it slowly declines to zero (day 81; Figure 1A).

The cathodic consumption of oxygen (COC) by cable bacteria started low with ~5% (day 2) and increased to ~75.5% (day 17), followed by a dip toward 32%–26% and another increase to 65% (day 40), only to decrease to a trailing 14%–28% toward the end of the experiment (Figure 1C).

The OPD varied during the 81 days from ~1.5 ± 0.2 mm at the start, where after it decreased to ~0.5 ± 0.15 mm on day 33 (data not shown), only to deepen again at the end to ~3 mm (Figure 1D). The depth of the cable bacteria activity based on the EP, increased from 1 mm (day 6) to 6 mm (day 17), and further increased to a maximum depth of 10–13 mm (day 33; data not shown), before retreating to 7 mm (day 46), ending in non-detectable EP (day 81; Figure 1D). The cable bacteria-created pH peak and minimum were not visible until day 11 and were strongest between day 17 and 33 (9 and 5.5), while the acidity mellowed out at the end, the pH peak increased again to around 8 (Figures 1D, 2A).

3.2. Cable bacteria relative abundance

A trend similar to that of the activity and geochemistry development was present in the relative abundance of the 16S rRNA specifically for *Ca.* Electronema aureum GS (Figure 1B). Cable bacteria relative abundance started with a near-zero lag phase (day 2–6) followed by a strong incline until they reached 49 and 37% (TS1, TS2) of the sequenced 16S rRNA as the highest relative abundances (TS1: day 33, TS2: day 27). The relative abundance of cable bacteria declined very slowly to 13% (day 81), but never reached zero within this timeframe (Figure 1B). At every sampled time point, cable bacteria rRNA was present (Figure 1B). This corresponded with microscopy observations of moving, living, cable bacteria filaments at each time point in both time series experiments (Supplementary Figure S3). Clear differences between amounts of actively moving (and therefore presumed to be living) cable bacteria were seen during microscopy observations (Supplementary Figure S3).

3.3. Flocker occurrence and morphology

At every time point, except for day 33 and 56, flocking was observed during one or more of the 4 observation days, and most often on days 17, 22 and 40 (Figure 2B). The number of flocking cells per cable bacteria cell varied between observations of individual flocking occurrences, but also between time points from ~1–2.2 at the lowest (days 2 and 22), to ~6.8 (day 12), with the highest counts observed as ~12.6 and ~16 (day 81 and 27; Figure 2C). Besides occurrence and number of cells, we derived cell shape, width, and length from the microscopy observations. Five different cell morphologies were identified: rods, cocci, vibrioids, spirochaetes, and spirillae (Figure 3). Vibrioids appeared at every time point that had flocking and were the most abundant flocker morphology (0.08–6.7 cells/cable cell) at all observations except for day 2, when rods were most prominent (Figure 4). Rod shaped flockers were the second most abundant type (0.22–0.07 cells/cable cell) and were observed at every time point except for day 81 (Figure 4). Rod-shaped flockers also appear to decrease in amount over time from being the most observed morphology on day 2 to day 81, where the rod-shaped flockers were absent (Figure 4). Cocci only appeared on days 16 and 40. On the second day, 0.55 coccus-shaped flockers were observed per cable cell (Figure 4). The other morphologies were very rare or restricted to few time points (Figure 4). Cell sizes of the flocking bacteria ranged from tiny (~0.5 × 1.6 µm) to large cells (~1.4 × 6.1 µm; Supplementary Figure S4).

4. Discussion

4.1. Freshwater cable bacteria development

The geochemical development in our *Ca.* Electronema aureum GS enrichment is generally comparable to what was previously seen in cable bacteria succession experiments: a decrease in OPD, a pH peak at the near-surface and a pH minimum in the anoxic zone indicative of cable bacteria activity (Figures 1D, 2A,B; Schauer et al., 2014; Xu et al., 2021). This activity corresponded to the changes in cable bacteria density (Figure 1B; Supplementary Figure S2). The formation of a pH peak indicated rapid sulfide oxidation, resulting in more

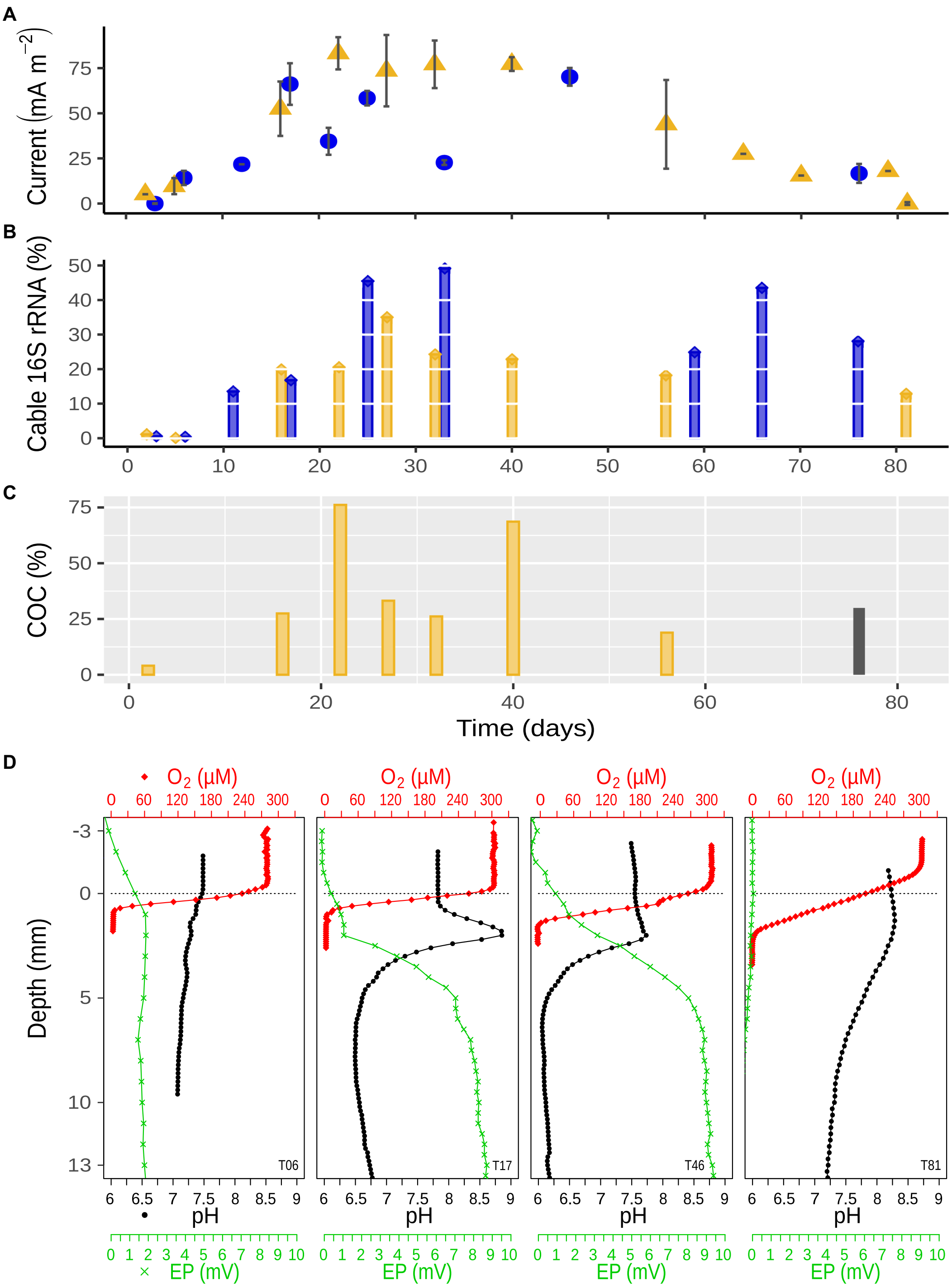

FIGURE 1
(A) Cable bacteria activity over 81 days of incubation displayed in current density (mean±SD, *n*=1–3 pairs of up and down microprofiles) between sediment surface and maximum EP within the sediment; blue circles, first time series (TS1); yellow triangles, second time series (TS2). **(B)** Relative abundance of cable bacteria 16S rRNA in anoxic zone over time; blue, first time series (TS1); yellow, second time series (TS2). **(C)** Cathodic oxygen consumption (COC) of cable bacteria over time calculated from the cores sampled for microscopy during TS2 (yellow); gray, calculated from TS1. **(D)** Examples of depth profiles of oxygen (red diamonds), pH (black dots), and EP (green crosses) at day 6, 17, 46 (TS1), and 81 (TS2). The dotted gray line indicates the sediment surface.

electrons to transport evident in the concurrent increase in current density, which eventually pushes the OPD toward the surface (Supplementary Figures 1B,D). The succession pattern of *Ca.* Electronema aureum GS rRNA showed an increase, then a long stable phase, followed by a decline, though this decline is slower than seen in other studies (Schauer et al., 2014; Xu et al., 2021). At every sampling point, cable bacteria were observed both in relative abundance numbers and to be moving in trench slides (Figure 1B; Supplementary Figure S3), suggesting that even in absence of a clear geochemical fingerprint, cable bacteria persist.

The cable bacteria's COC shows that the majority of oxygen is consumed by cable bacterial respiration at these time points. This

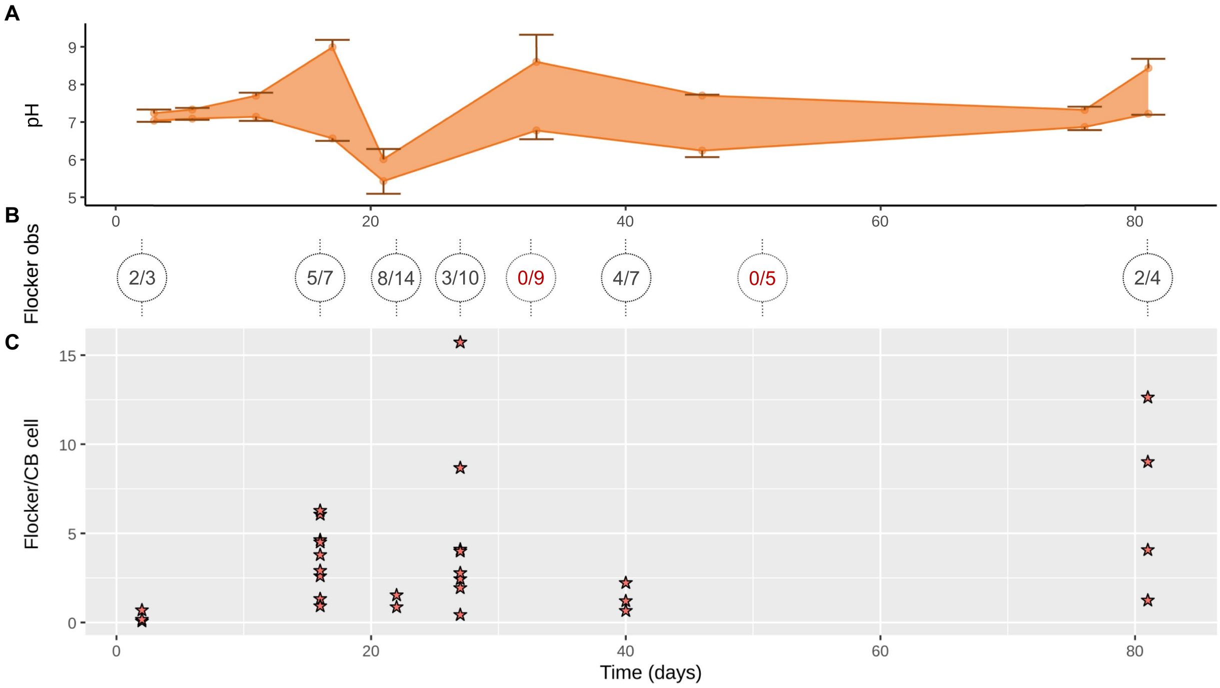

FIGURE 2
(A) Range of pH minima and maxima in the anoxic zone (down to 13 mm) where cable bacteria and flockers were observed (mean±SD, *n*=2–4). **(B)** Flocking observed over 1–4 days (on trench slides during TS2) in x/y where x is number of trench slides with successful flocking observations with y as total observation attempts, circles show individual time points with lines indicating the time points the sediment originated from; red, no detected flocking. **(C)** Flocking was often observed in multiple instances on a single trench slide, each instance is represented by a star. Each star indicates the number of flocking bacteria per cable bacterium cell within 50 μm on each side of the cable bacteria filament in a single still frame of a high-quality video of the given time point.

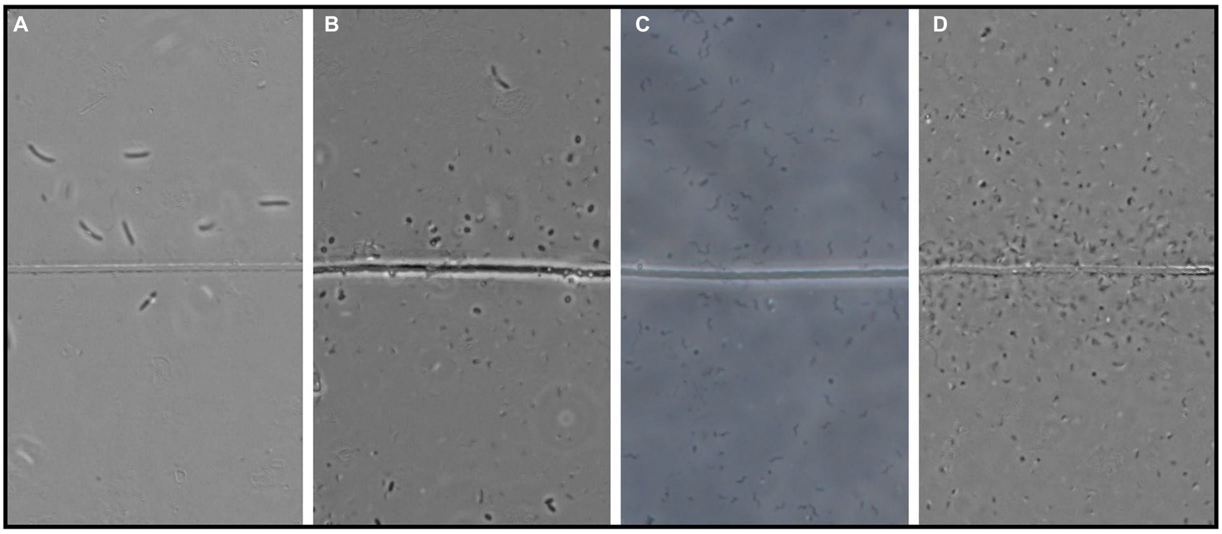

FIGURE 3
Four examples of the observed flocker morphologies. **(A)** Large curved rods, **(B)** Coccoids, **(C)** Spirillae, and **(D)** Vibrioids. "Line" in the middle is the cable bacteria filament. Scale bar, 5 μm.

COC, combined with a retreating OPD, may push (micro-) aerobic bacteria, that live at the oxic-anoxic interface, to resort to alternatives such as donating their electrons through interspecies electron transport to the cable bacteria, instead of directly to oxygen. If donor concentrations are higher below the oxic-anoxic interface, this might be a favorable option for a flocking bacterium. Bjerg et al. (in press) suggested that the electron donors might be either sulfide, organic compounds or even Fe^{+2} with an unknown soluble mediator as an intermediary. A closer look at the gradients of these electron donors below the oxic-anoxic interphase might shed light on why these

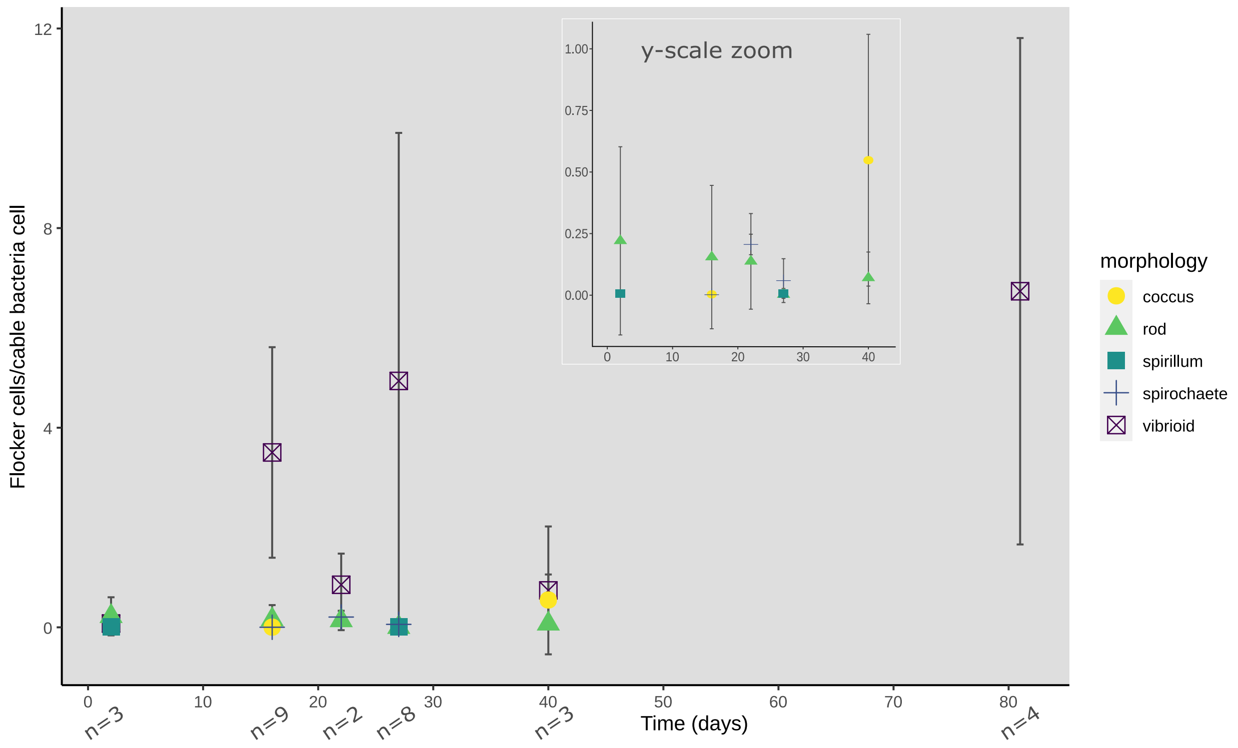

FIGURE 4
Morphologies of flocking cells normalized against cable bacteria cells observed per time point of TS2. Inset shows y-axis zoomed onto 0–1.0 flocking cells/cable bacteria cells until day 40 for low abundancy flocking morphologies. Absence of a morphology-indicator at a certain timepoint depicts zero observed cells of that morphology, with n showing the number of video-frames used for cell counting.

flocking bacteria are attracted to cable bacteria rather than trying to find oxygen.

4.2. Flocker occurrence and morphology

In each observation of flocking, we identified different morphologies and sizes of flockers as previously described by Bjerg et al. (in press). Out of the five different morphologies of flockers, the most prominently present were vibrioids, however this category also encompassed cells that were too small to determine differences in morphology by light microscopy (Figures 3, 4). The second largest group was described by rod-shaped flockers and followed a downward trend while the vibrioids were increasing over time and were the sole morphology observed on day 81 (Figures 3, 4). The other morphologies: cocci, spirilla, and spirochaetes, were only sporadically present and in low abundances (Figures 3, 4). The different morphologies we described were present at almost every time point in this study, which shows that the flocking community was not made up of a singular species of bacterium (Figure 4). Most of the observed flocking cells were small (0.5–1 × 0.9–2 μm; Supplementary Figure S4). Cell sizes of flockers that we recorded in this study diverge from Bjerg et al. (in press), who reported more medium sized cells (1 × 2–3 μm) than we do here (Supplementary Figure S4). Such a clear majority of small cells could be explained by a lower motility cost for smaller cells (Mitchell, 2002). The diverse cell sizes and morphologies do not provide specific taxonomic information but underline previous findings of high taxonomic diversity among the flockers, which suggests that they use a common mechanism of interspecies interaction. One such mechanism could be interspecies electron transfer, provided by electron shuttles not produced by specific bacterial species but intrinsic to the sediment, for example humic substances or flavins (Monteverde et al., 2018; Bjerg et al., in press).

Contrary to our initial expectation, flocking was present for the majority of the cable bacteria's succession in the sediment (Figures 1A,B, 2C). Flocking appeared already on day 3 of the cores' lifetime suggesting that the flocking bacteria are carried over when the core is inoculated. Cable bacteria are unlikely to be limited in electron donors at such an early stage in the life of the core. This is evident from the rapid increase in cable bacterial density in the first days and suggests an exponential increase congruent with low to no resource limitation. Flocking thus does not appear limited to periods of low electron donor availability for the cable bacteria. The disappearance of flocking on days 33 and 56 is puzzling, as these appear not any different from days where flocking is present, according to the measured parameters. This absence could be due to the limitations of flocking detection, as the trench slides became very crowded around 20–40 days into the incubation period (Supplementary Figures S1, S3), and very seldom free-laying cable bacteria were encountered. Finally, flocking was observed on the last days of the incubation. Non-moving cable bacteria, without connection to oxygen, and sometimes fragmented with partially degraded cells (therefore presumed dead), were often encountered in these trench slides, likely washed out from the central sediment trench when the slide was made. Flocking was never observed around these dead cable bacteria but was very prevalent around the few remaining living filaments, which were characterized by their high motility, length, and with almost always flocking on them. If the flockers were beneficial to cable bacteria, this could explain the perceived health of these surviving filaments, suggestive of the flockers' providing electron donors to the cable filament at what is likely starving conditions. Alternatively, a parasitic relationship between flocker and cable bacterium would have the flockers attracted to the few remaining active cable bacteria in the slide.

There is no apparent pattern between the measured parameters in this study: pH, EP, O_2, and the appearance of flockers around cable bacteria. This strongly suggests that flocking is governed by parameters not measured yet or not measured at sufficiently fine scale. Flocking occurs in a zone around 50–100 μm distance from a cable bacterium (Bjerg et al., in press). It is currently unknown and difficult to measure how the fine scale gradients in the trench slides directly around the cable bacteria filaments and thus in the 'flocking ranges' are. Especially, when we consider the cable bacterial metabolism of sulfide oxidation, strongly influencing both sulfide and sulfate availability and pH due to proton release within the "flocker range," possibly generating strong gradients close to the filaments. A better understanding of the fine scale gradients of pH and sulfide around the cable bacteria, in the flocking area, which are created by the cable bacteria's metabolism would tell us whether these environmental parameters are relevant for the flocker community. It may be more useful to do manipulation experiments in the starvation phase near the end of the incubation as a response to addition of a suitable electron donor for cables, or flocking bacteria should be more evident. With flocking showing up so early and so late in the incubation's timeline, it is increasingly likely that any electron shuttle is endemic to the sediment, rather than produced by cables or flockers. Electron shuttle usage is highly dependent on the presence of shuttles, therefore we suggest to measure this as a parameter, combined with on-slide fine scale geochemistry, to get a step closer to whether flocking is a form of shuttle-based IET.

4.3. Conclusion

Candidatus Electronema aureum GS showed activity and succession patterns comparable to enrichments of marine and freshwater cable bacteria populations.

Diverse flocking bacteria were observed around cable bacteria throughout the succession of *Ca.* Electronema aureum GS, independent of relative abundance or sediment pH. Our main conclusion is that as long as there are actively electron-conducting cable bacteria filaments present, flockers can be seen around these.

Data availability statement

The datasets presented in this study can be found in online repositories. The names of the repository/repositories and accession number(s) can be found in the article/Supplementary material.

Author contributions

JL and LB conceived experiments. JL, LB, JB, and AS designed experiments. JL, LB, and JB conducted experiments. JL, JB, LB, IM, and LN performed the analyses. JL, JB, LN, AS, and IM wrote the manuscript with input from all authors. All authors contributed to the article and approved the submitted version.

Funding

This research was financially supported by the Danish National Research Foundation (grant DNRF136 to LN) and the Carlsberg Foundation (grants CF19-0666 and CF21-0409 to JB).

Acknowledgments

Lykke Bamdali, Britta Poulsen, Marie Rosenstand Hansen, and Susanne Nielsen are thanked for their excellent support with the molecular work. Lars Borregaard Pedersen and Ronny M. Baaske have our gratitude and thanks for microsensor production and support and helping with sieving and retrieving sediment. We would also like to thank Ugo Marzocchi and Lars Riis Damgaard for helpful insights into data analyses.

Conflict of interest

The authors declare that the research was conducted in the absence of any commercial or financial relationships that could be construed as a potential conflict of interest.

Publisher's note

Supplementary material

The Supplementary material for this article can be found online at: https://www.frontiersin.org/articles/10.3389/fmicb.2023.1008293/full#supplementary-material

References

Bjerg, J. J., Lustermans, J. J. M., Marshall, I. P. G., Mueller, A. J., Brokjær, S., Thorup, C. A., et al. (in press). Cable bacteria with electric connection to oxygen attract flocks of diverse bacteria. *Nat. Commun.*

Burdorf, L. D. W., Tramper, A., Seitaj, D., Meire, L., Hidalgo-Martinez, S., Zetsche, E. M., et al. (2017). Long-distance electron transport occurs globally in marine sediments. *Biogeosciences* 14, 683–701. Available at:. doi: 10.5194/bg-14-683-2017

Callahan, B. J., McMurdie, P. J., Rosen, M. J., Han, A. W., Johnson, A. J. A., and Holmes, S. P. (2016). DADA2: high-resolution sample inference from Illumina amplicon data. *Nat. Methods* 13, 581–583. Available at:. doi: 10.1038/NMETH.3869

Damgaard, L. R., Risgaard-Petersen, N., and Nielsen, L. P. (2014). Electric potential microelectrode for studies of electrobiogeophysics. *J. Geophys. Res. G: Biogeosci.* 119, 1906–1917. doi: 10.1002/2014JG002665

Herlemann, D. P., Labrenz, M., Jürgens, K., Bertilsson, S., Waniek, J. J., and Andersson, A. F. (2011). Transitions in bacterial communities along the 2000 km salinity gradient of the Baltic Sea. *ISME J.* 5, 1571–1579. doi: 10.1038/ismej.2011.41

Liu, F., Wang, Z., Wu, B., Bjerg, J. T., Hu, W., Guo, X., et al. (2021). Cable bacteria extend the impacts of elevated dissolved oxygen into anoxic sediments. *ISME J.* 15, 1551–1563. doi: 10.1038/s41396-020-00869-8

Martin, M. (2011). Cutadapt removes adapter sequences from high-througput sequencing reads. *EMBnet J.* 17:10, 10–12. doi: 10.14806/ej.17.1.200

Marzocchi, U., Thorup, C., Dam, A. S., Schramm, A., and Risgaard-Petersen, N. (2022). Dissimilatory nitrate reduction by a freshwater cable bacterium. *ISME J.* 16, 50–57. doi: 10.1038/S41396-021-01048-Z

McMurdie, P. J., and Holmes, S. (2013). Phyloseq: an R package for reproducible interactive analysis and graphics of microbiome census data. *PLoS One* 8:e61217:e61217. doi: 10.1371/journal.pone.0061217

Meysman, F. J. R., Risgaard-Petersen, N., Malkin, S. Y., and Nielsen, L. P. (2015). The geochemical fingerprint of microbial long-distance electron transport in the seafloor. *Geochim. Cosmochim. Acta* 152, 122–142. doi: 10.1016/j.gca.2014.12.014

Mitchell, J. G. (2002). The energetics and scaling of search strategies in bacteria. *Am. Nat.* 160, 727–740. doi: 10.1086/343874

Monteverde, D. R., Sylvan, J. B., Suffridge, C., Baronas, J. J., Fichot, E., Fuhrman, J., et al. (2018). Distribution of extracellular Flavins in a coastal Marine Basin and their relationship to redox gradients and microbial community members. *Environ. Sci. Technol.* 52, 12265–12274. doi: 10.1021/acs.est.8b02822

Otte, J. M., Harter, J., Laufer, K., Blackwell, N., Straub, D., Kappler, A., et al. (2018). The distribution of active iron-cycling bacteria in marine and freshwater sediments is decoupled from geochemical gradients. *Environ. Microbiol.* 20, 2483–2499. doi: 10.1111/1462-2920.14260

Pfeffer, C., Larsen, S., Song, J., Dong, M., Besenbacher, F., Meyer, R. L., et al. (2012). Filamentous bacteria transport electrons over centimetre distances. *Nature* 491, 218–221. doi: 10.1038/nature11586

Quast, C., Pruesse, E., Yilmaz, P., Gerken, J., Schweer, T., Yarza, P., et al. (2012). The SILVA ribosomal RNA gene database project: improved data processing and web-based tools. *Nucleic Acids Symp. Ser.* 41, D590–D596. doi: 10.1093/nar/gks1219

Revsbech, N. P. (1989). An oxygen microsensor with a guard cathode. *Limnol. Oceanogr.* 34, 474–478. doi: 10.4319/lo.1989.34.2.0474

Revsbech, N. P., and Jørgensen, B. B. (1986) *Microelectrodes: Their use in microbial ecology in Advances in Microbial Ecology*. ed. K. C. Marshall (Springer Science and Business, Media, LLC, Boston MA), 293–352.

Risgaard-Petersen, N., Kristiansen, M., Frederiksen, R. B., Dittmer, A. L., Bjerg, J. T., Trojan, D., et al. (2015). Cable bacteria in freshwater sediments. *Appl. Environ. Microbiol.* 81, 6003–6011. doi: 10.1128/AEM.01064-15

Risgaard-Petersen, N., Revil, A., Meister, P., and Nielsen, L. P. (2012). Sulfur, iron-, and calcium cycling associated with natural electric currents running through marine sediment. *Geochim. Cosmochim. Acta* 92, 1–13. doi: 10.1016/j.gca.2012.05.036

Schauer, R., Risgaard-Petersen, N., Kjeldsen, K. U., Tataru Bjerg, J. J., B Jørgensen, B., Schramm, A., et al. (2014). Succession of cable bacteria and electric currents in marine sediment. *ISME J.* 8, 1314–1322. doi: 10.1038/ismej.2013.239

Schindelin, J., Arganda-Carreras, I., Frise, E., Kaynig, V., Longair, M., Pietzsch, T., et al. (2012). Fiji: an open-source platform for biological-image analysis. *Nat. Methods* 9, 676–682. doi: 10.1038/nmeth.2019

Scilipoti, S., Koren, K., Risgaard-Petersen, N., Schramm, A., and Nielsen, L. P. (2021). Oxygen consumption of individual cable bacteria. *Sci. Adv.* 7, 1–6. doi: 10.1126/sciadv.abe1870

Thorup, C., Petro, C., Bøggild, A., Ebsen, T. S., Brokjær, S., Nielsen, L. P., et al. (2021). How to grow your cable bacteria: establishment of a stable single-strain culture in sediment and proposal of Candidatus Electronema aureum GS. *Syst. Appl. Microbiol.* 44:126236. doi: 10.1016/J.SYAPM.2021.126236

Vasquez-Cardenas, D., van de Vossenberg, J., Polerecky, L., Malkin, S. Y., Schauer, R., Hidalgo-Martinez, S., et al. (2015). Microbial carbon metabolism associated with electrogenic Sulphur oxidation in coastal sediments. *ISME J.* 9, 1966–1978. doi: 10.1038/ismej.2015.10

Xu, X., Huo, S., Zhang, H., Li, X., and Wu, F. (2021). Identification of cable bacteria and its biogeochemical impact on sulfur in freshwater sediments from the Wenyu River. *Sci. Total Environ.* 769:144541. doi: 10.1016/J.SCITOTENV.2020.144541

Frontiers in
Microbiology

Explores the habitable world and the potential of microbial life

The largest and most cited microbiology journal which advances our understanding of the role microbes play in addressing global challenges such as healthcare, food security, and climate change.

Discover the latest Research Topics

See more →

Frontiers in
Microbiology

Frontiers

Avenue du Tribunal-Fédéral 34
1005 Lausanne, Switzerland
frontiersin.org

Contact us

+41 (0)21 510 17 00
frontiersin.org/about/contact